Wrocław University of Technology
Centre of Advanced Materials and Nanotechnology

Materials Science
Poland

E-MRS 2004 Fall Meeting
Warsaw, Poland, 6-10 September, 2004

Guest Editors:
Krzysztof Jan Kurzydłowski
Marek Niezgódka
Erich Wimmer

Vol.23   •   No. 2   •   2005

Materials Science is an interdisciplinary journal devoted to experimental and theoretical research into the synthesis, structure, properties and applications of materials.

Among the materials of interest are:
- glasses and ceramics
- sol-gel materials
- photoactive materials (including materials for nonlinear optics)
- laser materials
- photonic crystals
- semiconductor micro- and nanostructures
- piezo-, pyro- and ferroelectric materials
- high-T_c, superconductors
- magnetic materials
- molecular materials (including polymers) for use in electronics and photonics
- novel solid phases
- other novel and unconventional materials

The broad spectrum of the areas of interest reflects the interdisciplinary nature of materials research. Papers covering the modelling of materials, their synthesis and characterisation, physicochemical aspects of their fabrication, properties and applications are welcome. In addition to regular papers, the journal features issues containing conference papers, as well as special issues on key topics in materials science.

Materials Science is published under the auspices of the Centre of Advanced Materials and Nanotechnology of the Wrocław University of Technology, in collaboration with the Institute of Low Temperatures and Structural Research of the Polish Academy of Sciences and the Wroclaw University of Economics.

All accepted papers are placed on the Web page of the journal and are available at the address:
http://MaterialsScience.pwr.wroc.pl

From the Guest Editors

The European Materials Research Society (E-MRS) 2004 Fall Meeting was held from 6th to 9th September 2004 in Warsaw, at Warsaw University of Technology, the largest technical university in Poland. The 2004 E-MRS Fall Meeting consisted of Plenary Sessions, 9 parallel interdisciplinary symposia, each involving oral and poster presentations, and three satellite events.

The symposium 'Computational Materials Science' was jointly organised by the Faculty of Materials Science of Warsaw University of Technology, the Interdisciplinary Centre for Mathematical and Computational Modelling of Warsaw University, and Materials Design, s.a.r.l., of Le Mans, France. The main objective was to bring together scientists from the 'old' European Union countries and worldwide with those in the EU New Member States working on numerical calculations in materials science. An important aspect, as with all E-MRS events, was the involvement of young scientists with the objective of increasing their knowledge and experience and interacting with world renowned experts in their field of interest. The symposium programme focussed on the following aspects;

- Connection between ab initio computations and macroscopic materials properties.
- Mechanical properties on materials.
- Prediction of temperature-dependent properties of materials.
- Structural, electronic and magnetic properties of solids, surfaces and interfaces.
- Surfaces and catalysis.
- Computational approaches for excited states.
- Magnetism, f-electron materials, and strongly correlated systems.
- Molecular systems.
- Computational approaches for nanostructures.
- Visualisation, image processing and analysis.

The symposium was attended by 80 participants from 13 countries in Europe, Asia and America. 18 invited lectures, 23 oral contributions and 39 posters were presented. In our opinion, shared by the participants, the symposium was highly motivating, as confirmed by numerous animated, but friendly, discussions within the formal sessions and during the breaks. The success of the symposium was due to the involvement of all participants, but particularly the invited speakers. We wish to express thanks and appreciation to all of them and to our colleagues, particularly Tomasz Wejrzanowski and Joanna Zdunek for their assistance in preparing the symposium making this publi-

cation possible. For a number of technical and practical reasons a few papers presented at the symposium will be published in later editions of Materials Science-Poland.

Krzysztof Jan Kurzydłowski,
Marek Niezgódka,
Erich Wimmer

Contents

594

The growing importance of computations in materials science. Current capabilities and perspectives

ERICH WIMMER[*]

Materials Design s.a.r.l, 44, av. F.-A. Bartholdi, 72000 Le Mans, France

Materials scientists are facing unprecedented challenges in many areas, such as energy conversion and storage, microelectronics, telecommunication, display technologies, catalysis, and structural materials. Experimental methods generate increasing amounts of data. New computational methods, high-performance computer hardware, and powerful software environments are evolving rapidly. As a result, the importance of computational materials science is growing. The following cases illustrate the current capabilities: computed thermochemical and mechanical properties of metal hydrides show trends in the heats of formation and the hydrogen-induced softening of elastic moduli; a study of the effect of impurities on the strength of a Ni grain boundary reveals hydrogen as an embrittler and boron as a strengthener; *ab initio* phonon calculations for hydrogen impurities in aluminum show a temperature-dependent site-preference; the screened-exchange approach predicts accurate energy band gaps of semiconductors; a computational screening of hydro-desulphurization catalysts points to new combinations. The major current challenges for computational materials science include more accurate total energies, unified methods to deal with multi-phase systems, e.g., solid/liquid, novel approaches to determine complex kinetic processes, and novel concepts to bridge the atomistic and the macroscopic scales.

Key words: *computations; property predictions; ab initio*

1. Background

1.1. Challenges for materials science

Our societies depend more than ever on a wide range of materials with specialized properties. For example, the transition to a hydrogen economy requires the development of viable materials for hydrogen storage. The current generation of materials is inadequate and intense worldwide research efforts are directed at the discovery and development of novel materials. In fact, the search for alternative forms of energy and

---

[*]E-mail: ewimmer@materialsdesign.com.

energy conversion systems has gained an unprecedented level of urgency. At the same time, concerns about the environment and the emission of greenhouse gases makes the quest for reliable, environmentally responsible, and globally sustainable energy systems for transportation, heating, refrigeration, and lighting even more difficult. New materials play a central role in meeting these challenges.

Communication, display technologies, and data storage are other major driving forces for the development of new materials and materials processes. For example, the discovery of the giant magnetoresistance effect (i.e. the change of the electrical conductivity due to an external magnetic field) has led to major progress in the storage capacity of magnetic disks. The development of GaN-based semiconductors has a profound impact on display technologies and lighting systems. Digital cameras are revolutionizing photography. Underlying this "disruptive technology" are charged-coupled devices used as photo-sensors which replace silver halides, light-sensitive organic pigments, and time-consuming chemical processes. However, the long-term storage of digital information is by no means guaranteed and may require new materials and technologies.

As the chemical industry strives for cleaner and environmentally sustainable processes, catalysts with high reactivity, selectivity, and durability play a central role in achieving these goals. For many of these processes, the reaction mechanisms are not understood and the development of catalytic systems is pursued by tedious empirical approaches.

1.2. The role of computational approaches

During the past decades, computational materials science has made major strides in becoming a predictive discipline, impacting fundamental science as well as the development programs of industrial materials. This progress is particularly striking for *ab initio* electronic structure methods, which are the major focus of the present conference contribution. The development of novel computational methods, algorithms, and implementations in the form of computer programs is fuelled by the breathtaking progress in computer hardware and software.

There are three major reasons for computations in materials science, namely (i) to gain a deeper understanding of materials on the atomic scale, (ii) to interpret experimental data, and (iii) to predict physical and chemical properties of materials prior to experiments.

Most materials in use are not in thermodynamic equilibrium with their environment. For example, all steel constructions in contact with the atmosphere are subject to a thermodynamic driving force towards oxides (they corrode); the complex multilayer structures forming microelectronic devices have a tendency to degrade by electromigration, diffusion and precipitation of stable phases; organic materials exposed to air, sunlight, and moisture eventually degrade to molecular systems with lower chemical potentials, ending at carbon dioxide, water, and similar small molecules.

This non-equilibrium character of materials has major consequences. It links the properties of a material intimately with the processing condition. Contrary to small molecules in the gaseous or liquid phase, solid-state materials can exhibit structures on the nano- and micro-scale, which can be decisive for their macroscopic properties. For example, the grain structure of an alloy determines the fracture toughness of a material.

In fact, structural control on the nanoscale has recently aroused considerable excitement and with good reason: starting with a small number of molecular-scale building blocks, an endless number of combinations (materials) can be created, each with different properties. Examples are the many possible forms of nanotubes and nanostructured surfaces for coatings, catalysts and sensors.

In view of all these factors, one has to conclude that computational materials science is well positioned to continue its growth and importance, helping to meet the many challenges to materials science. It is also clear that the computational materials science journey has just begun and that there are vast opportunities before us, which need to be conquered. The following sections provide a brief overview of current computational methods and a selection of illustrative examples. An analysis of the current situation and a perspective on future developments will conclude this contribution.

1.3. Theoretical foundation and computational approaches

Figure 1 illustrates the hierarchy of theoretical concepts and approaches used in computational materials science. Macroscopic systems are described by continuum
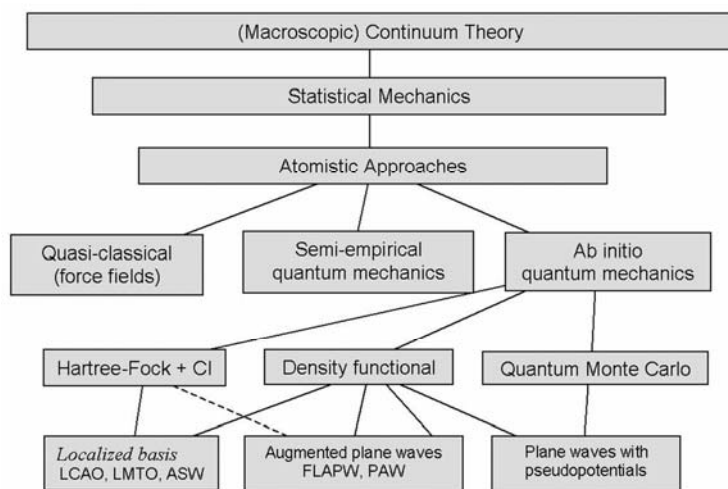
Fig. 1. Hierarchy of computational approaches for the description of molecular and solid state systems. An explanation of the abbreviations is given in the text

theory using analytical models and numerical finite element methods (FEM). In fact, FEM structural analysis and computational fluid dynamics (CFD) have become major tools in the design of cars, aircrafts, buildings, bridges, and many other engineered objects. As the resolution of FEM methods is refined, the atomistic nature of matter comes into play. It is a most intriguing question, at what scale does the atomistic aspect need to be taken into account to describe a given material and property. Is it possible to apply *ab initio* methods to systems so large that one can step directly from the *ab initio* level to continuum theory?

Statistical mechanics provides the link between assemblies of atoms and properties of macroscopic materials. The critical connection between atomistic approaches and statistical mechanics is the total energy of a system as a function of the position of the atoms in an assembly. As will be shown in the examples, the ability to compute the total energy for any type of atoms, in any arrangement, with sufficient accuracy and speed has become the cornerstone of today's computational materials science.

For convenience, the key thermodynamic and quantum mechanical definitions and formulas are given in the following section. Readers interested in the practical applications rather than the background can safely skip this theoretical part.

The Gibbs free energy is defined as

$$G = E_{\text{int}} + PV - TS \tag{1}$$

with the internal energy, E_{int}, given by

$$E_{\text{int}} = E_{\text{el}} + E_{\text{kin}} \tag{2}$$

For typical systems, the dominant term is the electronic energy, E_{el}, which includes the kinetic energy of the electrons, the electrostatic attraction between electrons and nuclei, and the repulsion between electrons and between nuclei. E_{kin} denotes the kinetic energy of moving nuclei. In the case of a solid, the kinetic energy can be written as

$$E_{\text{kin}} = E_{\text{zp}} + E_{\text{vib}} \tag{3}$$

where E_{zp} is the zero-point energy and E_{vib} the vibrational energy relative to the lowest vibrational state.

The terms P, V, and T are pressure, volume, and temperature, respectively. The entropy of a solid is given by

$$S = S_{\text{vib}} + S_{\text{config}} \tag{4}$$

with S_{vib} being the vibrational entropy and S_{config} the configurational entropy. It is now possible to compute the electronic energy as well as the zero-point energy, the vibrational internal energy, and the vibrational entropy by *ab initio* quantum mechanical methods for systems with up to approximately 100 atoms per unit cell. This capability has opened many exciting avenues, as will be illustrated in this contribution.

1.4. Atomistic approaches

On the atomic scale, three basic approaches are used, namely *ab initio* quantum mechanics, quasi-classical approaches using force fields, and semiempirical methods. By definition, *ab initio* methods are based on fundamental physical laws and constants and there are no system-specific parameters. In contrast, quasi-classical methods use interaction potentials (force fields) and parameters to describe interatomic interactions. There is a trade-off in computational efficiency and predictive capability between *ab initio* and force-field methods. A word of caution: force-field methods can be more accurate than *ab initio* methods, in particular in the description of weakly interacting systems (e.g. layers of graphite, methane molecules, and polymer chains). However, reliable and transferable force-fields for inorganic materials are difficult, or perhaps impossible, to construct. Semi-empirical methods try to strike a compromise between the rigour of electronic structure methods and the computational efficiency of parameterized force-field methods. Tight-binding theory and embedded atom or effective medium theory belongs to this class of approaches.

Ab initio methods have gained a prominent place in the description of inorganic solid-state materials while force-field methods and semi-empirical methods continue to be hampered by tedious, system-specific parameter developments.

Within *ab initio* electronic structure methods, there are currently two major many-electron theories in use, and a third approach is emerging. The two main approaches are (i) the Hartree-Fock theory with configuration interaction expansions of the many-electron wave function and (ii) density functional theory (DFT) [1] in its spin-polarized form [2] with the semi-local generalized gradient approximation (GGA) [3]. The third and emerging many-body approach is quantum Monte Carlo (QMC) method [4]. At present, DFT dominates *ab initio* computational materials science.

One of the basic tasks of quantum mechanical computations is determination of the total energy, E, of a given system as a function of the position of the atoms. This is accomplished by solving Schrödinger's equation

$$\mathbf{H}\,\Psi = E\Psi \tag{5}$$

where the Hamiltonian, $\mathbf{H}$, defines the position and charge of the atomic nuclei in the system and Ψ denotes the many-electron wave function.

In DFT, the many-electron Eq. (5) is mapped onto a set of effective one-electron equations. Each of these is a one-particle Schrödinger's equation of the form

$$\boldsymbol{h}\psi_i = \varepsilon_i \psi_i \tag{6}$$

where $\boldsymbol{h}$ is an effective, one-electron Hamiltonian, ε_i are one-particle eigen values, and ψ_i are effective one-electron wave functions. Eqs. (6) are called the Kohn–Sham equations.

The total electron density, ρ, links the Kohn–Sham equations with the original many-electron Schrödinger's equation by

$$\rho = \Psi^* \Psi = \sum_i \psi_i^* \psi_i \qquad (7)$$

In current electronic structure methods of molecular and solid-state systems, the one-electron wave functions, ψ_i, are expanded in a variational basis set, $\{\varphi_j\}$

$$\psi_i = \sum_j c_{ij} \varphi_j \qquad (8)$$

Since the choice of the basis set is so important, specific computational methods are often named after the type of the basis set. This is the case for localized basis sets using Gaussian functions, which belong to the class of methods called linear combination of atomic orbital (LCAO) methods. It is the case for the linearized muffin-tin orbitals (LMTO) and the full-potential linearized augmented plane wave (FLAPW) methods, and it applies to pseudopotential plane wave methods. It would be beyond the scope of the present paper to review each of these methods. The interested reader is referred to review articles such as Ref. [5] and the references therein.

During recent decades, there have been heated discussions about the virtues of all-electron methods such as FLAPW versus pseudopotential methods using plane waves. During the past decade, a remarkable synthesis has been achieved between all-electron methods and pseudopotential plane wave methods by the development of the projector augmented wave (PAW) method [6] as implemented notably in the Vienna *ab initio* simulation package (VASP) [7]. This approach combines the physical aspects of all-electron methods with the elegance and computational efficiency of plane wave methods. Thus, a significant step has been achieved in advance of earlier non-local pseudopotentials and ultrasoft pseudopotentials.

2. Examples

2.1. Trends in metal hydrides

Metal hydrides are potential candidates for hydrogen storage materials. Computations are ideally suited to reveal systematic trends in the bonding geometry and the binding energy of hydrogen. Figure 2 shows such trends in the metal-hydrogen bond distance for hydrides of alkali metals, alkaline earth metals, and 3d-transition metals in cubic crystal structures.

There are three striking observations: (i) the experimental data are incomplete and computations fill in the missing data, (ii) the agreement between computed and available experimental data is excellent such that computed data can be used instead of experimental values, (iii) clear trends are visible across the transition metal series, which are not obvious using only experimental data.
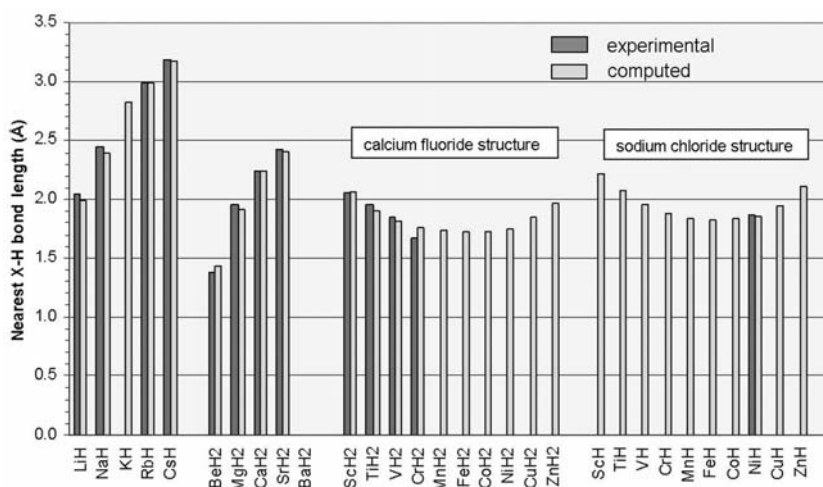
Fig. 2. Metal-hydrogen bond distances in cubic metal hydrides. Note the clear trends across the 3d-transition metal series. These trends become obvious only from the systematic computations

Figure 3 displays computed heats of formation for the reaction

$$M + \tfrac{1}{2} H_2 \rightarrow MH \tag{9}$$

with M being a transition metal and MH is a metal hydride in the rock salt structure.
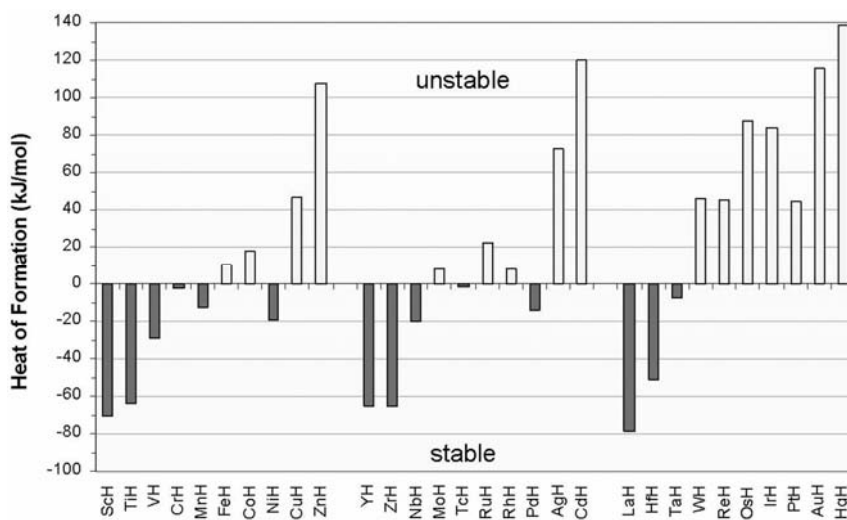
Fig. 3. Computed heats of formation of metal hydrides in the rocksalt structure

All calculations were performed on the DFT-GGA level of theory using VASP with PAW potentials. The reference state of the metal is the most stable crystalline form and gas phase molecules are used as the reference for hydrogen. In this study,

only the electronic part of the total energy is used, which is sufficient to establish the trends. The heat of formation decreases with an increasing number of d-electrons. Ni, Pd, and Pt are somewhat exceptional, which may be related to the ease of s-d re-hybridization.

2.2. Elastic moduli of crystalline solids

The second example demonstrates the calculation of mechanical properties on two simple systems, namely metallic nickel and nickel hydride. Nickel crystallizes with a face-centred-cubic structure. In NiH, all octahedral interstitial sites of this lattice are filled with hydrogen atoms, resulting in a rock salt structure as shown in Fig. 4.
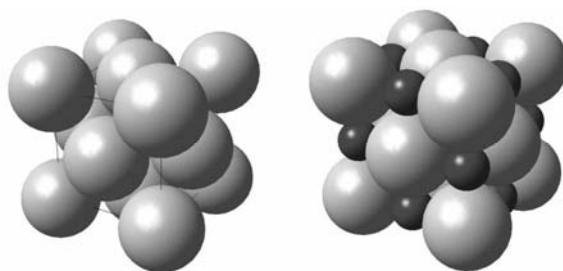
Fig. 4. Crystal structure of metallic nickel and nickel hydride

Ab initio calculations of the lattice parameter and the elastic moduli reveal an expansion of the lattice upon introduction of the hydrogen atoms. The bulk modulus remains almost unchanged, but the shear modulus and Young's modulus are reduced by more than 50%. The lowering of the shear modulus and Young's modulus imply a loss of stiffness of the material, i.e. given the same force of pulling on two opposite sides of a crystal, NiH extends more than metallic Ni.

Table 1. Computed equilibrium lattice parameters
and elastic moduli for nickel and nickel hydride

Parameter	Ni	NiH
Lattice parameter (Å)	3.50	3.72
Bulk modulus (GPa)	207	198
Shear modulus (GPa)	98	41
Young's modulus (GPa)	254	116

An illustrative example of the computational accuracy of elastic constants is given by the case of aluminum nitride (Table. 2). Given the relatively large deviation between the two experimental data sets and the fact that the computed values fall overall between the experimental data, it is difficult to say, which of the three sets is actually

the most reliable. In other words, it appears that the reliability of the computed data is comparable with that of experiment.

Table 2. Experimental and computed elastic constants, C_{ij}, and the bulk modulus of hexagonal aluminum nitride. All values are given in GPa

AlN	Experiment[a]	Experiment[b]	Computation
C_{11}	345	411	375
C_{12}	125	149	130
C_{13}	120	99	100
C_{33}	395	389	347
C_{44}	118	125	113
C_{66}	110	131	122
B	202	212	195

[a]K. Tsubouchi, N. Mikoshiba, IEEE Trans. Sonics Ultrason., SU-32, 634, 1985.
[b]L. E. McNeil, M. Grimsditch, R. H. French, J. Am. Ceram., Soc. 76, 1132, 1993.

This accuracy is a most remarkable accomplishment of *ab initio* electronic structure theory. No system-specific parameters are used in the computational procedures and yet the properties of computed materials are similar to the measured data.

The computation of elastic constants for any symmetry [8] and its automation within the software environments for computational materials science [9] has now become a routine task for many systems of significant complexity. For example, this approach has been successfully applied to a mineral known as "Schorl", which belongs to the tourmaline group and has a chemical composition of $NaFe_3B_3Al_6O_{27}(OH)_3F$.

2.3. Effect of impurities on the fracture at grain boundaries

The degradation of structural engineering materials used, for example, in nuclear power reactors, is a topic of a great importance. Despite this fact, the detailed understanding of degradation processes, in particular stress corrosion cracking, is still fragmentary and there is a great need to deepen our knowledge in this field.

In this context, the effect of alloying elements, impurity atoms and nuclear transmutation products including B, Cr, H, S, P, Li have been investigated using an *ab initio* approach [10]. A Ni $\Sigma 5$ {001} twist grain boundary was chosen as a prototypical case. The modelling approach of the effect of these impurity atoms on the strength of this grain boundary is illustrated in Fig. 5.

Starting with a model of a relaxed, pure grain boundary, an impurity atom is inserted into the grain boundary. Total energy calculations are used to determine interstitial vs. substitutional impurity sites. After relaxation, the total energy of the grain boundary with the impurity is obtained. Subsequently, the system is cleaved and each of the two surfaces is relaxed. From the difference of the total energy of the surface and the grain boundary, a cleavage energy (Griffith energy) is computed.
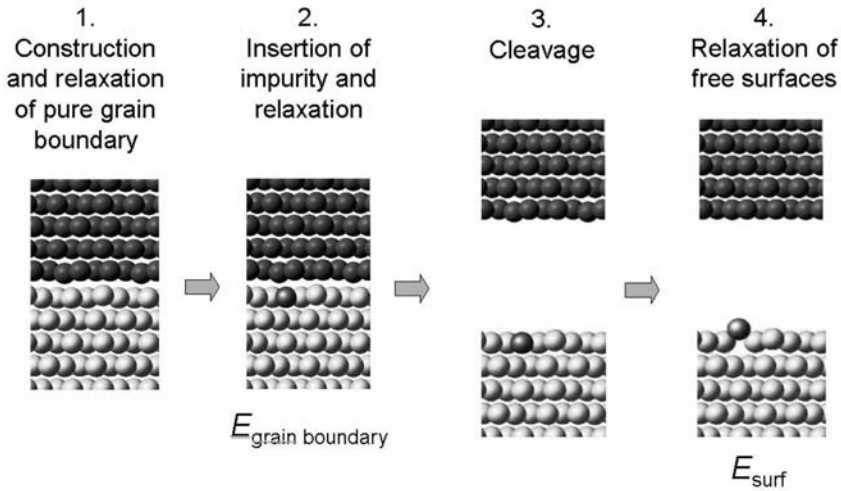
Fig. 5. Modelling of the cleavage of a grain boundary. Light and dark spheres
indicate atoms of the lower and upper grain

Figure 6 illustrates the results for a series of single impurities and selected pairs of impurities.
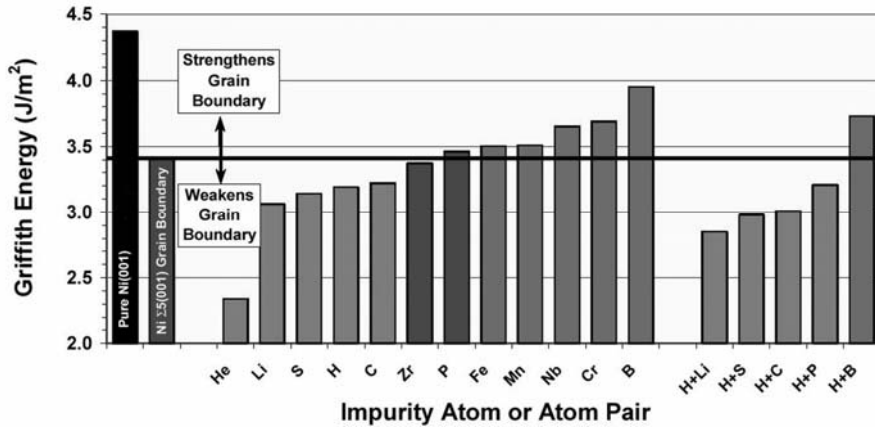
Fig. 6. Cleavage energy (Griffith energy) of bulk Ni in the (001) plane, a Ni Σ5 {001} twist grain
boundary, and a series of impurity atoms and impurity pairs in this grain boundary.
Note a strong weakening effect of He and Li and the strengthening of the grain boundary by boron

The cleavage energy of bulk Ni along the (001) plane is 4.4 J/m^2, which drops to 3.4 J/m^2 for a Σ5 twist grain boundary. The atoms He, Li, S, H, and C are found to weaken this grain boundary; Zr, P, Fe, and Mn are indifferent; and Nb, Cr, and especially B have a strengthening effect. Impurity pairs involving hydrogen show an additive effect on the grain boundary strength, which indicates only a weak interaction within impurity pairs.

This type of systematic, atom-by-atom comparison is a unique feature of computational modelling, since experimentally it is extremely difficult to measure the effect of each impurity atom under comparable conditions. All the calculations in this study were carried out with VASP using PAW potentials and the DFT-GGA level of theory.

2.4. Site preference of hydrogen in aluminum

The calculations discussed so far ignore any temperature dependence. Although many useful results can be obtained in this way, there are many cases, where temperature effects play a decisive role and therefore need to be included in the computational approach. An example is the behaviour of hydrogen impurities in bulk aluminum [11].

A fundamental question in the study of impurities in solids is the site preference. A conventional unit cell of an *fcc* lattice (Fig. 7) offers four octahedral and eight tetrahedral interstitial sites.

H at octahedral site   H at tetrahedral site
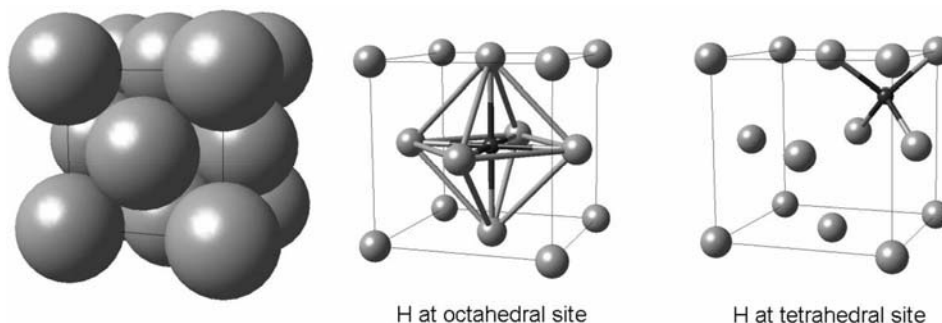
Fig. 7. Octahedral and tetrahedral interstitial sites in a face-centred cubic lattice

Using a 2×2×2 supercell containing 32 Al atoms, structural optimizations and total energy calculations show the tetrahedral site to be preferred by 12 kJ/mol compared to the octahedral site in terms of the electronic energy. However, the equilibrium of a system at finite temperature is governed by the Gibbs free energy, which contains the temperature dependence of the internal vibrational energy as well as vibrational and configurational entropy terms. In fact, low vibrational frequency modes lead to a large vibrational entropy, which lowers the Gibbs free energy at high temperature through the term $-TS$. Therefore, knowledge of the vibrational modes is a critical aspect of the system.

Using a direct phonon approach [12] and VASP, the phonon dispersion of a hydrogen impurity in aluminum was computed using a supercell of the composition $Al_{32}H$ with hydrogen in the octahedral and the tetrahedral sites. The results show (Fig. 8) that the vibrational modes associated with the hydrogen atom are shifted from 25.2 THz for H in the tetrahedral site to 10.8 THz in the octahedral site.
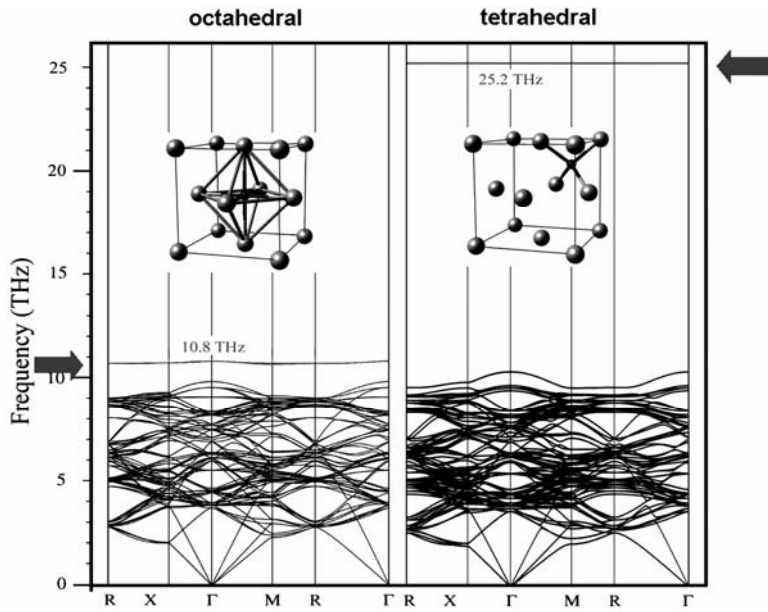
Fig. 8. Phonon dispersions of a hydrogen impurity in bulk aluminum at an octahedral
and tetrahedral interstitial site. Note the dramatic shift of the H-related phonon mode
(marked by arrows) between the octahedral and tetrahedral sites

As a consequence, the vibrational entropy at the octahedral site is significantly larger than at the tetrahedral site.

Figure 9 shows the difference in vibrational entropy between hydrogen in the tetrahedral and the octahedral sites.
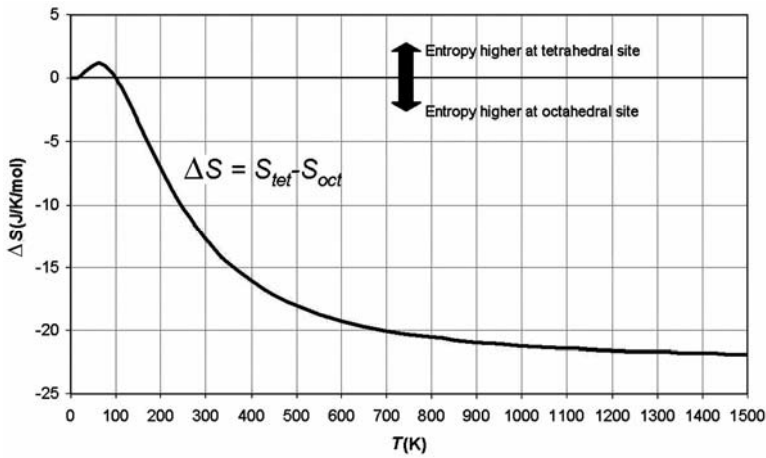
Fig. 9. Computed difference in the vibrational entropy of aluminum with a hydrogen impurity
at a tetrahedral and an octahedral interstitial site. For the most part, the entropy
at the octahedral site is significantly larger

As a consequence, the Gibbs free energy as a function of temperature, computed with *ab initio* theory with a phonon approach, reveals that the octahedral site is more stable for temperatures above about 400 K (Fig. 10).
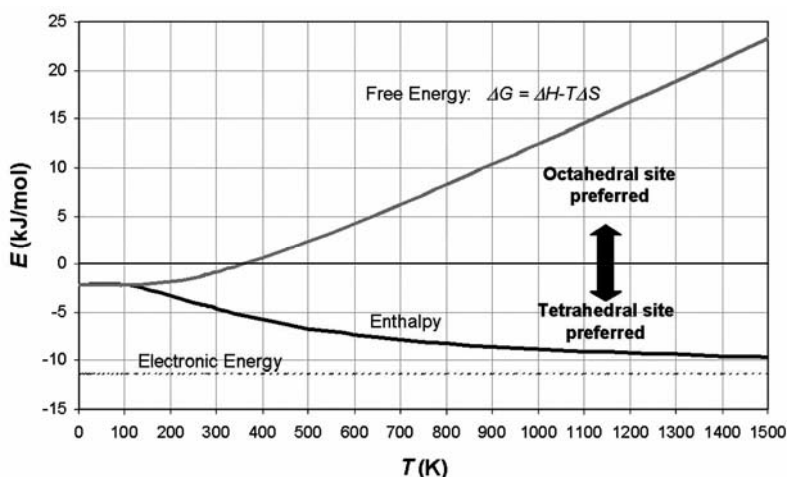
Fig. 10. Computed difference in the enthalpy and free energy of aluminum
with a hydrogen impurity at a tetrahedral and an octahedral interstitial site

The results also show the importance of the zero-point energy for hydrogen. At $T = 0$, the energy difference between the tetrahedral and the octahedral sites is only about 2 kJ/mol if zero-point energy effects are included, while the electronic energy itself gives an energy difference of 12 kJ/mol in favour of the tetrahedral site.

2.5. Band gaps in semiconductors

The previous examples deal with structural, mechanical, and thermochemical properties, although in each case, the electronic wave functions and the electron densities are computed implicitly. In this example of energy band gaps, the focus is on the electronic structure involving one-electron excitation energies.

In the development of density functional theory, it was not immediately understood why the computed band gaps in semiconductors were significantly too small. Progress over the past three decades has clarified this issue and novel methods have emerged, which allow the accurate prediction of energy band gaps. One of these methods is the so-called screened-exchange approach [13], which introduces a non-local part in the effective one-electron Hamiltonian of density functional theory.

This screened-exchange approach has been implemented in the FLAPW method, leading to a remarkable accuracy in the predictions of energy band gaps for a range of semiconducting materials [14], as shown in Fig. 11. Compared with the local density approximation (LDA), the sX results are in excellent agreement with experiment, especially for narrow-band gap semiconductors such as InAs.
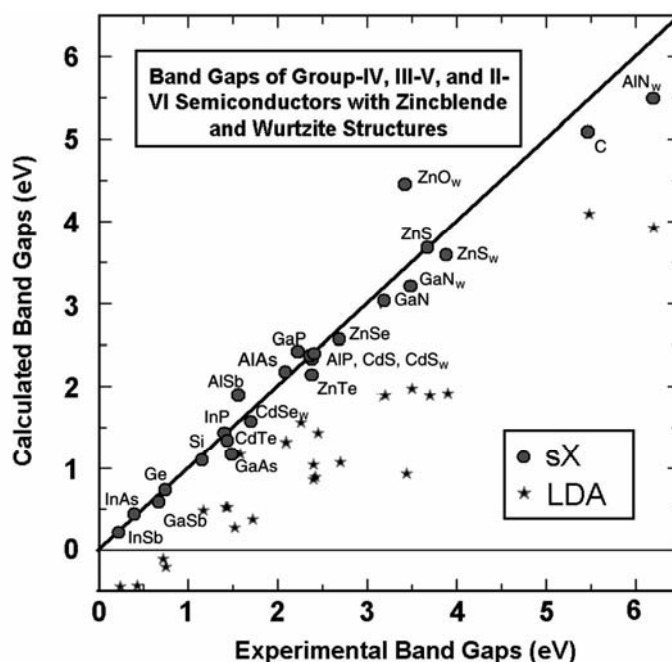
Fig. 11. Computed vs. experimental band gaps in elemental and binary semiconductors.
The screened-exchange (sX) results are shown as full circes and the results
from the local density approximation (LDA) are marked as stars (after Ref. 14)

The band gaps computed with the LDA are consistently too low, in some cases by
as much as 50%. For narrow band gap materials, LDA predicts a "negative" band gap,
i.e. the valence band and the conduction bands are predicted to overlap. Furthermore, the
LDA values show a large scatter. In other words, the deviation is not due to simple scaling.

2.6. Hydrodesulphurization catalysts

The final example is taken from the field of heterogeneous catalysis. The goal of
this research is the identification of the best catalytic materials, which bind selectively
sulphur-containing molecules and decompose them by reactions with molecular hy-
drogen. This process of hydrodesulphurization plays an important role in the produc-
tion of cleaner fuels (especially Diesel fuel) with reduced sulphur content.

The left side of Figure 12 shows experimentally determined catalytic activities for
a list of transition metal sulphides. Unfortunately, the best materials contain rare and
expensive transition metals such as ruthenium, osmium, and iridium. A large group of
cheaper transition metal sulphides exhibit little activity. Intuitively, one is tempted to
discard the poorly performing systems and focus the efforts on the best candidates.
But where would one start?
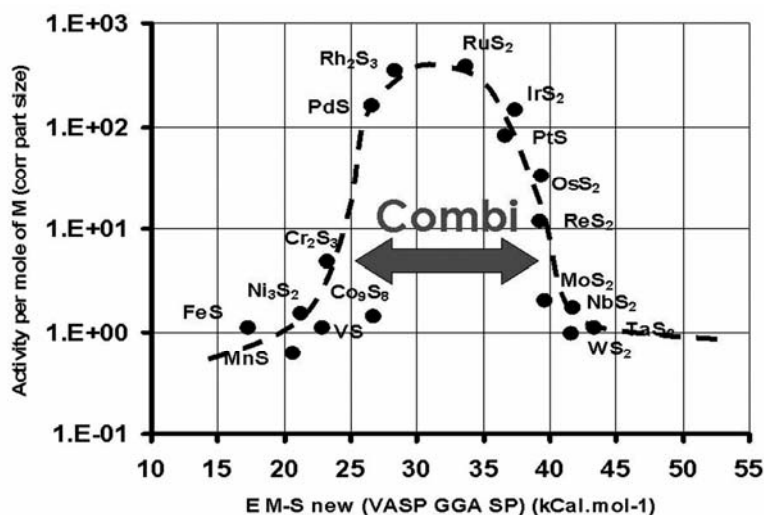
Fig. 12. Activity of metal sulfides in the catalytic hydrodesulfurization of dibenzothiophene vs. computed metal–sulfur bond strength. Experimental activity data are taken from Ref. 15

Researchers at the Institut Français du Pétrole (IFP) near Paris have developed a methodology, which tackles this challenge in an elegant and efficient way [16]. These researchers started with a concept initially proposed by Paul Sabatier at the beginning of the 20th century [17]. This principle states that a successful catalytic reaction of a molecule with a surface requires a binding between the molecule and the surface, which is neither too weak (the molecule would not stay on the surface long enough to react) nor too strong (the molecule would block the surface).

In the case of sulphur-containing molecules, it is plausible that the key interaction between the molecule and the surface is the metal–sulphur bonding. Now, if a molecule containing a sulphur atom binds to a metal atom at the surface of a sulphide, then the chemical environment of this metal atom resembles that of a bulk metal atom in that sulphide. This means that the bonding strength between a metal atom and sulphur of *bulk* sulphides contains information, which is pertinent to the catalytic activity.

To probe this idea, the researchers from the IFP under the leadership of H. Toulhoat formulated an approach to use electronic structure calculations to obtain bond strengths for systems such as transition metal sulphides. By taking experimental activity data as given in Table 3, for the bulk structures of the sulphides, they obtained a bond strength for each compound [16]. By plotting the catalytic activity as a function of this metal–sulphur bond strength, a remarkable correlation emerges in the form of a volcano curve (Fig. 12). Two classes of poorly performing catalysts emerge from this analysis. Some sulphides such as MnS bind too weakly and some compounds such as WS_2 too strongly.

Equipped with this understanding, the IFP researchers then proceeded to consider catalysts, which are combinations of sulphides from the left and the right of the peak

of the volcano. One such compound is MoS_2 combined with Co. In fact, Co-doped MoS_2 catalysts have been found earlier by empirical means and these catalysts are actually used in current processes. This validates the approach in a beautiful way. There is a large number of other possible combinations, which the current computational approach has identified, thus offering promising new candidates.

Table 3. Experimental activity data from Pecoraro and Chianelli [15] for the hydrodesulphurization of dibenzothiophene over transition metal sulphide catalysts

Metal sulphide	Activity	Metal sulphide	Activity
RuS_2	379.50	WS_2	3.20
OsS_2	216.30	NbS_2	1.70
IrS_2	171.80	Ni_3S_2	1.50
Rh_2S_3	106.10	Co_9S_8	1.40
ReS_2	39.40	VS	1.10
PtS_2	16.00	FeS	1.10
PdS	12.50	TaS_2	1.10
MoS_2	8.00	MnS	0.60
Cr_2S_3	4.80		

3. Perspectives

The current situation of computational materials science, which is illustrated by the examples discussed in this conference contribution, has opened the following exciting perspectives.

3.1. Computations have become a reliable source of materials property data

The accuracy of today's *ab initio* method has matured to a point, were properties including structural, mechanical and thermochemical properties can be calculated at a level of accuracy and reliability, which makes computations a viable source of primary materials property data. This capability is particularly valuable for systems such as point defects at low concentrations and interfaces, where experimental methods are difficult or impossible to perform. This use of computational materials science is likely to fill gaping holes in experimental data sets. For example, currently about 30,000 reliable crystal structures exist for known inorganic compounds. However, elastic constants for only several thousand are reported in literature. Computations can clearly help to fill this gap in a reliable, consistent, and cost-effective way.

3.2. Data and understanding derived from computations have the potential for breakthrough discoveries

As illustrated for the case of catalyst development, the combination of judiciously chosen physical and chemical concepts (e.g. Sabatier's principle), structural data-

bases, and *ab initio* total energy calculations on a series of compounds, new correlations and insight can be gained, which can guide the search for novel materials.

In the past, *ab initio* calculations have typically been performed for a single, or a few, systems at a time. This has provided detailed information of the electronic structure and energy potentials of these systems, thereby providing a deeper understanding of matter. With the current and future capabilities in terms of computational power, algorithmic efficiency, and automated computational software environments, large-scale investigations of hundreds or even thousands of compounds have become possible. This opens unprecedented and exciting perspectives. Systematic trends will emerge, which are not discernable from just a few systems. Possibly, systematic deviations between experimental data and computed values will reveal systematic shortcomings in the current level of theory, thereby helping to improve the accuracy of computational approaches. *Vice-versa,* erratic deviations between theory and experiment may also reveal problems in experimental data. A major benefit from such large-scale studies will be an increased confidence in the quality of computed and experimental data.

3.3. Connection of macroscopic continuum models with *ab initio* atomistic approaches

The traditional picture of connecting atomistic and macroscopic scales was a hierarchical approach. Quantum mechanical calculations feed into semi-empirical and force-field methods. These simplified computational approaches allow the simulation of larger systems over longer time scales, reaching mesoscopic eventually macroscopic dimensions. This type of "coarse-graining" is appealing and has worked to some extent in the simulation of biomolecular systems (proteins and DNA). However, attempts to use this approach in the field of inorganic materials has consistently run into the difficulties of generating transferable and reliable interatomic interaction parameters. It is possible, that in the field of inorganic materials such as metallic alloys, ceramics, and semiconductors, *ab initio* methods can be pushed far enough so that intermediate steps of simplified models can be skipped. In fact, this has been achieved in approaches such as the cluster variation methods. The calculations of elastic constants and thermochemical properties, as illustrated in the present paper, point in this direction. This direct link between *ab initio* and continuum models will be further facilitated by the growing interest in nanostructured materials. Current *ab initio* methods are operating on the nano-scale, at least as far as the length scale is concerned.

3.4. The industrial impact of computational materials science is growing

Given the current capabilities of computational methods, there is a worldwide growing interest by major industrial laboratories to employ computational materials

science as an integral part of their research and development efforts. This trend is very clear in Japan and in the U.S.A., whereas European companies tend to be more hesitant. Inevitably, this trend will increase the demand for carefully validated, highly robust, convenient, comprehensive, and well supported software systems. The trend will create new job opportunities for computational scientists, who are able to communicate effectively with materials engineers and who are able to formulate research strategies, which allow the efficient deployment of computational methods in solving industrial materials problems.

3.5. Computers are becoming a commodity

It is possible that the silicon industry will follow a similar trajectory in the 21st century as the steel industry did in the 20th century, namely transforming from a high-tech industry to a commodity business. As a consequence, the rate of computer hardware performance increase will start to taper off in the coming decades, but prices will continue to fall. This will unleash unprecedented computer power with thousands of processors and many terabytes of memory connected in single systems at affordable prices. Fault-tolerant software systems for large-scale computational jobs will be needed to harness this enormous computational power and therefore software will become the limiting factor in using this power. In order to anticipate this development, high-performance supercomputers are needed to enable the development and testing of algorithms and software systems, which in the future will run on low-cost computers.

The evolution of computational materials science depends on three factors, namely (i) fundamental theoretical concepts such as density functional theory and quantum Monte Carlo, (ii) computer programs which implement these concepts, and (iii) computer hardware, which allows the application of these programmes. These three factors evolve in very different time scales: fundamental concepts take of the order of 30-50 years to mature. Once introduced, they can change the field disruptively, as has been witnessed when DFT penetrated computational chemistry. Computer programs are developed and accepted by a larger community in the time frame of about 10 years. Computer hardware changes in 1–2 years.

There are significant consequences from these facts. It is very dangerous to develop software systems, which are dependent on a given generation of computer hardware. By the time the software is completed, the hardware will have changed. Fundamental changes based on the introduction of novel theoretical concepts take a long time, i.e. several decades.

4. Challenges for computational material science

A critical review of the current situation reveals the following key scientific challenges for computational materials science.

4.1. Accuracy of electronic energy

While computed structural properties are acceptable, there is an urgent need to improve the accuracy of electronic energies. This need becomes painfully obvious, if one tries to predict thermodynamic properties such as the melting point of a solid. The current level of standard *ab initio* calculations for solids, namely DFT-GGA, produces errors of the order of 100 K. This is very humbling. At the moment, it is not clear, which theoretical approach will improve this shortcoming. Will better functionals of DFT be sufficient, or will approaches such as quantum Monte Carlo be needed? Will they achieve the necessary accuracy or are entirely new approaches needed?

4.2. Better description of weak interactions

It is embarrassing that standard DFT-GGA methods are incapable of describing correctly the interplanar interactions in graphite or the interactions of two Mg atoms.

4.3. Unified computational approaches for multi-phase systems, e.g. solid–liquid

At present, solids, liquids, and molecules have their own optimal computational approach. Molecules are typically computed with Gaussian-type methods while solids are treated with plane wave approaches. Liquids such as water are described with force-fields. There is an urgent need for unified approaches, which will allow the description of systems such as solid/liquid interfaces, which play such an important role in areas such as corrosion and electrochemistry.

4.4. Novel approaches for reaction mechanisms

If one considers any industrially important chemical process, including combustion and corrosion, any attempt to use computational approaches face at least two major challenges, (i) these systems are ill defined and change with time and process conditions, (ii) there is an overwhelming multitude of possible chemical reactions that would need to be considered. At present, there are no generally practiced approaches that deal with these uncertainties and complexities. An attempt to use *ab initio* methods runs the risk of solving a highly idealized case, which may not even occur in a real system. Novel concepts are needed to deal with these complex systems.

4.5. Linking atomistic models with continuum models

There are many research opportunities to find better ways of linking atomistic approaches with continuum models. One of the challenges is simply communication between different scientific and engineering communities. To a large extent, scientists

and engineers working with finite element methods are not fully aware of the capabilities and approaches of computational materials science and vice versa. Interdisciplinary centres play a critical role in establishing communication channels between these communities, eventually leading to new and creative ways to combine these domains.

5. Conclusion

In conclusion, computational materials science is at an exciting stage of its development. Remarkable accomplishments have already been achieved, industry is starting to take notice, and powerful scientific and technological factors are fuelling the field. Thus, computational materials science is a vibrant and exciting field of growing importance.

References

[1] HOHENBERG P., KOHN W., Phys. Rev., 136 (1964), B864; KOHN W., SHAM L.J., Phys. Rev., 140 (1965), A1133.

[2] GUNNARSSON O., LUNDQVIST B.I., LUNDQVIST S., Solid State Commun.11 (1972), 149; VON BARTH J., HEDIN L., J. Phys., C 5 (1972), 1629.

[3] WANG Y., PERDEW J.P., Phys. Rev. B, 44 (1991), 13298; PERDEW J.P., WANG Y., Phys. Rev. B, 45 (1992), 13244.

[4] FOULKES W.M.C., MITAS L., NEEDS R.J., RAJAGOPAL J., Rev. Mod. Phys., 73 (2001), 33.

[5] WIMMER E., *Prediction of Materials Properties*, *Encyclopedia of Computational Chemistry*, P. von Ragué-Schleyer (Editor-in-Chief), Wiley, New York, 1998.

[6] BLÖCHL P.E., Phys. Rev. B, 50 (1994), 17953

[7] KRESSE G., FURTHMÜLLER J., Phys. Rev. B, 54 (1996), 11169; Computat. Mat. Sci. 6 (1996), 15; KRESSE G., JOUBERT D., Phys. Rev. B, 59 (1999), 1758.

[8] LE PAGE Y.P., SAXE P., Phys. Rev. B, 65 (2002), 104104.

[9] MedeA 1.8, Materials Design, Inc., Taos, New Mexico, USA (2004) – www.materialsdesign.com

[10] YOUNG, G.A. JR., NAJAFABADI R., STROHMAYER W., BALDREY D.G., HAMM W.L., HARRIS J., STICHT J., WIMMER E., [in:] Proceedings of the 11th International Conference on Environmental Degradation of Materials in Nuclear Power Systems – Water Reactors, Stevenson, WA (2003); see also www.osti.gov.

[11] WOLVERTON C., OZOLINS C., ASTA M., Phys. Rev. B, 69 (2004), 133109.

[12] PARLINSKI K., LI Z.Q., KAWAZOE Y., Phys. Rev. Lett., 78 (1997), 4063.

[13] BYLANDER B.M., KLEINMAN L., Phys. Rev. B, 41 (1990), 7868; SEIDL A., GÖRLING A., VOGL P., MAJEWSKI J.A., LEVY M., Phys. Rev. B, 53 (1996), 3764.

[14] GELLER C.B., WOLF W., PICOZZI S., CONTINENZA A., ASAHI R., MANNSTADT W., FREEMAN A.J., WIMMER E., Appl. Phys. Lett.,. 79 (2001), 368.

[15] PECORARO T.A., CHIANELLI R.R., J. Catalysis, 67 (1981), 430.

[16] TOULHOAT H., RAYBAUD P., J. Catalysis, 216 (2003), 63.

[17] SABATIER P., Beri. Deuts. Chem. Gesellschaft, 44 (1911), 1984.

Structure and stability of binary metal alloys.
Precipitation treated via ab-initio calculations

STEFAN MÜLLER[*]

Universität at Erlangen-Nürnberg, Lehrstuhl für Festkörperphysik Staudtstr. 7,
D-91058 Erlangen, Germany

Theoretical studies of substitutional ordering phenomena in binary metal alloys demands the consideration of both huge parameter-spaces (e.g. for ground-state searches) and systems containing more than a million atoms (e.g. for precipitation). The combination of density functional theory calculations (DFT) with cluster expansion methods (CE) and Monte-Carlo (MC) simulations fulfills these requirements. They can be applied to study properties of a metal alloy which possess a delicate temperature-dependence without any empirical parameters, but with such accuracy that quantitative prediction of experimental data becomes possible. The concept is applied to study the structure and distribution of coherent precipitates in binary metal alloys.

Key words: *cluster expansion; density functional theory; Monte-Carlo simulation; metal alloys; precipitation*

1. Introduction

The keyword "Computational Materials Science" includes a huge number of different theoretical approaches reaching from continuum theory and semi-empirical models to so-called first-principles methods, mostly based on the density functional theory (DFT) [1, 2]. Although the latter would be the most elegant solution for describing material properties, because it is based on the rules of quantum mechanics and, therefore, has a predictive power, it is restricted to model systems containing no more than about 200 atoms, i.e. the concept allows studying material properties on an atomic scale only. Moreover, the description of many ordering phenomena in alloy systems demands the consideration of exchange processes between atoms. In other words, the configurational entropy has to be taken into account which is not the case in DFT calculations. These two problems are summarized in Fig. 1.

_____

[*]E-mail: stefan.mueller@physik.uni-erlangen.de
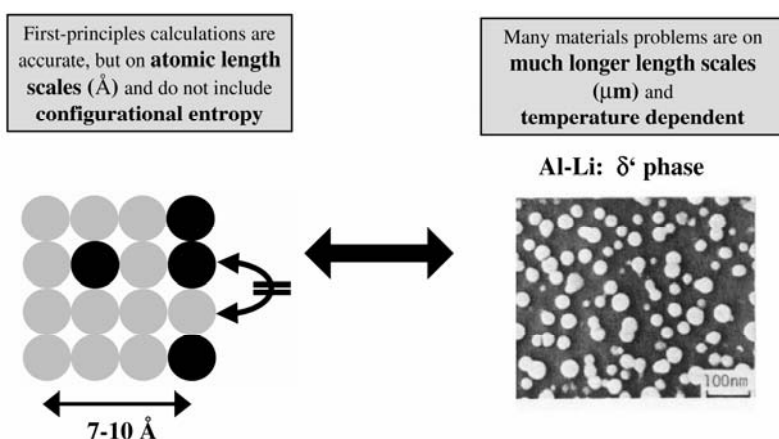
Fig. 1. While DFT calculations allow for a quantitative description of alloy properties
on the atomic scale, they fail to describe material properties demanding
a mesoscopic scale and exchange processes. As example, the right side shows
a TEM picture [3] of the δ' phase in Al–Li alloys

The transmission electron microscopy (TEM) image on the right [3] shows the so-called δ' phase of an Al-rich fcc-based Al–Li alloy. Spherical precipitates can be observed possessing the famous $L1_2$ structure (Al_3Li) which does not exist as an intermetallic compound in the Al–Li phase diagram. Indeed, precipitates define an important part of the microstructure of many alloy systems and have practical importance, as they act to impede dislocation motion. A quantum-mechanical based treatment of phases as the precursor phase in Fig. 1 represents a big challenge, because the theoretical concept applied must be able to: (i) deal with model systems containing millions of atoms and (ii) allow a temperature-dependent description of the alloy's properties.

In the following, it will be shown that these problems can be solved by combining DFT with concepts from statistical physics. A central role is played by the so-called Cluster Expansion (CE) method [4] which permits the gap between the atomic and the mesoscopic scale by the construction of characteristic interactions based on first-principles calculations to be bridged. The extension to finite temperatures is then achieved by using these interactions in Monte-Carlo (MC) simulations. This will be briefly described in section 2. The concept will be applied to study one of the most important decomposition reactions in binary metal alloy systems, namely precipitation (section 3). It is shown that the results even allow a quantitative prediction of the size–shape–temperature relationships for coherent precipitates.

2. Methods

Firstly, formation enthalpies for a set (about 15–20) of geometrically fully relaxed intermetallic compounds with typically 2–16 basis atoms are calculated via DFT.

Thereby, the formation enthalpy $\Delta H_f(\sigma)$ per atom of a compound σ consisting of m A and n B atoms per a unit cell is defined by the energy gain or loss with respect to the bulk constituents at their equilibrium lattice constants a_A and a_B

$$\Delta H_f (\sigma, A_m B_n) = \frac{1}{m+n}\Big[E^{\text{tot}} (\sigma, A_m B_n) - m E_A^{\text{tot}} (a_A) - n E_B^{\text{tot}} (a_B) \Big] \qquad (1)$$

with $E_A^{\text{tot}} (a_A)$ and $E_B^{\text{tot}} (a_B)$ being the total energies of the elements A and B in bulk form. Since all total energy values are negative, a positive sign of ΔH_f stands for phase-separation, while a negative sign of ΔH_f means ordering.

These DFT based formation enthalpies are now used to construct so-called effective cluster interactions in order to bridge the gap between atomistic and mesoscopic scale. The basic idea by Sanchez, Ducastelle and Gratias [4] is called "Cluster Expansion" (CE): for a given underlying lattice, the crystal structure is divided into characteristic figures such as pairs, triangles, etc. Then, the energy of any configuration σ on this lattice can be uniquely written [4] as a linear combination of the characteristic energies J of the individual figures. The construction of the so-called effective interactions J is realized by an inversion method [5] with the goal of finding that set of values for the interactions, $\{J\}$, which minimizes the deviation between the formation enthalpies resulting from CE and DFT for all input structures σ. In practice, the predictive power of $\{J\}$ plays the most important role, i.e. the ability to predict the formation enthalpy of an arbitrary structure which was not used for the construction of the interactions (for details, see e.g. ref. [6] and references therein). Mostly, the effective cluster interactions on average only causes a prediction error of no more than 1–3 meV/atom compared to the direct DFT energies.

Moreover, as first shown by Laks et al. [7], any CE in real space fails to predict the energy of long periodic coherent superlattices – a prerequisite for studying precipitation on a mesoscopic scale from first-principles. In principle, this problem can be solved by transforming a group of interactions to the reciprocal space, which is easiest to do for the pair interactions and considering the long-periodic limit separately [8]. Finally, this leads to the Hamiltonian of the "Mixed-Space Cluster Expansion (MSCE)" [7, 8]. Here, any configuration σ is defined by specifying the occupations of each of the N lattice sites by an A atom (spin-index $\hat{S}_i = -1$) or a B atom ($\hat{S}_i = +1$). The formation enthalpy of any configuration σ at its atomically relaxed state is then given by

$$\Delta H_{CE} (\sigma) = \sum_k J_{\text{pair}} (k)\big| S(k,\sigma)\big|^2$$
$$+ \sum_f^{MB} D_f J_f \bar{\Pi}_f (\sigma) + \frac{1}{4x-1}\sum_k \Delta E_{CS}^{eq} (\hat{k},x)\big| S(k,\sigma)\big|^2 \qquad (2)$$

The first two terms represent the chemical energy, E_{chem} (often referred to as *interfacial energy*). Here, the first sum describes all possible pair figures. $J_{\text{pair}}(k)$ is the

lattice Fourier transform of the real space pair interactions, and $S(k, \sigma)$ are structure factors. The second sum describes many-body figures, such as triangles, tetrahedra, etc. J_f is the reAl–space effective many-body interaction of figure f, D_f stands for the number of equivalent clusters per lattice site and $\Pi_f(\sigma)$ are spin products. The third term, the constituent strain, E_{CS} (often referred to as coherency strain), describes the strain energy necessary to maintain coherency between bulk element A and B along an interface with orientation k. It can be calculated by deforming the bulk elements from their equilibrium lattice constants a_A and a_B to a common lattice constant a perpendicular to k. The constituent strain is a function of composition x and direction k only, but does not include information about the strength of chemical interactions between A and B atoms.

Figure 2 gives a survey about our concept which demands neither empirical parameters nor simplifications in the quantum-mechanical based Hamiltonian in order to get access to huge system sizes and finite temperatures.
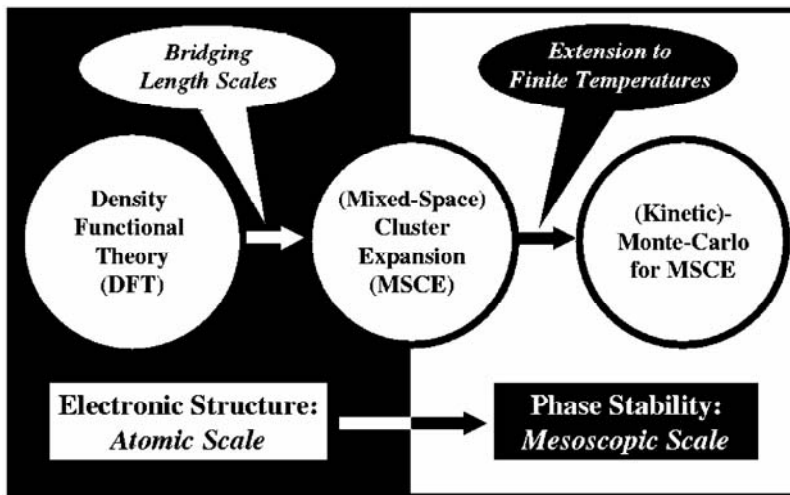
Fig. 2. The combination of DFT plus MSCE [8] plus MC [11] allows for a description
of phase stability of metal alloys on a mesoscopic scale without any empirical parameters

For the latter, the MSCE Hamiltonian (Eq. (2)) is used in Monte-Carlo (MC) simulations. The field of applications to dynamic processes can be extended by switching from thermodynamic MC to kinetic MC [9]. For this, activation barriers for individual exchange processes between neighbouring atoms have to be calculated via DFT. This can be rather complicated and time consuming, because the calculation of diffusion coefficients demands the consideration of vacancies. In the case of precipitation, the number of different structural environments considered for exchange processes can, however, often be restricted by the fact that the alloy typically only contains a few percent of the precipitates-forming solute material (here called B atoms).

Then, the dominant process is the temperature-dependent diffusion of a B atom in material A. In many cases, as e.g. Al-rich Al–Zn alloys, this apparently rough approximation already allows a prediction of realistic precipitate distributions as function of ageing time, as will be discussed in the next section. Furthermore, first-principles based simulations of precipitation demand the possibility to consider long ageing times (many hours or days). Since precipitation is a phase-separating process, the probability that any atom of the precipitate forming species will ever diffuse from the precipitate to which it is already attached, back into the solid solution, becomes very low. Consequently, in standard MC algorithms most of such exchange processes are practically never performed which makes the simulation rather inefficient. Here, advantage is taken from the fact that the CE is able to calculate the probabilities for *all* possible exchange processes (even many thousands) within a few seconds which permits the concept of the so-called "residence time algorithm" [10] to our simulations to be applied: since now the time corresponding to each individual exchange process is known a priori, atoms can be forced to switch their sites (for details, see ref. [11]).

3. Precipitation

Quenching a solid solution of a metal alloy deep into the two phase-region of the phase diagram, followed by sample ageing, leads to the formation of so-called precipitates which comprise an important part of the microstructure of many alloy systems. The early stage of these reactions typically involves the formation of coherent precipitates that adopt the crystallographic lattice of the alloy from which they emerge [12]. Coherent precipitates have practical relevance, as they impede dislocation movement, and thus lead to "precipitation-hardening" in many alloys [12–14]. Thus, their size versus shape distribution as a function of temperature and ageing time is of special interest. Despite their importance, it is only recently [15] that, precipitate microstructures have been amenable to first-principles theories, since their description requires "unit cells" containing 103–106 atoms or more. The concept presented in section 2 gives access to such huge model systems.

The shape of precipitates is controlled by two competing energies [14]: interfacial or chemical energy E_{chem} and strain energy E_{CS}. While the former leads to a compact shape, the latter leads to a flattening along the elastically soft direction of the precipitate. Our MSCE Hamiltonian allows for a separation into these two characteristic energy parts: as already mentioned in section 2, the first two terms of Eq. (2) include information about strength and importance of the indvidual pair and multibody interactions and therefore, represent the chemical energy of the system. The last term, however, reflects the elastic properties of the alloy. This separation is used to analyse the ratio between chemical energy E_{chem} and strain energy E_{CS} as a function of the precipitate size. As examples, the focus is on Al-rich fcc-based Al–Li and Al–Zn alloys. Their precipitate distributions for a given ageing time and temperature are

shown in the upper part of Fig. 3, whereby only the Li and Zn atoms are shown. The MC cell used for the simulations consists of $56 \times 56 \times 56 = 175\,616$ atoms in order to achieve sufficient statistics.
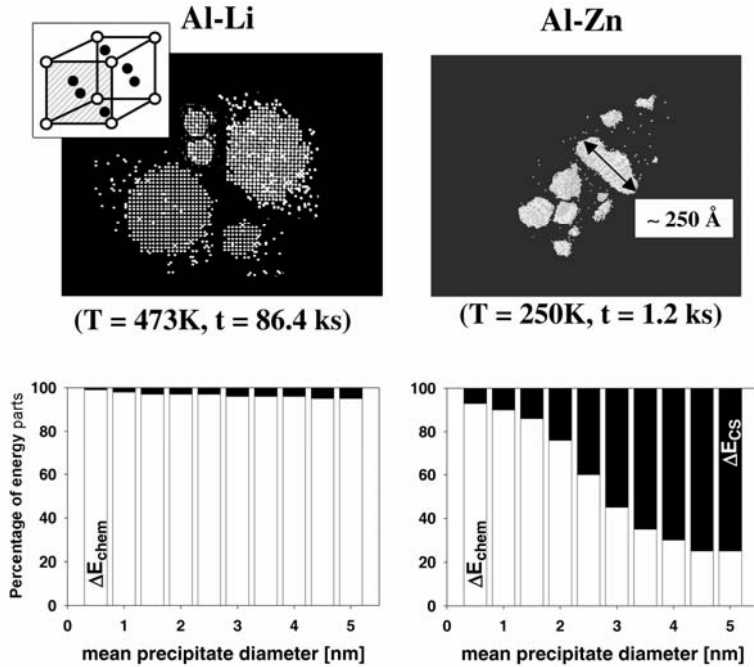
Fig. 3. Size-shape distribution of precipitates in Al-rich fcc-based
Al–Li and Al–Zn alloys (no Al atoms are shown) and their corresponding percentage
of strain and chemical energy as a function of the precipitate size.
Precipitates of Al–Li form the $L1_2$ structure as shown in the top left corner

In the case of Al–Li, precipitates of the considered size up to 5 nm never flatten, but always possess a spherical shape, in excellent agreement with experimental results [3, 16]. This behaviour becomes understandable by analysing E_{chem}/E_{CS} for different precipitate sizes as shown in the lower part of Fig. 3 for a sample containing 9.7% Li atoms: for all sizes the chemical energy E_{chem} (white bars) clearly dominates the strain energy E_{CS} (black bars). Following experimental results, it must be expected that this dominance of E_{chem} over E_{CS} even holds for precipitates of about 50 nm in diameter, because they still possess a spherical shape. The Li atoms seem to form a simple cubic lattice. This is due to the fact that the precipitates themselves show a Al_3Li stoichiometry forming the $L1_2$ structure sketched on the top left corner of Fig. 3: while all corners of the unit cell are occupied by Li atoms, all faces are occupied by Al atoms. Since only the Li atoms are displayed in the real space image, they form a simple cubic lattice. This observation also makes clear that there are practically no antiphase boundaries within the Al_3Li precipitates which would demand the occupation of Al sites by Li atoms.

Unlike Al–Li, for Al–Zn a strong size-dependence of the precipitate shape is found: Zn precipitates up to about 2.5 nm are more compact, i.e. chemically dominated, while larger precipitates become more and more ellipsoidal (strain dominated) [17]. It is interesting to note that for low temperatures a third component becomes important, namely the anisotropy of the chemical part which controls quantitatively the extent to which the precipitates facet at low temperatures. Figure 4 shows equilibrium shapes resulting from calculations considering the chemical part only: At low temperatures, when entropy is unimportant, the strong anisotropy of the chemical energy creates facets along planes of low interfacial energy.
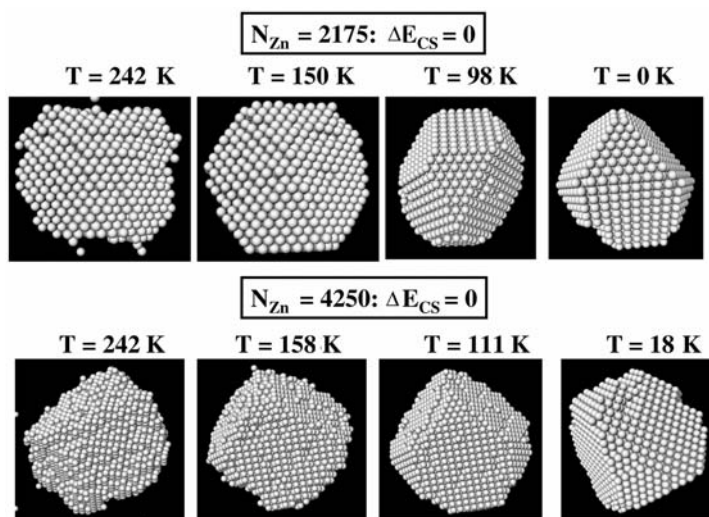
Fig. 4. Equilibrium precipitate shapes for different temperatures and sizes resulting from calculations where the constituent strain energy was neglected [6]. The size is given by the number of Zn atoms, N_{Zn}. For low temperatures, the faceting caused by the anisotropy of the chemcial energy in Al–Zn becomes visible

These are mostly (100) and (111) planes whose interfacial energies are lowest and nearly degenerated. In contrast, at high temperatures, where many configurations co-exist due to entropy, the chemical anisotropy is largely averaged out and therefore, the precipitates become spherical. Another remarkable feature of the coherent Zn precipitates is the fact that their short axis is always along the [111] (and symmetric equivalent) directions. Indeed, at first glance, this appears a little surprising, because most fcc elements are elastically soft along the [100] direction, and consequently hard along [111]. However, it should not be forgotten that it is necessary to inquire about the stability and elastic properties of an unusual phase: fcc-Zn: while Zn is stable in the hcp structure, fcc-Zn shows an instability when deformed rhombohedrally along [111] [18]. As a consequence, fcc-Zn precipitates flatten along this direction [17]. This feature allows the definition of a *c/a* ratio and therefore, a quantitative measure for the description of the precipitate shape as used in many experimental studies and

schematically shown on the left side of Fig. 5. While *a* represents the long axis of the ellipsoid (perpendicular to [111]), *c* is its thickness (parallel to [111]). The size is given by the radius of the associated sphere having the same volume as the corresponding precipitate.
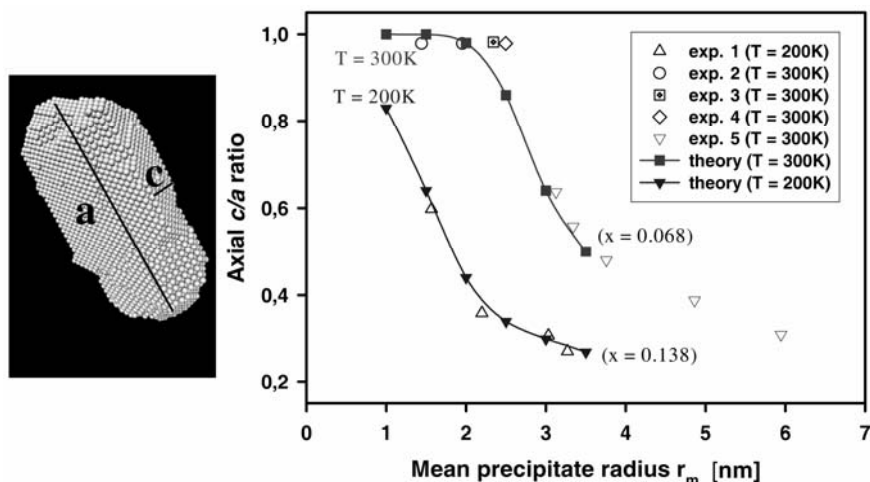
Fig. 5. Shape (*c/a*) vs. size relation of Zn precipitates for two different temperatures. The lines denote the results from our calculations [24], the open points are taken from different experimental studies (exp. 1–5 correspond to ref. [19–23])

Figure 5 compares the experimental size-shape relation for two different ageing times and concentrations [19–23] with those predicted by this method. For both temperatures, the agreement is excellent, i.e. the method allows for a quantitative prediction of the size versus shape versus temperature relation of coherent precipitates [24].

4. Conclusions

The combination of DFT with MSCE and MC is probably one of the most successful approaches to study binary alloy properties without any empirical parameters. At the moment, the limitation of the presented access is given by the underlying lattice which does not, for example, permit the study of melting processes. Regarding ordering phenomena in the solid phase, the method allows a quantitative prediction of experimental data. This paper has focussed on just one important example: precipitation in binary metal alloys. Here, there is profit from the fact that the approach applied allows study of configurations consisting of millions of atoms. In the case of Al–Zn, it was demonstrated that the prediction even goes through a quantitative comparison of the size-shape-temperature relation with experimental results. The presented method is by no means restricted to the two characteristic ordering phenomena, but it can also

be applied for example to surface problems such as adsorbate systems [25] or surface segregation [26].

References

[1] HOHENBERG P., KOHN W., Phys. Rev., 136 (1964), 864B.

[2] KOHN W., SHAM L.J., Phys. Rev., 140 (1965), 1133A.

[3] SATO T., KAMINO A., Mat. Sci. Eng. A, 146 (1991), 161.

[4] SANCHEZ J.M., DUCASTELLE F., GRATIAS D., Physica A, 128 (1984), 334.

[5] CONOLLY J.W.D., WILLIAMS A.R., Phys. Rev. B 27, (1983), 5169.

[6] MÜLLER S., J. Phys. Condens. Matt., 15 (2003), R1429.

[7] LAKS D.B., FERREIRA L.G., FROYEN S., ZUNGER A., Phys. Rev. B, 46 (1992), 12587.

[8] ZUNGER A., [in:] NATO ASI on Statics and Dynamics of Alloy Phase Transformations, P.E.A. Turchi, A. Gonis (Eds.), Plenum Press, New York, 1994, p. 361.

[9] VOTER A.F., Phys. Rev. B, 34 (1986), 6819.

[10] BORTZ A.B., KALOS M.H., LEBOWITZ J.L., J. Comp. Phys., 17 (1975), 10.

[11] MÜLLER S., WANG L.-W., ZUNGER A., Model. Sim. Mat. Sci. Eng., 10 (2002), 131.

[12] GUINIER A., Solid State Physics, 9 (1959), 293.

[13] COHEN J.B., Solid State Physics, 39 (1986), 131.

[14] KHACHATURYAN A.G., *Theory of Structural Transformations in Solids*, Wiley, New York, 1983.

[15] WOLVERTON C., Phil. Mag. Lett., 79 (1999), 683.

[16] LENDVAI J., GUDLADT H.-J., WUNDERLICH W., GEROLD V., Z. Metallkde., 80 (1989), 310.

[17] MÜLLER S., WOLVERTON C., WANG L.-W., ZUNGER A., Acta Mater., 48 (2000), 4007.

[18] MÜLLER S., WANG L.-W., ZUNGER A., WOLVERTON C., Phys. Rev. B, 60 (1999), 16448.

[19] LASLAZ G., GUYOT P., Acta Metall., 25 (1977), 277.

[20] BUBECK E., GEROLD V., KOSTORZ G., Cryst. Res. Technol., 20 (1985), 97.

[21] FUMERON M., GUILLOT J.P., DAUGER A.P., CAISSO J., Scripta Metall., 14 (1980), 189.

[22] DEGUERCY J., DENANOT M.F., FUMERON M., GUILLOT J. P., CAISSO J., Acta Mater., 30 (1982), 1921.

[23] GEROLD V., SIEBKE W., TEMPUS G., Phys. Stat. Sol. (a), 104 (1987), 213.

[24] MÜLLER S., WOLVERTON C., WANG L.-W., ZUNGER A., Europhys. Lett., 55 (2001), 33.

[25] DRAUTZ R., SINGER R., FÄHNLE M., Phys. Rev. B 67, (2003), 035418.

[26] WIECKHORST O., MÜLLER S., HAMMER L., HEINZ K., Phys. Rev. Lett., 92 (2004), 415.

First-principles calculations of vibrational and thermodynamical properties of solids

KRZYSZTOF PARLIŃSKI[*]

Institute of Technics, Pedagogical University, ul. Podchorążych 2, 30-084 Cracow, Poland

The presented first-principle phonon calculations make use of the standard DFT program, and the direct method. The procedure requires optimization of the structure, calculation of the forces, and construction of the dynamical matrix. This method has already been applied to a large number of crystalline systems to calculate the phonon dispersion curves, phonon density of states, and thermodynamic functions, which were required for a description of phase transitions.

Key words: *phonons; ab initio calculations; direct methods; vibrations in crystals*

1. Introduction

The dynamic and thermodynamic properties of solids depend upon the lattice vibrations related to phonons. Therefore, knowledge of phonon characteristics is required to describe the mechanical, acoustic, dynamic, spectroscopic and thermodynamic properties of crystals at finite temperature.

The possibility to calculate phonons directly from first-principles has existed for several years. The easiest and most convenient way to do it, is to use existing and well-tested DFT software [1–4], which can calculate crystalline structures, electronic bands, magnetic properties, and the so-called Hellmann–Feynman (HF) forces. To avoid surface effects, the DFT programs use supercells on which three-dimensional periodic boundary conditions are imposed.

The HF forces allow the atomic response forces for the displacement of any other atom to be found. To find harmonic phonons it is sufficient to convert the response HF forces to force constants and then to use the basic equations of the dynamical lattice theory. The last task has been coded in PHONON [5] software.

_____

[*]E-mail: krzysztof.parlinski@ifj.edu.pl

2. Direct method

Traditionally, the ground state energy E (at $T = 0$) as a function of atomic positions $\mathbf{R}(\mathbf{n}, \mu)$, where $\mathbf{n}$ is the primitive unit cell index and μ is the atomic index, can be expanded over small displacements as

$$E\big(\mathbf{R}(\mathbf{n},\mathbf{\mu}),...\ R(\mathbf{m},\mathbf{\nu}),...\big) = E_0 + \frac{1}{2}\sum_{n,\mu,m,\nu} \mathbf{\Phi}(\mathbf{n},\mathbf{\mu},\mathbf{m},\mathbf{\nu})\mathbf{U}(\mathbf{n},\mathbf{\mu})\mathbf{U}(\mathbf{m},\mathbf{\nu}) \qquad (1)$$

where the force constant matrix

$$\mathbf{\Phi}_{i,j}\big(\mathbf{n},\mathbf{\mu},\mathbf{m},\mathbf{\nu}\big) = \frac{\partial^2 E}{\partial \mathbf{R}_i\big(\mathbf{n},\mathbf{\mu}\big)\partial \mathbf{R}_j\big(\mathbf{m},\mathbf{\nu}\big)}\bigg|_0 \qquad (2)$$

is defined at the extremum configuration $(\partial E)/\partial \mathbf{R}_i(\mathbf{n},\mathbf{\mu})\big|_0 = 0$ at which all first order derivatives vanish.

The dynamical matrix is defined as

$$D(k;\mathbf{\mu},\mathbf{\nu}) = \frac{1}{\sqrt{M_\mu M_\nu}}\sum_m \Phi(0,\mathbf{\mu};\mathbf{m},\mathbf{\nu})\exp\{-2\pi i\mathbf{k}\big[\mathbf{R}(0,\mathbf{\mu})-\mathbf{R}(\mathbf{m},\mathbf{\nu})\big]\} \qquad (3)$$

Here, summation $\mathbf{m}$ runs over all atoms of the crystal, M_μ, M_ν are masses of atoms, and $\mathbf{k}$ is the wave vector. Eigenvalues of the dynamical matrix

$$\omega^2(\mathbf{k},j)\mathbf{e}(\mathbf{k},j) = D(\mathbf{k})\mathbf{e}(\mathbf{k},j) \qquad (4)$$

give the phonon frequencies $\omega^2(\mathbf{k}, j)$ and polarization vectors $\mathbf{e}(\mathbf{k}, j)$.

Any atomic displacement $\mathbf{U}(\mathbf{m}, \mathbf{\nu})$ generates HF forces

$$F(\mathbf{n},\mathbf{\mu}) = -\frac{\partial E}{\partial R(\mathbf{n},\mathbf{\mu})} \qquad (5)$$

on all other atoms. Using the expansion of Equation (1), one finds

$$F_i(\mathbf{n},\mathbf{\mu}) = -\sum_{m,\nu,j} \Phi_{i,j}(\mathbf{n},\mathbf{\mu},\mathbf{m},\mathbf{\nu})U_j(\mathbf{m},\mathbf{\nu}) \qquad (6)$$

which relates the generated forces with the force constant matrices and atomic displacement. The calculations of vibrational properties start from minimizing the total energy of the crystal with respect to the electronic part, lattice constants and atomic positions. At the minimized state all HF forces should vanish. Now, the HF forces should be calculated for configurations with a single atom displaced from the equilibrium position. The HF forces are calculated in the supercell with periodic boundary conditions, and that brings some modifications. Consider a supercell and displace an

atom $(\mathbf{m}, \boldsymbol{\nu})$ by $\mathbf{U}(\mathbf{m}, \boldsymbol{\nu})$. Due to periodic boundary conditions this displacement causes the same displacements of corresponding atoms $(\mathbf{m} + \mathbf{L}, \boldsymbol{\nu})$ in all images of the supercell.

Here, $\mathbf{L} = (L_a, L_b, L_c)$ are the indices of lattice constants of the supercell. Thus, according to Eq. (6), a displacement of a single atom $(\mathbf{m}, \boldsymbol{\nu})$ in the original supercell generates a net force

$$F_i(\mathbf{n}, \boldsymbol{\mu}) = -\sum_L \boldsymbol{\Phi}_{i,j}(\mathbf{n}, \boldsymbol{\mu}, \mathbf{m} + \mathbf{L}), \boldsymbol{\nu})U_j(\mathbf{m}, \boldsymbol{\nu}) \tag{7}$$

We may introduce the cummulant force constant defined as

$$\Phi_{i,j}^{(\Sigma)}(\mathbf{n}, \boldsymbol{\mu}, \mathbf{m}, \boldsymbol{\nu}) = \sum_L \Phi_{i,j}(\mathbf{n}, \boldsymbol{\mu}, \mathbf{m} + \mathbf{L}, \boldsymbol{\nu}) \tag{8}$$

and the summation $\mathbf{L}$ runs over all supercell images. Thus, from the first-principle program one can only calculate the force constants $\Phi_{i,j}^{(\Sigma)}(\mathbf{n}, \boldsymbol{\mu}, \mathbf{m}, \boldsymbol{\nu})$. The solution of Eq. (7) is the essence of the direct method [6, 7].

The program PHONON solves Eq. (7) with respect to cummulant force constants, Eq. (8), which, in turn, are introduced to the dynamical matrix. For wave vectors, which are commensurate with the supercell, the summation over all atoms of the crystal in Eq. (3) leads to an exact dynamical matrix, and hence it provides exact phonon frequencies and polarization vectors. The phonon frequencies, which do not belong to the commensurate wave vectors, could hold some uncertainties. But, if the supercell is so large that the force constants decay at half of the supercell linear size (i.e., they are three orders of magnitude smaller), then phonons at all wave vectors are correct. The program PHONON ensures that the force constants have the correct symmetry required by the crystal space group. It is also able to impose the translational-rotational invariance conditions causing the acoustic phonon modes to start at zero frequencies from the Brillouin zone centre.

Selection of the supercell shape is essential. It should have a form closest to a cube. Symmetry of the supercell should not break the crystal point group. Also it is necessary that all coordination shells defined within the supercell have a complete list of atoms. Supercells of other shapes could reduce the crystal symmetry since the supercell acts as an external field. Elongated supercell shapes can help to supplement the list of exact phonon frequencies calculated with the direct method in a particular crystal direction. For polar crystals the macroscopic electric field splits the infrared active phonon modes to LO and TO components. This splitting can be satisfactorily handled when knowing the Born effective charges and the dielectric constant.

3. First-principle phonons

The VASP [1, 2] and PHONON [5] programs have been applied to a number of crystalline systems. It was possible to confirm the soft mode at the *X* reciprocal lattice

point in the cubic zirconia ZrO_2 [6]. This soft mode transforms the crystal to the observed tetragonal phase. Calculations of phonon dispersion curves in cubic carbides TiC [8] and ZrC [9] showed that the calculations within the general gradient approximation lead to a slightly better agreement with the measured phonon branches. Other cubic systems studied were magnesium oxide MgO [10] and boron nitride BN [11]. Both possess the LO/TO splitting, which could have been quite successfully calculated by the elongated supercell method. Reduction of crystal symmetry increases the complexity of the calculation. The tetragonal rutile structures of tin oxide SnO_2 [12] and germanium oxide GeO_2 [13] have been studied. Their phonon dispersion relations, although having only 18 branches, were never measured. Under pressure both systems show soft modes of B_{1g} symmetries. These soft modes lead to a ferroelastic phase transition, seen also experimentally.

Of course, the calculations can be applied to lower-symmetry phases, like hexagonal GaN, having a wurzite structure [14]. It was optimized for rhombohedral symmetry, which lowers the wurzite space group. To restore the full wurzite space group symmetry some of the calculated force constants were additionally symmetrized. The calculated phonon dispersion curves were later measured by the inelastic X-ray scattering technique [15], and the agreement proved to be very good.

The phonon dispersion curves of zero-gap semiconductor HgSe have been computed and measured [16] and the agreement is very good. This crystal shows LO/TO splitting which quite strongly depends on the concentration of the charge carriers. The phonon dispersion curves of another semiconductor ZnTe at high-pressure has been calculated [17] and satisfactorily compared with the measured Raman data.

Some minerals are also interesting from the point of view of their stability. The optimization of a supercell within a given structure does not yet mean that this structure is the most stable. To state that a structure is dynamically stable all phonon frequencies should be positive. Under this guideline the phonon dispersion relation calculations for several structures of $MgSiO_3$ [18] and $CaTiO_3$ [19] have been undertaken. For these crystals the $Pm\overline{3}m$, $I4/mcm$, $Immm$, $P4/mbm$ and $Pmnb$ symmetries were checked. Except for $Pmnb$ all the mentioned phases show soft modes. Therefore, the low-temperature space groups of these crystals are of the $Pmnb$ type.

Especially interesting are the phonon calculations for the rhombohedral crystals. The phonon density of states of $FeBO_3$ has been measured by nuclear inelastic absorption of synchrotron radiation [20]. Since this compound is antiferromagnetic, it was necessary to include the magnetic interaction in the first-principle calculations in order to get an agreement between the measured and calculated phonon densities. In this case, the effect of magnetic interaction on the phonons is exceptionally large. The crystal is magnetostrictive and the magnetic interaction changes interatomic distances and hence the phonon force constants.

Another rhombohedral compound is $LiNbO_3$. It possesses a ferroelectric phase transition from $R3c$ to $R\overline{3}c$. The phonon calculations [21] show that the paraelectric phase $R\overline{3}c$ has a soft mode of the same symmetry as the irreducible representation

which drives the phase transition to the ferroelectric phase *R*3*c*. The phonon dispersion curves of the ferroelectric phase do not have any soft mode. This is an example of how the phonon calculations could clarify the nature of phase transitions.

First-principle calculations have also been used to find the phonon dispersion curves, and phonon density of states for a number of chalcopyrites such as $AgGaS_2$ [22], $AgGaSe_2$ [23], $AgGaTe_2$, $CuInS_2$ [25], $CuInSe_2$ [24] and $ZnSnP_2$ [26]. These are body-centred tetragonal structures with 8 atoms in the primitive unit cells. The $AgGaSe_2$ [27] and $CuInSe_2$ [28] belong to the most complex crystals for which the phonon dispersion curves have ever been measured. The agreement of these experimental data with our calculated phonon branches is very good. The $CuInSe_2$ material [29] shows a special property. It crystallizes in two structures: the chalcopyrite and of AuCu-type. The ground state energies and phonon calculations show that the free energies of both polymorphic phases are equal over the whole temperature interval. Moreover, the lattice constants of the two phases match perfectly, therefore these two phases coexist.

The first-principle phonon calculations are limited to $T = 0$ K. However, quantities in which harmonic phonons play a leading role can also be calculated within the so-called quasiharmonic approximation. As an example we quote the γ-Mg_2SiO_4 system [30, 31]. The phonon dispersion curves of this cubic crystal have been calculated for several positive and negative pressures *P*, and for each *P* the harmonic free energy *F* has been plotted. The minimum of *F* as a function of the lattice constant gives a lattice constant at a given temperature. Hence, one obtains thermal expansion as a function of temperature, a quantity which has been calculated ab initio and which agrees with the experimental data.

Special attention has been devoted to the shape memory alloy NiTi [32]. This crystal has a high-temperature cubic austenite phase and a low-temperature monoclinic martensite phase. The transition between the phases is accompanied by the appearance of a hexagonal *R*-phase, and incommensurate state. The ab initio phonon dispersion curves revealed a soft mode in the austenite phase, which is able to drive NiTi to the orthorhombic phase, and to the R-phase. But the monoclinic phase can be attained only by condensation of two order parameters. However, for the R-phase, orthorhombic and monoclinic phases all have positive phonon frequencies, hence one may calculate the free energies for each of these phases. Knowing also the ground state energies one find that below the phase transition temperature T_c the free energy of the monoclinic phase is the lowest, while above T_c the R-phase has minimal free energy. The orthorhombic phase never becomes stable, and indeed it has not been observed for the stoichiometric composition of NiTi.

In the second order structural tetragonal to orthorhombic phase transition of $CaCl_2$ the free energy of one phase changes continuously into the free energy of the other phase. Then, the usual procedure with the intersection of two free energies cannot be used. However, since at constant volume the harmonic phonon frequencies do not depend on temperature, one may find the critical volume, at which the phase transition takes place, even at $T = 0$ K. The second order phase transition temperature is

then defined at a point where the minimum of the free energy as a function of volume coincides with the critical volume determined at $T = 0$ K [33].

4. Discussion

The direct method has some advantages and disadvantages.

• A great advantage is that it could use the data calculated by any standard DFT program, which is able to calculate the HF forces. One should, however, ensure that the forces are calculated with high accuracy to an order of 0.0001 eV/Å.

• Calculation of HF forces is not time-consuming since it needs only electronic optimization for a fixed ionic configuration.

• A small regular supercell provides exact phonon frequencies at the Γ point.

• For complex crystals for which the supercell is as big as the unit cell, and for which the interaction range is confined to the supercell, the phonon frequencies are exact for any wave vector. One may check the decay of the force constants parameters before calculating the phonon dispersion relations.

• Anharmonic effects and molecular dynamic calculations can be treated within the same framework.

There are also some disadvantages:

• Crystals having small unit cells must be represented by larger supercells.

• During calculations of the HF forces the displaced atom usually breaks the symmetry of the system. This changes the Brillouin zone integration in the DFT code.

• Within the direct method it is not easy to calculate the LO/TO splitting. It could be performed when the ionic effective Born charges and electronic dielectric constant are known.

• The largest error of phonon frequencies is expected for the low-energy modes. The error will still enlarge with the increasing dimension of the dynamical matrix, i.e. with increasing the number of atoms in the unit cell.

Only results for three-dimensional periodic systems have been referred to above. With a similar effort one may calculate phonons for other objects. Constructing several layers in a supercell one can study phonons on the surface. Placing an atom on the surface one may find the vibration spectrum of the adsorbed atoms. In a similar way multilayers can be treated. Another direction of research is to replace, within a suitable sized supercell, an atom by a vacancy or another atom, and thereby form a defect. One then may carry out the first-principle phonon calculations for point defects, pairs of defects, and clusters of defects. These calculations require, however, larger computer power, since all these systems possess less symmetry, and hence, the number of independent parameters to be found by the first-principle program is greater.

References

[1] KRESSE G., HAFNER J., Phys. Rev., B 47, 5 (1993), 58; ibid 49, 14 (1994), 251.

[2] KRESSE G., FURHTMÜLLER J., Phys. Rev., B 54, 11 (1996), 169, Comput. Mat. Science, 6 (1996), 15; Software VASP, Vienna (2002); http://cms. mpi. univie. ac. at/vasp/vasp. html.

[3] BLAHA P., SCHWARZ K., MADSEN G.K.H., KVASNICKA D., LUITZ J., WIEN2k, *An Augmented Plane Wave Plus Local Orbitals Program for Calculating Crystal Properties*, Karlheinz Schwarz, Techn. Universität WIEN, Austria, 2001, ISBN 3-9501031-1-2; http://www. wien2k. at/

[4] ARTACHO E., GALE J., GARCIA A., JUNQUERA J., ORDEJON P., SANCHEZ-PORTAL D., SOLER J.M., Software SIESTA (2001); http://www. uam. es/siesta/.

[5] PARLINSKI K., PHONON software, Cracow (2002); http://wolf. ifj. edu. pl/phonon/.

[6] PARLINSKI K., LI ND Z.Q., KAWAZOE Y., Phys. Rev. Lett., 78 (1997), 4063.

[7] PARLINSKI K., Conference Proceedings 479, *Neutrons and Numerical Methods – N_2M*, M.R. Johnson, G.J. Kearley, H.G. Büttner(Eds.), Am. Inst. Phys. (1999), p. 121.

[8] JOCHYM P.T., PARLINSKI K., STERNIK M., Eur. Phys. J., B 10 (1999), 9.

[9] JOCHYM P.T., PARLINSKI K., Eur. Phys. J., B 15 (2000), 265.

[10] PARLINSKI K., LAZEWSKI J., KAWAZOE Y., J. Phys. Chem. Solids, 61 (1999), 87.

[11] PARLINSKI K., J. Alloys and Compounds, 328 (2001), 97.

[12] PARLINSKI K., KAWAZOE Y., Eur. Phys. J., B 13, 679 (2000).

[13] LODZIANA Z., PARLINSKI K., HAFNER J., Phys. Rev., B 63 (2001), 134106.

[14] PARLINSKI K., KAWAZOE Y., Phys. Rev., B 60, (1999), 15, 511.

[15] RUF T., SERRANO J., CARDONA M., PAVONE P., D'ASTUTO M., SUSKI T., GRZEGORY I., LESZCZYNSKI M., Phys. Rev. Lett., 86 (2001), 906.

[16] LAZEWSKI J., PARLINSKI K., SZUSZKIEWICZ W., HENNION B., Phys. Rev,. B 67 (2003), 134300.

[17] CAMACHO J., PARLINSKI K., CANTARERO A., SYASSEN K., Phys. Rev., B 70 (2004), 033205.

[18] PARLINSKI K., KAWAZOE Y., Europ. Phys. J., B 16 (2000), 49.

[19] PARLINSKI K., KAWAZOE Y., J. Chem. Phys., 114 (2001), 2395.

[20] PARLINSKI K., LAZEWSKI J., JOCHYM P.T., CHUMAKOV A., RÜFFER R., KRESSE G., Europhysics Lett., 56 (2001), 2.

[21] PARLINSKI K., LI Z.Q., KAWAZOE Y., Phys. Rev., B 61 (2000), 272.

[22] LAZEWSKI J., PARLINSKI K., J. Phys. Chem., 328 (2001), 162.

[23] LAZEWSKI J., PARLINSKI K., J. Phys. Condens. Matter, 11 (1999), 9673.

[24] LAZEWSKI J., PARLINSKI K., HENNION B., FOURET R., J. Phys. Condens. Matter, 11 (1999), 9665.

[25] LAZEWSKI J., JOCHYM P.T., PARLINSKI K., J. Chem. Phys., 117 (2002), 2726.

[26] LAZEWSKI J., PARLINSKI K., J. Alloys Compounds, 114 (2001), 6734.

[27] FOURET R., DEROLLEZ P., LAAMYEM A., HENNION B., GONZALEZ J., J. Phys. Condens. Matter 9 (1997), 6579.

[28] DOROLLEZ P., FOURET R., LAAMYEM A., HENNION B., GONZALEZ J., J. Phys. Condens. Matter, 11 (1999), 3987.

[29] LAZEWSKI J., NEUMANN H., PARLINSKI K., LIPPOLD G., STANBERY B.J., Phys. Rev., B 68 (2003), 144108.

[30] LAZEWSKI J., JOCHYM P.T., PARLINSKI K., PIEKARZ P., J. Mol. Structure, 596 (2001), 3.

[31] PIEKARZ P., JOCHYM P.T., PARLINSKI K., LAZEWSKI J., J. Chem. Phys., 117 (2002), 3340.

[32] PARLINSKI K., PARLINSKA-WOJTAN M., Phys. Rev. B 66 (2002), 0604307.

[33] LAZEWSKI J., JOCHYM P.T., PIEKARZ P., PARLINSKI K., Phys. Rev., B 70 (2004), 104109.

Vibrational properties
and thermochemistry from first principles

WALTER WOLF[1*], JÜRGEN STICHT[1], ALEX MAVROMARAS[1],
BENOIT LEBLANC[1], PAUL SAXE[2], ERICH WIMMER[1]

[1]Materials Design s.a.r.l., 44, avenue F.-A. Bartholdi, 72000 Le Mans, France

[2]Materials Design Inc., PMB #262, 1008 Paseo del Pueblo Sur, Taos NM 87571, USA

The simulation of vibrational properties and finite temperature effects based on ab initio calculation of phonons within the direct approach is discussed. The implementation of the approach within an automated computational framework is outlined, and applications in rather diverse fields are demonstrated: phonon dispersion of GaAs, Kohn anomaly in Niobium, rattling modes in thermoelectric skutterudites, reaction enthalpies and formation enthalpies of hydrides and hydrogen storage materials, phase transformations, surface reconstruction of Si(111), and adsorption of CO molecules on a Ni(001) surface.

Key words: *computations; property predictions; ab initio*

1. Introduction

For decades, ab initio calculations have been largely viewed as being restricted to 0 K, or more precisely, as being condemned to operate without any concept of temperature. Nowadays, this major constraint has been lifted, and routine methods to evaluate vibrational properties and temperature dependent thermodynamic functions have become available, at least within the harmonic approximation. In this paper, the basic concepts of the so-called direct approach [1, 2] to vibrational properties are summarized and a number of applications in rather diverse fields are discussed. In a routine manner, free energies, vibrational enthalpies and entropies of solid compounds can be evaluated, thus enabling the study of the thermochemistry of chemical reactions as well as phase stability from ab initio theory. As will be shown, in particular for hydrogen containing compounds, neglecting zero point vibrations in many

_____

*Corresponding author, e-mail: wwolf@materialsdesign.com

cases may cause qualitatively wrong answers. In addition, phonon instabilities of metastable phases may point towards possible phase transformations to other stable phases. Furthermore, vibrational spectra of transition states are well suited for the study of chemical kinetics as well as transport properties, thus opening the field for simulating diffusion processes. The methodology is, however, not restricted to the solid state: vibrations of molecules and molecules on surfaces may help to analyze spectral data, and the calculation of surface phonons is well suited to confirm the stability of a suggested surface or may reveal possible reconstructions, to indicate some of the rather promising, though challenging, applications.

2. Computational approach and implementation

During the last decade two different approaches for evaluating vibrational properties of condensed, ordered systems from first principles have evolved. Density functional perturbation theory has been implemented mainly in plane wave based density functional codes to obtain force constant matrices directly from linear response expressions [3]. In contrast, in this paper, the alternative, so-called direct approach [1, 2] is discussed, that does not require specialized ab initio codes, but can operate with any first principles code able to accurately compute the forces on atoms. From the structure model of 3D translational symmetry, a suitably large supercell is constructed to ensure that the range of interaction of each atom of the structure is, to a large extent, confined inside this supercell. Within this supercell, each asymmetric atom of the structure model is displaced in three independent directions, and for each displacement, the forces on all the other atoms arising from this displacement are calculated by an ab initio method. The number of displacements, though, may be reduced by the site symmetry. From the computed data, the force constant matrices are assembled. The Fourier transformation of the force constant matrix yields the dynamical matrix defined in reciprocal space, the diagonalization of which provides the complete phonon spectra together with the polarization vectors. Sampling the phonon spectra for a large number of q vectors in the Brillouin zone provides the phonon density of states, from which thermodynamic functions and neutron scattering data are obtained.

Based on the work of Parlinski [1], the above procedure has been implemented to operate in a fully automatic fashion together with the Vienna Ab-initio Simulation Package (VASP) [4] within the MedeA scientific modeling environment [5]. The whole process is automatically executed, starting from the supercell setup, symmetry analysis, displacing atoms, farming out VASP calculations to the available computers in a distributed network, collecting and retrieving ab initio results, assembling the force constants matrix and its diagonalization, evaluation of thermodynamic functions, down to the analysis and display of results. Even though for complex systems a large number of steps and calculations are required, this implementation enables such calculations to be performed in a rather routine manner.

3. A wide range of applications

The accuracy of the methodology is demonstrated for two cases where accurate experimental data on phonon frequencies are available from neutron scattering: GaAs and Nb. Applications are given in different fields to show the possible large impact the methodology may have on the research process: rattlers in thermoelectric skutterudite compounds, formation and reaction enthalpies, bcc to hcp phase transformations, surface reconstructions and the adsorption of molecules on surfaces.

The site preference of hydrogen in aluminum is a further example discussed in the paper by Wimmer presented in this issue [6]. For conciseness, a detailed discussion of computational aspects and results has to be presented elsewhere.

3.1. Assessment of the accuracy: GaAs and Nb

The accuracy of phonon frequencies is demonstrated for the case of GaAs in Fig. 1. Rather typically, the discrepancies between measured and calculated frequencies do not exceed a few tenths of a THz (except for the LO mode at Γ that cannot be obtained). Of course, GaAs is not a challenging test case since the phonons are well-behaved. Rather the opposite case is the phonon dispersion of bcc-Nb that exhibits drastic Kohn anomalies throughout the Brillouin zone. The rather peculiar dispersion curves along the Γ–H direction obtained experimentally and by the computation are compared in Fig. 2, revealing excellent agreement even for this outstanding case.
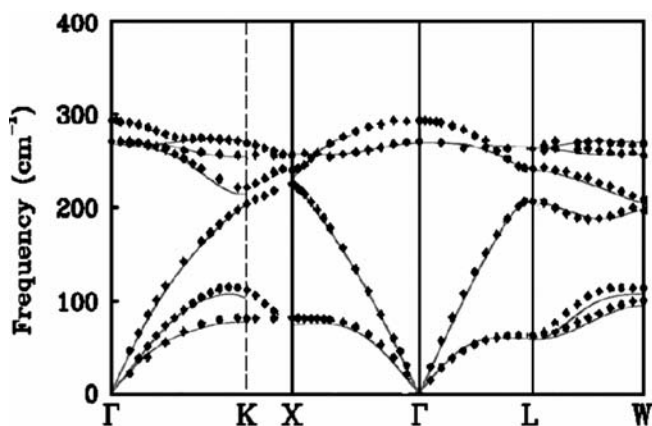
Fig. 1. Experimental phonon dispersion data (diamonds) from Ref. 7
and calculated phonon spectra from first principles (lines) for GaAs

It is noted, furthermore, that the vibrational modes of molecules are obtained with the same precision as phonon modes, provided the molecule is embedded in a suitably large cell to minimize the interaction to translational symmetry copies.
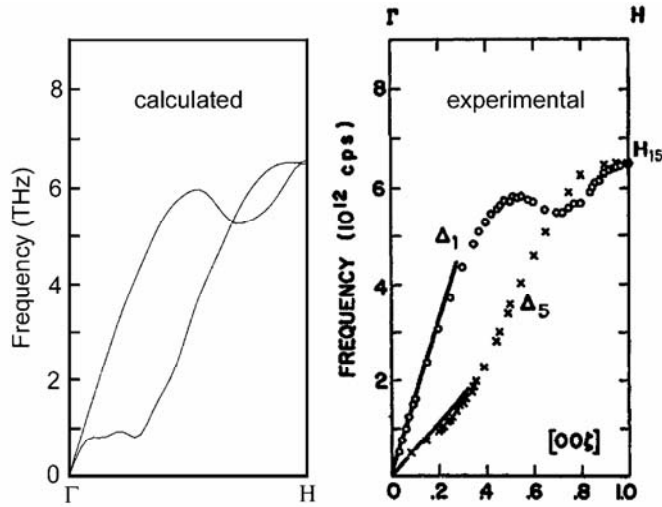
Fig. 2. The Kohn anomaly in bcc Nb along the *Γ–H* direction. Experimental phonon dispersion data from Ref. 8 and calculated phonon spectra from an elongated supercell of 45 Å in the (001) direction

3.2. Thermoelectric skutterudite materials

   In recent years, renewed efforts have been undertaken to find and improve thermoelectric materials for cooling and the generation of electricity. The thermoelectric figure of merit *ZT*

$$ZT = \frac{\sigma S^2 T}{\kappa}$$

can be optimized by combining high electric conductivity σ (like a metal), high thermopower or Seebeck coefficient S (like a semiconductor) and low thermal conductivity κ (like ceramics or glass). Skutterudites MX_3 (M = Co, Rh, Ir, and X = P, As, Sb) are promising materials for thermoelectric applications [9]. The thermal conductivity of the antimonides could successfully be reduced by filling the voids of the structure by large and heavy atoms such as lanthanides, actinides or earth alkaline metals, thus improving considerably their figure of merit. It was speculated that the mechanism for reducing thermal conductivity might be attributed to long wavelength phonons emitted by the loosely bound filling atoms in the voids, which may couple with those phonons mainly responsible for thermal conduction. Indeed, the calculated phonon dispersion and densities of states of $LaFe_4P_{12}$ and $LaFe_4Sb_{12}$ strongly support the existence of these 'rattler modes' in the vibrational spectrum. Whereas for the phosphide the La related modes are completely separated from the others (see Fig. 3), the modes of Sb character couple strongly with the La modes.
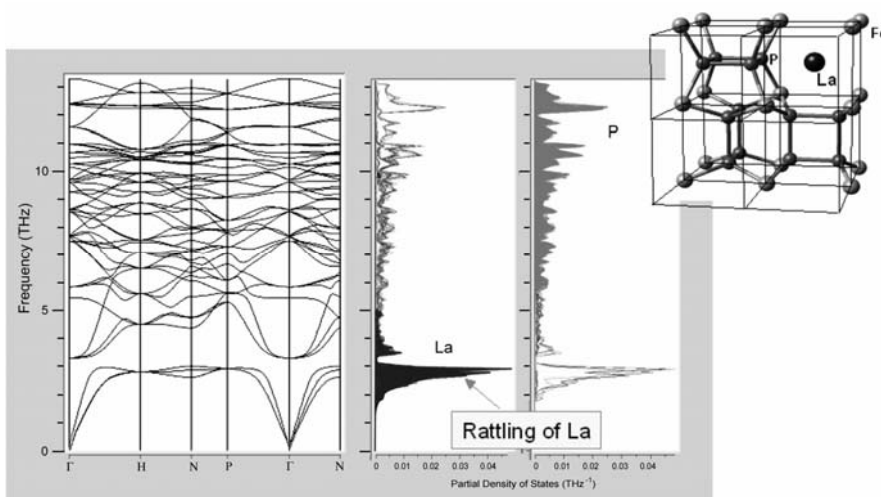
Fig. 3. Calculated phonon dispersion and phonon density of states of $LaFe_4P_{12}$.
The unit cell is shown in the insert

Thermal conductivity is considered to be mainly mediated by the pnicogene (P, As, Sb) sublattice. Thus, the experimental finding that filling voids with heavy atoms is able to reduce thermal conductivity of antimonides but not of phosphides can, on the basis of the calculated phonon spectra, be understood.

3.3. Thermochemistry: enthalpies of formation and reaction enthalpies

The direct approach to vibrations is directly applicable to thermochemistry once the reactants are solid state phases or gases. The importance of vibrational contributions is emphasized by two examples in hydrogen chemistry. Table 1 provides several contributions to the reaction enthalpy of the chemical reaction of hydrogen with vanadium; the electronic part as calculated from first principles, the zero point energy, and

Table 1. Enthalpy of the reaction for the hydration of vanadium. Calculated electronic
and vibrational contributions and experimental results from Ref. [10]. Energies in $kJ \cdot mol^{-1}$

Value	$2V + \frac{1}{2}H_2 \rightarrow V_2H$	$V + H_2 \rightarrow VH_2$
Electronic energy (ab initio)	−40	−67
Energy including zero point vibration	−38	−45
Enthalpy at 298 K	−41	−54
Experiment	−35	−40

the temperature dependent free energy including the vibrational entropy. The small contribution of electronic enthalpy originating from exciting electrons into excited

states with increasing temperature is neglected. In fact, different vanadium hydrides may form, V_2H and VH_2. Whereas vibrational contributions to the reaction enthalpy are almost negligible for the formation of V_2H, for VH_2 the zero point energy contribution amounts to as much as 1/3 of the electronic part. In conclusion, even for quite related systems the estimation of vibrational effects is difficult and calculations are required.

Much research effort is put into the development of hydrogen storage materials as an enabling technology for future replacement of natural oil based industries. Table 2 lists the calculated results for temperature dependent heats of formation of some complex hydrides that are among the most promising candidates. Experimental data are included. For all compounds the electronic energy turns out to be quite close to experimental results. Including zero point vibrations causes considerable deviation, however, raising the temperature to the standard condition of 298 K, the good agreement is restored. These data illustrate that good agreement between the energies of formation, as calculated from first principles, and experimental data obtained at standard temperature, may often be due to the zero point energy and temperature effects cancelling out each other.

Table 2. Formation enthalpy of hydrogen storage materials. Calculated electronic and vibrational contributions compared to experimental results of Ref. [11] and references therein. Energies in $kJ \cdot mol^{-1}$

Value	$LiAlH_4$	Li_3AlH_6	LiH
Electronic energy (ab initio)	−98	−295	−83
Energy including zero point vibration	−77	−258	−77
Enthalpy at 298 K	−96	−288	−84
Experiment	−107	−300	−91

3.4. Soft modes and phase transformations

Soft modes in the phonon dispersion indicate phase transformations and may be used to explore the transformation path towards a stable phase. However, approximations or computational issues may cause unphysical complex frequencies, too, and careful studies are necessary. A rather simple example is the bcc to hcp transformation of rhenium. Whereas tungsten is stable in the bcc structure, as demonstrated by its phonon dispersion shown in Fig. 4a, the dispersion of the neighbouring element rhenium in this structure exhibits strong soft modes at the H and N point, in particular (see Fig. 4b).

Indeed, Re is known to be stable in the hcp structure. Soft phonon modes at the N point correspond to collective movements of atoms in the (110) direction without restoring forces. As illustrated in Fig. 4c, this movement leads to a bcc to hcp phase transformation path.
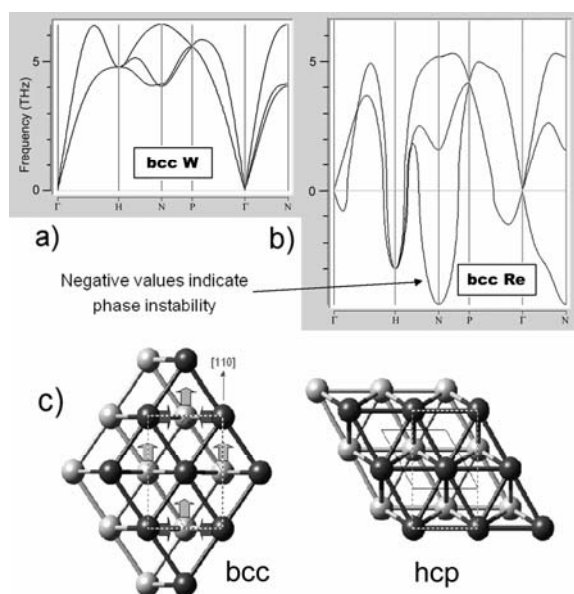
Fig. 4. Calculated phonon dispersion of bcc W (a), bcc Re (b),
and bcc to hcp phase transformation path (panel c)
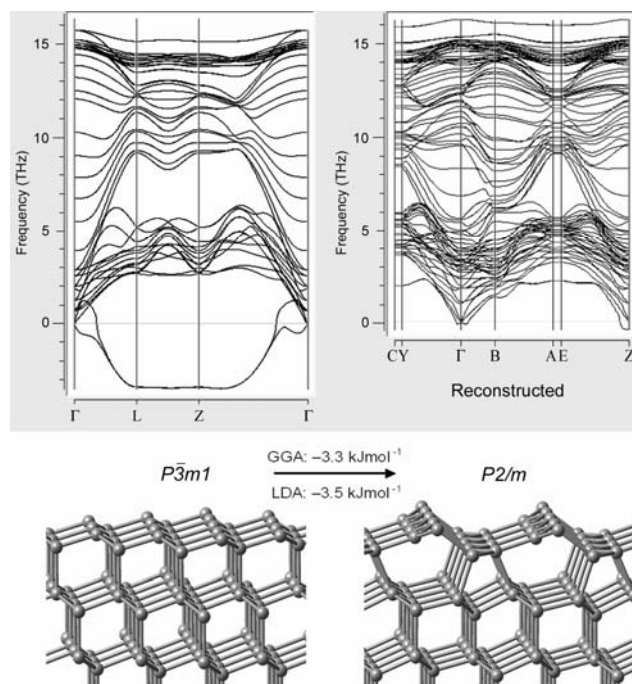
Fig. 5. Calculated phonon dispersion of unreconstructed and 2x1 reconstructed Si(111) surface.
The surface structures are shown below the corresponding dispersion curves

3.5. Surface phonons and surface reconstructions

The calculation of vibrational spectra is not limited to bulk phases or molecules, because surfaces or interfaces may also be tackled by the method. As a two-dimensional analogue of the phase transformation of bulk materials, soft modes of surface phonon spectra may indicate surface reconstructions. It is well known from low-energy electron diffraction experiments (LEED) [12] that the Si(111) surface exhibits a 2×1 π-bonded chain reconstruction. The calculated phonon dispersion of slab models for the unreconstructed and 2×1 reconstructed Si(111) surfaces are shown in Fig. 5.

The unreconstructed surface is destabilized by soft phonon modes corresponding to vibrations of the surface Si atoms. On the other hand, the phonon dispersion of the reconstructed Si(111)2×1 surface slab model is mostly free of soft modes. The complex frequencies close to the Γ and Z point of the slab model's Brillouin zone are due to vibrations of the whole slab against its symmetry copy, i.e. an artifact of the slab model to surfaces.

3.6. Molecules on surfaces

Adsorption processes of molecules on surfaces are studied experimentally by measuring the change of the vibration spectra upon adsorption. In fact, shifts of fre-
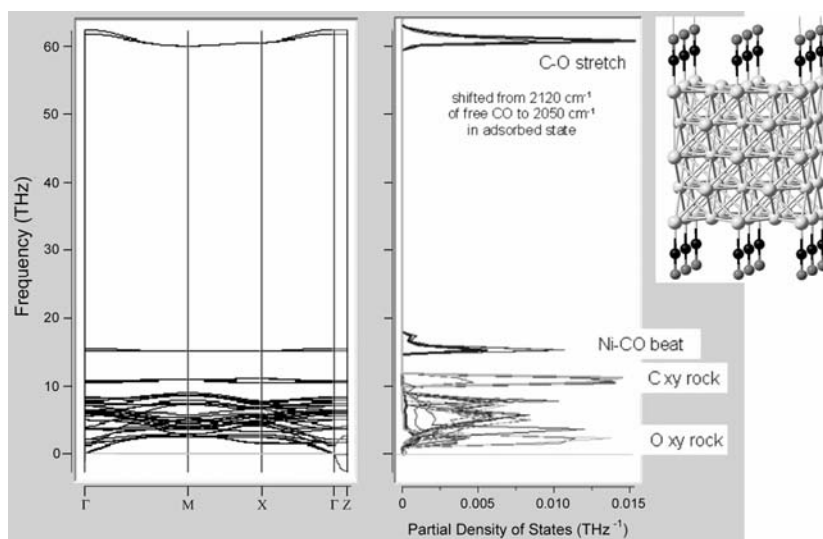
Fig. 6. Calculated phonon spectrum and density of states
of the Ni(001) with (2×2) adsorbed CO molecules

quencies may occur and are interpreted in order to gain insight into adsorption geometry and coverage. Comparison to calculated vibration frequencies for different model structures provides a valuable insight and may considerably facilitate interpretation of experimental data.

In Figure 6, the phonon dispersion curves and density of states of a 5-layer slab model for the c(2×2) coverage of CO molecules on the Ni(001) surface is shown.

The highest frequency of 2050 cm^{-1} is found to correspond to the C-O stretch vibration. A reference calculation for the isolated gas phase CO molecule yields a stretch frequency of 2120 cm^{-1}. Indeed, experimental data indicate a shift of the gas phase frequency of 2140 cm^{-1} down by about 70 cm^{-1} upon adsorption [13], which is in good agreement to the calculation. Furthermore, Ni-CO beat, C *xy* rock and O *xy* rock vibration frequencies can be attributed to animating corresponding phonon modes, thus supporting interpretation of the features in experimental spectra.

4. Summary

In summary, the direct approach to lattice vibrations and its implementation in an automated computational framework is discussed, enabling computation of vibrational properties and temperature effects from first principles in a routine manner. In order to demonstrate the huge potential of the approach for industrial research, the method is applied to a wide range of problems in materials science. The examples of applications are intended to provide hints and ideas of how this methodology may enrich the scope of simulation techniques and may have a significant impact on industrial research strategies.

References

[1] PARLINSKI K., LI Z. Q., KAWAZOE Y., Phys. Rev. Lett., 78 (1997), 4063.
[2] KRESSE G., FURTHMÜLLER J., HAFNER J., Europhys. Lett., 32 (1995), 729.
[3] BARONI S., DE GIRONCOLI S., DAL CORSO A., GIANOZZI P., Rev. Modern Phys., 73 (2001), 515.
[4] KRESSE G., FURTHMÜLLER J., Phys. Rev. B, 54 (1996), 11169; Computat. Mat. Sci., 6 (1996), 15; KRESSE G., JOUBERT D., Phys. Rev. B, 59 (1999), 1758.
[5] MedeA 1.8, Materials Design, Le Mans, France (www.MaterialsDesign.com).
[6] WIMMER E., Mat. Sci.-Poland, 23 (2005), 325.
[7] STRAUCH D., DORNER B., J. Phys. Condens. Matter, 2 (1990), 1457.
[8] POWELL B. M., MARTEL P., WOODS A.D.B., Phys. Rev., 171 (1968), 727.
[9] UHER C., *Skutterudites: Prospective Novel Thermoelectrics, in Semiconductors and Semimetals*, Vol. 69, Academic Press, 2001, p. 139.
[10] WISWALL R., [in:] G. Alefeld, J. Völkl (Eds.), *Topics in Applied Physics*, Vol. 29, Springer-Verlag, Berlin, 1978, p. 201; GRIESSEN R., RESITERER T., in: L. Schlapbach (Ed.), Topics in Applied Physics, Vol. 63, Springer, Berlin, 1988, p. 218.
[11] LØVVIK O.M., OPALKA S.M., BRINKS H.W., HAUBACK B.C., Phys. Rev. B, 69 (2004), 134117.; CHASE M.W. JR., *NIST-JANAF Themochemical Tables*, Fourth Edition, J. Phys. Chem. Ref. Data, Monograph 9 (1998), 1–1951.
[12] HIMPSEL F.J., MARCUS P. M., TROMP R., BATRA I. P., COOK M. R., JONA F., LIU H., Phys. Rev. B, 30 (1984), 2257.
[13] http://www.cem.msu.edu/~cem924sg/Topic11.pdf.

Magnetic and electronic properties of the new ferrimagnet Sr$_8$CaRe$_3$Cu$_4$O$_{24}$

MASANORI KOHNO[*], XIANGANG WAN, XIAO HU

Computational Materials Science Center,
National Institute for Materials Science, Tsukuba, 305-0047, Japan

Magnetic and electronic properties of the recently-discovered material Sr$_8$CaRe$_3$Cu$_4$O$_{24}$ were investigated by means of a quantum Monte Carlo simulation, the Green function method and the LSDA+U (local spin-density approximation plus the Hubbard-U term) method. The LSDA+U calculation shows that the ground state is an insulator with magnetic moment $M = 1.01$ μ_B/f.u., which is consistent with experimental results. The magnetic sites were specified and an effective model for the magnetic properties of this compound derived. The resultant effective model is a three-dimensional Heisenberg model with spin-alternation. Finite-temperature properties of this effective model are investigated by the quantum Monte Carlo method (continuous-time loop algorithm) and the Green function method. The numerical results are consistent with experimental results, indicating that the model is suitable for this material. Using the analysis of the effective model, some predictions for the material are made.

Key words: *ferrimagnetism; quantum spin system; quantum Monte Carlo*

1. Introduction

Strong electronic correlations produce a rich variety of phenomena. High-T_c superconductivity [1] is one such a phenomenon. It is widely believed that the origin of high-T_c superconductivity is related to the nature of undoped systems [2], which are Mott insulators with an antiferromagnetic order. Recently-discovered perovskite cuprate Sr$_8$CaRe$_3$Cu$_4$O$_{24}$ [3] is a magnetic insulator which has spontaneous magnetization at room temperature and in some respects resembles parent materials of high-T_c superconductors. It is expected that the ferromagnetism of Sr$_8$CaRe$_3$Cu$_4$O$_{24}$ might be caused by strong electronic correlations due to a similar mechanism to the antiferromagnetism of parent materials of high-T_c superconductors. Furthermore, among ferromagnetic cuprates this material has an unusually high magnetic transition tempera-

_____

[*] Corresponding author, e-mail: KOHNO.Masanori@nims.go.jp

ture (T_c) up to 440 K, although those of other ferromagnetic cuprates are at most 30 K [4]. Thus, the material is interesting for its high T_c induced by strong electronic correlations. The purpose of this paper is to clarify the origin of magnetism and to predict the possible magnetic properties of this material.

2. Local spin-density approximation

The lattice structure is shown in Fig. 1, which is determined experimentally [3]. In order to investigate the electronic properties of the compound, the local spin-density approximation plus the Hubbard-U term (LSDA+U) method using the package WIEN2K [5], which is an implementation of the density-functional APW-lo method
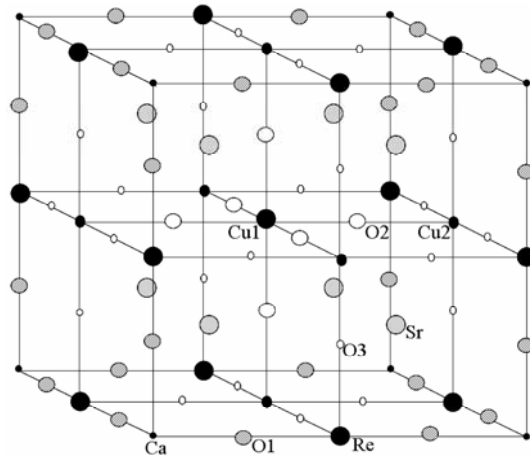
Fig. 1. Unit cell of $Sr_8CaRe_3Cu_4O_{24}$

[6], has been used. The cutoff values were set at $RK_{max} = 7$, the LSDA + U parameters $U = 10$ eV and $J_{LSDA+U} = 1.2$ eV [7]. For the exchange correlation, the standard generalized gradient approximation (GGA) [8] has been applied. The numerical results show that the ground-state is an insulator with a ferrimagnetic order: the charge gap is estimated as about 1.68 eV. Magnetic moments are almost localized at Cu sites, and their directions at Cu1 and Cu2 sites are opposite. The absolute values of the magnetic moments at Cu1 and Cu2 are 1.01 μ_B and 0.86 μ_B per formula unit (f.u.), respectively, and those of other sites are less than 0.07 μ_B/f.u. The total magnetic moment is 1.01 μ_B/f.u., which is comparable to the experimental result (0.95 μ_B/f.u.) [3]. The LSDA+U calculation shows that the orbital degrees of freedom are also ordered. The high T_c could be due to the large overlap between the orbitals of O_2 and Cu originated from orbital ordering. The mechanism of the antiferromagnetic coupling is the super-exchange [9] as in the parent materials of high-T_c superconductors. Details of the LSDA + U calculation are presented in a separate paper [10].

3. Effective model for magnetism

By using LSDA+U method, the magnetic sites of this compound have been identified. Since the system is an insulator, it is natural to expect that the effective model for magnetism is a Heisenberg model. It was assumed that the spins on nearest-neighbour sites interact with each other. Then, the Hamiltonian of the effective model is expressed as

$$H = J \sum_{i,p} \mathbf{S}_i \cdot \mathbf{s}_{i+p/2} \tag{1}$$

where $\mathbf{S}_i$ and $\mathbf{s}_{i+p/2}$ denote spin operators at Cu1 (i) and Cu2 ($i+p/2$) sites, respectively. Here, p represents the unit vectors ($p - \pm\hat{x}, \pm\hat{y}, \pm\hat{z}$). The unit cell of this effective model is illustrated in Fig. 2.
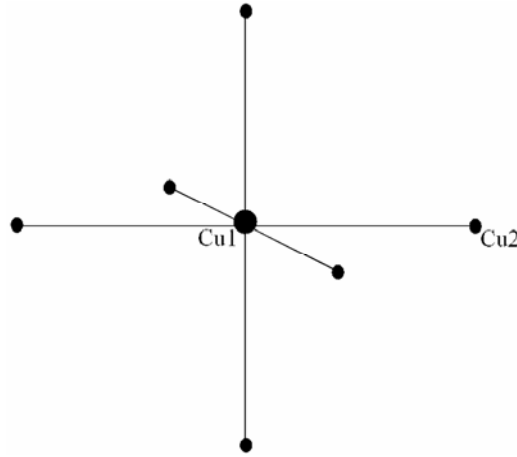
Fig. 2. Unit cell of the effective model

Consider the appropriate combination of spin length (S, s), where S and s denote the spin length at Cu1 and Cu2 sites, respectively. In order to determine these, the magnetization of the ground state (M_{GS}) and that of the fully-polarized state (M_{FP}) for the effective model in a unit cell were calculated. In the case of (S, s) = (1/2, 1/2), $M_{GS} = 1$ and $M_{FP} = 2$, which correspond to 2 μ_B/f.u. and 4 μ_B/f.u., by setting the g-factor 2. For (S, s) = (1/2, 1), (1, 1/2), (1, 1), (M_{GS}, M_{FP}) becomes (5/2, 7/2), (1/2, 5/2), (2, 4), respectively. Here, M_{GS} and M_{FP} obtained by the LSDA+U method are 1.01 μ_B/f.u. and 5 μ_B/f.u.. Hence, (S, s) = (1, 1/2) is the most suitable for this compound.

It should be noted that M_{GS} and M_{FP} of the effective model are exactly 1/2 and 5/2 (equal to 1 μ_B/f.u. and 5 μ_B/f.u.) in any size of system due to the Marshall–Lieb–Mattis theorem [11]. The ground-state magnetization of the effective model (1 μ_B/f.u.) is comparable to the experimental results [3].

Next, the strength of antiferromagnetic coupling J was consdiered. The energy difference between the ground state and the fully-polarized state in a unit cell was calculated by the exact diagonalization method. The result is $8J$. The energy difference was calculated for $Sr_8CaRe_3Cu_4O_{24}$ also by the LSDA+U method. The result was $0.036Ry$. Hence, by comparing these results, $J = 0.0045Ry$ (710 K) was obtained.

4. Green function method

Using the above arguments, the effective model for magnetism of $Sr_8CaRe_3Cu_4O_{24}$, which is a spin-alternating Heisenberg model in three dimensions has been obtained. In order to investigate finite-temperature properties of this compound, the Green function method [12] was applied to the effective model where Green functions are defined as Fourier components of time-dependent correlation functions:

$$G^{Ss}(k,\omega) = \frac{1}{N}\int dt \sum_{i,j}\left\langle\left\langle S_i^+(t); s_{j+\frac{p}{2}}^-\right\rangle\right\rangle e^{ik\left(r_i - r_{j+\frac{p}{2}}\right) - i\omega t} \tag{2}$$

Since there are four sites in a unit cell, 16 (4×4) Green functions are necessary. Here, the double-bracket correlation function is defined as

$$\left\langle\left\langle A(t); B\right\rangle\right\rangle \equiv -\theta(t)\left\langle\left[A(t), B\right]\right\rangle$$

Coupled equations were obtained for 16 Green functions by using a decoupling approximation [13]

$$\left\langle\left\langle S^z(t)s^+(t); s^-\right\rangle\right\rangle \cong \left\langle S^z\right\rangle\left\langle s^+(t); s^-\right\rangle$$
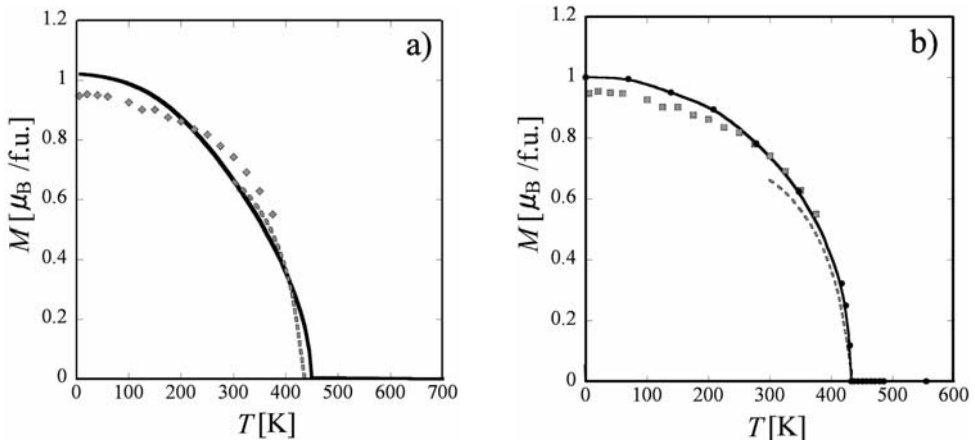

Fig. 3. Temperature dependence of spontaneous magnetization obtained by (a) the Green function method and (b) the quantum Monte Carlo method (solid curves). Dots and dotted line denote the experimental results [3]

These equations were solved analytically and the temperature dependence of magnetizations was obtained using these Green functions by following Callen's scheme [14]. Figure 3a shows the result of the Green function method. The agreement with the experimental result is good, indicating that the effective model is suitable for describing the magnetic properties of $Sr_8CaRe_3Cu_4O_{24}$. From the LSDA+U result J was set as $J = 710$ K.

5. Quantum Monte Carlo simulation

In order to investigate magnetic properties of this compound more quantitatively, a quantum Monte Carlo method was applied to the effective model. The algorithm used was the continuous-time loop algorithm (see Refs. in [15]), which is a powerful method for non-frustrated spin systems. More than one million updates for each simulation were performed. The system size was up to 16×16×16 unit cells which correspond to 16,384 sites.

Spontaneous magnetization can be obtained by extrapolating $\bar{S}(N)$ which is defined as $\bar{S}(N,T) \equiv \sqrt{3\langle S_0^z S_l^z \rangle_T}$, where S_0^z and S_l^z are the z-component of Cu1-spin at the centre of the system and that of the furthest site from the centre, respectively. Here, N denotes the number of unit cells. By extrapolating $\bar{S}(N,T)$ in the thermodynamic limit, we obtain the temperature dependence of spontaneous magnetization as shown in Fig. 3b. The quantum Monte Carlo result is consistent with experimental results. By tuning J to fit the transition temperature, we obtain $J = 695$ K. The first estimation of $J = 710$ K based on LSDA+U results was not far from the fitted value, suggesting that the above mapping is valid. To date, the temperature dependence of the spontaneous magnetization is the only quantity that has been measured experimentally [3]. However, since the effective model for this compound has been derived, further predictions of its magnetic properties through the investigation of this effective model can be made.

The temperature dependence of the inverse of uniform and staggered susceptibilities above the critical temperature are shown in Fig. 4. As is evident from this figure, both susceptibilities diverge toward the critical point. In general, physical quantities show a power-law behaviour at the critical point of the second-order phase transition. The universality class is characterized by the exponents of physical quantities such as length scale $\xi \propto \Delta T^{-\nu}$, magnetization $M \propto |\Delta T|^{\beta}$ and susceptibility $\chi \propto \Delta T^{-\gamma}$, where $\Delta T \equiv T - T_c$. In finite-size systems, the magnetization and the susceptibility can be expressed in terms of scaling functions as [16]

$$M \approx |\Delta T|^{\beta} \bar{M}\left(L|\Delta T|^{\nu}\right) \tag{3}$$

$$\chi \approx \Delta T^{-\gamma} \bar{\chi}\left(L\Delta T^{\nu}\right) \tag{4}$$
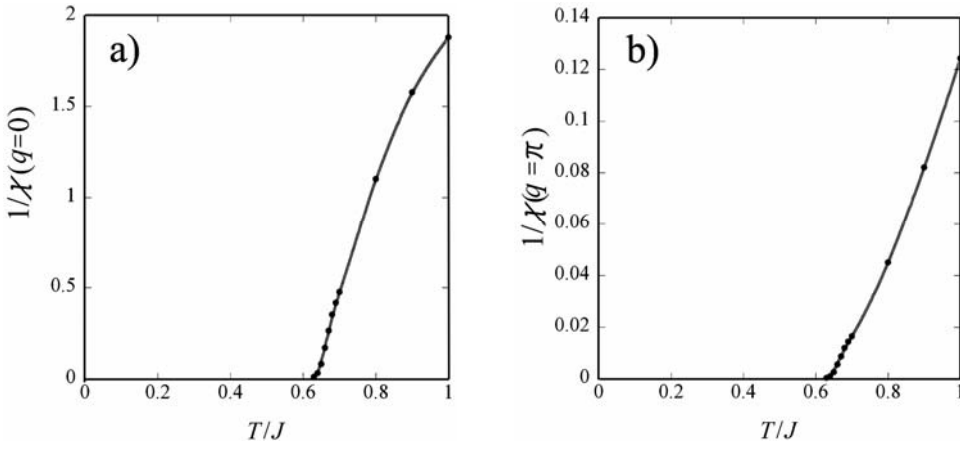
Fig. 4. Temperature dependence of the inverse of uniform (a)
and staggered susceptibilities (b) above the critical temperature
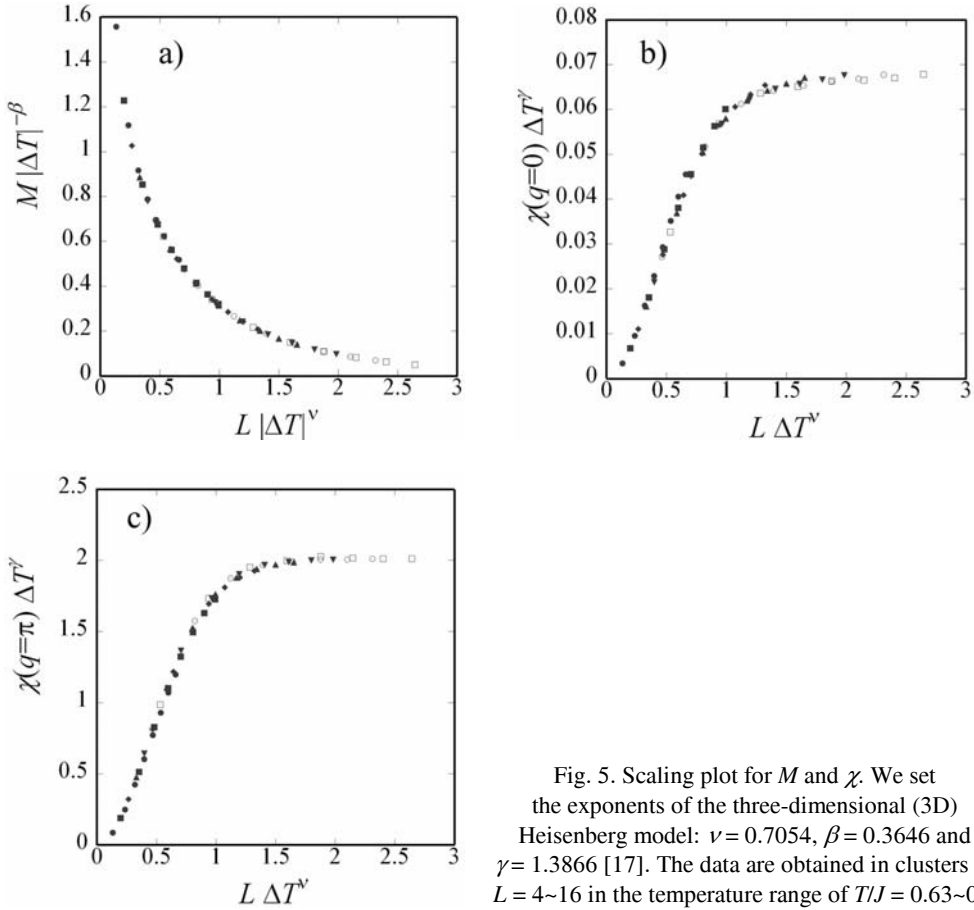
Fig. 5. Scaling plot for M and χ. We set
the exponents of the three-dimensional (3D)
Heisenberg model: $\nu = 0.7054$, $\beta = 0.3646$ and
$\gamma = 1.3866$ [17]. The data are obtained in clusters of
$L = 4\sim16$ in the temperature range of $T/J = 0.63\sim0.7$

$M\left|\Delta T\right|^{-\beta}$ and $\chi\Delta T^{\gamma}$ were plotted as a function of $L\left|\Delta T\right|^{\nu}$ in Fig. 5, where we use the exponents of the three-dimensional (3D) Heisenberg model: $\nu = 0.7054$, $\beta = 0.3646$ and $\gamma = 1.3866$ [17]. The figure shows that data in various sizes and various temperatures near the critical point fall into single curves, suggesting that the universality class is that of the 3D Heisenberg model.
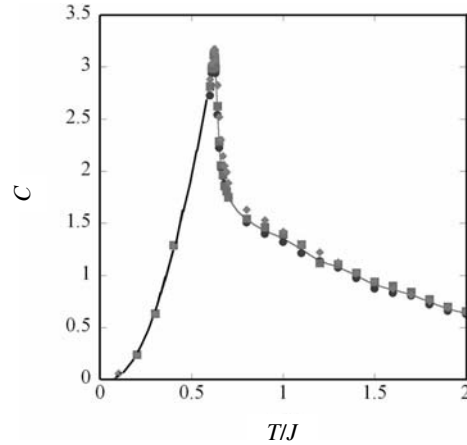
Fig. 6. Temperature dependence of the specific heat. Circles, squares and diamonds denote the data of $L = 12$, 14 and 16, respectively. Solid line is a guide to the eye

The temperature dependence of the specific heat is plotted in Fig. 6. The size dependence of the specific heat is small. The maximum value is almost saturated at about 3.1. The critical temperature was estimated as 0.622 ± 0.002, assuming that the specific heat is a maximum at the critical temperature. Since the specific heat has little size-effect, it is expected that the specific heat at the critical temperature remains finite in the thermodynamic limit. This is consistent with the scaling property of the 3D Heisenberg model: $C \propto \Delta T^{-\alpha}$, $\alpha = -0.1162 < 0$ [17].

6. Conclusions

The magnetic and electronic properties of $Sr_8CaRe_3Cu_4O_{24}$ have been investigated by means of the quantum Monte Carlo method, the Green function method and the LSDA+U method. Since the LSDA+U calculation shows that magnetic moments are localized at Cu sites, a Heisenberg model was introduced as an effective model for magnetic properties. The spin lengths at Cu1 and Cu2 sites as one and one half, respectively, were obtained by comparing the result given by the effective model in a unit cell and that given by the LSDA+U method. The finite-temperature properties of the effective model were investigated by the Green function method and the quantum Monte Carlo method. The agreement on magnetization at finite temperatures between the numerical results and the experimental results was good, suggesting that the effective model is suitable for describing the magnetic properties of $Sr_8CaRe_3Cu_4O_{24}$. The

properties of the effective model were further investigated and revealed that the universality class of the critical point is that of the 3D Heisenberg model. Some of the results given by the effective model may be accessible by experiments.

Acknowledgements

References

[1] BEDNORZ J.G., MULLER K.A., Zeit. Phys. B, 64 (1986), 189.

[2] ZHANG F.C., RICE T.M., Phys.Rev. B, 37 (1988), 3759.

[3] TAKAYAMA-MUROMACHI E., DREZEN T., ISOBE M., ZHIGADLO N.D., KIMOTO K., MATSUI Y., KITA E., J. Solid State Chem., 175 (2003), 366.

[4] MIZUNO F., MASUDA H., HIRABAYASHI I., TANAKA S., HASEGAWA M., MIZUTANI U., Nature, 345 (1990), 788; I.YAMADA, J. Phys. Soc. Jpn., 33 (1972), 979; KOHN K., INOUE K., HORIE O., AKIMOTO S., J. Solid State Chem., 18 (1976), 27.

[5] BLAHA P., SCHWARZ K., MADSEN G., KVASNICKA D., LUITZ J., WIEN2K, *An Augmented Plane Wave + Local Orbitals Program for Calculating Crystal Properties*, Karlheinz Schwarz, Tech. Universität Wien, Austria, 2001, ISBN 3-9501031-1-2.

[6] SJÖSTEDT E., NORDSTRÖM L., SINGH D.J., Solid State Commun., 114 (2000), 15; MADSEN G.K.H., BLAHA P., SCHWARZ K.H., SJÖSTEDT E., NORDSTRÖM L., Phys. Rev. B, 64 (2001), 195134.

[7] ANISIMOV V.I., KOROTIN M.A., NEKRASOV I.A., PCHELKINA Z.V., SORELLA S., Phys. Rev. B, 66 (2002), 100502.

[8] PERDEW J.P., BURKE K., ERNZERHOF M., Phys. Rev. Lett., 77 (1996), 3865.

[9] KRAMERS H.A., Physica, 1 (1934), 182; ANDERSON P.W., Phys. Rev., 115 (1959), 2.

[10] WAN X., KOHNO M., HU X., Phys. Rev. Lett., 94 (2005), 087205.

[11] MARSHALL W., Proc. Roy. Soc. A 232 (1955), 48; LIEB E.H., MATTIS D., J. Math. Phys. 3 (1962), 749.

[12] BOGOLYUBOV N.N., TYABLIKOV S.V., Dokl. Acad. Nauk. SSSR 126 (1959), 53; [Sov. Phys. Dokl. 4 (1959), 604].

[13] TYABLIKOV S.V., Ukr. Mat. Zh., 11 (1959), 287.

[14] CALLEN H.B., Phys. Rev., 130 (1963), 890.

[15] EVERTZ H.G., Adv. Phys., 52 (2003), 1.

[16] PRIVMAN V., FISHER M.E., Phys. Rev. B, 30 (1984), 322.

[17] LE GUILLOU J.C., ZINN-JUSTIN J., Phys. Rev. Lett., 39 (1977), 95.

Theoretical study of electron transport properties of an organic molecule

Jun Nara[1*], W.T. Geng[1], Hiori Kino[1], Nobuhiko Kobayashi[2], Takahisa Ohno[1, 3]

[1]Computational Materials Science Center (CMSC), National Institute for Materials Science (NIMS),
1-2-1 Sengen, Tsukuba, Ibaraki 305-0047, Japan

[2]Research Consortium for Synthetic Nano-Function Materials Project (SYNAF),
National Institute of Advanced Industrial Science and Technology (AIST),
Tsukuba Central 2, 1-1-1 Umezono, Tsukuba, Ibaraki 305-8568, Japan

[3]Institute of Industrial Science (IIS), University of Tokyo, 4-6-1 Komaba,
Meguro, Tokyo, 153-8505, Japan

Electron transport properties of benzene-(1,4)-dithiolate sandwiched between two gold electrodes were investigated using first-principles calculations. It was found that the peak energies and the peak widths in the transmission spectra are strongly dependent on the contact structures. Furthermore, the contributions of MOs to the transmission coefficients also depend on the contact structures. Especially, only the channel related to HOMO-3, HOMO, and LUMO+1 contributes to the conductance at zero bias. These results suggest that the determination of the contact structure is essential for estimating the properties of molecular devices.

Key words: *electron transmission; first principles calculations; organic molecule; benzenedithiolate*

1. Introduction

Recently, transport properties of single-organic molecules have attracted much attention. One of the most prominent systems in this field is the dithiolate molecule between gold surfaces. Since the conductance of a benzene-(1,4)-dithiolate (BDT) sandwiched between two gold electrodes was measured experimentally [1], it has been intensively investigated theoretically. However, it is still unclear how the conductance depends on the atomic configurations around the contact. Knowing how the contact geometry influences the conductance through the metal–molecule–metal sand-

---

*Corresponding author, e-mail: NARA.Jun@nims.go.jp

wich structure requires both, a precise determination of the molecule–metallic-electrode interface structure, and an evaluation of the conductance for different geometries with fair accuracy. The transmission properties of the BDT molecule sandwiched between two gold electrodes by means of *ab initio* method were investigated, and the effect of the contact structures was examined. The transmission coefficients were evaluated with the Lippmann–Schwinger equation. It was found that the peak energies and the peak widths in the transmission spectra are sensitively dependent on the contact structures. Furthermore, the contributions of molecular orbitals (MOs) of the BDT molecule to the transmission coefficients also depend on the contact structures. Especially, only some of MOs contribute to the conductance at zero bias. These results suggest that the determination of the contact structure is essential to estimate the transport properties of molecular devices.

2. Calculation method

The transmission coefficients are evaluated by using the Lippmann–Schwinger equation. The details are described in Refs. [2–4]. The wave function is expressed with the two dimensional plane waves parallel to the surface and the real-space mesh along the surface normal. The electrodes are replaced by bi-jellium which corresponds to the metallic gold ($r_s \sim 3$) and the organic molecule is inserted between the bi-jellium. This method uses the non-local pseudopotentials, which allow organic materials to be studied. The electronic states were decomposed into eigenchannels [5]. The conductance is evaluated within the Landauer formula [6], in which the conductance unit is $G_0 = 2e^2/h$.

3. Results

The electron transport properties of the BDT molecule sandwiched between two gold electrodes have been studied so far, and it was found that the transmission coefficients and the projected density of states (pDOS) are sensitively dependent on the contact structures [4, 7]. Here, the results for two typical structures are shown. Figure 1 shows the atomic configurations of the two. In Figure 1a, one Au atom is inserted between the molecule and the jellium electrode at each side, rendering a model of adsorption at the on-top site. In this geometry, the benzene ring is upright to the electrode surface and the C, S and Au atoms form a straight line. In Figure 1b, three Au atoms are inserted at each side to simulate the hollow site structures [8]. In this case, the benzene ring is slightly tilted from the surface normal by about 20 degrees.

Figure 2 shows (a) the eigenchannel transmission and (b) the pDOS as a function of the incident electron energy for the structure shown in Fig. 1a. The Fermi level is set to be 0.

Fig. 1. Metal–molecule–metal junction structures:
a) one Au atom is inserted between the molecule
and the jellium electrode to each side
to simulate the ontop adsorption structure
and (b) three Au atoms are inserted to simulate
the follow site adsorption structure

Fig. 2. Transmission spectrum (a) and pDOS as a function of the incident
electron energy (b) for the structure in Fig. 1(a)

In Figure 2a, two transmission channels with non-vanishing magnitudes are plotted. The first one has two peaks, located at −2.0 eV and −1.0 eV. These two peaks have the same symmetry. The second channel has one peak at −1.5 eV, with a different symmetry. The magnitudes of other channels are too small to be visible. Figure 2b shows the pDOS with respect to the MOs of an isolated BDT molecule, in order to clarify which MOs contribute to the transmission properties. The MOs from HOMO-3 to LUMO+1 were considered here, neglecting other MOs with only marginal or vanishing contribution. HOMO-3, HOMO, LUMO, and LUMO+1 are related to π orbitals, whereas HOMO-2 and HOMO-1 are related to σ orbitals. It is noteworthy that HOMO-3, HOMO and LUMO+1 bear one kind of symmetry when projected to the plane normal to the transmission direction, and HOMO-2 and HOMO-1 bear another [4]. These symmetries are important to analyse the transmission spectra and the con-

ductance. HOMO-3 has a peak at −2.0 eV matching well to the peak at the −2.0 eV in the transmission spectrum (Fig. 1a). Similarly, HOMO-2, HOMO-1, and HOMO have peaks corresponding to the transmission resonance. In Figure 2a, the two peaks related to HOMO-3 and HOMO form the first channel, as the two have the same symmetry. Similarly, HOMO-2 and HOMO-1 form the second channel, as they have a different symmetry.
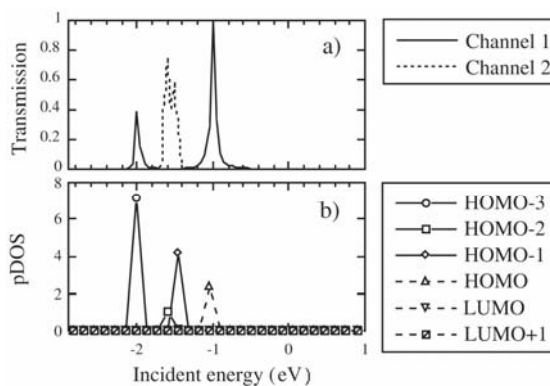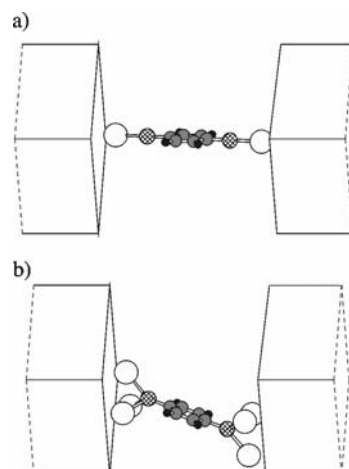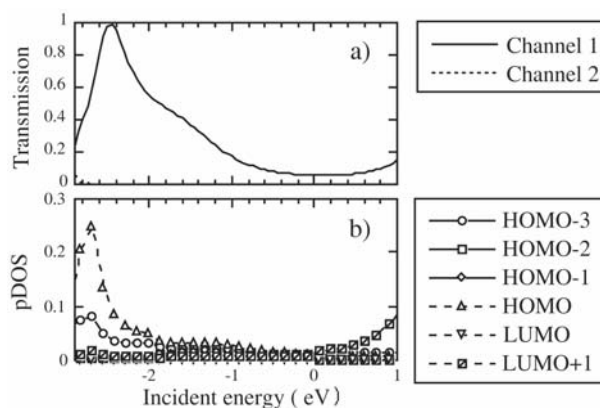

Fig. 3. Transmission spectrum (a) and pDOS as a function of the incident
electron energy (b) for the structure in Fig. 1b

Figure 3 shows (a) the eigenchannel transmission and the (b) pDOS as a function of the incident electron energy for the structure shown in Fig. 1b.The position and width of the conductance peaks are very different from those in Fig. 2. Only one channel is visible in Fig. 3a, with one resonance taking place at −2.5 eV. The peak width is much larger than that in Fig. 2. This may be readily understood by the fact that the S−Au interaction is greatly strengthened as a direct result of the increased coordination number. In the same way as in Fig. 2, the peaks of the transmission spectra can be attributed to the MOs. For the structures shown in Fig. 1b, there is only one channel bearing remarkable transmission, and no contribution from other MOs than HOMO-3 and HOMO to the transmission coefficient. Thus these first principles calculation results demonstrate that the contributions of MOs to the transmission properties can vary strongly with the contact configurations.

The conductance at zero bias corresponds to the sum of the eigenchannel transmissions at the Fermi level. For both structures, only the first channel contributes to the conductance, suggesting that among all MOs, only HOMO-3, HOMO and LUMO+1 contribute to the conductance at zero bias, while HOMO-2, HOMO-1, LUMO and other MOs do not. Although the reason for this difference among the MOs' contribution is unclear at this point, it must be concerned with the MOs symmetry. The conductances are calculated to be $0.003G_0$ and $0.058G_0$ for the structures shown in Figs. 1a and b, respectively. The conductance of the former is very small compared to the latter.

These results are extremely different from the previous experimental results [1], which shows a very small conductance ($\sim 10^{-5}G_0$). Although some theoretical groups, including us, have tried to overcome the discrepancy between the experimental and the theoretical results, it remains a problem. This may mean that the models adopted here are inappropriate to explain the experiments. One of the reasons for this discrepancy is the lack of the information about the atomic configurations in the experiment. Recently, a new experimental report [9] shows a greatly higher conductance ($0.01G_0$) for the Au–BDS–Au system. This new experimental result is very welcome to theorists because it shows the same order of conductance. However, the comparison between experimental and theoretical works must be done carefully. There is a remarkable experimental report about the measurement of the conductance through a single organic molecule sandwiched between two gold electrodes [10]. It showed that the conductance measured at low temperature is very different from that at room temperature. Further examinations into both measurements and simulations are still necessary to clarify the transport properties of a single organic molecule.

4. Conclusion

Electron transport properties of a benzene-(1,4)-dithiolate molecule sandwiched between two gold electrodes were studied by using first-principles transmission calculations. It was found that the transmission spectra and the contributions of the molecular orbitals (MOs) to the transmission coefficients are strongly dependent on the contact structures, and furthermore, not all MOs contribute to the conductance.

References

[1] REED M.A., CHOU C., MULLER C.J., BURGIN T.P., TOUR J.M., Science, 278 (1997), 252.
[2] LANG N.D., Phys. Rev. B, 52 (1995), 5335 and references therein.
[3] KOBAYASHI N., AONO M., TSUKADA M., Phys. Rev. B, 64 (2001), 121402.
[4] NARA J., GENG W.T., KINO H., KOBAYASHI N., OHNO T., J. Chem. Phys., 121 (2004), 6485.
[5] BRANDBYGE M., SORENSEN M.R., JACOBSEN K.W., Phys. Rev. B, 56 (1997), 14956.
[6] BUETTIKER M., IMRY Y., LANDAUER R., PINHAS S., Phys. Rev. B, 31 (1985), 6207.
[7] NARA J., KINO H., KOBAYASHI N., TSUKADA M., OHNO T., Thin Solid Films, 438-439 (2003), 221.
[8] NARA J., HIGAI S., Y.MORIKAWA, T.OHNO, J. Chem. Phys., 120 (2004), 6705.
[9] XIAO X., XU B.,.TAO N.J, Nano Lett., 4 (2004), 267.
[10] REICHERT J., WEBER H.B., MAYOR M., VON LÖNEYSEN H., Appl. Phys. Lett., 82 (2003), 4137.

Specific heat related to details of the vibrational modes for a 2D nanocrystalline material

WOLFGANG HAHN[*]

Polish Academy of Sciences, High Pressure Research Center (UNIPRESS),
Sokołowska 29/37, 01-142 Warsaw, Poland

"What – if" analyses of the interfacial component of nanocrystalline materials (NCM), especially at higher temperatures, were performed using a two-dimensional model. What influence would thermal excitations have on the pair distribution function, the vibrational spectra and the specific heat, over the temperature range of 30–1200 K, if the NCM would be stable over this temperature range, i.e. if grain growth cannot occur? It turned out that reduction of the grain size and increase in temperature influenced the pair distribution function, the vibrational spectra and specific heats in a similar manner. The changes in the vibrational spectra and the specific heat with decreasing grain size or increasing temperature could be related to changes in the occupation of the vibrational modes. The so-called participation ratio (PR) proved to be a suitable means of measuring the occupation of the modes and to classify the spectra. The differences in the specific heat could be largely attributed to parts of a subspectrum, filtered out from the complete vibrational spectrum by collecting the modes of a certain participation ratio range.

1. Introduction

Nanocrystalline materials (NCM) are polycrystalline materials with grain sizes below 100 nm. The preparation of nanocrystalline materials of ever finer grain size has been addressed by many active research projects in physics, chemistry and engineering. The research is motivated by the search for materials with new properties and the desire to tailor these materials' properties at will. Among other applications, there is interest in nanostructured chemical sensors, more reactive catalysts, materials with optimised mechanical and thermodynamic properties, new magnetic materials for, e.g. information storage, optoelectronic detectors and lasers, nano-engineered superconductors and interactions of nanoparticles with biological molecules. General introductions to nanocrystalline materials and nm sized clusters can be found in [1–3].

_____

[*]E-mail: wh-sb@gmx.net

Knowledge of the atomic-scale structure and its relation to the physical properties of materials is an indispensable prerequisite to understand and predict their properties. Computational materials science aims to give this link between structure and properties. Besides the collection and interpretation of a steadily increasing number of experimental data, gained, e.g. by neutron scattering, a major goal of computational materials science, nowadays, is to predict properties of materials, some of which being difficult to access experimentally. Multiscale simulation of polycrystalline materials could bridge the gap between macroscopic and atomic-scale systems [4]. Introductions to computational materials science and molecular simulations are provided in [5, 6].

The wave functions of electrons and phonons in NCM are modified, in contrast to their counterparts in coarser-grained normal polycrystals, due to the confinement prescribed by the characteristic length scale of microstructure of the order of 10 nm. Several experiments on metallic nanocrystals show interesting lattice dynamical properties [7–12]. A low frequency enhancement of the vibrational density of states (VDOS) was found in, e.g. [8]. In order to gain more insight into the nature of the VDOS changes of nanocrystalline materials as a function of grain size and temperature, as well as how these changes affect the stability and the specific heat of NCM, the molecular-dynamics (MD) simulations, described below, were undertaken. This paper is organised in four sections. In the second section the computational procedure will be explained, in section 3 the results concerning VDOS and specific heat are presented, and finally some conclusions are drawn.

2. Computational procedure

2.1. Boundary conditions

In the case of nanocrystalline materials (NCM) the usual periodic boundary conditions would impose constraint forces on the ensemble of the grains, due to missing translational symmetry of the model system. Therefore, the model system was subdivided in an inner and an outer region, which completely enshrouded the inner region. The thickness of the outer region corresponded to the cutoff radius of the potential. The dynamical matrix (see below) was set up with the atoms of the inner region, whereby the atoms of the outer shell served as additional neighbours for the atoms of the inner region (pseudoperiodic boundary conditions).

2.2. Molecular statics (MS)

Within a single crystal, small hexagonal crystal cores were marked and rotated by a random angle. These cores consisted of about 100–400 atoms. The rest of the atoms ("matrix atoms") were then displaced randomly and the volume of the matrix increased homogeneously to about that of the fluid material. The energy of this atomic

arrangement was then minimised by a conjugate gradient method. During the computation, the atoms of the hexagonal crystal cores were allowed to move only translationally as a whole in order to preserve the given orientation relationships of the nanocrystal. The matrix atoms could move individually.

2.3. Molecular dynamics (MD)

The nanocrystalline structures computed by molecular statics served as the starting configuration to solve the equations of motion using the Verlet algorithm:

$$\mathbf{x}(t+dt) = \mathbf{v}(t) + \big(\mathbf{fx}(t+dt)\big) + f\left(\mathbf{x}(t)\frac{dt}{2}\right)dt \tag{1}$$

$$\mathbf{v}(t+dt) = \mathbf{v}(t) + \big(\mathbf{f}\big(\mathbf{x}(t+dt)\big) + f\big(\mathbf{x}(t)\big)\big)\frac{dt}{2} \tag{2}$$

where $\mathbf{x}$ is the coordinates vector, $\mathbf{v}$ – velocities vector, $\mathbf{f}$ – force vector, t – time.

A Morse pair potential with parameters corresponding to gold was used. The starting velocities were distributed according to the Maxwell Boltzmann distribution. The time step of 0.01 psec was chosen. The system properties were averaged at 30, 150, 300, 600, 900 and 1200 K.

2.4. Computation of the vibrational spectra

The vibrational density of states (VDOS) was computed by determination of the eigenvalues (and eigenvectors) of the dynamical matrix [13].

$$\omega_j^2 e_\alpha (k|j) = \sum_{k'}\sum_{\beta} D_{\alpha\beta}(k,k')e_\beta(k'|j) \tag{3}$$

$$D_{\alpha\beta}(k,k') = \frac{1}{\sqrt{m_k m_{k'}}}\phi_{\alpha\beta}(k,k') = \frac{1}{\sqrt{m_k m_{k'}}}\left(\frac{\partial^2\phi}{\partial x_\alpha(k)\partial x_\beta(k')}\right)_0 \tag{4}$$

where $k = 1, 2, \ldots, n$ indexes the atomic cores, m_k denotes the mass of core k, $D_{\alpha\beta}(k, k')$ denotes the dynamical matrix, Φ is the effective potential, Greek letters serve as coordinate indices, $x_\alpha(k)$, $\alpha = 1, 2$ [3] are the Cartesian coordinates of the core k and $E(k|j)$ – its eigenvectors, $\Phi_{\alpha\beta}(k, k')$ are effective force constants. The vibrational spectra are obtained from the eigenfrequencies ω by histogram formation.

2.5. Computation of the specific heats

The heat capacity at constant volume (c_v) is obtained by taking the partial derivative of the energy with respect to the temperature [1]:

$$c_v = \left(\frac{\partial E}{\partial T}\right)_V = k \sum \frac{(h\nu_i / kT)^2 \, e^{h\nu_i / kT}}{(e^{h\nu_i / kT} - 1)^2} \qquad (5)$$

where E is energy, T – temperature, ν_i – i-th eigen frequency, k – Boltzmann's constant, h – Planck's constant. It can therefore be computed directly from the vibrational spectra.

2.6. Participation ratio (PR)

In order to characterise the vibrational spectra of a system more precisely, one can try to determine the degree of their localisation. One possibility is to form an appropriate ratio PR of moments of the kinetic energy [14]:

$$PR(\omega) = \frac{M_1^\varepsilon M_1^\varepsilon}{M_0^\varepsilon M_2^\varepsilon} = \frac{1}{N}\frac{(M_1^\varepsilon)^2}{M_2^\varepsilon}, \qquad M_n^\varepsilon(\omega) = \sum_{i=1}^{N} \varepsilon_i^{2r} \quad \text{with} \quad \varepsilon_i = m\left|r_i\right|^2 \quad (6)$$

where $M_n^\varepsilon(\omega)$ is kinetic energy moment of the n-th order, ω – vibrational frequency, ε_i – mean kinetic energy of the i-th atom participating in the normal mode, r_i – vibrational amplitude, N – total number of atoms.

The moments of the kinetic energy $M_n^\varepsilon(\omega)$ are proportional to the moments which can be formed from eigenvectors of the vibrational modes. The proportionality factor hauls out in the definition of the PR and one obtains the following simplified equation:

$$PR(\omega) = \frac{1}{N}\frac{M_1^2}{M_2}, \qquad M_n(\omega) = \sum_{i=1}^{N} u_i^{2r} \qquad (7)$$

$M_n(\omega)$ is the moment of the n-th order, ω – vibrational frequency, u_i – eigenamplitude, N – total number of atoms.

The participation ratio lies between 0 and 1. For three known vibrational states, the following participation ratios arise: $PR = 1/N$ – localised mode, only one atom vibrates, $PR = 1$ – extended mode, all atoms are displaced with equal amplitude (pure translation of the system), $PR \approx 0{:}5$ corresponds to the plane waves, characteristic of perfect crystals.

3. Results of the molecular dynamic (MD) simulations

3.1. Vibrational spectra (VDOS)

Figures 1–4 show the vibrational spectra of nanocrystalline materials (NCM) obtained by diagonalization of the dynamical matrix. In addition subspectra are shown,
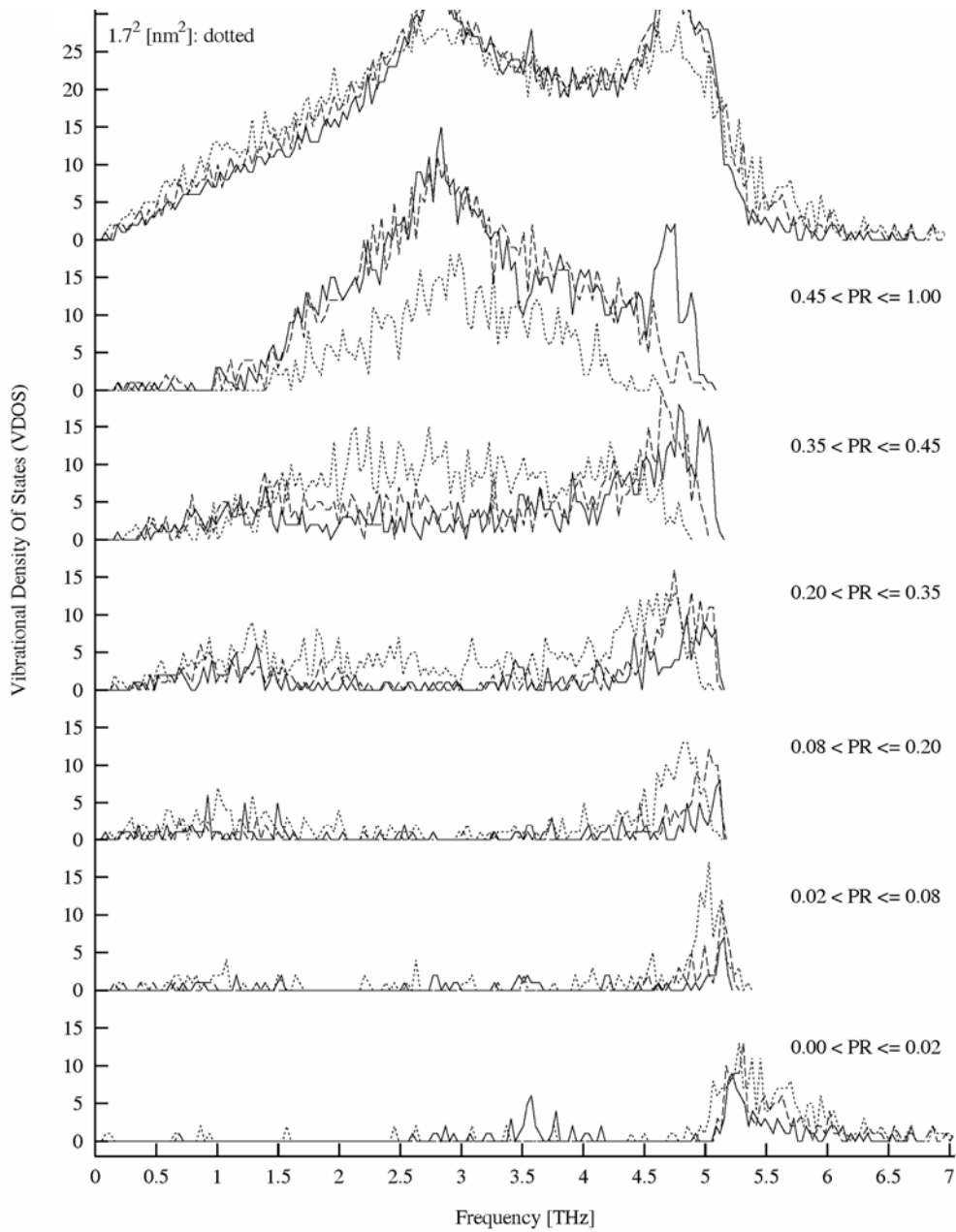
Fig. 1. Vibrational spectra of NCM with an average grain size of 6.5^2 nm^2 (solid curves), 3.3^2 nm^2 (dashed curves) and 1.7^2 nm^2 (dotted curves) for the temperature of 30 K. In addition, the decomposition of the complete spectrum in subspectra according to participation ratio intervals (PRI) of the modes is shown. The topmost array of curves shows the complete spectra of the NCM (PR $\in$]0; 1]), the arrays of curves there under show subspectra with PR $\in$]0.45; 1] until PR $\in$]0; 0.02])
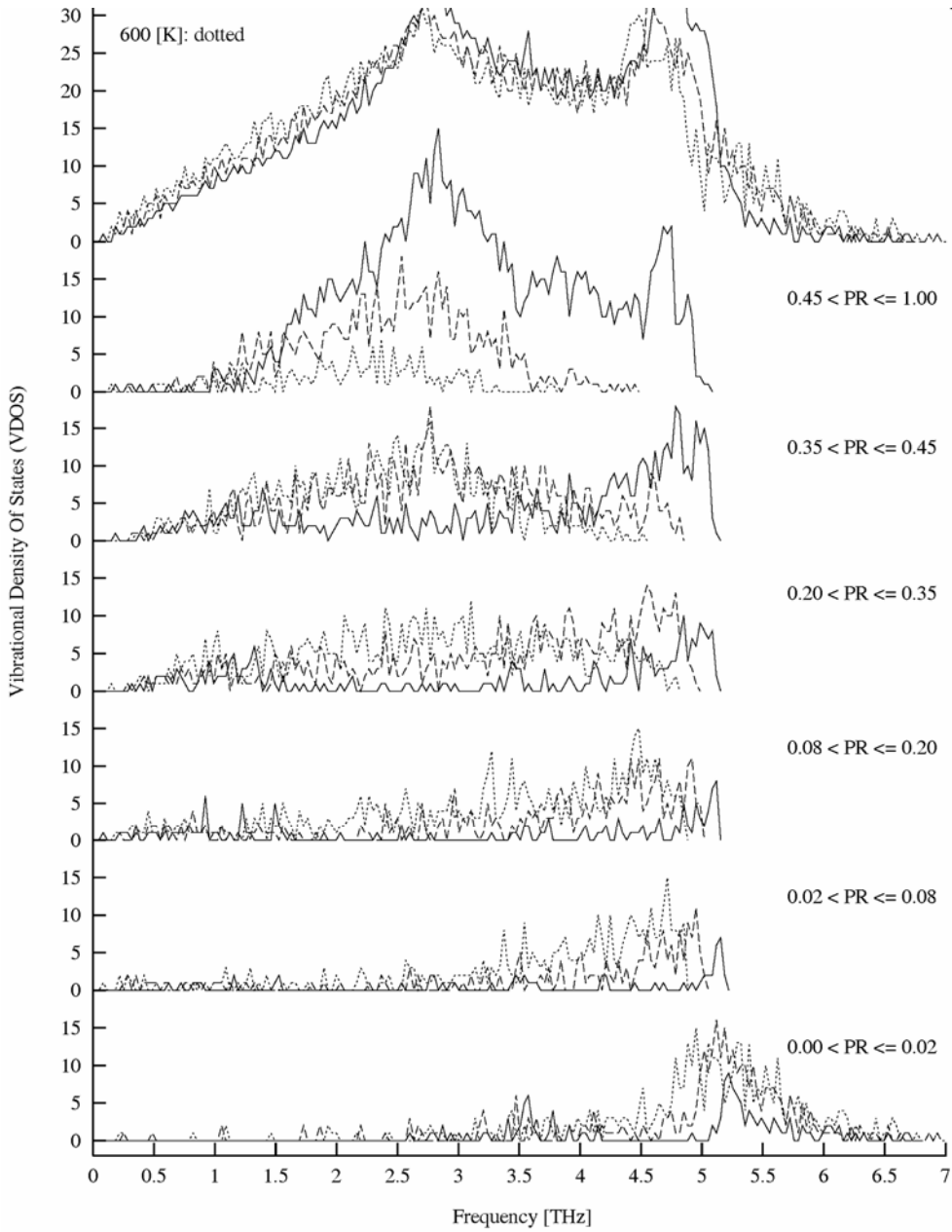
Fig. 2. Vibrational spectra of NCM with an average grain size of 6.5^2 nm^2 for the temperatures of 30 (solid), 300 (dashed) and 600 K (dotted curves). In addition, the decomposition of the complete spectrum in subspectra according to participation ratio intervals (PRI) of the modes is shown. The topmost array of curves shows the complete spectra of the NCM (PR $\in$]0; 1]), the arrays of curves thereunder show subspectra with PR $\in$]0.45; 1] until PR $\in$]0; 0.02])
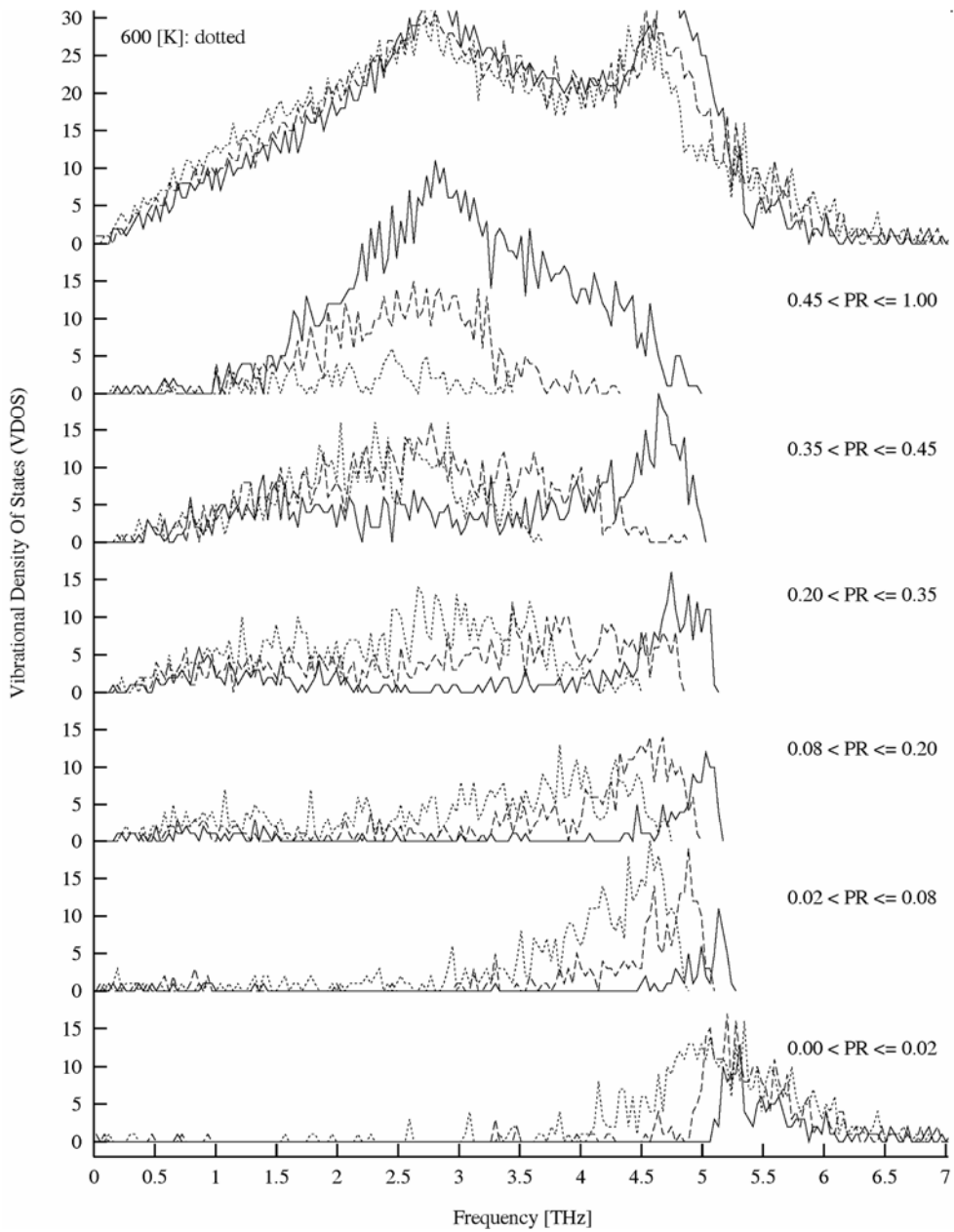
Fig. 3. Vibrational spectra of NCM with an average grain size of 3.3^2 nm^2 for 6 temperatures from 30 to 1200 K. In addition the decomposition of the complete spectrum in subspectra according to participation ratio intervals (PRI) of the modes is shown. The topmost array of curves shows the complete spectra of the NCM (PR $\in$]0; 1]), the array of curves there under show subspectra with PR $\in$]0.45; 1] until PR $\in$]0; 0.02])
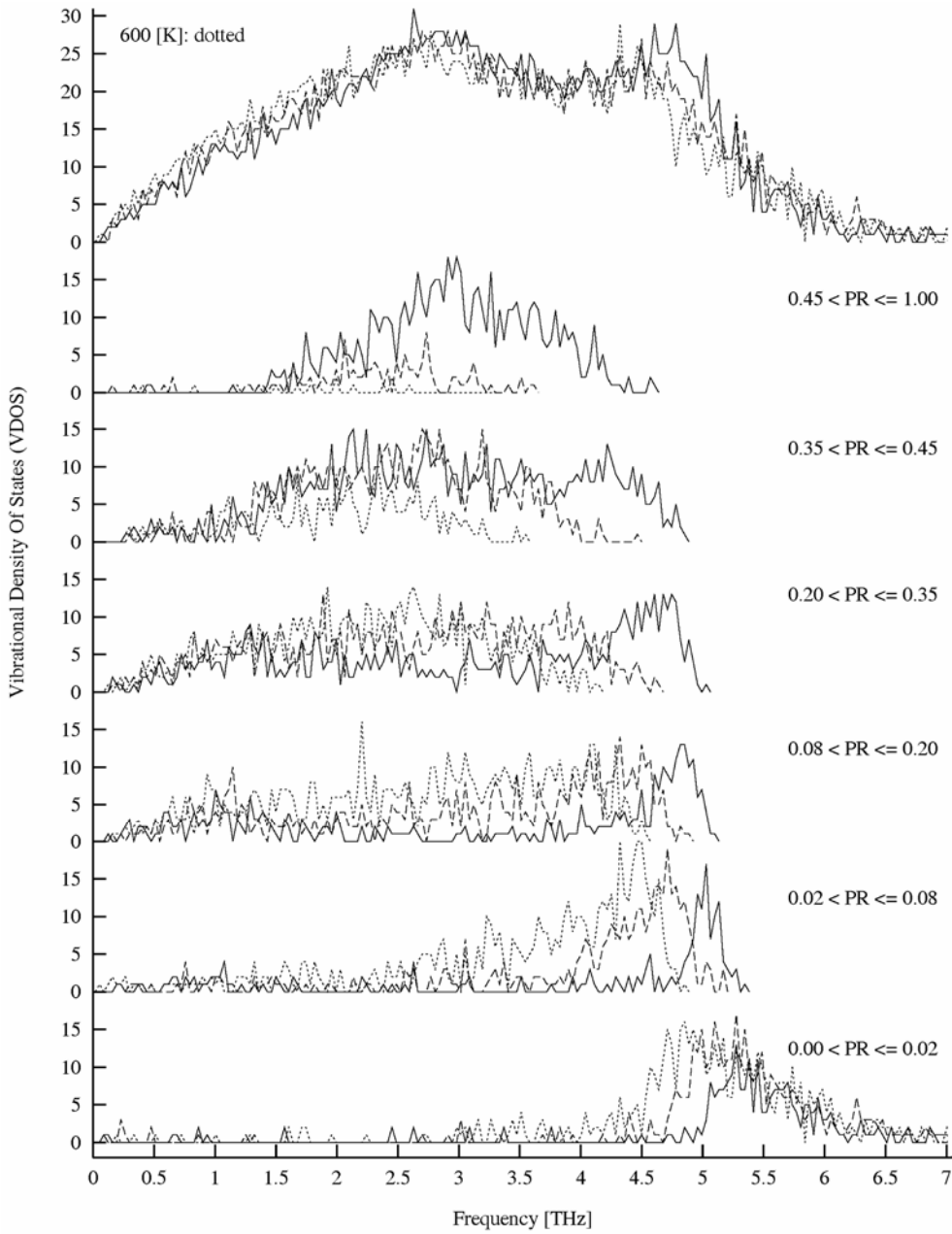
Fig. 4. Vibrational spectra of NCM with an average grain size of 1.7^2 nm^2 for the temperatures of 30 (solid), 300 (dashed) and 600 K (dotted curves). In addition, the decomposition of the complete spectrum in subspectra according to participation ratio intervals (PRI) of the modes is shown. The topmost array of curves shows the complete spectra of the NCM (PR $\in$]0; 1]), the arrays of curves thereunder show subspectra with PR $\in$]0.45; 1] until PR $\in$]0; 0.02])

which result from splitting of the complete VDOS according to participation ratio (PR) intervals. The grain size effect is shown in Fig. 1 for three different grain sizes. The effect of temperature is shown in Figs. 2–4 for 30, 300 and 600 K for the grain sizes of Fig. 1.

In the case of a single crystal the subspectrum, which belongs to the PR interval]0.45; 1], corresponds to all but the over-all spectrum (PR $\in$]0; 1]). Nearly no modes contribute to the subspectra with PR $\leq$ 0.45.

In the case of a NCM, the subspectra with PR $\leq$ 0.45 contribute substantially to the total spectrum. Their contribution increases with decreasing grain size. In particular, modes from the transversal peak shift to subspectra with a lower participation ratio. The high-frequency offshoot of the VDOS, which is peculiar to a NCM (not present in a single crystal), is characterised by very low participation ratios (PR $\leq$ 0.08). These modes are strongly localised. NCM with 6.5^2 nm^2 grain size have vibrational modes similar to those of a single crystal in the medium frequency range (~1.1–5.2 THz), i.e. they have modes with participation ratios $\in$]0.45; 1]. But the subspectra with PR $\leq$ 0.45 of these NCM contain already low- and high-frequency modes, which are not present in a perfect crystal.

With decreasing grain size, the vibrational modes of the medium frequency range of a NCM lose participants to subspectra of lower PR-intervals. More and more modes are shifted from the longitudinal and transversal peak sites to mainly the longitudinal rising peak edge (towards lower frequencies). The transversal peak gets disintegrated from its trailing edge. Also the number of new high-frequency modes in the spectra increases.

The temperature behaviour of the VDOS of NCM is reciprocal to that of their grain size: the low (~0–1.5 THz), medium (~1.5–5.2 THz) and high ($\geq$ 5.2 THz) frequency ranges of the modes experience with increasing temperature similar changes as occur with decreasing grain size.

An example of the similarity of the grain size and temperature effects is given by a comparison of the subspectra of 2 NCM with different grain sizes at different temperatures: The solid curves in Fig. 4, for a grain size of 1:72 nm^2 at 30 K, show a remarkable similarity with the dashed curves in figure 2, which were obtained with a grain size of 6.5^2 nm^2 at 300 K.

The weakening of the transversal modes as a function of decreasing grain size with respect to increasing temperature leads – together with the continuous transition from long to short range order, found in the pair distribution functions – to the following issue: With decreasing grain size (or increasing temperature) the NCM should exhibit an amorphisation by shear instability of the grains.

3.2. Specific heats

Figure 5 shows the specific heats of the NCM with three grain sizes (6.5^2; 3.3^2; 1.7^2 nm^2) and the difference to the specific heat of a perfect crystal with the same number of atoms at 0 K, computed from spectra obtained by diagonalization of the dynamical matrix.
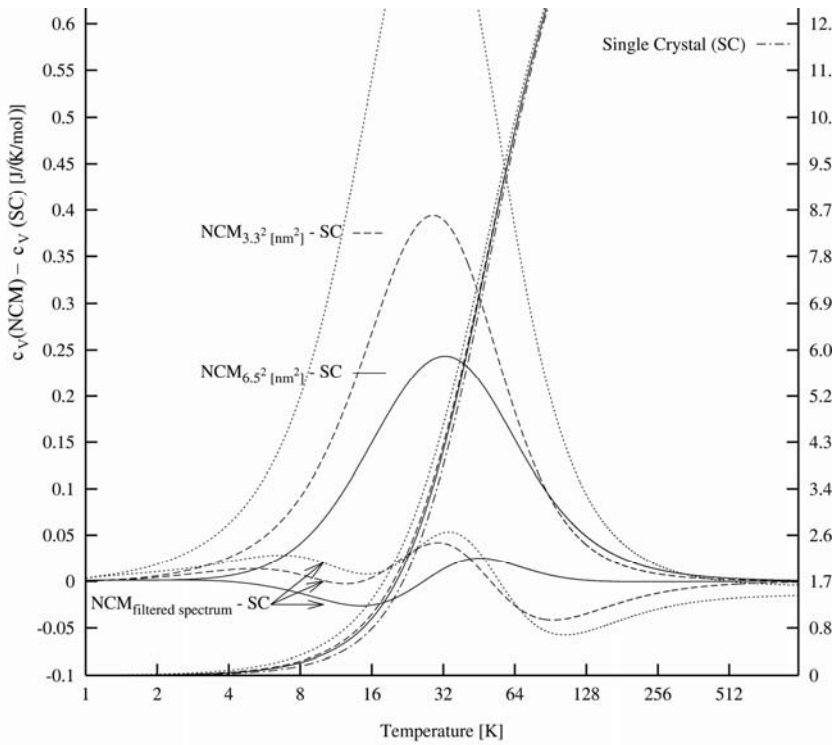
Fig. 5. Specific heats of 3 NCM with different grain sizes (indicated by $NCM_{x.x^2[nm^2]}$) and their difference to the specific heat of a single crystal (indicated by $NCM_{x.x^2[nm^2]}$- SC''), as well as the specific heat of the single crystal (indicated by SingleCrystal (SC)). In addition, differences in the specific heat of the same NCM to those the single crystal are drawn, which were computed by filtering from the vibrational spectra of the NCM parts of a subspectrum with PR $\in$]0.2; 0.35] (indicated by $NCM_{filteredspectrum} - SC$).
The specific heats of the NCM were computed from vibrational spectra, which were obtained by diagonalization of the dynamical matrix of an instantaneous configuration of the MD simulation at 30 K

In the range around 28 K the specific heat of the NCM is increased, compared to that of the perfect crystal. The difference of the specific heat of the NCM and single crystal increases with decreasing grain diameter D, approximately proportional to $1/D$.

The increase of the specific heat of the NCM can be attributed to parts of a sub-spectrum with PR $\in$]0.2; 0.35] in such a manner that after filtering out of these parts from the complete spectrum of the NCM, the specific heats of NCM and perfect crystal differ only by circa 15% of the value of the original increase.

4. Summary and conclusions

Two-dimensional nanocrystalline materials (NCM) were simulated by molecular static and molecular dynamic methods as a function of grain size and temperature. The vibrational density of states (VDOS) was examined in detail. It was subdivided

into subspectra by means of the so-called participation ratio (PR), which measures the fraction of the atoms contributing effectively to a given mode.

The weakening of the transversal modes as a function of decreasing grain size with respect to increasing temperature together with the continuous transition from far to short range order, found in the pair distribution functions suggests that NCM should exhibit an amorphisation because of shear instability of the grains under these conditions.

The specific heat of the NCM was increased in the temperature range of about 28 K compared with that of a single crystal. The increase is broadly reciprocally proportional to the grain diameter. The differences in the specific heat could be largely attributed to parts of a subspectrum of the VDOS obtained by interval formation according to the PR.

References

[1] *Nanomaterials*, A.S. Edelstein, R.C. Cammarata (Eds.) Institute of Physics Publ., Bristol, 1996.

[2] *Handbook of Nanostructured Materials and Nanotechnology*, H.S. Nalwa (Ed.), Academic Press, San Diego, 2000.

[3] GLEITER H., Acta Mater., 48, (2000), 1.

[4] HASLAM A.J., MOLDOVAN D., PHILLPOT S.R., WOLF D., GLEITER H., Comp. Mater. Sci., 23 (2002), 15.

[5] RAABE D., *Computational Materials Science: The Simulation of Materials, Microstructures and Properties*, Wiley-VCH, Weinheim, 1998.

[6] FRENKEL D., SMIT B., *Understanding Molecular Simulation: From Algorithms to Applications*, Academic Press, San Diego, 2002.

[7] SUZUKI K., SUMIYAMA K., Mater. Trans. JIM, 36, (1995), 188.

[8] TRAMPENAU J., BAUSZUZ K., PETRY W., HERR U., Nanostruct. Mater., 6 (1995), 551.

[9] VOLOKITIN Y., SINZIG J., DE JONGH L.J., SCHMID G., VARGAFTIK M.N., MOISEEV I.I., Nature 384 (1996), 621.

[10] FRASE H.N., NAGEL L.J., ROBERTSON J.L., FULTZ B., Phil. Mag. B, 75 (1997), 335.

[11] STUHR U., WIPF H., ANDERSEN K.H., HAHN H., Phys. Rev. Lett., 81 (1998), 1449.

[12] HU X., WANG G., WU W., JIANG P., ZI J., J. Phys.Condens. Matter, 13 (2001), L835.

[13] BORN M., HUANG K., *Dynamical Theory of Crystal Lattices*, Oxford University Press, 1954, reprint 1988.

[14] BELL R.J., DEAN P., HIBBINS-BUTLER D.C., J. Phys. C, Solid State Phys., 3, (1970), 2111.

First principles molecular dynamics simulations for amorphous HfO_2 and $Hf_{1-x}Si_xO_2$ systems

MINORU IKEDA[1*], GEORG KRESSE[2], TOSHIHIDE NABATAME[1], AKIRA TORIUMI[3, 4]

[1]MIRAI, Association of Super-Advanced Electronics Technologies (ASET),
AIST Tsukuba West 7, 16-1 Onogawa, Tsukuba, 305-8569, Japan

[2] Institut für Materialphysik, Universität Wien, Sensengasse 8/12, A-1090 Wien, Austria

[3] MIRAI, Advanced Semiconductor Research Center (ASRC),
National Institute of Advanced Industrial Science and Technologies (AIST),
AIST Tsukuba West 7, 16-1 Onogawa, Tsukuba, 305-8569, Japan

[4] Department of Materials Science, School of Engineering, University of Tokyo,
7-3-1, Hongo, Bunkyo-ku, Tokyo, 113-8656, Japan

Amorphous phases of HfO_2 and $Hf_{1-x}Si_xO_2$ were obtained using the Projector Augmented Plane Wave method through the melt and quench technique. For the pure HfO_2 system, several pore channels appear in the structures. Changes to x in the $Hf_{1-x}Si_xO_2$ were also studied. As the concentration of Si increases, the size of the pore channels increases, much space appears and two-fold oxygen atoms increase. By calculating the heat of formation energy, it was found that phase separation between amorphous HfO_2 and SiO_2 occurs at x>0.1.

Key words: *HfO2; Hf1−xSixO2; amorphous; first principles; molecular dynamics*

1. Introduction

Recently, hafnia (HfO_2) grown on Si substrates has been widely studied as a potential candidate for replacing silicon dioxide as the gate dielectric in scaled complementary metal oxide semiconductor(CMOS) devices [1]. To avoid the crystal orientation, misfit and grain boundary problems at the interface, good amorphous thin films are required for a high-k gate oxide like a SiO_2. In order to increase the crystallization temperature and improve the device performance, several ingredients such as Si, N and Al atoms are incorporated into the high-k gate oxides. Although many theoretical

*Corresponding author, email:ikeda.minoru@mirai.aist.go.jp

calculations are done for the monoclinic HfO_2 [2, 3], the amorphous HfO_2 has not been studied theoretically.

In this report, the amorphous phase of HfO_2 and $Hf_{1-x}Si_xO_2$ using the first principles molecular dynamics method is presented. The effects of the inclusion of Si atoms on the local structure and phase separation by changing the Si concentration was also analyzed.

2. Methodologies

Throughout this work, the Projector Augmented Plane Wave (PAW) method with the local density functional theory corrected by the generalized gradient approximation [4–6] was used. Using the first principles molecular dynamics method, amorphous structures of HfO_2 and $Hf_{1-x}Si_xO_2$ were obtained by employing the melt and quench method as shown in Fig. 1.
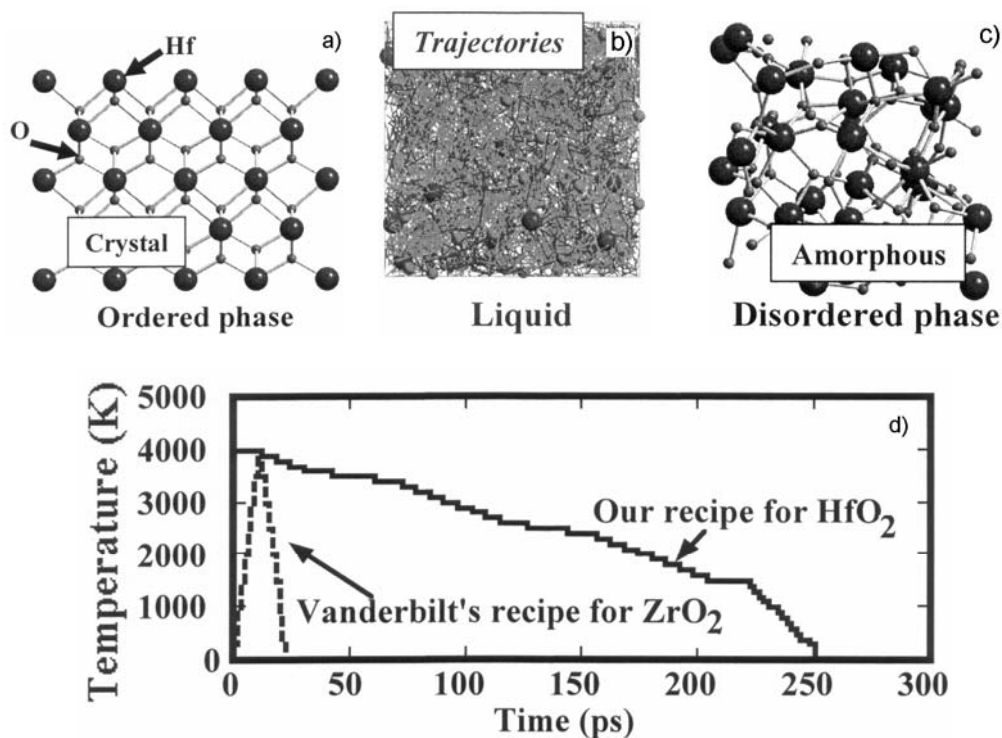
Fig. 1. The melt and quench method is schematically shown in (a) to (c). (a) shows the initial configuration in cubic cell. The atomic arrangements are tetragonal ones. (b) illustrates the trajectories of Hf (black lines) and O (grey lines) atoms at 4000 K during 12 ps. (c) shows the quenched disordered phase of HfO_2. The thermal recipe of this computer experiment is shown in (d). Our total simulation time is longer than Zao–Vanderbilt's by 10 times

The time step is 2 fs and the temperature is controlled by the Nose dynamics. The models consist of 96 and 117 atoms in the cubic cell. According to Zhao–Vanderbilt prescription [7], the volume of the cubic cell is increased by 7% to be able to melt the system at 4000 K.

3. Results and discussions

The temperature of the system was first raised to 4000 K and the system melted in 12 ps. Then the temperature was gradually decreased in 236 ps. The method is shown in Fig. 1d. After quenching the system, the cell volume was optimized. However, the volume change was within 1%, in contrast to the ZrO_2 case in which the volume reduction was as high as 9% [7].

Figure 2 shows the pair correlation functions between Hf and Hf for the crystal, liquids and amorphous phase. The amorphous phase obtained is very close to the liquid phase as shown in the figure.
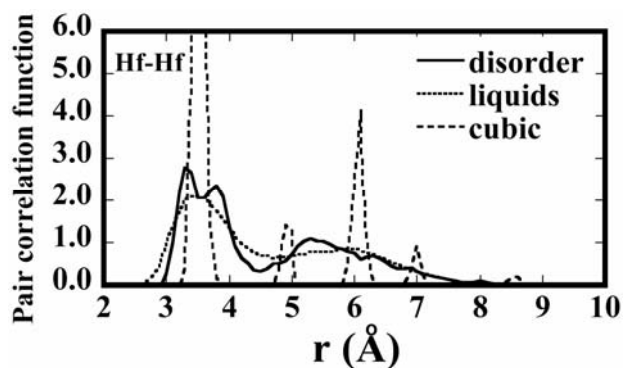
Fig. 2. The pair correlation functions of Hf and Hf in crystal (broken line), liquid (dotted line) and amorphous (solid line) phases are compared. The amorphous phase is very close to the liquid phase as shown in the figure

In the amorphous structures several pore channels exist as in the case of SiO_2. In pure hafnia, several pore channels exist with diameters 3–4 Å as indicated in Fig. 3a. If the Si concentration x of $Hf_{1-x}Si_xO_2$ is increased, the size of the pore channels increases and much space appears as can be easily seen from Figs. 3a–d.

In Figure 3c, a connected SiO_2 networks appears and the remaining HfO_2 molecules are also linked each other. It seems that the phase separation between HfO_2 and SiO_2 occurs at $Hf_{0.3}Si_{0.7}O_2$. The heat of formation energy of $Hf_{1-x}Si_xO_2$ was calculated using those of the amorphous HfO_2 and SiO_2 as reference energies according to the formula $H(x) = E(am\text{-}Hf_{1-x}Si_xO_2) - (1 - x)E(am\text{-}HfO_2) - xE(am\text{-}SiO_2)$ where am denotes amorphous form as shown in Fig. 3e. This graph shows that the phase separation between the amorphous HfO_2 and SiO_2 starts at $x > 0.1$.
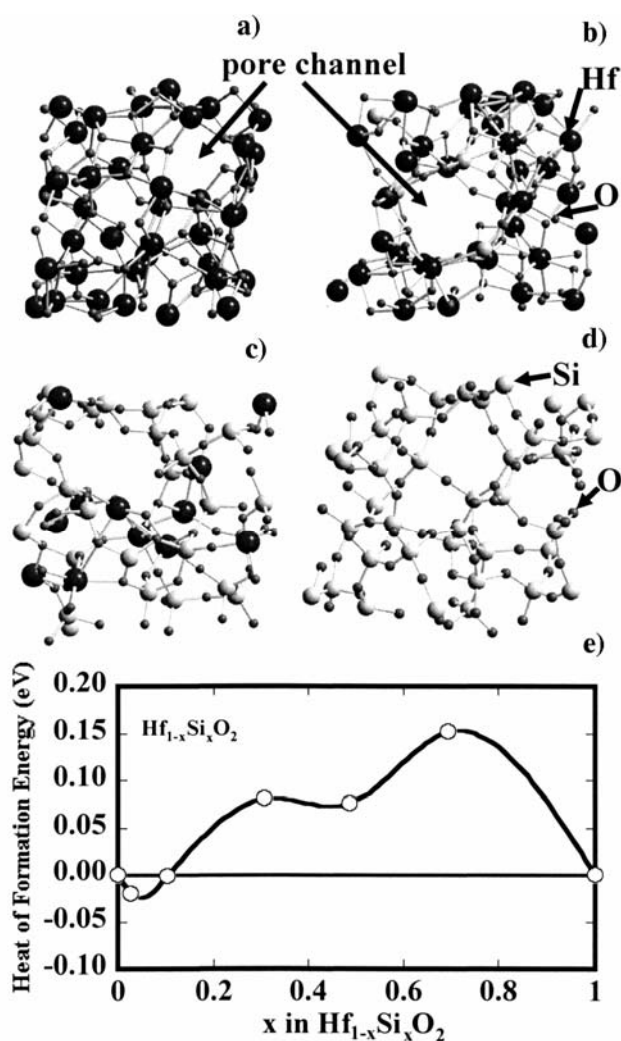
Fig. 3. The theoretically determined amorphous structures are shown in (a)–(d). The dark atoms denote Hf, whereas white ones indicate Si. The small atoms are oxygen. In obtaining these structures, we used 117 atoms in the cubic super cell; (a) is a pure amorphous HfO_2 structure, (b) and (c) are $Hf_{1-x}Si_xO_2$ structure with $x = 0.1$ and 0.7, respectively. (d) corresponds to the amorphous SiO_2. Pore channels are indicated by arrows in (a) and (b). In (e), the heat of formation energy is plotted as a function of Si concentration. The phase separation between amorphous HfO_2 and SiO_2 starts at $x > 0.1$

In Figures 4a–d, the coordination numbers of $Hf_{1-x}Si_xO_2$ with $x = 0$, 0.1, 0.3 and 1 are compared. The oxygen atoms with the coordination number 2 increase linearly with the Si concentration. If the configuration of Si in Figs. 3b and c are examined, the nearest neighbour atoms of Si are all oxygen atoms.

By using the pure amorphous hafnia model, the problem of boron atoms doped in the poly-Si gate penetrating into the Si substrate through the amorphous hafnia were
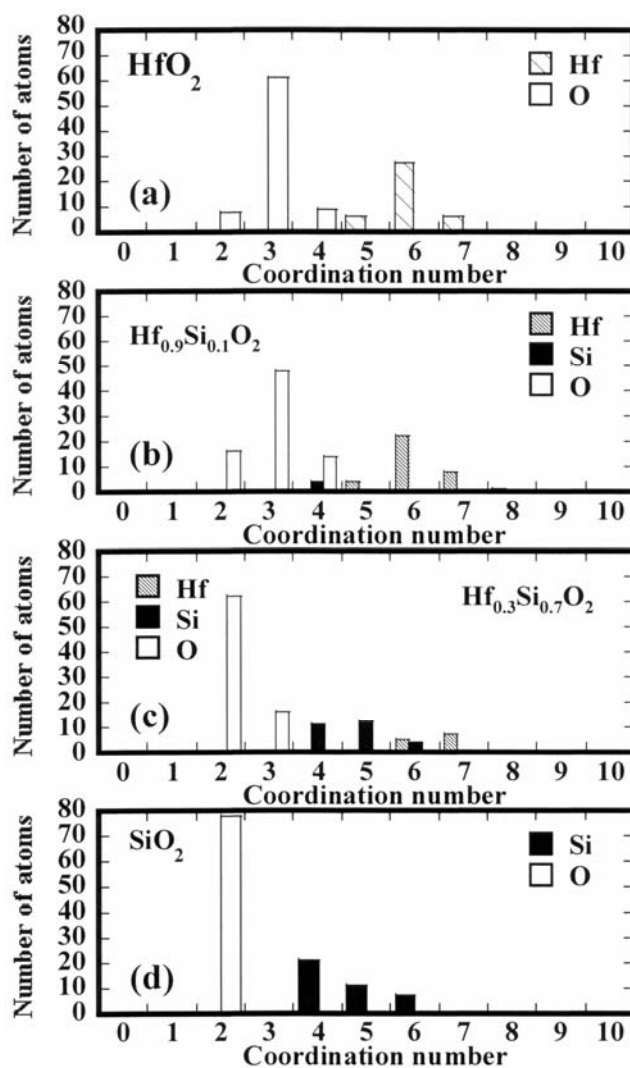
Fig. 4. The coordination numbers of $Hf_{1-x}Si_xO_2$ with $x = 0$, 0.1, 0.3 and 1 are illustrated in (a)–(d). (a) is a hafnia case, whereas (d) refers to the SiO_2 case. As the Si concentration x increases, then the number of oxygen with coordination number 2 increases

analysed. The fast diffusion of boron in amorphous HfO_2 can be explained successfully. In this analysis, the pore channel structures in HfO_2 which we found through the computer experiments, play a very important role [8]. Thus the amorphous structure models seem to be useful in understanding the actual systems.

Acknowledgement

References

[1] WILK G.D., WALLACE R.M., ANTHONY J.M., J. Appl. Phys., 89 (2001), 5243.

[2] FOSTER A.S., SHLUGER A.L., NIEMINEN R.M., Phys. Rev. Lett. 89 (2002), 225901; FOSTER A.S., LOPEZ GEJO F.L., SHLUGER A.L., NIEMINEN R.M., Phys. Rev. B 65 (2002),174117.

[3] IKEDA M., KRESSE G., NABATAME T., TORIUMI A., Extended Abstracts of Solid State Devices and Materials (SSDM) 2003, (2003), 824; MRS 2003 Fall Meeting, 786 (2003), 17.

[4] KRESSE G., HAFNER J., Phys. Rev. B 47 (1993), 558; KRESSE G., Technischen Universität Wien, Thesis, 1993.

[5] BLÖCHL P.E., Phys. Rev. B 50, 17953 (1994).

[6] KRESSE G., JOUBERT D., Phys.Rev. B59 (1998), 1758.

[7] VANDERBILT D.,ZHAO X., presented at MRS 2003 Fall Meeting in Boston; ZHAO X., CERESOLI D., VANDERBILT D., Phys. Rev. B, 71 (2005), 085107.

[8] IKEDA M., KRESSE G., NABATAME T., TORIUMI A., Extended Abstracts of SSDM 2004 (2004), 798.

Atomic modelling of point defects in B2-RuAl

ROBERT SOT[1, 2*], KRZYSZTOF J. KURZYDŁOWSKI[1]

[1]Warsaw University of Technology, Faculty of Materials Science and Engineering,
Wołoska 141, 02-507 Warsaw, Poland

[2]Warsaw University, Interdisciplinary Centre for Mathematical and Computational
Modelling (ICM), Pawinskiego 5a, 02-106 Warsaw, Poland

Ab initio calculations based on density functional theory (DFT) and the pseudopotential method have been used to study B2-structured RuAl. The structural parameters, volume changes of single defects and pressure caused by the presence of point defects in B2-RuAl intermetallic compound were computed by the ab initio pseudopotential method with the plane-wave basis set and a generalized gradient approximation (GGA). The calculated structural parameters are in good agreement with available experimental data.

Key words: *Ab initio calculations; density functional calculations*

1. Introduction

In recent years, ab initio computations have become one of the tools in modern computational materials science. These calculations, based on the concept of DFT developed by Walter Kohn [1] in 1960s, can be used to predict the positions of individual atoms in cells (super-cells) of various systems and in particular in intermetallic compounds. By this method the inter-planar distances, energy of cohesion and relative energies of point defects, such as vacancies and foreign atoms can also be estimated. These in turn can be used to explain most of the likely crystal structures and the positions of defects which are relevant to modelling mesoscopic properties of crystalline materials.

In the present work, calculations from first principles have been performed for B2-RuAl. This compound is known to crystallize in a cubic lattice, of the CsCl type, with the space group $Pm3m$. B2-structured RuAl has been considered to be one of the potential materials for high temperature applications in aggressive environments because of its high temperature strength, oxidation and corosion resistance and good room temperature toughness [2].

_____

*Corresponding author, e-mail: rsot@inmat.pw.edu.pl

2. Computations

For the computations of the crystal structure of RuAl ultrasoft pseudopotentials under the assumption of the gradient generalized approximation (GGA) has been adopted. CASTEP [3] and VASP [4, 5] packages have been employed and the computations have been carried out at the ICM of Warsaw University. CASTEP and VASP are a DFT pseudopotential total-energy codes. The Monkhorst–Pack scheme was used to sample the Brillouin zone. The calculations were considered to have converged when forces acting on the atoms were less then 0.01 eV/atom and the residual bulk stress was smaller than 0.02 GPa.

3. Results

3.1. Structural parameters

The cell constant and the cohesion energy have been calculated. The cohesive energy of a solid is defined as the energy required to separate the condensed material into isolated free atoms. The total energy for the supercell and for free atoms has also been determined. The results of computations are plotted in Fig. 1 in the form of graph of cohesion energy E_c against the cell constant. It should be noted that the energy minimum $E_c = -6.44$ eV/at) is attained for $a = b = c = 2.9825$ Å. This value agrees well with the literature data (e.g., $a = b = c = 2.967$ Å [6], 2.95–3.03 Å [7]).
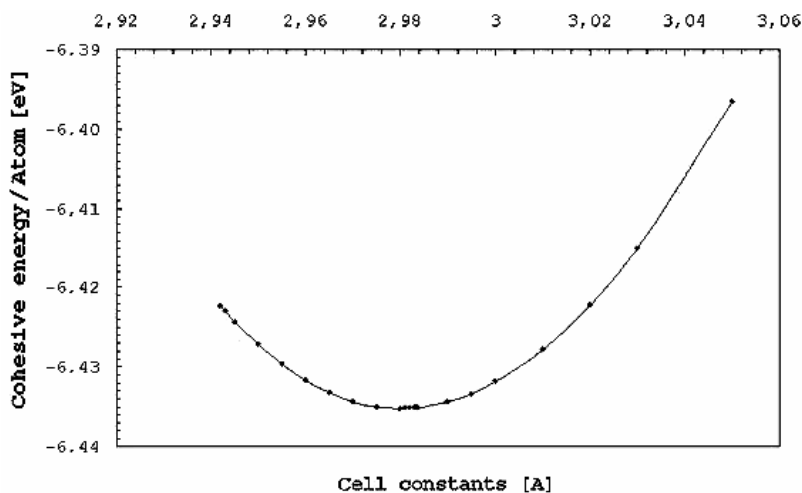
Fig. 1. Cohesion energy [eV] against the cell constant [Å]

First principles computations have been used to calculate the formation energy, E_{form}, of the B2-RuAl. This alloy is formed directly from the constituent Ru and Al

crystals. As the first step, the energies of Ru (hcp) and Al (fcc) in the most stable crystalline states were calculated. As the second step, the energies of the compound described above were obtained. The variation of E_{form} with supercell size is given in Table 1.

Table 1. VASP calculations of the variation of E_{form} with supercell size

Supercell size	1×1×1	2×2×2	3×3×3	Experimental
E_{form} [eV/at]	–0.6689	–0.6699	–0.6645	0.64 [8]

Ab initio computations have been also used to calculate the bulk modulus of the system *B* which is equal to 203 GPa. Again this is close to the literature value of 208 GPa [9].

3.2. Point defects in B2-RuAl

Ab-inito computations of crystal lattice defects can be carried out by following two routes. Firstly, it can be estimated how a given defect changes the cell size of the respective crystal lattice. In this case, the cell structure is numerically optimized after the defect in question is generated (e.g., one atom is removed to form a vacancy). The new positions of atoms are subsequently computed and the change in crystal volume is determined. The second computational route of concerns the local pressure induced by a point defect. The stresses in the unit cell containing the given defect are computed with the assumption that atoms are frozen in the same positions as in defect-free structure. For computations based on 2×2×2 super-cells the latter approach seems to be more appropriate, as the defect coordination zones are "submerged" into the crystal with the equilibrium positions of atoms. The useful information which can be obtained with this assumption is an estimate of the energy needed to generate the defects of interest and their preferential positions.

3.3. Volume changes of single defects

Ab-initio computations were also carried out for vacancy and substitutional atoms of Cr, Fe and Co. In the ground state energy calculations, the primitive unit cell was used. The elements Al, Co, and the alloy RuAl were treated as being non-magnetic, Cr as antiferromagnetic and Fe(α) was considered as ferromagnetic. Since RuAl is non-magnetic the defect ground state energies were also calculated as non-magnetic. For this case 2×2×2 and 3×3×3 super-cells have been used. The vacancy, antisite atoms and the ternary alloying elements have been studied in the position of Al and Ru atoms. The results are summarized in Table 2 which lists super-cell ground state energies E_c and single defect volume changes, $\Delta V/V$.

Table 2. Calculated ground state energies E(A,B), volume V
and relative to RuAl volume change $\Delta V/V$ of a single defect
in the 2×2×2 and 3×3×3 supercells. VASP calculations

System (A, B)	E(A, B) [eV]	V [Å^3]	$\Delta V/V$ [%]
(8Ru, 8Al)	−113.216	217.83	0.0
(27Ru, 27Al)	−381.810	735.41	0.0
(8Ru, 7Al Ru)	−116.660	219.22	0.638
(27Ru, 26Al Ru)	−385.127	737.10	0.229
(7Ru Al, 8Al)	−107.479	221.08	1.492
(26Ru Al, 27Al)	−376.438	738.36	0.399
(8Ru, 7Al vac.)	−105.236	212.24	−2.566
(27Ru, 26Al vac.)	−373.837	729.40	−0.817
(7Ru vac., 8Al)	−107.479	221.08	−1.196
(26Ru vac., 27Al)	−371.107	732.81	−0.355
(8Ru, 7Al Cr)	−117.795	215.94	−0.868
(27Ru, 26Al Cr)	−386.545	732.84	−0.349
(7Ru Cr, 8Al)	−111.743	217.32	−0.234
(26Ru Cr, 27Al)	−380.644	734.51	−0.122
(8Ru, 7Al Fe)	−115.682	215.02	−1.290
(27Ru, 26Al Fe)	−384.227	732.17	−0.441
(7Ru Fe, 8Al)	−111.505	214.56	−1.501
(26Ru Fe, 27Al)	−380.095	731.64	−0.513
(8Ru, 7Al Co)	−114.572	215.00	−1.299
(27Ru, 26Al Co)	−383.145	732.13	−0.446
(7Ru Co, 8Al)	−110.978	214.24	−1.648
(26Ru Co, 27Al)	−379.583	731.26	−0.564

3.4. Pressure caused by the presence of a point defect

The pressure, P [GPa] caused by the presence of a point defect in 2×2×2 super-cell
were determined. The results are summarized in Table 3.

Table 3. The cohesive energy (in eV) per a supercell composed of 2×2×2 cells
and having its constants as in an equillibrium crystal, and the pressure P,
in GPa, caused by a presence of a point defect. CASTEP calculations

System (A, B)	E_{koh} (A, B) [eV]	P [GPa]
(8Ru, 8Al)	−104.67	0.0
(8Ru, 7Al Ru)	−106.88	2.76
(7Ru Al, 8Al)	−99.13	1.65
(8Ru, 7Al vacans)	−96.12	−2.04
(7Ru vacans, 8Al)	−95.11	−2.45

4. Conclusions

Ab initio calculations have been used to determine cohesion energy E_c against the cell constant, formation energy, E_{form}, of the B2-RuAl. First principles computations of crystal lattice defects were carried out following two routes. Firstly, changes the size of the respective crystal lattice cell caused by the presence of a given defect have been estimated. The second computational route concerned the local pressure induced by a point defect.

References

[1] KOHN W., SHAM L.J., Phys. Rev. 140 (1965), A1133.

[2] WOLFF I.M., JOM, 49 (1997), 34.

[3] SEGALL M.D., LINDAN P.L.D., PROBERT M.J., PICKARD C.J., HASNIP P.J., CLARK S.J., PAYNE M.C., J. Phys. Cond. Matt., 14 (2002), 2717.

[4] KRESSE G., FURTHMÜLLER J., Comput. Mat. Sci., 6 (1996), 15.

[5] KRESSE G., FURTHMÜLLER J., Phys. Rev. B, 54 (1996), 11169.

[6] MANH D.N., PETTIFOR D.G., Intermetallics, 7 (1997), 1095.

[7] VILLARS P., CALVERT L.D., *Pearson's Handbook of Crystallographic Data for Intermetallic Phases*, American Society for Metals, Metals Park,1986.

[8] JUNG W.G., KLEPPA O.J., Metall. Trans. B, 23 (1992), 53.

[9] HACKENBRACHT D., KUBLER J., J. Phys. F, 10 (1980), 427.

[10] PARLINSKI K., JOCHYM P.T., KOZUBSKI R., ORAMUS P., Intermetallics, 11 (2003), 157.

Atomic configurations of breaking nanocontacts of aluminium and nickel

P. García-Mochales[1*], P.A. Serena[1], C. Guerrero[2], E. Medina[2], A. Hasmy[2]

[1]Instituto de Ciencia de Materiales de Madrid, Consejo Superior de Investigaciones Científicas, Cantoblanco, E-28049-Madrid, Spain

[2]Centro de Física, IVIC, Apdo. 21827, Caracas 1020A, Venezuela

A statistical study of favourable atomic configurations of aluminium and nickel nanocontacts during their fracture at 4 K and 300 K was performed. Nanowire breaking events are simulated by using molecular dynamics (MD), the atomic interactions being represented by the state-of-the-art embedded atom method (EAM) interatomic potentials, which are able to fit bulk and surface properties with a high degree of accuracy. A complete determination of atomic positions during the contact allows evaluation of the evolution of the minimum-cross section S_m during stretching. By accumulating S_m traces, obtained from many independent fractures of nanowires, minimum cross-section histograms $H(S_m)$ were built. These simulated histograms reveal the presence of preferential geometrical arrangements during the breaking of the nanocontact and allow a direct comparison with experimental conductance histograms. In particular, aluminium histograms show a remarkable agreement between conductance and minimum cross-section peaks. However for Ni, the interpretation of experimental conductance peaks is more difficult due to the presence of magnetic effects and the possible presence of contaminants.

Key words: *molecular dynamic; metallic nanowires; metallic nanocontacts; conductance histograms*

1. Introduction

Metallic wires with diameters of the order of few nanometers (metallic nanowires) are key components for the future development of nanoelectronics [1]. Electron transport in metallic nanowires below room temperature (RT) is ballistic since the electron elastic mean free path is larger than the characteristic nanocontact dimensions. Furthermore, well defined quantized propagating modes appear in nanowires with diame-

---

[*]Corresponding author: e-mail: pedrog@icmm.csic.es

ters of the order of few Fermi wavelengths λ_F. At such limits, the electric conductance G is described by the Landauer formula

$$G = G_0 \sum_{n}^{N} T_n$$

where $G_0 = 2e^2/h$ is the conductance quantum, e being the electron charge and h Planck's constant, T_n is the transmission probability of the n-th mode, and N is the number of propagating modes [2].

Methods based on scanning tunnelling microscopy (STM) [3, 4] and mechanically controllable break junctions (MCBJ) [5] are widely used to form metallic nanowires, although they can be also formed between macroscopic wires in "table-top" experiments [6], using electron-beam irradiation [7] or applying electrochemical methods [8].

The electrical characterisation of a metallic nanowire is done by measuring its conductance G as a function of the nanowire elongation during its rupture. The electronic transport of a given metallic species can be characterised by means of its so-called conductance histogram $H(G)$ [9] which is built from conductance curves acquired during many independent breaking events. These conductance histograms present well defined peaks. These peaks are associated with preferred conductance values which reflect the presence of conductance quantization [10] or the existence of energetically favourable atomic arrangements [11–14]. Although an exact interpretation of conductance histograms is very difficult, since they include mechanical and electronic information, they have become a standard characterisation tool for metallic nanowires.

The behaviour of $H(G)$ is even more complex for polyvalent metals since several electronic transport channels per atom are available [15]. For instance, aluminium conductance histograms obtained at 4 K [11] and room temperature [13] show well defined peaks at conductance values close to integer values of G_0, although three channels per atom are involved in electron transport. The analysis of $H(G)$ becomes even more complex in magnetic nanowires due to the presence of a new degree of freedom, the electron spin. In particular, the structure of Ni conductance histograms is not fully understood [16–20]. At RT different conductance histograms have been obtained for Ni. Some experiments have reported the existence of a featureless conductance histogram [16] whilst others reported histograms with peaks showing a strong dependence on the applied magnetic fields as well as the temperature [17]. Finally, several experiments obtained peaks located at integer values of $G_0/2$ [18, 19]. The situation is very different at $T = 4$ K in ultra high vacuum (UHV) conditions, where conductance histograms show two well defined peaks around $1.6G_0$ and $3G_0$ which do not show any dependence on the applied magnetic field [20].

The difference between low-temperature and RT Ni conductance histograms is not well understood since, in both cases, the system is below its bulk Curie temperature ($T_c = 630$ K) and similar magnetic behaviour should be expected. A possible explanation could be related to the presence of different structural Ni nanowire configurations

as a function of the temperature. The aim of the present work is to determine the validity of this hypothesis using molecular dynamics simulations to find favourable configurations in Al and Ni nanocontacts.

2. Computational procedure

Molecular dynamics (MD) has been extensively used to study the structure of breaking metallic nanowires using different interatomic potentials [12, 13, 21–23]. From knowledge of the dynamic behaviour of the nanowire, a conductance against time curve can be derived using several approaches. However, the construction of conductance histograms needs huge computational resources. A different approach is based on the construction of histograms which are able to detect the presence of favourable atomic configurations [12, 13] and this is the approach that was followed in this case.

Atomic interactions have been described within the embedded atom method (EAM) approach, using state-of-the-art interatomic potentials able to describe high and low coordinated systems [24]. Atomic trajectories and velocities were determined using the conventional Verlet velocity algorithms. Velocity scaling procedures were imposed to perform simulations at constant temperature T. In this work, the situations at $T = 4$ K and $T = 300$ K were studied.

A typical MD simulation starts with an FCC ordered supercell with 1008 atoms consisting of a parallelepiped formed of 18 (111) layers. The lattice constant a for such an initial configuration was chosen as the experimental one ($a = 3.52$ Å for Ni and $a = 4.05$ Å for Al). The z direction (stretching direction) corresponds to the (111) direction. The simulation of a single breaking event is described in detail elsewhere [12, 13]. A MD breaking event consists of two computational stages. Firstly, a balancing stage, resulting in an optimized nanowire, and secondly, a stretching stage at constant velocity until the nanowire breaks. Within the first stage the initial bulk-like configuration relaxes for 2000 MD steps keeping periodic boundary conditions (PBC) for x, y and z directions. The time interval of a MD step is $dt = 10^{-2}$ ps. Once the bulk relaxation is completed, two supporting bilayers at the top and bottom of the supercell were defined. Atomic x and y co-ordinates within these bilayers were kept constant for the rest of the simulation. Furthermore, from this moment PBC along the x and y directions were imposed uniquely to atoms forming these bilayers. The balancing procedure ends with 3000 MD steps in order to optimise the nanowire geometry prior to stretching.

During the stretching stage, both supporting bilayers are moved in opposite directions at a constant velocity of 2 m/s (2×10^{-4} Å per MD step). The dynamical evolution of nanowire atoms is driven by interatomic EAM forces. Accurate knowledge of the atomic positions permits computation of the nanowire minimum cross-section S_m using standard procedures [22]. The stretching stage is completed when the nanowire breaks (i.e. $S_m = 0$). By accumulating the geometry evolution for hundreds of breaking

events (each providing a specific $S_m(t)$ curve), minimum cross-section histograms $H(S_m)$ can be constructed.

3. Results and discussion

Figure 1 and 2 show typical minimum cross-section versus time $S_m(t)$ curves at $T = 4$ K and $T = 300$ K for Al and Ni, respectively.
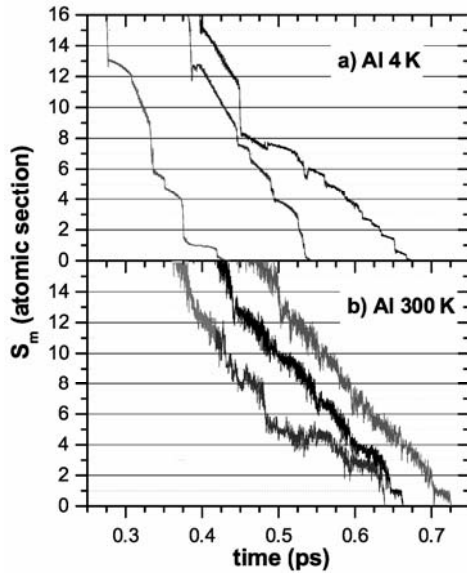
Fig. 1. Evolution of the minimum cross-section S_m (in units of atoms) as a function of time for three Al nanowires during their breaking process at: a) $T = 4$ K and b) $T = 300$ K
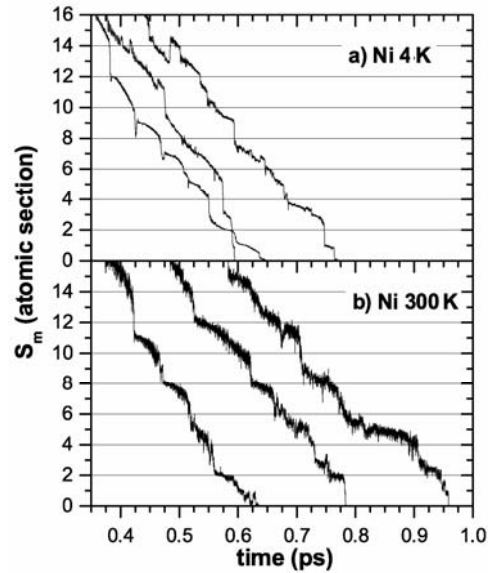
Fig. 2. Evolution of the minimum cross-section S_m (in units of atoms) as a function of time for three Ni nanowires during their breaking process at: a) $T = 4$ K and b) $T = 300$ K

The $S_m(t)$ curves show well marked jumps associated with atomic rearrangements in the nanowire. Such section jumps are correlated with jumps in the force acting on supporting slabs [21]. In general, the section steadily decreases between two subsequent jumps reflecting the existence of elastic stages during the nanowire rupture. For $T = 300$ K it can be noticed that $S_m(t)$ shows, as expected, larger fluctuations than those seen at $T = 4$ K. Minimum cross-section histograms $H(S_m)$ for Al and Ni, including 150 breaking events, are depicted in Figures 3 and 4, respectively.

Figure 4b illustrates that the statistical sampling is good since no significant differences exist between the histograms showing 50, 100 or 150 breaking events. For the low temperature ($T = 4$ K) it is clear that $H(S_m)$ presents well-defined peaks, indicating the presence of favourable atomic configurations in Al and Ni nanowires during stretching. For Al, $H(S_m)$ peak heights steadily decrease as S_m increases whereas

for Ni, certain peaks located at $S_m = 5$, 8, and 13 have higher a probability with respect to their neighbouring peaks. These maxima can be interpreted as precursors of ionic shell structures appearing at higher temperatures that have been observed in alkali nanowires at low temperatures [25], and Au and Al nanowires at RT [14].
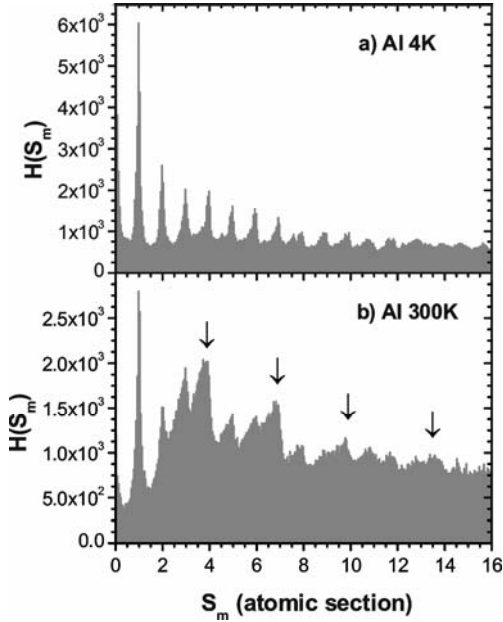
Fig. 3. Minimum cross-section histogram $H(S_m)$ obtained from 150 independent aluminium nanowire breaking events as those shown in Fig. 1 at (a) $T = 4$ K and (b) $T = 300$ K. Arrows in (b) denote those configurations with more statistical weight
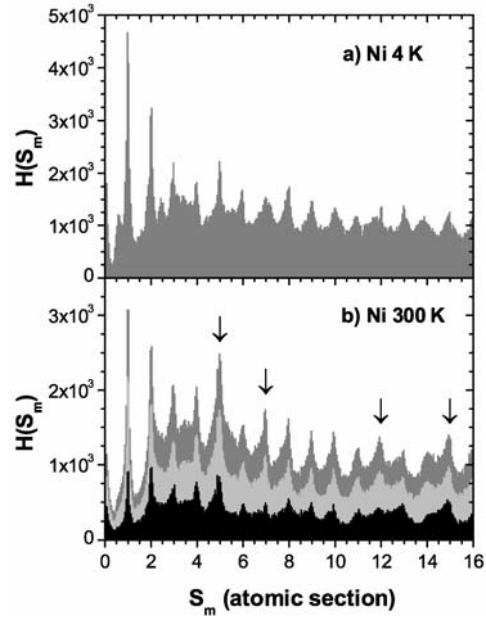
Fig. 4. Minimum cross-section histogram $H(S_m)$ obtained from 150 independent nickel nanowire breaking events as those shown in Fig. 1 at (a) $T = 4$ K and (b) $T = 300$ K. (b) shows histograms using 50 (black), 100 (light grey) and 150 (dark grey) breaking events. Arrows in (b) denote those configurations with most statistical weight

At 300 K we notice that the Al $H(S_m)$ presents a background structure, with broad peaks. The steadily decreasing sequence of local maxima is replaced by a different global shape with local maxima appearing at $S_m = 1$, 4, 7, 10, and 14. However, the Ni histogram at 300 K is essentially the same obtained as at $T = 4$ K, with small shifts in the higher probability peaks (now located at $S_m = 1$, 5, 7, 12, and 14). Such high-stability configurations could be interpreted as ionic magic configurations and the present set of simulations also show their existence for nickel nanocontacts. Therefore a temperature increase to 300 K strongly modifies $H(S_m)$ in the case of Al nanowires, whereas the Ni histogram keeps its main features over a wide temperature range. This difference could be explained in terms of a very different number of accessible configurations during breaking processes at RT due to the large difference between cohesion energies of Al (melting point at 960 K) and Ni (melting point at 1700 K).

4. Conclusions

It has been demonstrated that Ni configuration histograms are not dramatically affected by a temperature increase within the range of 4–300 K. However, Al histograms show a noticeable change over the same temperature range. For Al, minimum cross-sections histograms are very similar to conductance histograms at low and room temperatures. Therefore it is possible to identify, one to one, favourable geometrical configurations with favourable conductance peaks.

However, this is not true for Ni. The calculations demonstrate that in the range of 4–300 K there is a high probability peak at $S_m = 1$ which can be associated with the first conductance peak of Ni at $T = 4$ K (centred around $G = 1.6G_0$). However, there is no evidence of such a peak at room temperature in the experiments. Therefore, different structural evolutions for Ni must be excluded as the origin for experimental differences between Ni conductance histograms at low and room temperature. Such differences could be due to (i) the presence of chemiadsorbed atoms on the nanowire [20] or (ii) ballistic magnetoresistance (BMR) effects due to the presence of an abrupt magnetic domain wall anchored at the narrowest cross-section of the nanowire [26].

References

[1] AGRAÏT N., LEVY-YEYATI A., VAN RUITENBEEK J.M., Phys. Rep., 377 (2003), 81 and references therein.
[2] LANDAUER R., Phil. Mag., 21 (1970), 863.
[3] PASCUAL J.I., MÉNDEZ J., GÓMEZ-HERRERO J., BARÓ A.M., GARCÍA N., BINH V.T., Phys. Rev. Lett., 71 (1993), 1852.
[4] OLESEN L., LAEGSGAARD E., STENSGAARD I., BESENBACHER F., SCHIOTZ J., STOLTZE P., JACOBSEN K.W., NORSKOV J.K., Phys. Rev. Lett., 72 (1994), 2251.
[5] MULLER C.J., VAN RUITENBEE K J.M., DE JONGH L.J., Phys. Rev. Lett., 69 (1992), 140.
[6] COSTA-KRÄMER J.L., GARCÍA N., GARCÍA-MOCHALES P., SERENA P.A., Surf. Sci., 342 (1995), L1144.
[7] KONDO Y., TAKAYANAGI K., Phys. Rev. Lett., 79 (1997), 3455; OHNISHI H., KONDO Y., TAKAYANAGI K., Nature (London), 395 (1998), 780.
[8] LI C.Z., TAO N.J., Appl. Phys. Lett., 72 (1998), 894.
[9] OLESEN L., LAEGSGAARD E., STENSGAARD I., BESENBACHER F., SCHOLTZ J., STOLTZE P., JACOBSEN K.W., NORSKOV J.K., Phys. Rev. Lett., 74 (1995), 2147.
[10] KRANS J.M., VAN RUITENBEEK J.M., FISUN V.V., YANSON I.K., DE JONGH L.J., Nature, 375 (1995), 767.
[11] YANSON A.I., VAN RUITENBEE K J.M., Phys. Rev. Lett., 79 (1997), 2157.
[12] HASMY A., MEDINA E., SERENA P.A., Phys. Rev. Lett., 86 (2001), 5574.
[13] DÍAZ M., COSTA-KRÄMER J.L., SERENA P.A., MEDINA E., HASMY A., Nanotechnol., 12 (2001), 118.

[14] Medina E., Díaz M., León N., Guerrero C., Hasmy A., Serena P.A., Costa-Krämer J.L., Phys. Rev. Lett., 91 (2003), 026802.

[15] Scheer E., Joyez P., Esteve D., Urbina C., Devoret M.H., Phys. Rev. Lett., 78 (1997), 3535.

[16] Costa-Krämer J.L., Phys. Rev. B, 55 (1997), R4875.

[17] Oshima H., Miyano K., Appl. Phys. Lett., 73 (1998), 2203.

[18] Ono T., Ooka Y., Miyajima H., Otani Y., Appl. Phys. Lett., 75 (1999), 1622.

[19] Shimizu M., Saitoh E., Miyajima H., Otani Y., J. Magn. Magn. Mater., 239 (2002), 243.

[20] Untiedt C., Dekker D.M.T., Djukic D., Van Ruitenbeek J.M., Phys. Rev. B, 69 (2004), 081401(R).

[21] Landman U., Luedtke W.D., Burnham N.A., Colton R.J., Science, 248 (1990), 454.

[22] Bratkovsky A.M., Sutton A.P., Todorov T.N., Phys. Rev. B, 52 (1995), 5036.

[23] Sorensen R., Brandbyge M., Jacobsen K.W., Phys. Rev. B, 57 (1998), 3283.

[24] Mishin Y., Farkas D., Mehl M.J., Papaconstantopoulos D.A., Phys. Rev. B, 59 (1999), 3393.

[25] Yanson A.I., Yanson I.K., Van Ruitenbeek J.M, Phys. Rev. Lett., 87 (2001), 216805.

[26] García N., Muñoz M., Zhao Y.W., Phys. Rev. Lett., 82 (1999), 2923.

Dynamical properties of $C_{60}(H_2O)_{50}$ mixture cluster. Molecular dynamics simulation

ALEKSANDER DAWID[*], MARIUSZ SOKÓŁ, ZYGMUNT GBURSKI

Institute of Physics, University of Silesia, Uniwersytecka 4, 40-007 Katowice, Poland

A small cluster composed of fifty water molecules evenly spread out over the surface of fullerene (C_{60}) has been studied by the MD simulation. The radial distribution function and velocity autocorrelation functions (linear and angular) of water molecules have been calculated. Both the solid and liquid phases of a water layer surrounding the fullerene molecule have been investigated. The simulation suggests that a plastic phase (active rotations and frozen translations of water molecules) of such a specific, ultrathin water layer develops at a low temperature, $T < 22$ K.

Key words: *water; molecular dynamics simulation; thin layer; confined water*

1. Introduction

Recently, there has been a great deal of interest in studying small (nanoscale) systems that are expected to possess properties significantly different from those of the bulk materials. Because of the significance of water to life, it is most important to understand the properties of water in various enviromnents [1–7]. The properties of water in a confined nanoscale environment are a particular subject of vital research. Motivated by this need, we have studied the dynamical properties of water molecules confined in ananoscale layer or "atmosphere" surrounding a C_{60} molecule by the molecular dynamics (MD) method.

2. Computational procedure

An approach involving the TIP4P model of the water molecule [8, 9] (Fig. 1), which provided a reasonable description of liquid water and aqueous solutions [9] was adopted.

_____

[*]Corresponding author, e-mail: dawid@us.edu.pl
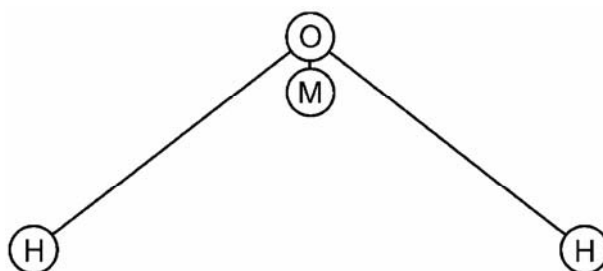
Fig. 1. The TIP4P model of the water molecule

The interaction between water molecules is described in terms of the pairwise potential composed of the Lennard–Jones (LJ) and Coulombic components

$$V(r_{ij}) = \sum_{m \in i} \sum_{n \in j} \frac{q_m q_n e^2}{r_{im,jn}} + \frac{B}{r_{OO}^{12}} - \frac{C}{r_{OO}^{6}} \qquad (1)$$

where r_{OO} is the distance between i-th and j-th oxygen atoms and $r_{im,jn}$ are the distances between all pairs of charges. The charges appearing in the potential are $q_H = 0.52e$, $q_M = -1.04e$, and $q_O = 0$, where $e^2 = 331.8$ kcal·Å/mol.

The fullerene and water molecules were treated as a rigid body. The interatomic potential between unlike C–O atoms was taken as the usual Lennard–Jones form

$$V(r_{ij}) = 4\varepsilon_{CO} \left[\left(\frac{\sigma_{CO}}{r_{ij}} \right)^{12} - \left(\frac{\sigma_{CO}}{r_{ij}} \right)^{6} \right] \qquad (2)$$

where r_{ij} is the distance between the i-th and j-th atoms, ε is the minimum of the potential at a distance $2^{1/6}\sigma$, $k\beta$ is the Boltzmann constant, L–J potential parameters ε and σ are given in Table 1.

Table 1. Parameters of the Lennard–Jones potential

Atom	$\frac{\varepsilon}{k_\beta}$ [K]	σ [Å]	m [10^{-25} kg]
O	88.4	3.15	0.265
C	58.2	3.35	0.199

The potential L–J parameters between unlike atoms C and O are given by the Lorentz–Berthelot rules [14] $\sigma_{CO} = (\sigma_C + \sigma_O)/2$ and $\varepsilon_{CO} = (\varepsilon_C \varepsilon_O)^{1/2}$.

The classical equations of motion have been integrated using the predictor-corrector Adams method [15] with the integration time step 0.8 fs, which ensured sufficient energy conservation.

3. Results

The investigated system was composed of $n = 50$ water molecules surrounding the fullerene surface (Fig. 2). The selection of $n = 50$ was because such a number of water molecules form an almost uniform monatomic layer.
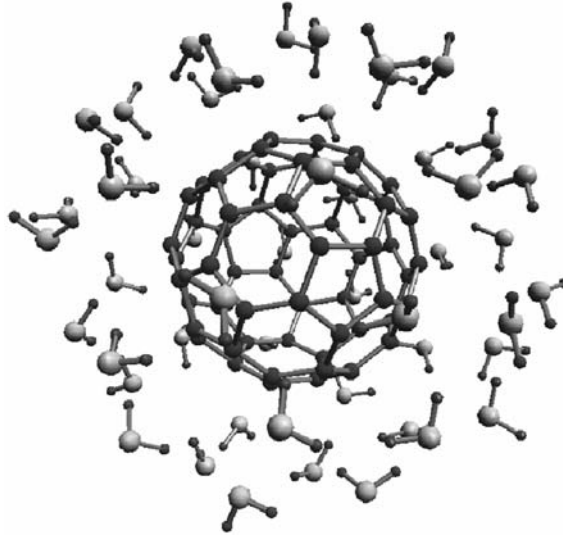
Fig. 2. The instantaneous configuration of
(C$_{60}$)(H$_2$O)$_{50}$ cluster at temperature $T = 86.7$ K

Firstly, the phases of condensation of the C$_{60}$(H$_2$O)$_{50}$ system were examined. The simulated mean square displacement $\langle \Delta r^2(t) \rangle$ at three temperatures (Fig. 3) shows the solid phase for $T = 11.3$ K and gradual development of the liquid phase of the water layer for higher temperatures. From the slope of $\langle \Delta r^2(t) \rangle$ the translational diffusion coefficient D of water molecule can be derived [14] and it is presented in Fig. 4.

We see that the transition (melting) point between solid and liquid phase develops arround $T \approx 22$ K. The linear velocity $\vec{v}$ autocorrelation function of water molecule $C_v(t)$

$$C_v(t) = \frac{\langle \vec{v}(0) \cdot \vec{v}(t) \rangle}{\langle \vec{v}(0) \cdot \vec{v}(0) \rangle} \qquad (3)$$

and its cosine Fourier transform $I(v)$

$$I(v) = \int_0^\infty C_v(t) \cos(2\pi v t) \, dt \qquad (4)$$

are presented in Figs. 5 and 6, respectively.
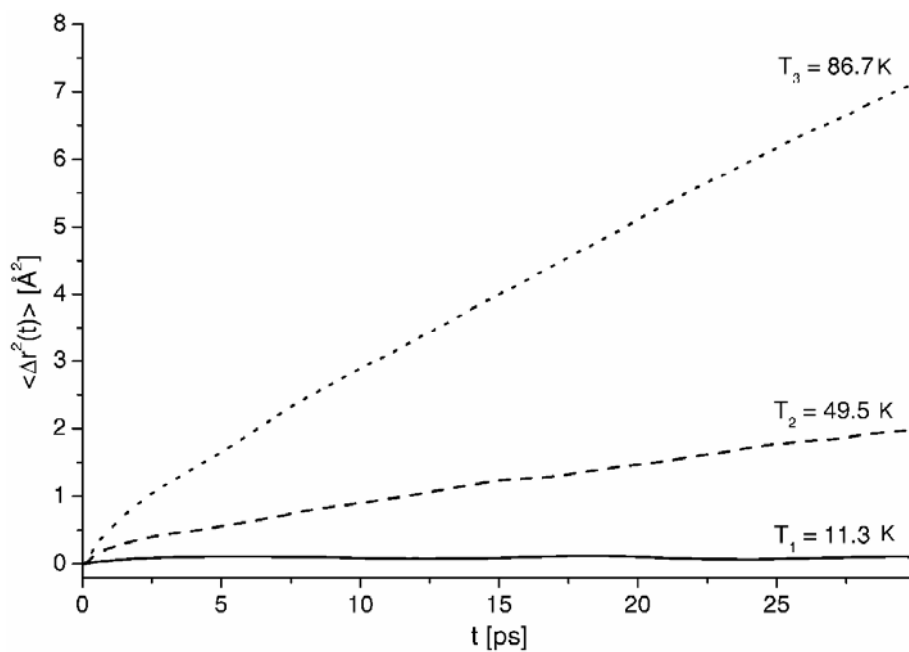
Fig. 3. The mean-square displacement function for $(C_{60})(H_2O)_{50}$ cluster at three different temperatures, $T_1 = 11.3$ K (solid line), $T_2 = 49.5$ K (dashed line) and $T_3 = 86.7$ K (dotted line)
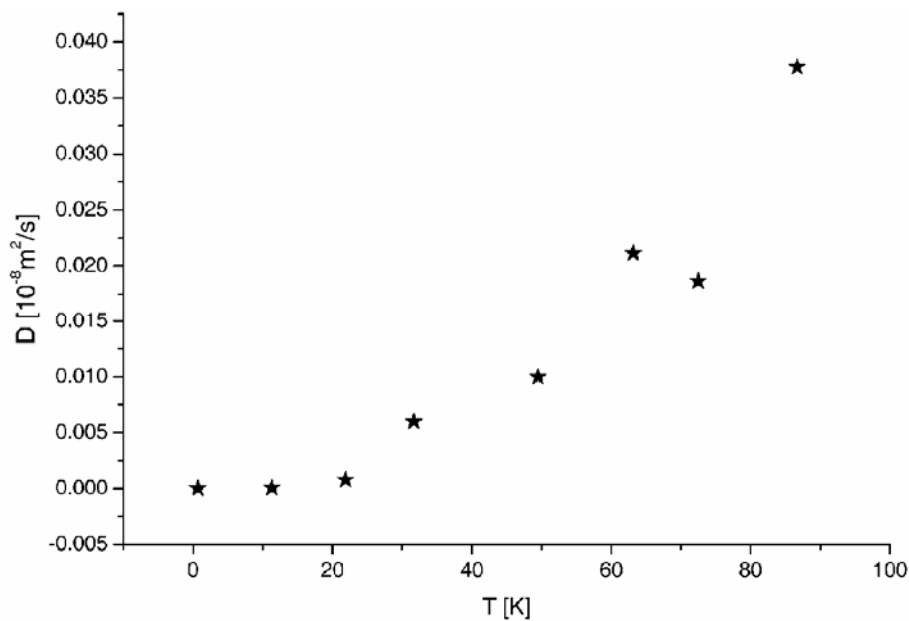
Fig. 4. The temperature dependence of the diffusion coefficient for $(C_{60})(H_2O)_{50}$ cluster
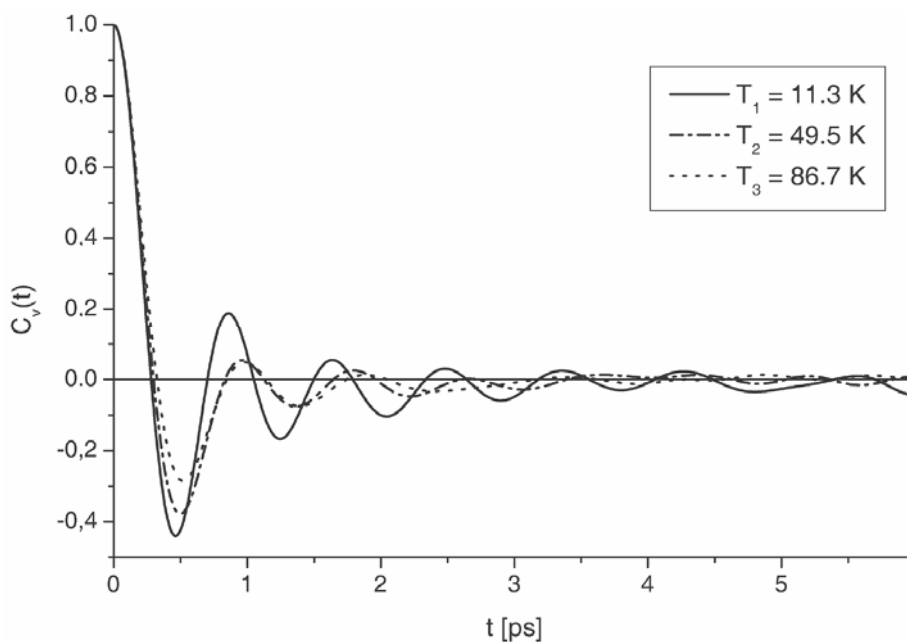
Fig. 5. The linear velocity autocorrelation function in solid and liquid phases
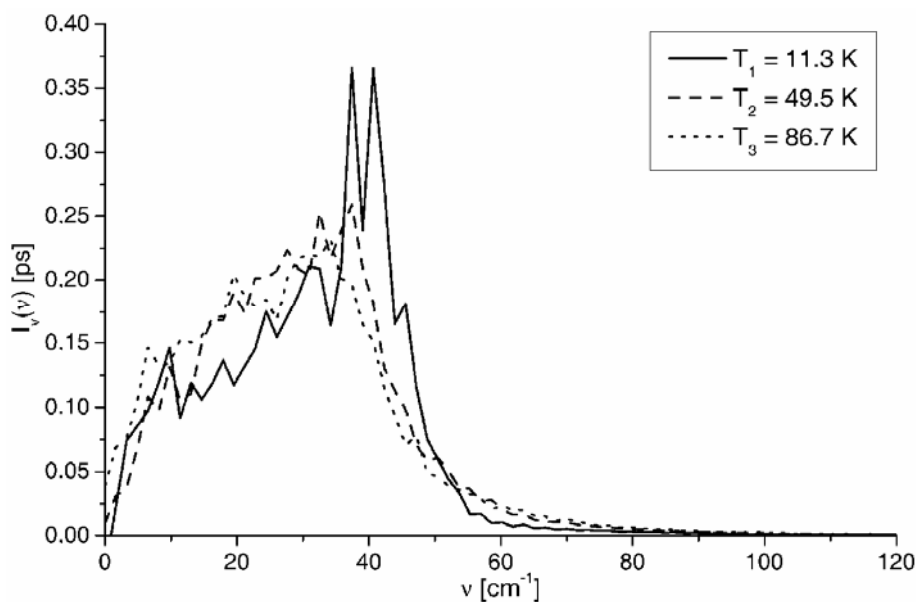
Fig. 6. Cosine Fourier transform of water linear velocity autocorrelation function
in (C$_{60}$)(H$_2$O)$_{50}$ cluster at three different temperatures, $T_1 = 11.3$ K (solid line),
$T_2 = 49.5$ K (dashed line) and $T_3 = 86.7$ K (dotted line)
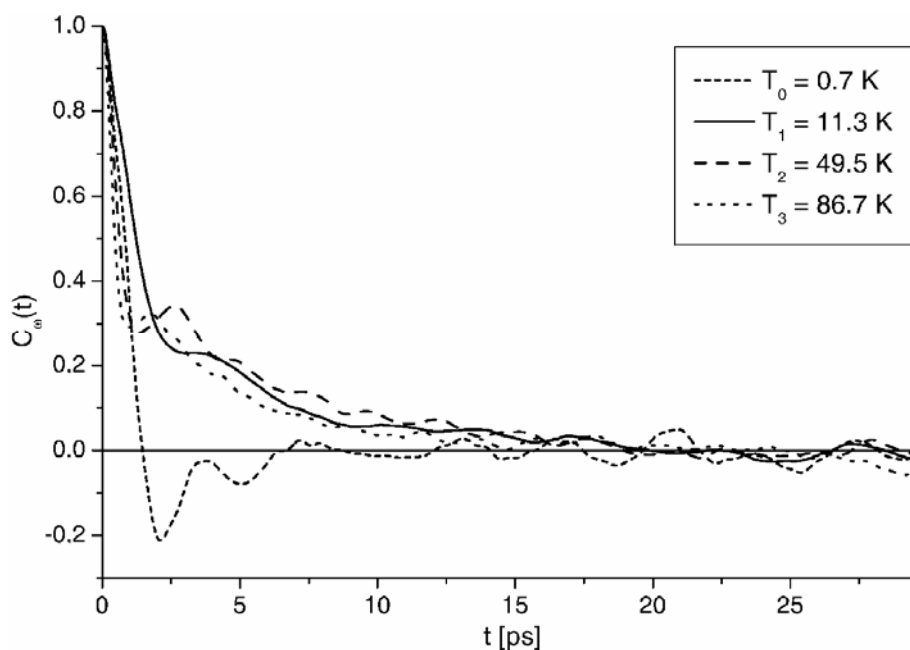
Fig. 7. The angular velocity autocorrelation function in solid and liquid phase
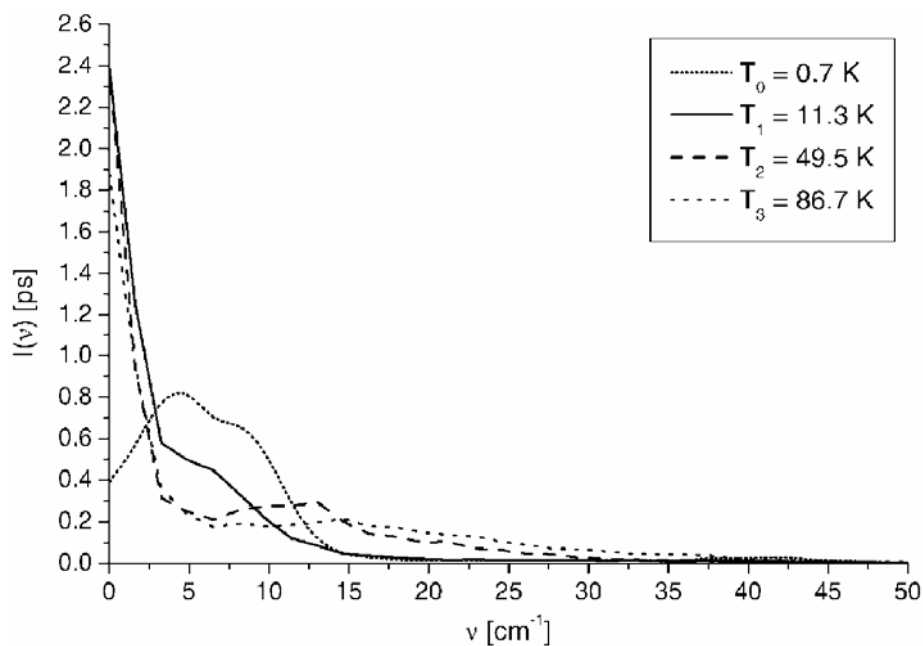
Fig. 8. Cosine Fourier transform of water angular velocity autocorrelation function in $(C_{60})(H_2O)_{50}$ at four different temperatures, $T_0 = 0.7$ K (short dotted line), $T_1 = 11.3$ K (solid line), $T_2 = 49.5$ K (dashed line) and $T_3 = 86.7$ K (dotted line)

The function $C_v(t)$ at low temperature $T = 11.3$ K has an oscillatory character (solid phase). At higher temperature $T = 86.7$ K $C_v(t)$ decays more regularly and is almost featureless after the first negative dip. This is the behaviour typical of a liquid phase. Inspecting the Fourier transform of $C_v(t)$ (Fig. 6) one observes that the narrow peaks of the solid phase are spread around $\nu \approx 40$ cm^{-1} ($T = 11.3$ K) and become much broader for the liquid state. To get deeper insight into the water motion in liquid phase of the spherically shaped layer surrounded C$_{60}$ the angular velocity autocorrelation function $C_\omega(t)$ was simulated:

$$C_\omega(t) = \frac{\langle \vec{\omega}(0) \cdot \vec{\omega}(t) \rangle}{\langle \vec{\omega}(0) \cdot \vec{\omega}(0) \rangle} \tag{5}$$

where $\vec{\omega}$ is the angular velocity of water molecule (Fig. 7) and its cosine Fourier transform (Fig. 8).

4. Conclusions

Even at low temperature ($T = 11.3$ K), the reorientations of light water molecules are observed, although at the same temperature the translational diffusion (mass transport over the layer) is absent ($D \cong 0$). The condensation state of matter with no translational diffusion but active rotational dynamics is often called the plastic phase. The research shows that the plastic phase of an ultrathin water layer appears at temperatures below $T = 22$ K. The dynamics of water molecules in an ultrathin, spherically shaped layer, differs from those in the bulk material. These computer studies may contribute to future experimental research of exotic layers covered with fullerene.

References

[1] JENA P., RAO B.K., KHANNA S.K., *The Physics and Chemistry of Small Clusters*, Plenum Press, New York, 1987.
[2] KROTO H.W., HEATH J.R., O'BRIEN S. C., CURL R.F., SMALLEY R.E., Nature, London, 318 (1985), 162.
[3] NARTEN A.H., THIESSEN W.E., BLUM L., Science, 217 (1982), 1033.
[4] NARTEN A.H., J. Chem. Phys., 56 (1972), 5681.
[5] KRINDEL P., ELIEZER I., Coord. Chem. Rev., 6 (1971), 217.
[6] STILLINGER F.H., Science, 209 (1980), 4455.
[7] JEDLOVSZKY P., VALLAURI R., RICHARDI J., J. Phys.Condens. Matter, 12 (2000), 115.
[8] JORGENSEM W.L., J. Chem. Phys., 77 (1982), 4156.
[9] JORGENSEM W.L., MADURA J.D, CHANDRASEKHAR J., J. Chem. Phys., 79 (1983), 926.
[10] STILLINGER F.H., RAHMAN A., J. Chem. Phys., 55 (1971), 3337.
[11] STILLINGER F.H., RAHMAN A., J. Chem. Phys., 57 (1972), 1281.
[12] STILLINGER F.H., RAHMAN A., J. Chem. Phys., 60 (1974), 1545.
[13] PADRÓ J.A., MARTI J., GUBDIAF E., J. Phys. Condens. Matter, 6 (1994), 2283.
[14] ALLEN M.P., TILDESLEY D.J., *Computer Simulation of Liquids*, Oxford University Press, 1989.
[15] RAPAPORT D.C., *The Art of Molecular Dynamics Simulation*, Cambridge University Press,1995.

Molecular dynamics of cholesterol
in a thin film surrounding a carbon nanotube

PRZEMYSŁAW RACZYŃSKI[*], ALEKSANDER DAWID,
MARIUSZ SOKÓŁ, ZYGMUNT GBURSKI

Institute of Physics, University of Silesia, Uniwersytecka 4, 40-007 Katowice, Poland

Molecular dynamics (MD) simulations of the system composed of a single walled carbon nanotube (SWNT) surrounded by a thin film of: a) cholesterol–water mixture and b) pure cholesterol have been carried out. The translational and rotational correlation functions and their Fourier transforms of both cholesterol and water molecules have been calculated for several temperatures and concentrations. The interpretation of translational and rotational dynamics of both cholesterol and water molecules in the specific environment is presented.

Key words: *single walled carbon nanotube; MD simulation; thin film; cholesterol; water*

1. Introduction

The discovery of carbon nanotubes [1] has initiated a number of scientific investigations devoted to the study of their mechanical, chemical, optical, thermal and electrical properties [2–6]. Recently, however, there has been increasing activity in investigating small, finite size SWNT-based mixture systems, because they are expected to exhibit interesting properties for nanotechnological applications [7, 8]. This paper presents a classical molecular dynamics simulation (MD) [9] study of the single-walled carbon nanotube surrounded by cholesterol molecules and a cholesterol–water mixture.

2. Simulation details

As a typical representative of the family of carbon nanotubes an armchair (10, 10) nanotube [7] was chosen. The Lennard–Jones (L–J) interaction potential V between

_____

[*] Corresponding author, e-mail: praczyns@us.edu.pl

the carbon atoms of the nanotube and the sites (atoms) of the cholesterol molecule (Fig. 1) as well as between cholesterol sites was applied.
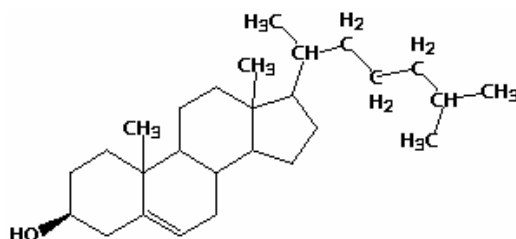
Fig. 1. The structure of the cholesterol molecule

The L–J potential energy is given by the formula:

$$V(r_{ij}) = 4\varepsilon \left[\left(\frac{\sigma}{r_{ij}} \right)^{12} - \left(\frac{\sigma}{r_{ij}} \right)^{6} \right] \tag{1}$$

where ε is the minimum of the potential at a distance of $2^{1/6}\sigma$, k_B is the Boltzmann constant and r_{ij} is the distance between the atoms i and j. The parameters used in Eq. (1) are given in Table 1 [10].

Table 1. Lennard–Jones potential parameters

Atoms	ε/k_B [K]	σ [Å]	m [10^{-25} kg]
C	58.2	3.851	0.199
O	88.7	2.95	0.26551
H	12.4	2.81	0.016594

The L–J potential parameters between unlike atoms are given by the Lorentz–Berthelot rules [9] $\sigma_{A-B} = (\sigma_A + \sigma_B)/2$ and $\varepsilon_{A-B} = \sqrt{\varepsilon_A \varepsilon_B}$, where A, B are C, O or H atoms. We applied an approach involving the TIP4P model of the water molecule [11, 12], which provides a reasonable description of liquid water and aqueous solutions [11]. This model is based on four interaction sites located in a planar configuration, two of which (H) are associated with protons and another two (M and O) are associated with the oxygen nucleus. The angle between H, O and another H site is $\sphericalangle$ HOH = 104°52′. The distances between O and H, and between the O and M sites are $r_{OM} = 0.15$ Å and $r_{OH} = 0.9572$ Å, respectively. The interactions between the molecules are described in terms of the pairwise potential composed of the Lennard–Jones and Coulombic components:

$$V_{\text{wat.}}(r_{ij}) = \sum_{m \in i} \sum_{n \in j} \frac{q_m q_n e^2}{r_{im,jn}} + \frac{A}{r_{OO}^{12}} - \frac{B}{r_{OO}^{6}} \tag{2}$$

where r_{OO} is the distance between the *i*-th and *j*-th oxygen atoms and $r_{im,jn}$ are the distances between all pairs of charges. The charges appearing in the potential are $q_H = 0.52e$, $q_M = -1.04e$ and $q_O = 0$, where $e^2 = 331.8$ (kcal·Å)/mol. As a part of the molecular design process, the negative charge has been shifted away from the O site by a small amount to the M site, which has been introduced specifically for this purpose. The rest of the parameters appearing in the L–J-part of Eq. (2), which acts only between the O sites, are $A = 600.0 \times 10^3$ (kcal·Å^{12})/mol and $B = 610.0$ (kcal·Å^6)/mol.

The classical equations of motion are integrated up to 5 ns by the predictor –corrector Adams–Moulton algorithm [13]. The integration time step was 0.4 fs which ensures total energy conservation within 0.01 %. The initial positions were generated by the Monte Carlo method [9] and initially equilibrated over 10^6 MD time steps before the MD data were calculated and collated.

3. Results

Firstly one single armchair carbon nanotube surrounded by a varying number $n = 3, 5, 9$ of cholesterol molecules was simulated, for several temperatures. In Fig. 2 the calculated mean square displacement $\left\langle \left| \Delta \vec{r}(t) \right|^2 \right\rangle$ of the centre of mass of cholesterol is presented, where

$$\left\langle \left| \Delta \vec{r}(t) \right|^2 \right\rangle = \left\langle \left| \vec{r}(t) - \vec{r}(0) \right|^2 \right\rangle$$

Fig. 2. The mean square displacement of the centre of mass of the cholesterol molecule for three concentrations at several temperatures: a) SWNT(chol)$_3$, b) SWNT(chol)$_5$ and c) SWNT(chol)$_9$. The legend concerning temperature is placed on subsection b) but it applies also to a) and c). This notation is used in all subsequent figures

and $\vec{r}$ is the position of the centre of mass of a single molecule [14]. The mean square displacement is connected with the diffusion coefficient *via* Einstein relation

$$\left\langle \left| \Delta \vec{r}\left(t\right) \right|^{2} \right\rangle \approx 6\,Dt$$

where D is the translational diffusion coefficient.

Fig. 3. The translational diffusion coefficient D of the centre of mass
of the cholesterol molecule for three concentrations as a function of temperature

It can be seen in Figures 2 and 3 that at low temperature, $T = 350$ K, a solid phase appears (no diffusion, $D \approx 0$), whereas the fluid phase is observed at higher temperatures. The distinction between solid ($T = 350$ K) and liquid ($T = 550$ K) phase can be also seen in Fig. 4, where an example of the radial distribution function $g(r)$ [9] of the centre of mass of cholesterol ($n = 9$) is given.

Fig. 4. The radial distribution function of the centre
of mass of cholesterol for three concentrations
and several temperatures: a) SWNT(chol)$_3$,
b) SWNT(chol)$_5$ and c) SWNT(chol)$_9$

Note that the translational mobility of cholesterol's fluid phase in the layer which covers the SWNT increases with a growing number *n* of cholesterol molecules. In the case of small *n* each particular molecule is in direct contact with the SWNT's surface being strongly attracted by the carbon atoms of the nanotube. More cholesterol molecules (larger *n*) means more interactions between the cholesterol sites, the tight binding of cholesterol molecules to the nanotube's surface is partially weakened by non-negligible cholesterol–cholesterol interactions and the increased ability of the cholesterol molecules to move over the nanotube's surface. A representative snapshot of the fluid state configuration of the system studied (*n* = 9) is presented in Fig. 5.
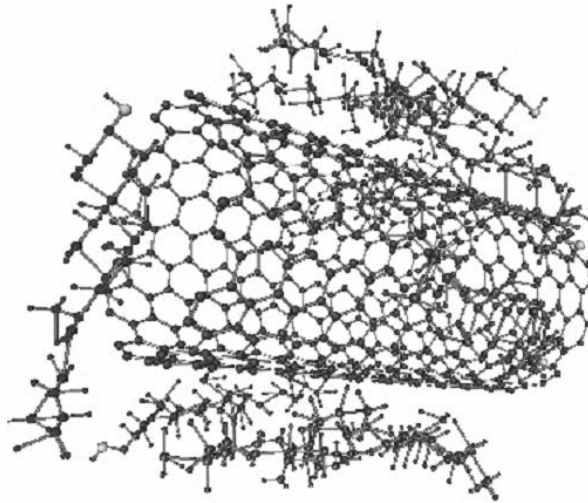
Fig. 5. An example of the liquid state instantaneous configuration of the SWNT(chol)$_9$ cluster at T=550 K
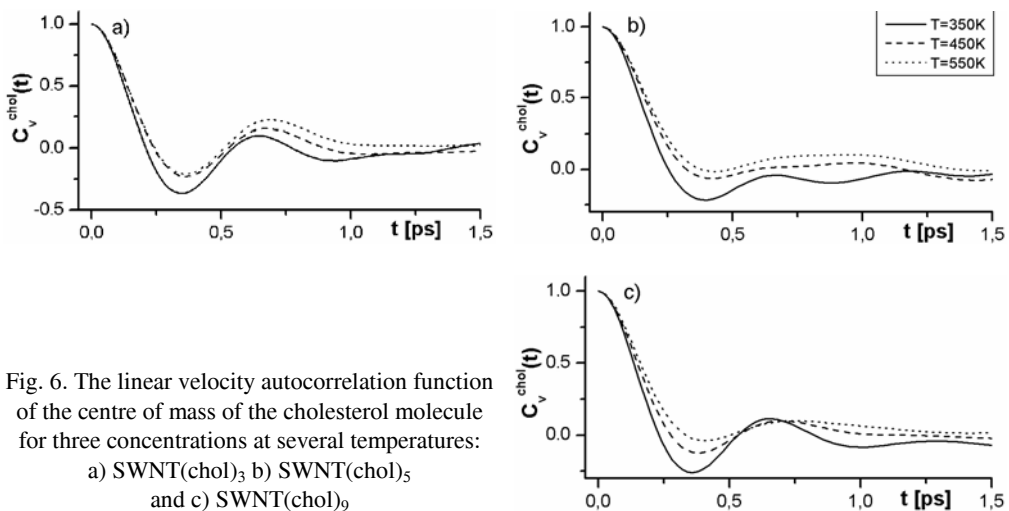
Fig. 6. The linear velocity autocorrelation function of the centre of mass of the cholesterol molecule for three concentrations at several temperatures: a) SWNT(chol)$_3$ b) SWNT(chol)$_5$ and c) SWNT(chol)$_9$

Closely connected with the translational motion is the velocity autocorrelation function $C_{\vec{v}}(t) = \langle \vec{v}(t)\vec{v}(0) \rangle \langle \vec{v}(0)\vec{v}(0) \rangle^{-1}$, where $\vec{v}(t)$ is the translational velocity of the molecule. The behaviour of the calculated correlation functions $C_v(t)$ of cholesterol can be seen in Fig. 6.

The strong oscillations of $C_v(t)$ at low temperatures – characteristic of the solid state [9] – become gradually smoother and less pronounced at higher temperatures as a result of significant randomization of $\vec{v}(t)$ in the liquid phase. Examples of the corresponding Fourier transforms

$$FT(C_{\vec{v}}(t)) = \int_0^\infty C_{\vec{v}}(t)\cos(2\pi\nu t)\,dt$$

are given in Fig. 7.
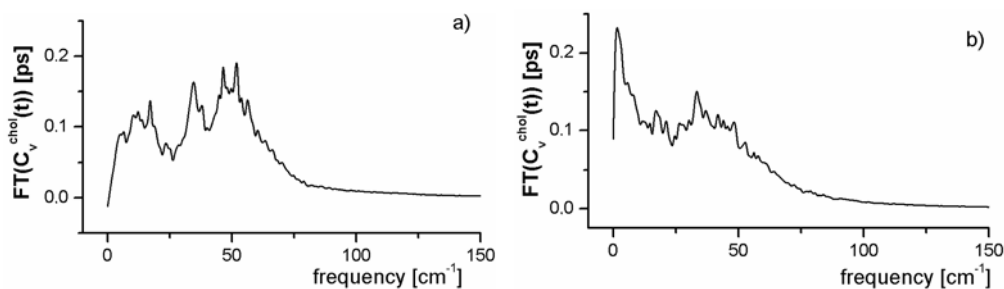
Fig. 7. The Fourier transform $FT(C_{\vec{v}}(t))$ of the linear velocity correlation function of the cholesterol for the solid a) and liquid b) phase of SWNT(chol)$_9$

Two characteristic modulation frequencies are clearly visible at low temperature. The lower frequency ($\nu \approx 20$ cm^{-1}) is associated with the back and forth pulling of cholesterol by the nanotube and the higher frequency ($\nu \approx 50$ cm^{-1}) is connected with cholesterol librations within the layer of cholesterol molecules composed around the nanotube. The higher frequency peak becomes broader and less defined as a result of mutual and random collisions of cholesterol molecules in the liquid state.
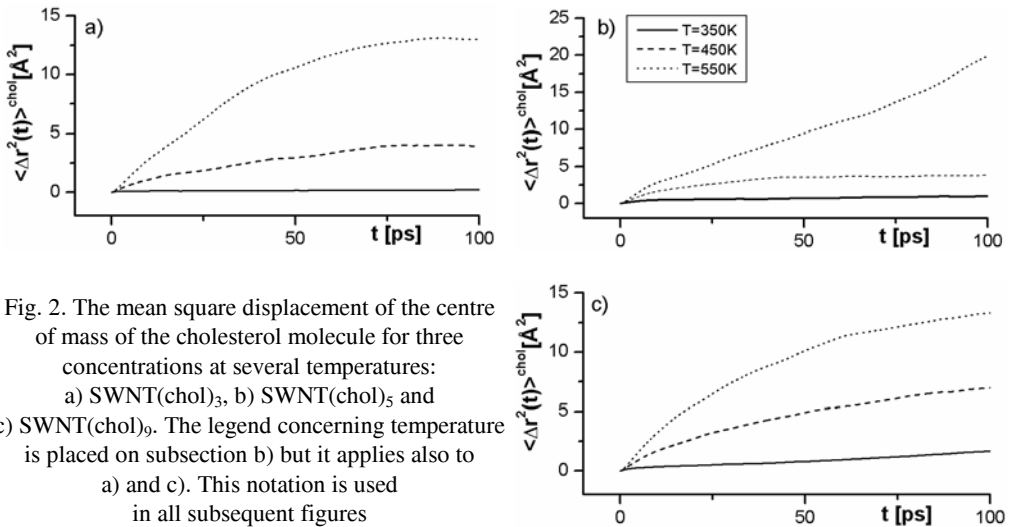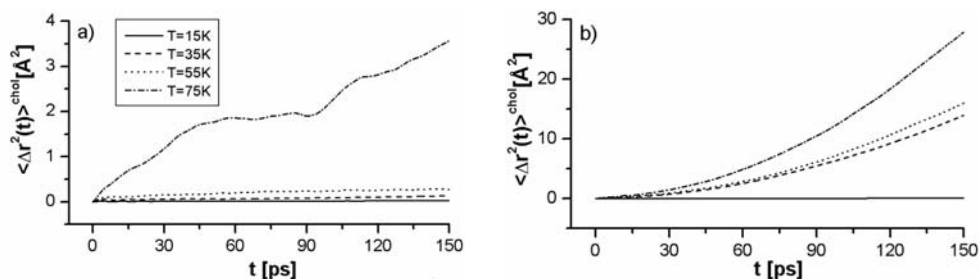

Fig. 8. The mean square displacement of the centre of mass of the cholesterol molecule for two concentrations at several temperatures: a) SWNT(chol)$_3$(water)$_{45}$ and b) SWNT(chol)$_2$(water)$_{80}$
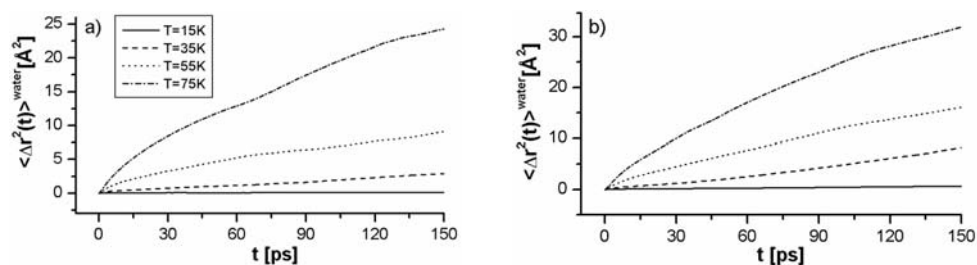
Fig. 9. The mean square displacement of the centre of mass of the water molecule for two concentrations at several temperatures: a) $SWNT(chol)_3(water)_{45}$ and b) $SWNT(chol)_2(water)_{80}$
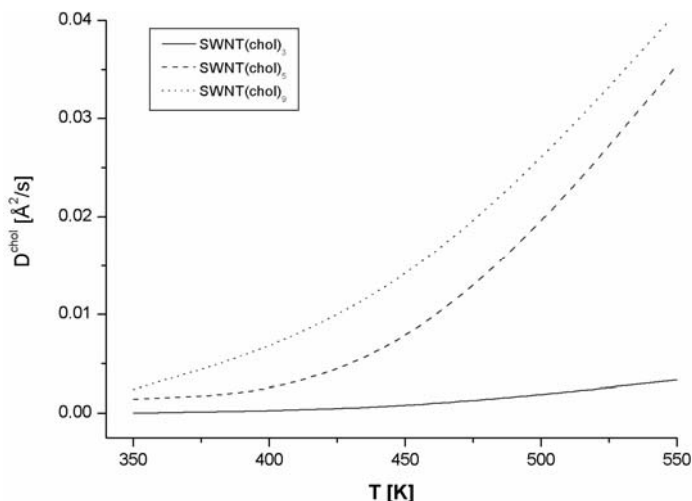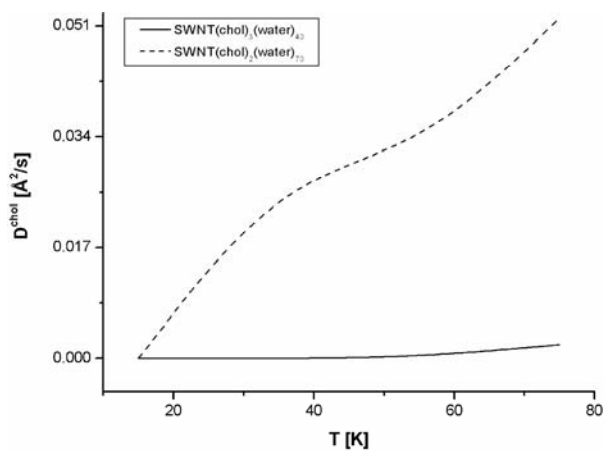

Fig. 10. The translational diffusion coefficient of the centre of mass of the cholesterol molecule for two concentrations as a function of temperature
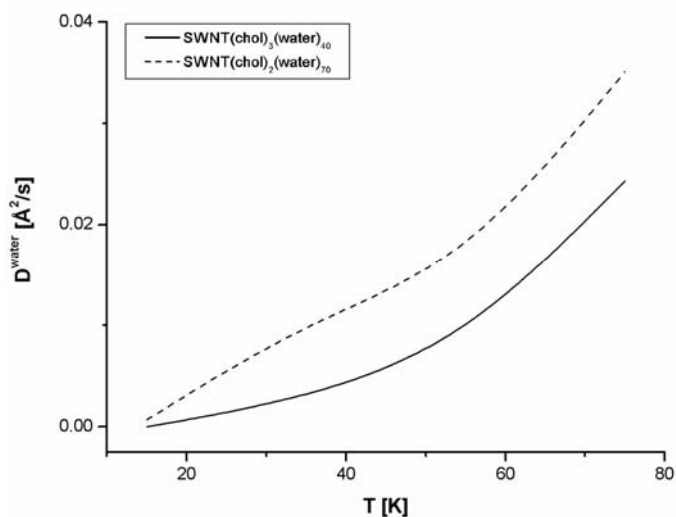
Fig. 11. The translational diffusion coefficient of the centre of mass of the water or two concentrations as a function of temperature

The second part of the work focussed on the properties of a cholesterol–water mixture surrounded an armchair (10, 10) single walled carbon nanotube. The motivation was, that in living cells, cholesterol usually appears accompanied by water. Two concentrations of the cholesterol–water mixture: $SWNT(chol)_3(water)_{45}$ and $SWNT(chol)_2(water)_{80}$ were studied. The mean square displacement of the centre of mass of both, cholesterol and water molecules, is shown in Figs. 8 and 9, respectively.

The liquid phase developed here at much lower temperature, comparing to the previous system (pure cholesterol layer). The diffusion coefficients of cholesterol and water molecules are presented in Fig 10 and Fig 11.

The presence of water molecules significantly changes the dynamics of the cholesterol molecules. Note the substantial increase of the value of D_{chol} for the cholesterol–water mixture compared to the cholesterol only layer. An example of the simulated radial distribution functions of the centre of mass of cholesterol and water molecules $SWNT(chol)_2(water)_{80}$ is given in Figs. 12 and 13.
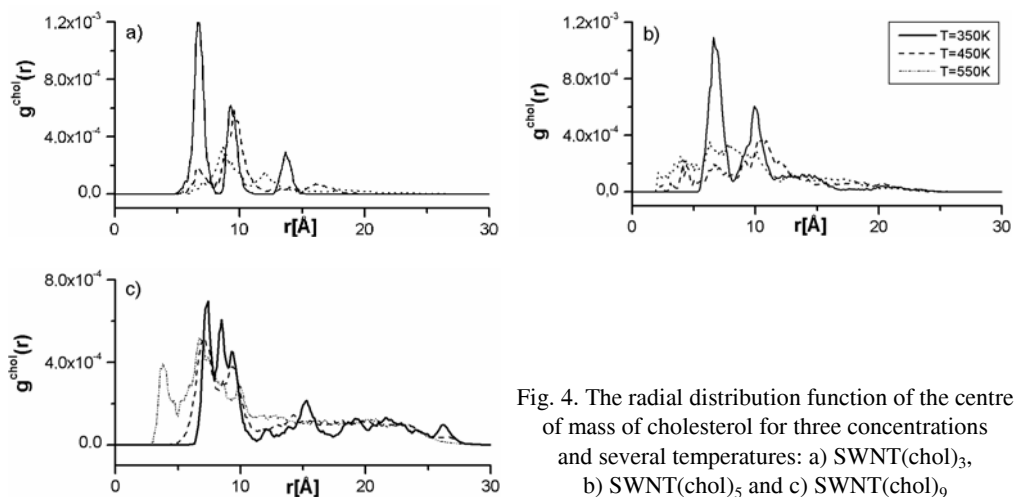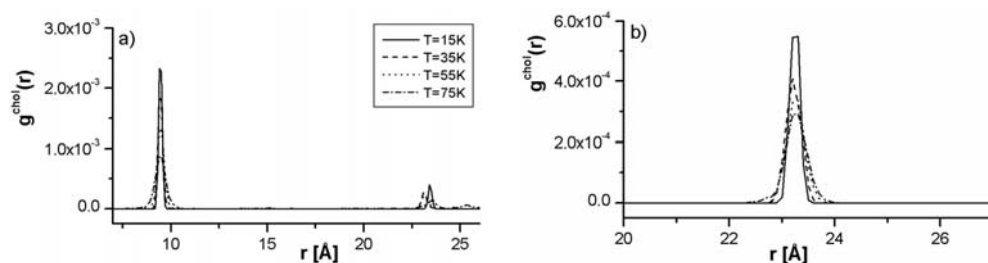
Fig. 12. The radial distribution function of the centre of mass of cholesterol for two concentrations and several temperatures: a) $SWNT(chol)_3(water)_{45}$ and b) $SWNT(chol)_2(water)_{80}$
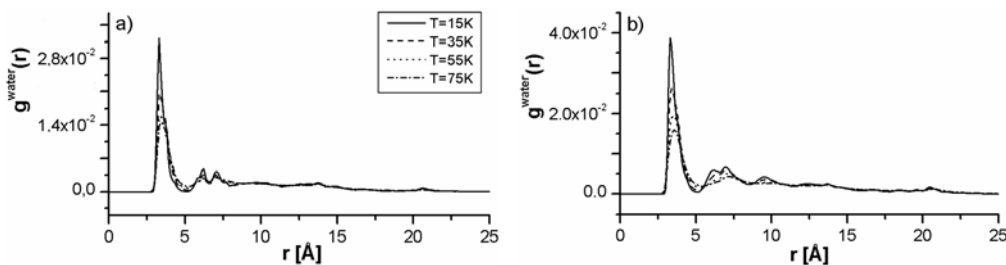
Fig. 13. The radial distribution function of the centre of mass of water for two concentrations and several temperatures: a) $SWNT(chol)_3(water)_{45}$ and b) $SWNT(chol)_2(water)_{80}$

The pronounced peak of $g_{chol}(r)$ at the large distance of $r \approx 23$ Å comes from two cholesterol molecules which happened to be positioned on the opposite side of the nanotube (for the snapshot of this configuration see Fig. 14).

The first peak of the $g_{water}(r)$ functions corresponds to the nearest neighbours average distance of water molecules surrounding the nanotube. As expected, the highest first peak corresponds to completely frozen water at $T = 15$ K and the lowest first

peak corresponds to the liquid phase at $T = 75$ K. The translational velocity autocorrelation functions for the cholesterol $C_{\tilde{v}}^{\text{chol}}(t)$ and water $C_{\tilde{v}}^{\text{water}}(t)$ molecule are given in Figs. 15 and 16, respectively.
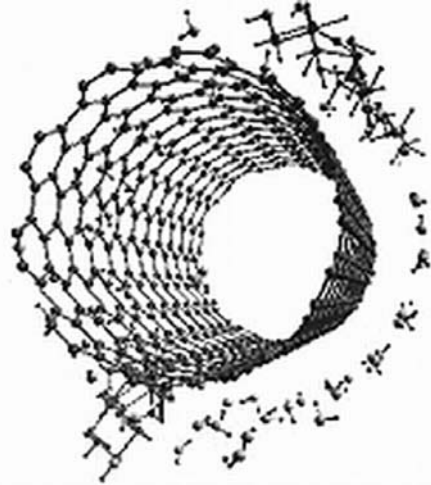
Fig. 14. Snapshot of the instantaneous configuration of SWNT(chol)$_2$(water)$_{80}$ at a temperature of $T = 55$ K
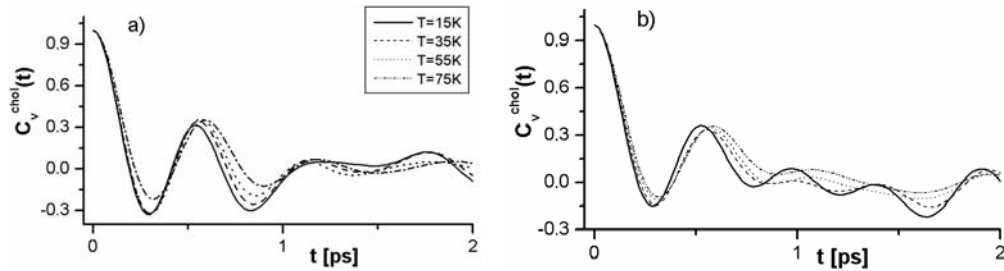
Fig. 15. The linear velocity autocorrelation function $C_{\tilde{v}}^{\text{chol}}(t)$ of the centre of mass of the cholesterol molecule for two concentrations at several temperatures: a) SWNT(chol)$_3$(water)$_{45}$ and b) SWNT(chol)$_2$(water)$_{80}$
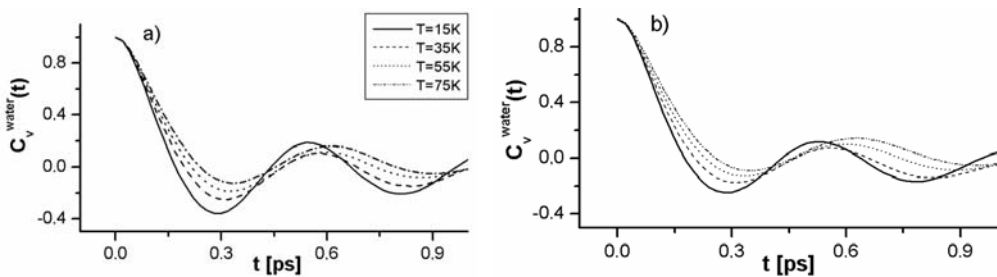
Fig. 16. The linear velocity autocorrelation function $C_{\tilde{v}}^{\text{water}}(t)$ of the centre of mass of the water molecule for two concentrations at several temperatures: a) SWNT(chol)$_3$(water)$_{45}$ and b) SWNT(chol)$_2$(water)$_{80}$

One can see a slight temperature and concentration sensitivity of $C_{\tilde{v}}^{chol}(t)$ for such a large molecule as cholesterol. Contrary to this, the $C_{\tilde{v}}^{water}(t)$ of the light water molecule significantly depends on temperature. The dumped oscillations of $C_{\tilde{v}}^{water}(t)$ in the solid phase at low temperature ($T = 15$ K) becomes gradually smoother and featureless when the water is liquid ($T = 75$ K). The time scale of the decay of $C_{\tilde{v}}^{chol}(t)$ and $C_{\tilde{v}}^{water}(t)$ is quite different, which reflects the disproportion between masses of cholesterol and water. The representative examples of the Fourier transforms $FT(C_{\tilde{v}}^{chol}(t))$ and $FT(C_{\tilde{v}}^{water}(t))$ are presented in Figs. 17 and 18, where a distinct difference between $FT(C_{\tilde{v}}^{water}(t))$ of frozen and liquid water is clearly observed.
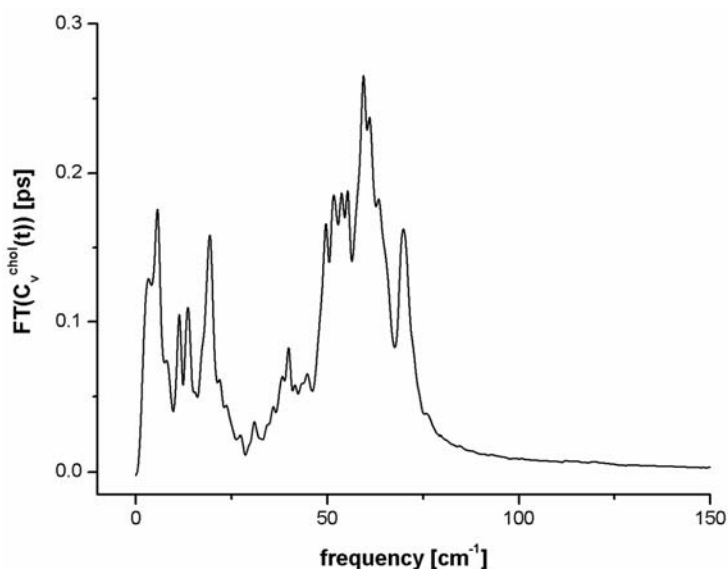
Fig. 17. An example of the Fourier transform $FT(C_{\tilde{v}}^{chol}(t))$ of the linear velocity correlation function of cholesterol for SWNT(chol)$_3$(water)$_{45}$ at $T = 55$K.
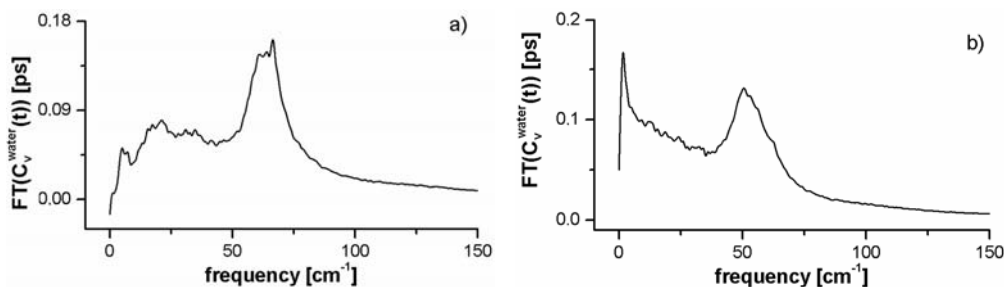
Fig. 18. An example of the Fourier transform $FT(C_{\tilde{v}}^{water}(t))$ of the linear velocity correlation function of the water molecule in solid a) and liquid b) phase of SWNT(chol)$_2$(water)$_{80}$

4. Conclusion

The preliminary MD simulations reported here may encourage future experimental studies, for example Raman spectroscopy, of carbon nanotubes coated by pure cholesterol and cholesterol–water mixture.

References

[1] IJIMA S., Nature, 354 (1991), 56.

[2] ODOM T. W., HUANG J.L., KIM P., LIEBER C.M., Nature, 391 (1998), 62.

[3] O'CONNEL M J., BACHILO S.M., HUFFMAN C.B., MOORE V.C., STRANO M.S., HAROZ E.H., RIALON K.L., BOUL P.J., NOON W.H., KITTRELL C., MA J., HAUGE R.H., WEISMAN R.B., SMALLEY R.E., Science, 297 (2002), 593.

[4] FAN S. WEI B.Q., VAJTAI R., JUNG Y., WARD J., ZHANG R., Science, 283 (1999), 512.

[5] KONG J. FRANKLIN N.R., ZHOU C., CHAPLINE M.G., PENG S., CHO K., DAI C., Science, 287 (2000), 622.

[6] ISLAM M.F. ALSAYED A.M., DOGIC Z., ZHANG J., LUBENSKY T.C., YODH A.G., Phys. Rev. Lett., 92 (2004), 088303-1.

[7] DRESSELHAUS M. S., DRESSELHAUS G. AND EKLUND P. C., *Science of Fullerenes and Carbon Nanotubes*, Academic Press, New York, 2000.

[8] DAWID A., GBURSKI Z., J. Phys. Condens. Matter, 15 (2003), 2399.

[9] ALLEN M.P., TILDESLEY D.J., *Computer Simulation of Liquids*, Oxford University Press, Oxford, 1989.

[10] DAWID A., GBURSKI Z., Phys. Rev. A, 68 (2003), 065202.

[11] JORGENSEM W.L., MADURA J. D., CHANDRASEKHAR J., J. Chem. Phys., 79 (1983), 926.

[12] SOKÓŁ M., DAWID A., DENDZIK Z., GBURSKI Z., J. Mol. Struct., 704 (2004), 341.

[13] RAPAPORT D.C., *The Art of Molecular Dynamics Simulation*, Cambridge University Press, Cambridge, 1995.

[14] KACZOR K., PAŁUCHA S. AND GBURSKI Z., J. Mol. Struct., 608 (2002), 9.

Molecular dynamics study
of the fullerene–cholesterol mixture cluster

PRZEMYSŁAW RACZYŃSKI[*], ALEKSANDER DAWID, ZYGMUNT GBURSKI

Institute of Physics, University of Silesia, Uniwersytecka 4, 40-007 Katowice, Poland

Molecular dynamics (MD) studies are presented for clusters composed of fullerene and cholesterol molecules. Several quantities of fullerene and cholesterol as a function of temperature have been dynamically investigated. The mean square displacement, diffusion coefficient, angular and linear velocity autocorrelation functions of both fullerene and cholesterol have been calculated. It has been shown the existence of both a solid and liquid phases of the cholesterol layer surrounding the fullerene "core". The translational diffusion of cholesterol molecules in the liqud phase significantly increase as the temperature rises. Moreover, the plastic phase of the fullerene "core" has been detected.

Key words: *fullerene; cholesterol; cluster, molecular dynamics simulation*

1. Introduction

In recent years, there has been increasing activity in investigating extremely small, finite size, fullerene-based systems, because they are expected to exhibit new physical and chemical properties. Experimental studies of these systems still encounter natural difficulties and so computer simulation methods have become valuable tools for exploratory research on these systems. The paper presents the findings of a computer simulation study (MD) of a nanosystem cluster composed of fullerene (C_{60}) and cholesterol (chol) molecules. Cholesterol plays an important role in mammals, especially humans.

2. Simulation details

The fullerene molecule was regarded as a rigid body composed of 60 carbon atom sites. The interatomic potential between C–C atoms of neighbouring fullerenes is taken to be the usual Lennard–Jones (L–J) form

_____

[*]Corresponding author, e-mail: praczyns@us.edu.pl

$$V(r_{ij}) = 4\varepsilon\left[\left(\frac{\sigma}{r_{ij}}\right)^{12} - \left(\frac{\sigma}{r_{ij}}\right)^{6}\right]$$

where r_{ij} is the distance between the atoms i and j, $-\varepsilon$ is the minimum of the potential at a distance $2^{1/6}\sigma$, k_B is the Boltzmann constant and L–J potential parameters ε and σ are given in Table 1 [1].

Table 1. The Lennard–Jones parameters

Atoms/pseudoatoms	ε/k_B [K]	σ[Å]	m [10^{-25} kg]
C	58.2	3.851	0.199
CH	43.3044	3.8	0,21559
CH$_2$	67.554312	3.92	0.232188
CH$_3$	101.0436	3.875	0.248782
OH	89.7	3.166	0.282104

The rigid-body cholesterol molecule includes 74 atomic sites (Fig. 1), but in line with the common procedure for large molecules [2] we treat the CH, CH$_2$, CH$_3$ and OH atomic groups as the supersites (pseudoatoms).
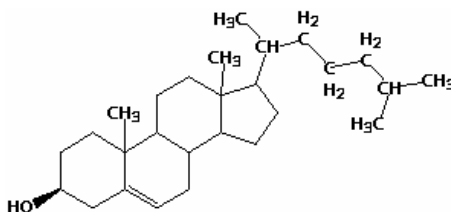
Fig. 1. Model of the cholesterol structure

The pseudoatom-pseudoatom L–J potential parameters for CH, CH$_2$, CH$_3$ and OH groups of interacting cholesterols are given in Table 1 (taken from [3, 4]). The L–J potential parameters between unlike atoms and pseudoatoms are given by Lorentz –Berthelot rules [5] $\sigma_{C-Ar} = (\sigma_C + \sigma_{Ar})/2$ and $\varepsilon_{C-AR} = \sqrt{\varepsilon_C \varepsilon_{AR}}$. The classical equations of motion are integrated up to 5 ns by the predictor-corrector Adams–Moulton algorithm [6]. The integration time step was 0.4 fs which ensured total energy conservation within 0.01%. The initial distribution of molecules was generated by the Monte Carlo (MC) algorithm [5] (10^6 MC steps).

3. Results

MD simulations for fullerene–cholesterol $(C_{60})_9(chol)_{11}$ cluster, at several temperatures, ranging from the solid phase at $T = 250$ K and ending at around $T \approx 550$ K (the

cluster vaporizes at $T \approx 600$ K) are presented. The calculated mean square displacement is [2]

$$\left\langle \left| \Delta \vec{r}(t) \right|^2 \right\rangle = \left\langle \left| \vec{r}(t) - \vec{r}(0) \right|^2 \right\rangle$$

where $\vec{r}$ is the position of the centre of mass of molecule shown in Fig. 2a for C_{60} and Fig. 2b for cholesterol.
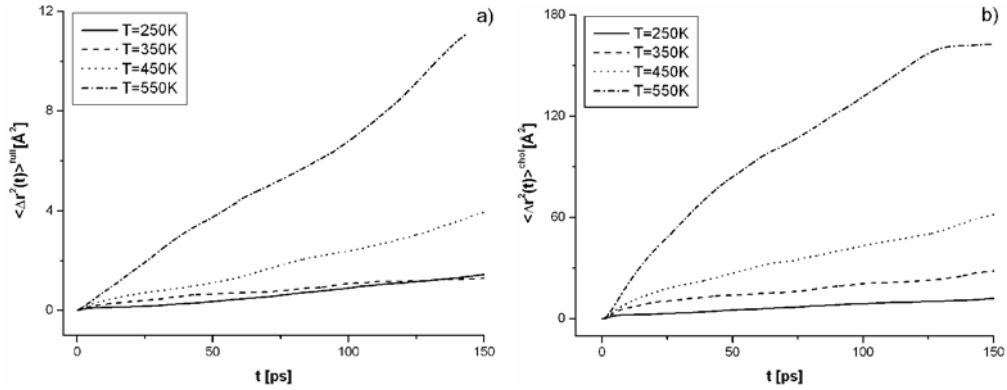
Fig. 2. The mean square displacement of the centre of mass of:
a) fullerene and b) cholesterol molecules in $(C_{60})_9(chol)_{11}$ cluster

It is evident, that at a temperature as low as $T \approx 250$ K, the solid phase develops. As the temperature increases, the slope of $<\Delta r^2(t)>$ strongly increases. The displacement of fullerene is much smaller than cholesterol, because of the large mass of fullerene molecule and a very strong C_{60}–C_{60} interaction. In fact, due to the very deep minimum of fullerene–fullerene interaction potential, the fullerene molecules keep together and do not mix with cholesterol molecules, while the cholesterol molecules form a kind of shell surrounding tight the fullerene core. The tight fullerene molecules are practically immobile; they perform only small librations about their equilibrium positions. The translational diffusion of cholesterol molecules over the cluster space is apparent (liquid phase), if one takes into account the Einstein relation [2]

$$D = \frac{1}{6} \frac{d \left\langle \left| \Delta \vec{r}(t) \right|^2 \right\rangle}{dt}$$

where D is the translational diffusion coefficient (see Fig. 3 for D of fullerene and cholesterol).

The diffusion coefficient of C_{60} is almost zero, and independent of the temperature studied, which means that the fullerene "core" is always in the solid state. In contrast, D of cholesterol is clearly dependent on temperature for $T > 400$ K, the liquid phase of the cholesterol layer is found. An example of the snapshot of the liquid state configuration of $(C_{60})_9(chol)_{11}$ at $T = 450$ K is shown in the Fig. 4.
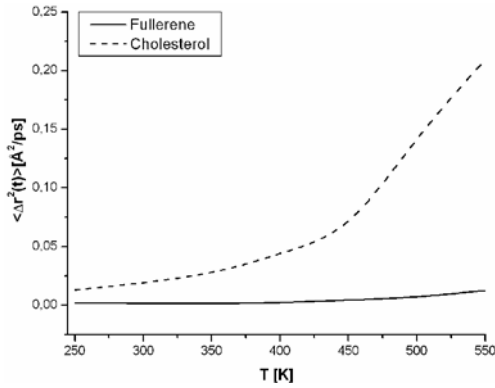
Fig. 3. The temperature dependence of the translational diffusion coefficient of fullerene and cholesterol molecules in $(C_{60})_9(chol)_{11}$ cluster
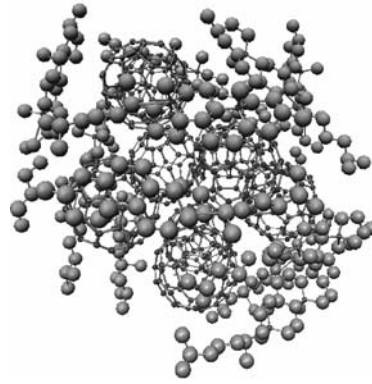
Fig. 4. An example of the cholesterol layer surrounded fullerene core, *i.e.* $(C_{60})_9(chol)_{11}$ cluster at $T = 450$ K

Note, that the mobility of cholesterol molecules in the liquid phase (the slope of $<\Delta r^2(t)> \sim D$) significantly increases with temperature. The time-depended velocity autocorrelation functions (ACF) [8] are valuable tools for studying translational and rotational dynamics in dense phases. The general form of an ACF of the vector property $\vec{A}(t)$ is given by [2]:

$$C_{\vec{A}}(t) = \left\langle \vec{A}(t) \cdot \vec{A}(0) \right\rangle \left\langle \vec{A}(0) \cdot \vec{A}(0) \right\rangle^{-1}$$

Some well known ACFs are associated to individual molecular properties, for example in the transational velocity $\vec{v}$ the autocorrelation function is

$$C_v(t) \ \left(\vec{A}(t) = \vec{v}(t) \right)$$

the averaging is over time and ensemble, in the angular velocity $\vec{\omega}$ the autocorrelation function is $C_\omega(t) \ \left(\vec{A}(t) = \vec{\omega}(t) \right)$ [2].

The behaviour of the correlations functions $C_{v,C_{60}}(t)$ and $C_{v,chol}(t)$ can be observed in Figs. 5a and b, respectively. The angular velocity correlation functions $C_\omega^{C_{60}}(t)$ and $C_\omega^{chol}(t)$ are given in Figs. 6a and b.

At low temperature ($T = 250$ K), both translational and angular velocity correlation functions exhibit dumped oscillations, characteristic of the solid phase [9, 10]. The short time scale pulsation of $C_\omega^{full}(t)$ reflects the fast librations of C_{60} molecule forming the fullerene core. The relaxation of $C_\omega^{chol}(t)$ for the liquid state covers a longer time scale, up to 8 ps, and this is connected with the translational diffusion (transport) of cholesterol molecules over the cholesterol layer. Although the fullere-

nes in the studied cluster do not dislocate, they perform the rotational motion as
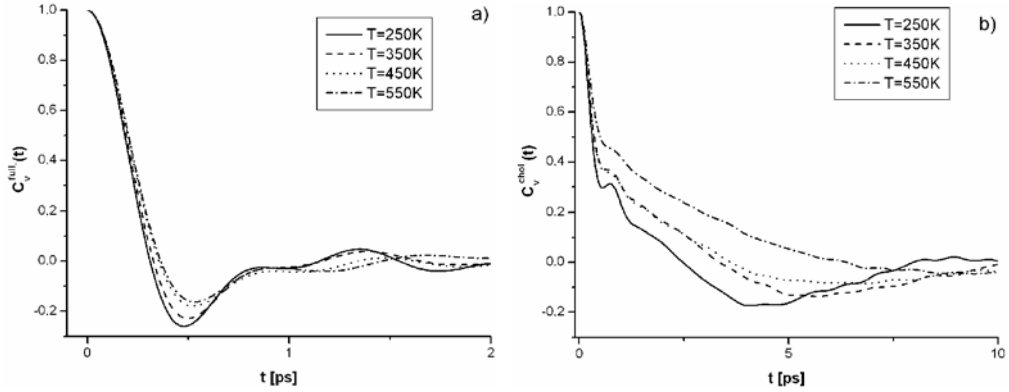
Fig. 5. The linear velocity autocorrelation function of the centre of mass of:
a) fullerene $C_v^{full}(t)$ and b) cholesterol $C_v^{chol}(t)$
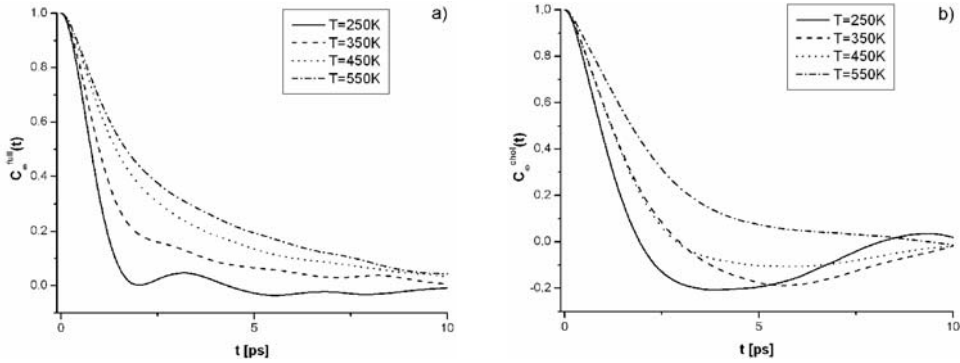
Fig. 6. The angular velocity autocorrelation function of: a) fullerne $C_\omega^{full}(t)$ and b) cholesterol $C_\omega^{chol}(t)$

shown in the $C_\omega^{full}(t)$ plot (Fig. 6a). The condensation phase with frozen translations and active rotations is called plastic, and so the existence of the plastic phase of fullerene core is reported. The plots of $C_v(t)$ and $C_\omega(t)$ for cholesterol at higher temperatures become gradually smoother which is typical of the liquid state.

4. Conclusions

It has been shown that in the $(C_{60})_9(chol)_{11}$ cluster the cholesterol molecules form a kind of layer surrounding the core of strongly bonded fullerenes. The plastic phase of the fullerene core has been detected. Both solid and liquid phases of the cholesterol layer exist. The mobility (translational diffusion coefficient) of cholesterol molecules in the liquid phase strongly increases as the temperature increases.

In this work, we have not attempted to analyse the computer experimental data obtained in terms of theoretical models, because the theoretical treatment of molecular dynamics in extremelly small clusters has not yet been developed. The same applies for comparison with 'real-life' experiments; to our knowledge, experimental data for the fullerene–cholesterol nanosystem are not available. The preliminary study reported here may provide a reference for future research into finite-size, fullerene–cholesterol clusters.

References

[1] DAWID A., GBURSKI Z., Phys. Rev. A, 68 (2003), 065202.

[2] FRENKEL D., SMIT B., *Understanding Molecular Simulation*, Academic Press, New York, 2002.

[3] VINCZE A., JEDLOVSZKY P., HORVAI G., Anal. Sciences, 17 (2001), 317.

[4] DAURA X., MARK A.E., VAN GUNSTEREN W.F., J. Comp. Chem., 19 (1998), 535.

[5] ALLEN M.P., TILDESLEY D.J., *Computer Simulation of Liquids*, Oxford University Press, 1989.

[6] RAPAPORT D.C., *The Art of Molecular Dynamics Simulation*, Cambridge University Press, Cambridge, 1995.

[7] GIRIFALCO L.A., J. Phys. Chem., 95 (1992), 5370.

[8] ABRAMO M.C., CACAMO C., J. Chem. Phys., 106 (1997), 6475.

[9] HANSEN J.P., MCDONALD I.R., *Theory of Simple Liquids*, Academic Press, London, 1986.

[10] DAWID A., GBURSKI Z., Phys. Rev. A, 56 (1997), 3294.

Depolarized light scattering from a thin fullerene layer confined between graphite planes Molecular dynamics study

MICHAŁ SKRZYPEK, PAWEŁ BROL, ZYGMUNT GBURSKI[*]

Institute of Physics, University of Silesia, Uniwersytecka 4, 40-007 Katowice, Poland

The dynamical properties of fullerene clusters, confined between graphite walls, have been investigated by molecular dynamics (MD) simulation. The fullerene molecules form two monolayers parallel to the graphite walls. The monolayers are quite stable, the migration of fullerene molecules between monolayers has not been observed. The polarizability anisotropy correlation function has been calculated for several separation distances d between the graphite walls. Both the solid and liquid phases of the confined fullerene layers have been detected, depending on the separation distance and the temperature.

Key words: *fullerene cluster; depolarized (Rayleigh) light scattering; interaction-induced spectra; molecular dynamics (MD) simulation.*

1. Introduction

Clusters provide a stage of aggregation from which the properties of condensed matter eventually emerge, which is of special interest in the study of the transition from the atomic scale to the bulk phase. Small clusters often display different chemical and physical properties when compared to both the atomic scale and the bulk samples. Rationalizing the evolution of these properties with the specific, many-body dynamics of atoms, or molecules, making up a cluster is a challenge to present-day condensed matter physicists. In recent years, considerable interest has been devoted to the study of confined fullerene, fullerene layers and carbon nanotube finite-size systems [1]. Closely connected with the many-body dynamics of the particles in a system is the phenomenon of depolarized (Rayleigh) light scattering [2–7]. Whether and how the peculiarities of molecular dynamics in the nanoscale confined fullerene layers influence the depolarized Rayleigh spectra is the subject of this computer simulation.

_____

[*] Corresponding author, e-mail: zgburski@us.edu.pl

2. Simulation details

The common potential proposed by Girifalco [8] to compute the interaction be-tween fullerene molecules was used. In this model, the molecule is treated as a perfect sphere, whose surface consists of a uniform density of carbon atoms. The C_{60} molecule is reduced to a material point with only three Cartesian coordinates. In this case, for a pair of C_{60} molecules i and j located at $\mathbf{r}_i$ and $\mathbf{r}_j$, the potential energy is:

$$u\left(r_{ij}\right) = -\alpha\left[\frac{1}{s\left(s-1\right)^3} + \frac{1}{s\left(s+1\right)^3} - \frac{2}{s^4}\right] + \beta\left[\frac{1}{s\left(s-1\right)^9} + \frac{1}{s\left(s+1\right)^9} - \frac{2}{s^{10}}\right] \quad (1)$$

where, $s = r_{ij}/(2a)$ and $a = 0.355$ nm is the fullerene radius. The values of the empiri-cal parameters α and β were obtained by Girifalco from the sublimation heat and the lattice constant of bulk fcc fullerite: $\alpha = 4.67735 \cdot 10^{-2}$ eV, $\beta = 8.48526 \cdot 10^{-5}$ eV [9]. Ruoff and Hickman's model [10] has been utilized to describe the C_{60}-*graphite* inter-action. As in the previous case the C_{60} molecule was replaced with a sphere, with the carbon atoms distributed uniformly on its surface, moreover the graphite has been modelled in a similar way, i.e. C atoms were uniformly distributed over the plane. The C_{60}-graphite plane binding energy is given by:

$$u\left(r\right) = -\alpha'\left[\frac{1}{\left(t-1\right)^3} - \frac{1}{\left(t+1\right)^3}\right] + \beta'\left[\frac{1}{\left(t-1\right)^9} - \frac{1}{\left(t+1\right)^9}\right] \quad (2)$$

where $t = r/a$, r is the distance between the centre of the C_{60} molecule and the graphite plane. Parameters α' and β' are 16α and 1024β, respectively. The molecular-dynamic (MD) simulation was carried out in the canonical ensemble using a velocity Verlet algorithm with the time step of 2 fs.

The depolarized light scattered by bulk monoatomic fluids has been studied for several decades [2]. The spectral line shape reflects the time dependence of the po-larizability anisotropy of colliding pairs of atoms. The major contribution to the ani-sotropy is described by the dipole-induced-dipole mechanism (DID) [3]. The DID interactions result from the fact that the incident light beam induces an oscillating dipole on the i-th particle and this dipole generates an oscillating local field at the j-th particle. The DID mechanism is a two-, three- and four-body correlation contributing to the intensity of scattered light.

The depolarized Rayleigh spectrum is the Fourier transform of the polarizability anisotropy autocorrelation function $G(t)$, which for a sample of N particles [3] is:

$$G(t) \propto \left\langle \sum_{i,j,k,l=1}^{N} \beta_{ij}\left(t\right)\beta_{kl}\left(0\right) \right\rangle \quad (3)$$

where i, j, k, l identify different particles. The pair anisotropy β_{ij} in the dipole-induced-dipole (DID) limit [11] is:

$$\beta_{ij} \propto \left[\frac{3 x_{ij}(t) z_{ij}(t)}{r_{ij}^5(t)} \right] \tag{4}$$

where x_{ij} and z_{ij} are the components of the separation vector $\mathbf{r}_{ij}$ between the i-th and j-th particle. The correlation function $G(t)$ can be decomposed into pair, triplet and quadruplet contributions as follows:

$$G(t) = G_2(t) + G_3(t) + G_4(t) \tag{5}$$

$$G_2(t) \propto \left\langle \sum_{i,j=1, i>j}^{N} \beta_{ij}(t) \beta_{ij}(0) \right\rangle \tag{6}$$

$$G_3(t) \propto \left\langle \sum_{\substack{i,j,k=1 \\ (i \neq j, k \neq i, j)}}^{N} \beta_{ij}(t) \beta_{ik}(0) \right\rangle \tag{7}$$

$$G_4(t) \propto \left\langle \sum_{\substack{i,j,k,l=1 \\ (i>j, k>l) \\ (i,j \neq k,l)}}^{N} \beta_{ij}(t) \beta_{kl}(0) \right\rangle \tag{8}$$

The first term $G_2(t)$ in Eq. (5) is responsible for depolarized light scattering in the low density limit (gas phase where $G(t) \cong G_2(t)$), while the other two can become important at high density. For the bulk samples at liquid densities, the positive two- and four-body contributions are almost exactly cancelled by the negative three-body term, and the total intensity is much smaller than any of the components.

3. Results

The computer experiment has been carried out for an ensemble of 19 fullerene molecules placed between two parallel graphite planes separated by the distance d. The normalized anisotropy correlation function $\hat{G}(t)$ simulated for three separation distances d = 18.4, 19.0 and 20.0 Å at the temperature of T = 550 K, is presented in Fig. 1 for the time up to 5 ns.

The plot of $\hat{G}(t)$ varies considerably with the change of d, the fastest decay of $\hat{G}(t)$ is observed for d = 18.4 Å, the slowest for d = 20.0 Å. It is known [7] that the
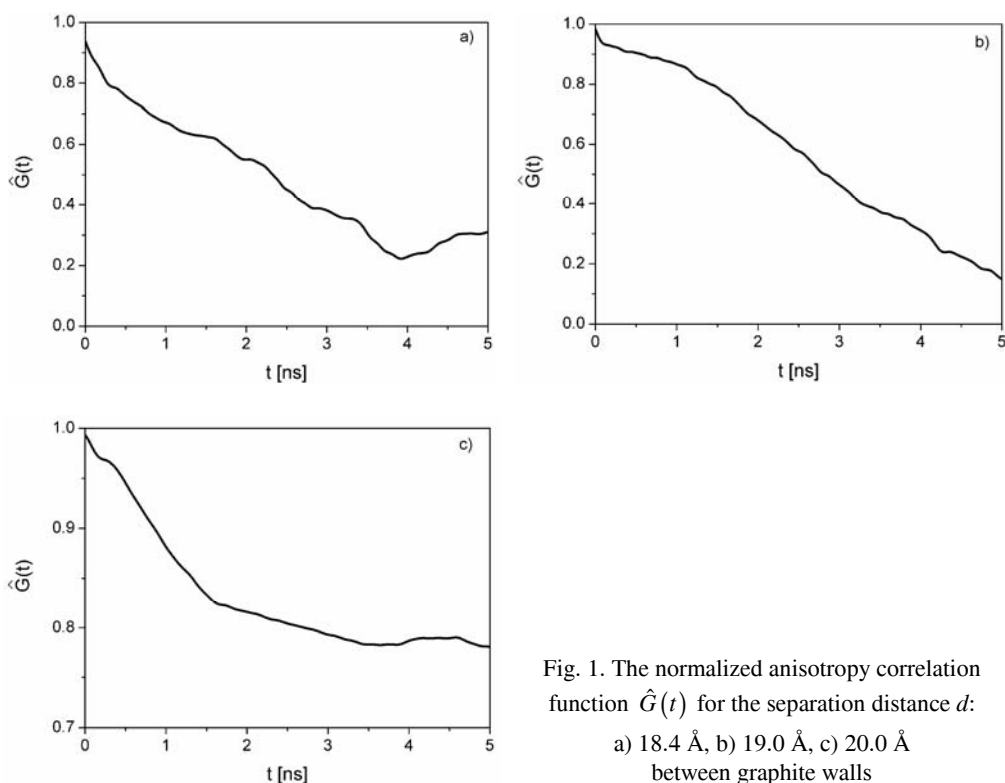
Fig. 1. The normalized anisotropy correlation function $\hat{G}(t)$ for the separation distance d:
a) 18.4 Å, b) 19.0 Å, c) 20.0 Å
between graphite walls

substantial differences between $\hat{G}(t)$ plots may be associated with the various phases of condensation of the small clusters (nanosytems). To see whether this has also happened in the nanosystem studied here, the mean square displacement $\left\langle \Delta \mathbf{r}^2 \left(t \right) \right\rangle = \left\langle \left| \mathbf{r}_j \left(t \right) - \mathbf{r}_j \left(0 \right) \right|^2 \right\rangle$ (Fig. 2) has been calculated, where $\mathbf{r}_j(t)$ is the position vector of the j-th molecule.
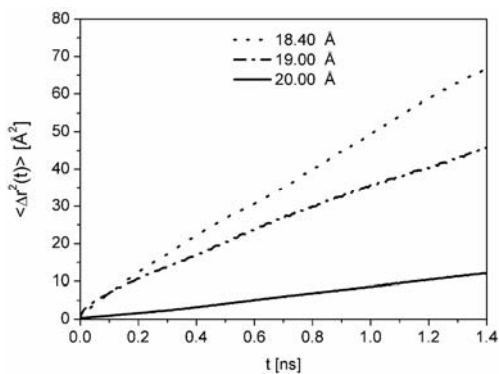
Fig. 2. The mean square displacement $\left\langle \Delta \mathbf{r}^2 \left(t \right) \right\rangle$ of a fullerene in $(C_{60})_{19}$ cluster placed between two parallel graphite planes, separated by the distance d

The $\left\langle \Delta \mathbf{r}^2 \left(t \right) \right\rangle$ is related to the translational diffusion coefficient D of a molecule via the Einstein relation [12] $\left\langle \Delta \mathbf{r}^2 \left(t \right) \right\rangle \approx 6 D t$, i.e. the slope of $\hat{G}(t)$ is proportional to D. The behaviour of $\left\langle \Delta \mathbf{r}^2 t \right\rangle$ is almost solid-like (very slow diffusion) for $d = 20$ Å and it becomes typical of the liquid phase when $d = 19.0$ and 18.4 Å. To explain this, it is necessary to take into account, that the minimum of the fullerene–graphite wall potential $V_{\text{full–wall}}$ is much deeper than the minimum of fullerene–fullerene potential $V_{\text{full–full}}$ [13, 14]. Therefore, for larger $d = 20.0$ Å the walls can "capture" fullerene molecules, thereby forming two monolayers, each located near its wall. The fullerenes trapped by the wall are less mobile, forming a solid-like layer. For smaller d the interplay between $V_{\text{full-wall}}$ and $V_{\text{full-full}}$ interaction potentials comes into play. As a result of the competition between $V_{\text{full-wall}}$ and $V_{\text{full-full}}$ the liquid like phase of the confined nanoensemble $(C_{60})_{19}$ occurs.

3. Conclusion

These computer experiments may contribute to future theoretical and "real-life" experimental studies of confined fullerenes. Particularly, it has been shown that the measurements of the interaction induced light scattering of fullerenes can be a sensitive indicator of the existing phases of condensation in the confined fullerene nano-systems.

References

[1] JENA P., TAO B.K., KHANNA S.H., *The Physics and Chemistry of Small Clusters*, Plenum Press, New York, 1987.

[2] MOUNTAIN R.D., BIRNBAUM G., J. Chem. Soc. Faraday Trans., 2 (1987), 1 and references therein.

[3] FROMMHOLD L., *Collision-Induced Absorption in Gases*, Cambridge University Press, Cambridge, 1994.

[4] DAWID A., GBURSKI Z., Phys. Rev. A, 56 (1997), 3294.

[5] DAWID A., GBURSKI Z., Phys. Rev. A, 58 (1998), 740.

[6] DAWID A., GBURSKI Z., J. Mol. Struct., 410 (1997), 507.

[7] DAWID A., GBURSKI Z., J. Mol. Struct., 482 (1999), 271.

[8] GIRIFALCO L.A., J. Phys. Chem., 96 (1992), 858.

[9] GARCIA-RODEJA C.R.J., GALLEGO L.J., Phys. Rev. B, 55 (1997), 7190.

[10] RUOFF R.S., HICKMAN A.P., J. Phys. Chem., 97 (1993), 2494.

[11] LAAD A., LITOVITZ T., MONTROSE C., J. Chem. Phys., 71 (1979), 4242.

[12] HANSEN J.P., MCDONALD I.R., *Theory of Simple Liquids*, Academic Press, London, 1986.

[13] SKRZYPEK M., GBURSKI Z., Europhys. Lett., 59 (2002), 305.

[14] SKRZYPEK M., DENDZIK Z., BROL P., GBURSKI Z., J. Mol. Struct., 704 (2004), 287.

Fullerene layers between graphite walls
A computer simulation

MICHAŁ SKRZYPEK[*], ZYGMUNT GBURSKI

Institute of Physics, University of Silesia, Uniwersytecka 4, 40-007, Katowice, Poland

The properties of ultra thin fullerene layers located between graphite planes have been studied using the molecular dynamics (MD) technique. In this arrangement, there is competition between the fullerene –fullerene and fullerene–graphite wall interaction potentials – both potentials being very strong. It appears that the confined fullerenes form two ultra thin layers, parallel to the graphite planes. The mean square displacement, velocity autocorrelation function and Lindemann index of fullerene molecule have been calculated for several temperatures and a range of distances between the graphite walls.

Key words: *fullerene; thin film; graphite wall; nanostructures; molecular dynamics (MD) simulation*

1. Introduction

Since the discovery of fullerene C_{60} [1], the studies of derived bulk materials have stimulated numerous experimental and theoretical works [2]. The investigations of finite size fullerene-based systems (clusters, ultra thin films, layers) are not so advanced [3–5], although their importance increases in the developing era of nanotechnology. Motivated by this importance, we present the computer simulation study of small fullerene cluster $(C_{60})_{19}$ located between two parallel graphite planes.

2. Simulation details

The computer experimentation has been carried out to compare the structural and dynamical properties of a fullerene cluster placed between two parallel graphite planes, separated by distances in the range of 1.8–2.1 nm.

The potential proposed by Girifalco [6] was used to compute interaction between molecules. In this model, the molecule is treated as a perfect sphere, whose surface consists of a uniform density of carbon atoms. The C_{60} molecule is reduced to a mate-

_____

[*] Corresponding author, e-mail: mskrzyp5@us.edu.pl

rial point with only three Cartesian coordinates. In this case for a pair of C_{60} mole-cules i and j located at r_i and r_j, the potential energy is:

$$u\left(r_{ij}\right) = -\alpha\left[\frac{1}{s(s-1)^3} + \frac{1}{s(s+1)^3} - \frac{2}{s^4}\right] + \beta\left[\frac{1}{s(s-1)^9} + \frac{1}{s(s+1)^9} - \frac{2}{s^{10}}\right] \quad (1)$$

where $s = r_{ij}/(2a)$ and $a = 0.355$ nm is the radius of a fullerene molecule. The values of empirical parameters α and β were obtained by Girifalco from the sublimation heat and the lattice constant of bulk fcc fullerite: $\alpha = 4.67735 \cdot 10^{-2}$ eV, $\beta = 8.48526 \cdot 10^{-5}$ eV [5]. The Ruoff and Hickman's model [7] has been used to describe the C_{60}–graphite interaction. As in the previous case, the C_{60} molecule was replaced with a sphere of carbon atoms distributed uniformly on its surface. The graphite was modelled in a similar way, i.e. C atoms were uniformly distributed over the plane. The C_{60}–graphite plane binding energy is given by:

$$u(r) = -\alpha'\left[\frac{1}{(t-1)^3} - \frac{1}{(t+1)^3}\right] + \beta'\left[\frac{1}{(t-1)^9} - \frac{1}{(t+1)^9}\right] \quad (2)$$

where $t = r/a$, r is the distance between the centre C_{60} of molecule and the graphite plane. Parameters α' and β' are 16α and 1024β, respectively. Note, that the Ruoff and Hickman potential is deeper than that of Girifalco, which is caused by a different number of interacting C atoms.

The molecular-dynamic (MD) simulation was carried out in the canonical ensem-ble using velocity Verlet algorithm with a time step of 2 fs, for the temperature range between 350 and 550 K. The initial positions of fullerene molecules were randomly generated, then the system was preliminary equilibrated by $5 \cdot 10^4$ time steps and af-terwards the proper calculations (production phase of simulation) was begun.

The dynamical properties of the cluster were studied using the velocity autocorre-lation function $C_{\mathbf{v}}(t) = \langle\mathbf{v}(t)\cdot\mathbf{v}(0)\rangle\big/\langle\mathbf{v}(0)\cdot\mathbf{v}(0)\rangle$ where $\mathbf{v}(t)$ is the velocity vector of the centre of mass of C_{60} molecule. Additionally, the mean squared displacement was determined(MSD) $\langle\Delta\mathbf{r}^2(t)\rangle = \langle|\mathbf{r}_j(t) - \mathbf{r}_j(0)|^2\rangle$, where $r_j(t)$ is the position vector of j-th molecule. The Lindemann index [8] was also computed, which is often used in cluster simulations to determine the phase transition in the clusters:

$$L_{\text{ind}} = \frac{2}{N(N-1)}\sum_{\substack{i=1\\j>1}}^{N}\frac{\sqrt{\langle r_{ij}^2\rangle - \langle r_{ij}\rangle^2}}{\langle r_{ij}\rangle} \quad (3)$$

where r_{ij} is the distance between the molecules. It is usually assumed that for $L_{\text{ind}} \approx 0.1$ the phase transition has occurred [9].

3. Results

The mean square displacement (MSD) of the centre of the mass of fullerene, calculated at the temperature of 550 K and for several separation distances $d = 1.87$, 1.9 and 2.1 nm, is shown in Fig. 1.

The slope of MSD for $d = 1.87$ and 1.9 nm is typical of the liquid phase [8], while for $d = 2.1$ nm its value is practically zero (a solid-like phase with no translational diffusion). This conclusion is supported by the plot of the calculated velocity autocorrelation function $C_v(t)$ (Fig. 2).
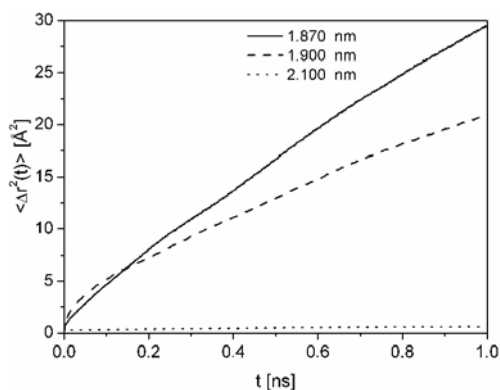
Fig. 1. The mean square displacement (MSD) of a fullerene molecule for separation distances between graphite walls: $d = 1.87$, 1.9 and 2.1 nm and temperature $T = 550$ K
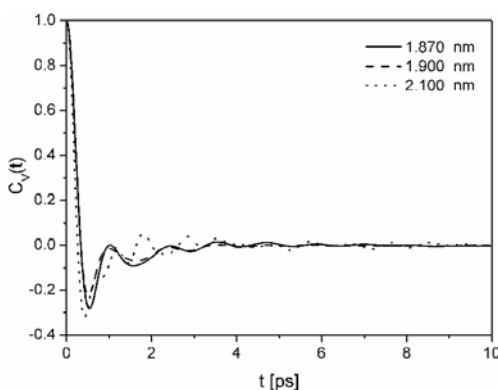
Fig. 2. The normalized velocity autocorrelation function $C_v(t)$ of a fullerene, for separation distances between graphite walls: $d = 1.87$, 1.9 and 2.1 nm and temperature $T = 550$ K

Here again, for $d = 2.1$ nm $C_v(t)$ exhibits several dumped oscillations, characteristic of the solid state [8]. For the separation distance $d = 1.87$ and 1.9 nm the plot of $C_v(t)$ becomes smoother and almost featureless (after the first dip) – the liquid phase behaviour. An example of the temperature dependence of MSD ($d = 1.9$ nm) is given in Fig. 3.

As expected, increasing the temperature leads to a steeper slope, i.e. a larger diffusion coefficient and stronger diffusion of fullerenes [10]. The existence of the different phases of condensation in small clusters can be detected by calculating the Lindemann index L. In Figure 4, L as a function of d, for several temperatures is plotted.

The jump of L arround $d \approx 1.9$ nm reflects the change of the condensation phase. Notice, that the solid-like behaviour of the $(C_{60})_{19}$ nanosystem confined between graphite walls separated by $d = 2.1$ nm is most likely the consequence of the stronger fullerene-graphite wall interaction, compared to the fullerene–fullerene one. Thus, for $d = 2.1$ nm the walls are able to capture the fullerene molecules "forever", forming two monolayers.
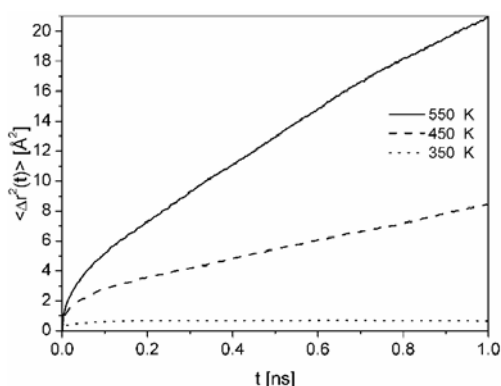
Fig. 3. The mean square displacement (MSD)
of a fullerene molecule, for separation distance
between graphite walls $d = 1.9$ nm and
temperatures: $T = 550$, 450 and 350 K
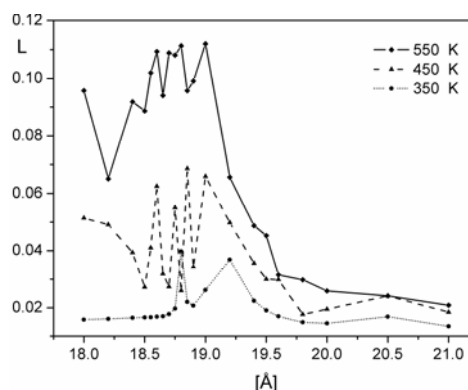
Fig. 4. The Lindemann index as a function
of separation distance between graphite walls d,
for temperatures: $T = 550$, 450 and 350 K

The most appealing aspect of the present study is the appearance of liquid phase of $(C_{60})_{19}$ nanosystem placed between graphite walls. As far as is known, *real life* experimental data of this kind are not yet available.

4. Conclusion

The computer experiment reported here may serve as a starting point for future experimental and theoretical studies of this interesting fullerene-based nanoscale system.

References

[1] Kroto H.W., Heath J.R., O'brien S.C., Curl R.F., Smalley R.E., Nature, 318 (1985), 162.

[2] Kuzmany H., Fink J., Mehring M., Roth S., Proceedings of the International Conference on Electronic Properties of Novel Materials, World Scientific, Singapore, 1998.

[3] Weaver J.H., Poirier D.M., [in:] Solid State Physics, H. Ehrenreich and F. Spacpen (Eds.), Academic Press, New York, 1994, Vol. 48, p. 1.

[4] Fujikawa Y., Sakurai M., Koma A., Jpn. J. Appl. Phys., 34 (1995), L188.

[5] Garcia-Rodeja C.R.J., Gallego L.J., Phys. Rev. B, 55 (1997), 7190.

[6] Girifalco L.A., J. Phys. Chem., 96 (1992), 858.

[7] Ruoff R.S., Hickman A.P., J. Phys. Chem., 97 (1993), 2494.

[8] Rapaport D.C., *The Art of Molecular Dynamics Simulation*, Cambridge University Press, UK, 1995, 85.

[9] Sugano S., *Microcluster Physics*, Springer-Verlag, Berlin, 1991.

[10] Skrzypek M., Dendzik Z., Brol P., Gburski Z., J. Mol. Struct., 704 (2004), 287.

Interaction-induced depolarized light scattering spectra of exohedral complexes of Ne and Ar with fullerenes and nanotubes

Z. Dendzik[*], M. Kośmider, A. Dawid, K. Kaczor, Z. Gburski

Institute of Physics, University of Silesia, Uniwersytecka 4, 40-007 Katowice, Poland

Recently, Dawid and Gburski (Phys. Rev. A, 68 (2003), 065202) have studied the molecular dynamics of a system consisting of a C_{60} molecule surrounded by a monolayer argon film and determined the interaction induced polarizability correlation function and the depolarized light scattering spectra of this system. In the present work a number of exohedral complexes of Ar and Ne forming an ultrathin monolayer film physisorbed on a fullerene or nanotube surface have been studied.

Key words: *nanotubes; fullerenes; adsorption; depolarized light scattering, molecular dynamics*

1. Introduction

Interaction induced depolarized light scattering spectra of monoatomic fluids has been studied both experimentally and by computer simulation for many years, as useful information concerning the dynamics of atoms can be provided [1–6]. Fullerenes and carbon nanotubes are of interest as gas adsorbents [7–13] because of their unique structural properties. Recently, Dawid and Gburski [1] have studied the interaction induced depolarized scattering in a system composed of a fullerene covered with an ultrathin spherical argon film using a rigid body model of the C_{60} molecule. In the present work a number of exohedral complexes composed of rare gas ultra-thin atomic films adsorbed on a fullerene or nanotube surface, were studied using more realistic modelling.

2. Simulation details

The intra-molecular interactions between the carbon atoms of the nanotubes and the fullerene have been modelled using the potential composed of the components

---

[*] Corresponding author, e-mail: dendzik@us.edu.pl

representing the energy of the bonded C atoms and the energy of the van der Waals interaction between the non-bonded C atoms [14, 15]

$$V = V_{\text{bond}} + V_{\text{vdW}} \tag{1}$$

The V_{bond} component is composed of terms representing the energies of the stretching (Morse), bending (harmonic cosine) and twisting (2-fold torsion angle) of the C–C bond

$$V_{\text{bond}}\,(r_{ij}\,,\Theta_{ijk}\,,\varphi_{ijkl}\,) = K_r\,(e^{-\gamma\,(r_{ij}-r_C\,)} - 1)^2 + \frac{1}{2}K_\Theta\,(\cos\Theta_{ijk} - \cos\Theta_C\,)^2$$
$$+ \frac{1}{2}K_\varphi\,(1 - \cos 2\varphi_{ijkl}\,)^2 \tag{2}$$

where r_{ij} is the distance between a given pair of bonded atoms, Θ_{ijk} is the bending angle between a given three atoms and φ_{ijkl} is the torsional angle between a given four atoms. The values of the K_r, K_Θ, K_φ, γ, r_C, Θ_C and φ_C parameters [3] are given in Table 1. The van der Waals interaction V_{vdV} between the non-bonded atoms is modelled as a pairwise additive Lennard–Jones (L–J) potential of the form

$$V_{\text{vdW}}\,(r_{ij}\,) = 4\varepsilon_{CC}\left[\left(\frac{\sigma_{CC}}{r_{ij}}\right)^{12} - \left(\frac{\sigma_{CC}}{r_{ij}}\right)^{6}\right] \tag{3}$$

over all pairs of atoms except 1–2 and 1–3 pairs. The values of the ε_{CC} and σ_{CC} parameters are given in Table 1.

Table 1. Parameters of the carbon interactions potentials

Parameter	Value	Parameter	Value
K_r	478.9 kJ/mol	Θ_C	120°
K_Θ	562.2 kJ/mol	γ	2.1867 Å^{-1}
K_φ	25.12 kJ/mol	ε_{C-C}	0.4396 kJ/mol
R_C	1.418 Å	σ_{C-C}	3.851 Å

The interactions between rare gas atoms have been modelled using the HFD–B potentials developed by Aziz and co-workers [16–18]

$$V\,(r_{ij}\,) = \varepsilon_a V^*\,(x_{ij}\,) \tag{4}$$

where

$$V^*\,(x_{ij}\,) = A^*\exp(-\alpha^* x_{ij} + \beta^* x_{ij}^{\;2}) - F(x_{ij})\sum_{j=0}^{2}\frac{c_{2\,j+6}}{x_{ij}^{\;2\,j+6}} \tag{5}$$

$$F(x_{ij}) = \begin{cases} \exp[-(D/x_{ij} - 1)^2], & x_{ij} < D \\ 1, & x_{ij} \geq D \end{cases} \tag{6}$$

$$x_{ij} = r_{ij} / r_m \tag{7}$$

The values of the parameters A^*, α^*, β^*, c_6, c_8, c_{10}, D, r_m, ε_a are given in Table 2.

Table 2. Parameters of the HFD–B Ar–Ne potential

Parameter	Value	
	Ne–Ne	Ar–Ar
A^*	895717.95	87393.3927
α^*	13.86434671	9.03228328
β^*	−0.12993822	−2.37132823
c_6	1.21317545	1.0948575
c_8	0.53222749	0.5917572
c_{10}	0.24570703	0.3450815
D	1.36	1.4
r_m	3.091 Å	3.759 Å
ε_a	0.35113975 kJ/mol	1.190334664 kJ/mol

The adsorption between the nanotube and rare gas film has been modelled atomically, using the potential developed by Carlos and Cole [19]

$$V(r_{ij}, \Theta_{ij-n}) = 4\varepsilon_{X-C} \left\{ \left(\sigma_{X-C}/r_{ij} \right)^{12} \left[1 + \gamma_R \left(1 - \frac{6}{5}\cos^2\Theta_{ij-n} \right) \right] \right.$$
$$\left. - \left(\sigma_{X-C}/r_{ij} \right)^6 \left[1 + \gamma_A \left(1 - \frac{3}{2}\cos^2\Theta_{ij-n} \right) \right] \right\} \tag{8}$$

where r_{ij} is the distance between *i*-th Ne and *j*-th C atoms, while Θ_{ij-n} is the angle between r_{ij} and the nanotube surface normal and *X* denotes Ne or Ar. In the case of the fullerene systems, the pairwise L–J potential has been employed as the adsorption potential. The values of the parameters ε_{X-C}, σ_{X-C}, γ_R, γ_A are given in Table 3.

Table 3. Parameters of the Ne–C and Ar–C adsorption potentials

Parameter	Value	Parameter	Value
ε_{Ne-C}	0.2786 kJ/mol	γ_A	0.40
σ_{Ne-C}	3.3 Å	ε_{Ar-C}	0.99768 kJ/mol
γ_R	−0.54	σ_{Ar-C}	3.4 Å

The depolarized light scattered by a monoatomic fluid provides information on the time characteristic of the polarizability anisotropy of colliding pairs of atoms. The major contribution to the anisotropy is described by the dipole-induced dipole (DID) mechanism [6]. The DID interaction results from the fact that the incident light beam induces an oscillating dipole on the i-th particle and this dipole generates an oscillating local field on the j-th particle. The DID mechanism is a two-body interaction which gives rise to the two-, three- and four-body correlations contributing to the intensity of the scattered light and can be described by the polarizability anisotropy correlation function

$$G(t) = G_2(t) + G_3(t) + G_4(t) \tag{9}$$

For a monoatomic sample of N atoms, pair, triplet and quadruplet contributions to $G(t)$ are calculated as

$$G_2(t) \propto \left\langle \sum_{i,j=1}^{N} \beta_{ij}(t) \beta_{ij}(0) \right\rangle \tag{10}$$

$$G_3(t) \propto \left\langle \sum_{i,j,k=1}^{N} \beta_{ij}(t) \beta_{ik}(0) \right\rangle \tag{11}$$

$$G_4(t) \propto \left\langle \sum_{i,j,k,l=1}^{N} \beta_{ij}(t) \beta_{kl}(0) \right\rangle \tag{12}$$

where i, j, k, l identify different atoms. The pair anisotrophy β_{ij} in the DID limit is [6]

$$\beta_{ij}(t) = \sigma^3 \frac{3 x_{ij}(t) z_{ij}(t)}{r_{ij}^5(t)} \tag{13}$$

where x_{ij} and z_{ij} are components of the separation vector between the i-th and j-th atom. The depolarized spectrum $I(\nu)$ is calculated as the cosine Fourier transform of the polarizability anisotropy autocorrelation function.

3. Results and discussion

A molecular dynamics study of the monolayer Ar and Ne atomic films adsorbed on the outer surface of the (5,5) single-walled carbon nanotube and the C_{60} fullerene molecule has been undertaken. The snapshots of the simulated systems are presented in Figs. 1–3.

In order to enable direct comparison between the dynamics of the rare gas films in different geometries, we have chosen the (5,5) armchair nanotube as a counterpart to
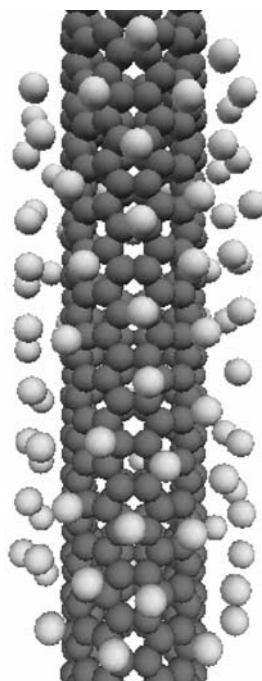
Fig. 1. Monolayer Ne atomic film covering (5,5) single-walled carbon nanotube
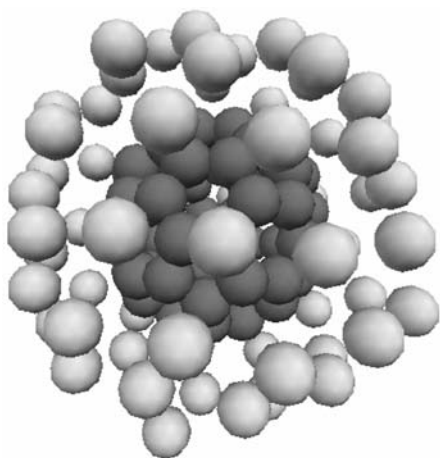
Fig. 2. Monolayer Ne atomic film (68 atoms) covering the fullerene C_{60} molecule
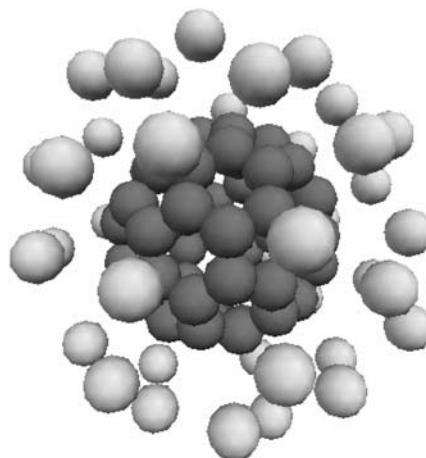
Fig. 3. Monolayer Ar atomic film (44 atoms) covering the fullerene C_{60} molecule

the fullerene systems, as its diameter is very close to the diameter of the fullerene. Liquid phases have been found in the case of the Ar and Ne films covering the C_{60} molecule and in the case of the Ne film covering the (5,5) nanotube. In the case of the Ar film covering the (5,5) nanotube no liquid phase was found and this system was excluded from further analysis. In the case of both fullerene systems, Ne and Ar film formed a complete monolayer covering the fullerene (44 Ar atoms or 68 Ne atoms). In

all cases studied, spectra have been determined for the highest temperature at which the film retains its liquid phase (35 K for the Ne–nanotube system, 20 K for the Ne–fullerene system and 50 K for the Ar–fullerene system).
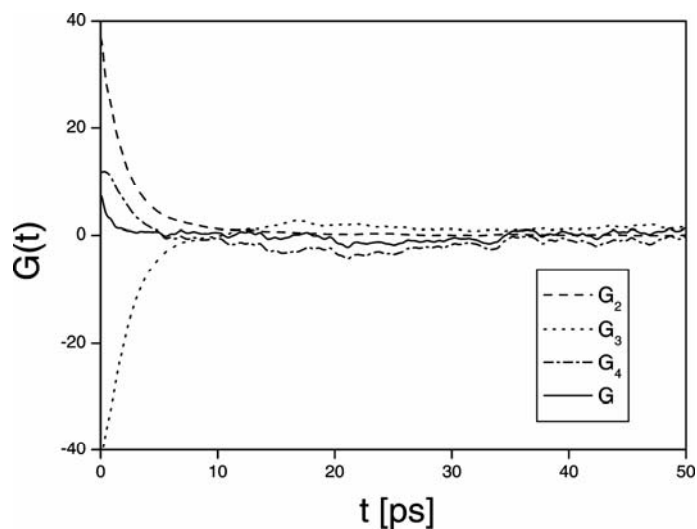
Fig. 4. The polarizability anisotropy correlation function $G(t)$ (solid line) along with its two- (dashed line), three- (dotted line) and four-particle (dash-dot line) components, of Ne film covering the (5,5) armchair nanotube at the temperature $T = 35$ K
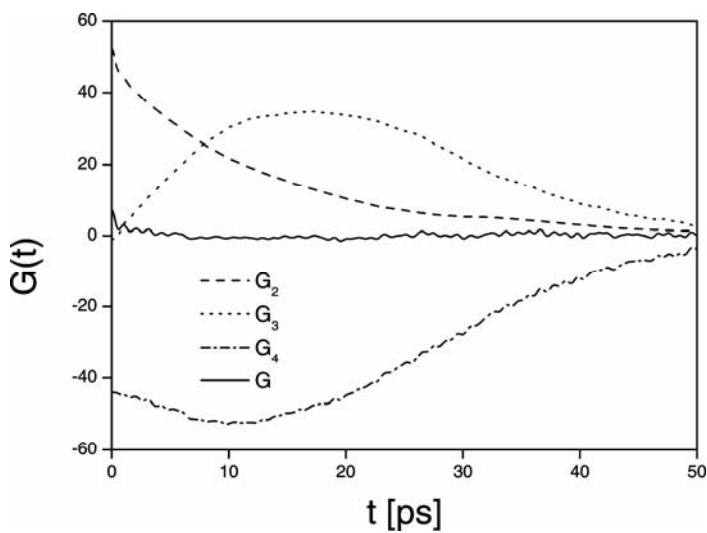
Fig. 5. The polarizability anisotropy correlation function $G(t)$ (solid line) along with its two- (dashed line), three- (dotted line) and four-particle (dash-dot line) components, of Ne film covering the fullerene C_{60} molecule $T = 20$ K

Figure 4 shows the polarizability anisotropy correlation function for the Ne film covering the (5,5) nanotube, along with the pair, triplet and quadruplet components of the correlation function. Analogous results for the case of the $(C_{60})Ne_{68}$ and $(C_{60})Ar_{44}$ systems are shown in Figs. 5 and 6.
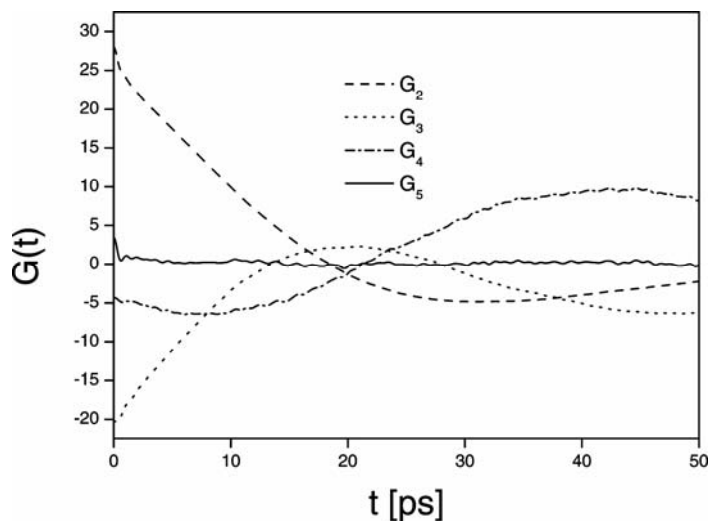
Fig. 6. The polarizability anisotropy correlation function $G(t)$ (solid line) along with its two- (dashed line), three- (dotted line) and four-particle (dash-dot line) components, of Ar film covering the fullerene C_{60} molecule $T = 50$ K
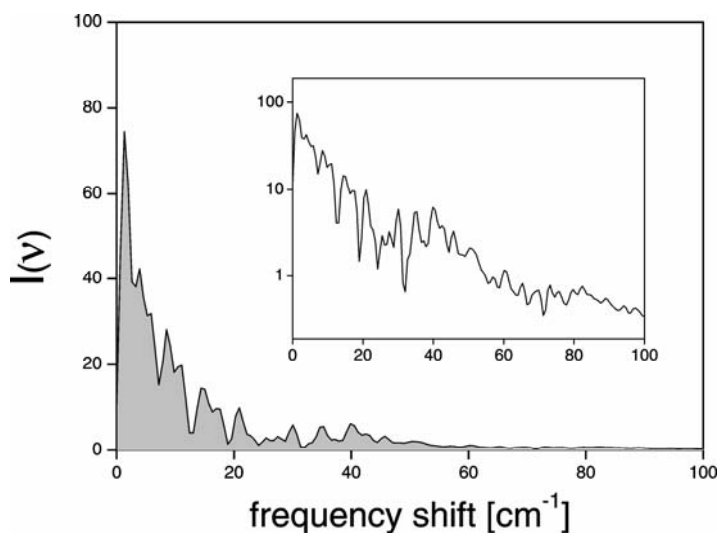
Fig. 7. The interaction induced depolarized scattering spectrum $I(\nu)$ of the Ne film covering the armchair (5,5) nanotube at the temperature $T = 35$ K. The inset shows the same in logarithmic plot

The interaction induced depolarized scattering spectra of all studied systems are shown in Figs. 7–9.
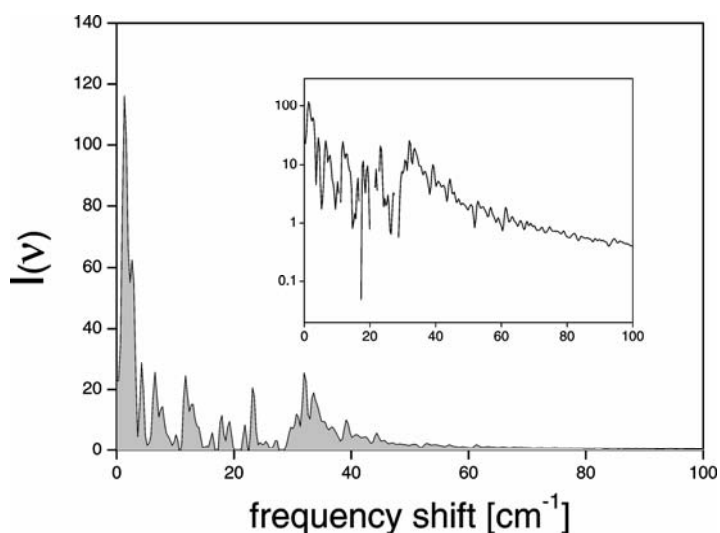
Fig. 8. The interaction induced depolarized scattering spectrum $I(\nu)$ of the Ne film covering the fullerene C_{60} molecule at the temperature $T = 20$ K. The inset shows the same in logarithmic plot
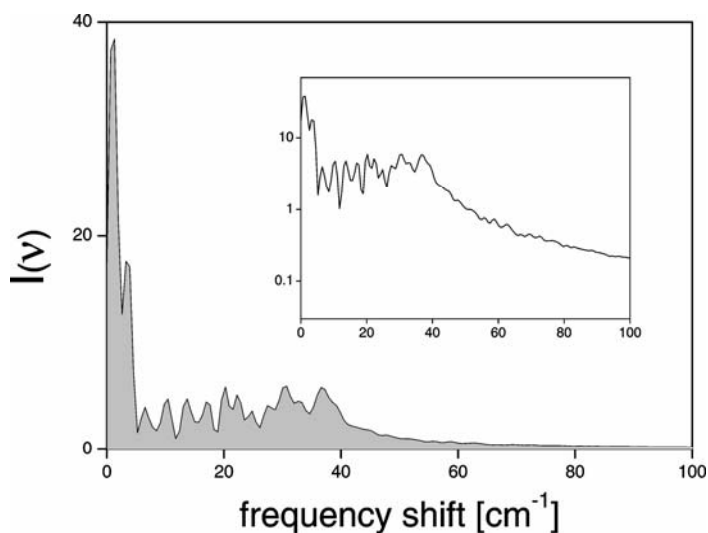
Fig. 9. The interaction induced depolarized scattering spectrum $I(\nu)$of the Ne film covering the fullerene C_{60} molecule at the temperature $T = 50$ K. The inset shows the same in logarithmic plot

It can be clearly discerned that the spectrum of the Ne film covering the (5,5) nanotube has almost exponential characteristic. The spectra of the Ne and Ar film covering the C_{60} molecule are considerably more complex. This may suggests that the

dynamics, in the case of the system covering the (5,5) nanotube, are more liquid-like than in the case of both fullerene systems, and that the adsorption potential between the rare gas atoms and the fullerene has more corrugated characteristic than in the case of the (5,5) nanotube system. Figure 10 shows the mean square displacement of the Ne and Ar atoms in the film covering the (5,5) nanotube and in the $(C_{60})Ne_{68}$ and $(C_{60})Ar_{44}$ systems, which agrees with the above findings and indicates the Ne film covering the (5,5) nanotube exhibit considerably higher diffusion coefficient than in the case of both fullerene based systems.
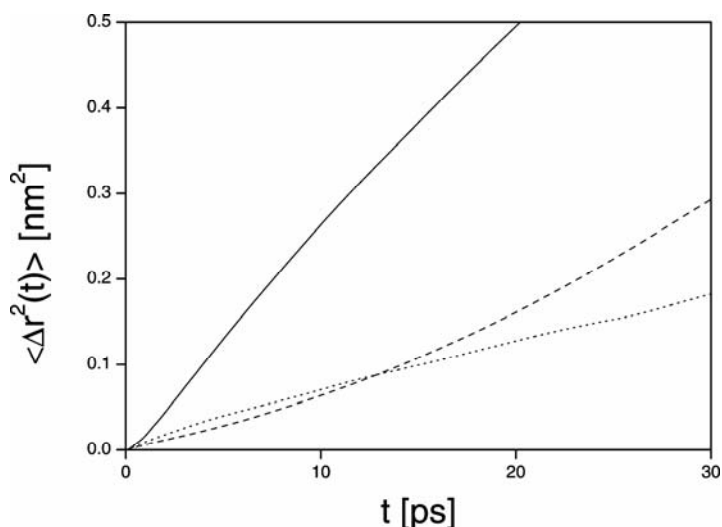
Fig. 10. The mean square displacement of Ne film covering the armchair (5,5) nanotube at the temperature $T = 35$ K (solid line), Ne film covering the fullerene C_{60} at the temperature $T = 20$ K (dashed line) and Ar film covering the fullerene C_{60} at the temperature $T = 35$ K (dashed line)

References

[1] DAWID A., GBURSKI Z., Phys. Rev. A, 68 (2003), 065202.
[2] LE DUFF Y., TEBOUL V., Phys. Lett. A, 157 (1991), 44.
[3] LADD A.J.C., LITOVITZ T.A., MONTROSE C.J., J. Chem. Phys., 71 (1979), 4242.
[4] DAWID A., GBURSKI Z., Phys. Rev. A, 56 (1997), 3294.
[5] MEUWLY M., DOLL J.D., Phys. Rev. A, 66 (2002), 023202-1.
[6] FROMMHOLD L., *Collision-Induced Absorption in Gases*, Cambridge University Press, Cambridge 1994.
[7] RUIZ A., HERNANDEZ-ROJAS J., BRETON J., GOMEZ LLORENTE J.M., J. Chem. Phys., 114 (2001) 5156.
[8] SIMONYAN V.V., JOHNSON J.K., J. Chem. Phys., 114 (2001), 4180.
[9] WEI SHI, JOHNSON J.K., Phys. Rev. Lett., 91 (2003), 015504-1.
[10] CVITAS M.T., SIBER A., Phys. Rev. B, 67 (2003), 193401.
[11] CALBI M.M., GATICA S.M., BOJAN M.J., COLE M.W., J. Chem. Phys., 115 (2001), 9975.
[12] GAO G., CAGIN T., GODDARD A., Phys. Rev. Lett., 80 (1998) 5556.
[13] ZHAO J., BULDUM A., HAN J., LU J.P., Nanotechnology, 13 (2002), 195.
[14] GUO Y., KARASAWA N., GODDARD W.A., Nature, 351 (1991), 464.

[15] WALTHER J.H., JAFFE R., HALICIOGLU T., KOUMOUTSAKOS P., J. Phys. Chem. B, 105 (2001), 9980.
[16] AZIZ R.A., SLAMAN M.J., Chem. Phys., 130 (1989), 187.
[17] BARROW D.A., AZIZ R.A., J. Chem. Phys., 89 (1988), 6189.
[18] AZIZ R.A., J. Chem. Phys., 99 (1993), 4518.
[19] CARLOS W.E., COLE M.W., Surf. Sci., 91 (1980), 339.

Dynamics of the exohedral complex composed of Ar atomic film adsorbed on the surface of single-walled carbon nanotube. Computer simulation study

Z. Dendzik[*], M. Kośmider, S. Pałucha, P. Brol, Z. Gburski

Institute of Physics, University of Silesia, Uniwersytecka 4, 40-007 Katowice, Poland

A molecular dynamics study of the monolayer Ar atomic film adsorbed on the outer surface of single-walled (10,10) carbon nanotube has been undertaken and the vibrational spectra of this system have been determined. It was found that vibrations of the atoms in the argon film considerably influence the low-frequency vibrational dynamics of the nanotube.

Key words: *adsorption; carbon nanotubes; molecular dynamics*

1. Introduction

Carbon nanotubes are of interest as gas adsorbents [1–7] because of their unique structural properties which make them prospective materials for many applications, including sensing, storing, purification and isotope separation of gases [8–11]. Studies of new carbon nanotube-based materials and devices require an understanding of the vibrational properties of nanotubes [12, 13] and the adsorbed atoms or molecules [14, 15].

In this work, a molecular dynamics simulation of the system composed of a monolayer of an Ar atomic film adsorbed on the outer surface of a single-walled (10,10) carbon nanotube has been carried out. This was performed in order to determine the vibrational properties of the system and to study the influence of the dynamics of the adsorbate Ar atoms on the low-frequency vibrational dynamics of the nanotube.

2. Simulation details

The intra-molecular interactions between the carbon atoms of the nanotubes and the fullerene has been modelled using the potential composed of the components rep-

---

[*] Corresponding author, e-mail: dendzik@us.edu.pl

resenting the energy of the bonded C atoms and the energy of the van der Waals inter-
action between the non-bonded C atoms [16, 17]

$$V = V_{\text{bond}} + V_{\text{vdW}} \tag{1}$$

The V_{bond} component is composed of terms representing the energies of the stretch-
ing (Morse), bending (harmonic cosine) and twisting (2-fold torsion angle) of the C–C
bond

$$V_{\text{bond}}\,(r_{ij}\,,\Theta_{ijk}\,,\varphi_{ijkl}\,) = K_r\,(e^{-\gamma\,(r_{ij}-r_C\,)} - 1)^2 + \frac{1}{2}K_{\Theta}\,(\cos\Theta_{ijk} - \cos\Theta_C\,)^2$$
$$+ \frac{1}{2}K_{\varphi}\,(1 - \cos 2\varphi_{ijkl}\,)^2 \tag{2}$$

where r_{ij} is the distance between a given pair of bonded atoms, Θ_{ijk} is the bending
angle between a given three atoms and φ_{ijkl} is the torsional angle between a given four
atoms. The values of K_r, K_{Θ}, K_{φ}, γ, r_C, Θ_C and φ_C parameters are given in Table 1.

Table 1. Parameters of the carbon interaction potentials

Parameter	Value	Parameter	Value
K_r	478.9 kJ/mol	Θ_C	120°
K_{Θ}	562.2 kJ/mol	γ	2.1867 Å^{-1}
K_{φ}	25.12 kJ/mol	$\varepsilon_{\text{C–C}}$	0.4396 kJ/mol
R_C	1.418 Å	$\sigma_{\text{C–C}}$	3.851 Å

The van der Waals interaction V_{vdW} between the non-bonded atoms is modelled as
a pairwise additive Lennard–Jones (L–J) potential of the form

$$V_{\text{vdW}}\,(r_{ij}\,) = 4\varepsilon_{CC}\left[\left(\frac{\sigma_{CC}}{r_{ij}}\right)^{12} - \left(\frac{\sigma_{CC}}{r_{ij}}\right)^{6}\right] \tag{3}$$

over all pairs of atoms except 1–2 and 1–3 pairs. The values of the ε_{CC} and σ_{CC} pa-
rameters are given in Table 1. The simulated nanotube consisted of 1600 C atoms.
Initial velocities of the carbon atoms were assigned according to the Maxwell distri-
bution, for the temperature of 15 K. The nanotube system was equilibrated for 200 ps.
The overall rotation and translation of the nanotube were continuously stopped. The
interactions between rare gas atoms have been modelled using the HFD-B potentials
developed by Aziz et al. [18–20]

$$V\,(r_{ij}\,) = \varepsilon_a V^*\,(x_{ij}\,) \tag{4}$$

where

$$V^*(x_{ij}) = A^* \exp(-\alpha^* x_{ij} + \beta^* x_{ij}^2) - F(x_{ij}) \sum_{j=0}^{2} \frac{c_{2j+6}}{x_{ij}^{2j+6}} \tag{5}$$

$$F(x_{ij}) = \begin{cases} \exp[-(D/x_{ij} - 1)^2], & x_{ij} < D \\ 1, & x_{ij} \geq D \end{cases} \tag{6}$$

$$x_{ij} = \frac{r_{ij}}{r_m} \tag{7}$$

The values of the parameters A^*, α^*, β^*, c_6, c_8, c_{10}, D, r_m, ε_a are presented in Table 2.

Table 2. Parameters of the HFD–B Ar–Ar potential

Parameter	Value
A^*	87393.3927
α^*	9.03228328
β^*	−2.371328328
c_6	1.0948575
c_8	0.5917572
c_{10}	0.3450815
D	1.4
r_m	3.759 Å
ε_a	1.190334664 kJ/mol

The simulated argon system was composed of 240 Ar atoms, forming a monolayer atomic film covering the nanotube. The temperature of the argon system was controlled by scaling the velocities. All calculations were performed for the temperature of 15 K.

The adsorption between the nanotube and rare gas film has been modelled atomically, using the potential developed by Carlos and Cole [21]

$$V(r_{ij}, \Theta_{ij-n}) = 4\varepsilon_{Ar-C} \left\{ (\sigma_{Ar-C}/r_{ij})^{12} \left[1 + \gamma_R \left(1 - \frac{6}{5}\cos^2 \Theta_{ij-n}\right)\right] \right.$$
$$\left. - (\sigma_{Ar-C}/r_{ij})^6 \left[1 + \gamma_A \left(1 - \frac{3}{2}\cos^2 \Theta_{ij-n}\right)\right] \right\} \tag{8}$$

where r_{ij} is the distance between i-th Ne and j-th C atoms, while Θ_{ij-n} is the angle between r_{ij} and the nanotube surface normal. The values of the parameters ε_{Ar-C}, σ_{Ar-C}, γ_R, and γ_A are given in Table 3.

Table 3. Parameters of the Ar–C adsorption potential

Parameter	Value
ε_{Ar-C}	0.99768 kJ/mol
σ_{Ar-C}	3.4 Å
γ_R	−0.54
γ_A	−0.40

The Newtonian equations of motion were integrated up to 250 ps (after equilibration) with the time step 0.2 fs.

3. Results and discussion

No liquid-like phase was found for the Ar layer adsorbed on the surface of the (10,10) nanotube studied. The argon cluster forming the monolayer atomic film adsorbed on the surface of the nanotube retains its solid-like phase at temperatures below 38 K. Above this temperature, the Ar atoms start evaporating. Figure 1 shows a snapshot of the simulated system. It can be seen that the argon atoms form chains oriented along the nanotube axis.
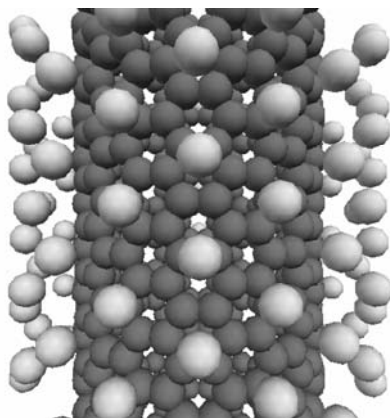
Fig. 1. Ar monolayer atomic film adsorbed on the outer surface
of the (10,10) armchair carbon nanotube

One of the standard methods for studying microscopic dynamics is the calculation of spectral densities from microscopic correlation functions. In this work, the dynamics of the system have been studied in terms of the spectral density

$$D(\omega) = \int\limits_0^\infty C_V(t)\cos(2\pi\omega t)\,dt$$

computed as the cosine Fourier transform of the atomic normalized velocity autocorrelation function

$$C_V(t) = \frac{<\mathbf{v}(t)\cdot\mathbf{v}(0)>}{<\mathbf{v}(0)\cdot\mathbf{v}(0)>}$$
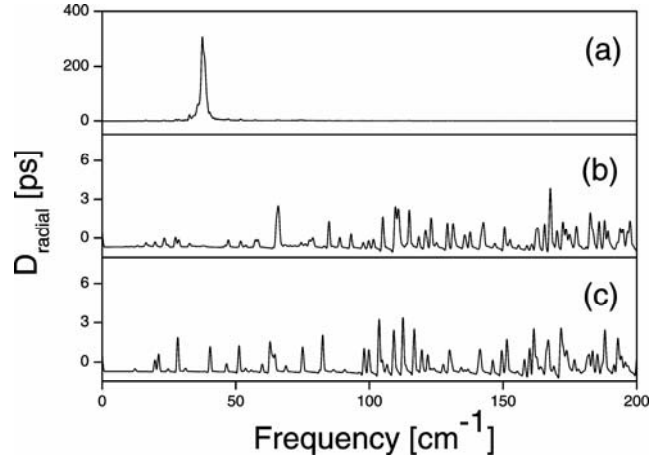
Fig. 2. The radial component of the vibrational spectrum $D_{radial}(\nu)$ of the Ar atoms (a)
and the low-frequency portion of the respective spectrum of the nanotube (b)
in the system composed of the Ar monolayer atomic film adsorbed on the surface
of the single-walled (10,10) carbon nanotube, compared to the low-frequency portion
of the vibrational spectrum of the (10,10) nanotube simulated without the adsorbed Ar layer (c)
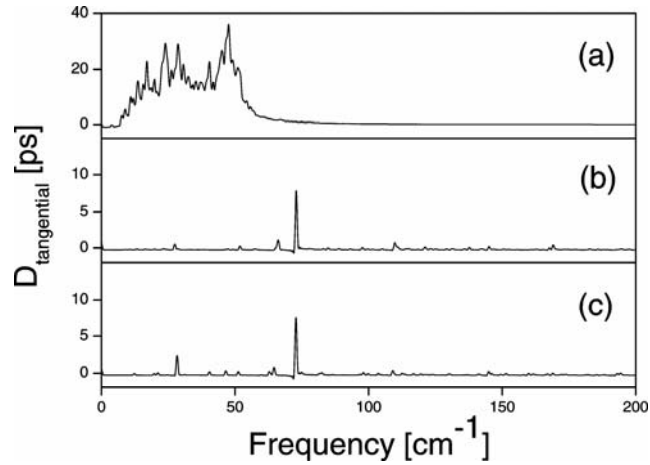
Fig. 3. The tangential component of the vibrational spectrum $D_{tangential}(\nu)$ of the Ar atoms (a)
and the low-frequency portion of the respective spectrum of the nanotube (b) in the system
composed of the Ar monolayer atomic film adsorbed on the surface of the single-walled
(10,10) carbon nanotube, compared to the low-frequency portion of the vibrational
spectrum of the (10,10) nanotube simulated without the adsorbed Ar layer (c)
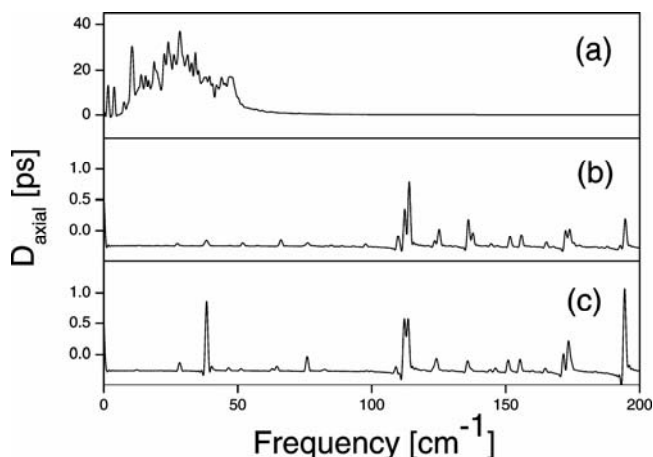
Fig. 4. The axial component of the vibrational spectrum $D_{axial}(\nu)$ of the Ar atoms (a) and the low-frequency portion of the respective spectrum of the nanotube (b) in the system composed of the Ar monolayer atomic film adsorbed on the surface of the single-walled (10,10) carbon nanotube, compared to the low-frequency portion of the vibrational spectrum of the (10,10) nanotube simulated without the adsorbed Ar layer (c).

which is usually employed in molecular dynamics simulations to study molecular or atomic vibrations and hindered translations. The radial $D_{radial}(\nu)$, tangential $D_{tangential}(\nu)$ and axial $D_{axial}(\nu)$ spectral densities are calculated from the respective velocity components: radial, tangential and axial (parallel) to the nanotube. Figures 2–4 show the radial, tangential and axial components of the vibrational spectra of the Ar film covering the nanotube and the low-frequency portion of the respective spectra of the nanotube.

To enable comparison between the dynamics of the nanotube covered with the adsorbed argon film, the spectra are accompanied by the low-frequency spectra calculated for the nanotube not covered with the argon layer (c). The vibrational spectrum of the argon monolayer adsorbed on the surface of the (10,10) nanotube shows the vibrations of the argon atoms at frequencies below 60 cm^{-1} and no vibrational modes at higher frequencies. Although the spectrum of the nanotube reveals the vibrational modes at frequencies up to about 1700 cm^{-1}, only its low-frequency portion, covering the frequency range comparable to that of the adsorbed argon layer, is presented in the figure. It can be observed that the vibrational modes of the nanotube at frequencies lower than 60 cm^{-1} are considerably influenced by the dynamics of the Ar atoms monolayer adsorbate. At higher frequencies, the constrained geometry imposed by the presence of the argon atoms in the vicinity of the nanotube have only a very slight influence on the internal dynamics of the nanotube.

References

[1] RUIZ A., HERNANDEZ-ROJAS J., BRETON J., GOMEZ LLORENTE J.M., J. Chem. Phys., 114 (2001), 5156.
[2] SIMONYAN V.V., JOHNSON J.K., J. Chem. Phys., 114 (2001), 4180.

[3] WEI SHI, JOHNSON J.K., Phys. Rev. Lett., 91 (2003), 015504-1.

[4] CALBI M.M., GATICA S.M., BOJAN M.J., COLE M.W., J. Chem. Phys., 115 (2001), 9975.

[5] GAO G., CAGIN T., GODDARD A., Phys. Rev. Lett., 80 (1998), 5556.

[6] ZHAO J., BULDUM A., HAN J., LU J.P., Nanotechnology, 13 (2002), 195.

[7] SIBER A., Phys. Rev. B, 68 (2003), 033406.

[8] KONG J., FRANKLIN N.R., ZHOU C., CHAPLINE M.G., PENG S., CHO K., DAI H., Science, 287 (2000), 622.

[9] DRESSELHAUS M.S., WILLIAMS K.A., EKLUND P.C., MRS Bull., 24 (1999), 45.

[10] DILLON A.C., HEBEN M.J., Appl. Phys. A: Mater. Sci. Process., 72 (2001), 133.

[11] WANG Q.Y., CHALLA S.R., SHOLL D.S., JOHNSON J.K., Phys. Rev. Lett., 82 (1999), 956.

[12] KAHN D., LU J.P., Phys. Rev. B, 60 (1999), 6535.

[13] SANCHEZ-PORTAL D., ARTACHO E., SOLER J.M., RUBIO A., ORDEJON P., Phys. Rev. B, 59 (1999), 12678.

[14] CVITAS M.T., SIBER A., Phys. Rev. B, 67 (2003), 193401.

[15] DENDZIK Z., KOSMIDER M., SKRZYPEK M., GBURSKI Z., J. Mol. Struct., in press.

[16] GUO Y., KARASAWA N., GODDARD W.A., Nature, 351 (1991), 464.

[17] WALTHER J.H., JAFFE R.., HALICIOGLU T.,, KOUMOUTSAKOS P., J. Phys. Chem. B, 105 (2001), 9980.

[18] AZIZ R.A., SLAMAN M.J., Chem. Phys. 130 (1989), 187.

[19] BARROW D.A., AZIZ R.A., J. Chem. Phys., 89 (1988), 6189.

[20] AZIZ R.A., J. Chem. Phys., 99 (1993), 4518.

[21] CARLOS W.E., COLE M.W., Surf. Sci., 91 (1980), 339.

Structural and dynamic properties of water confined inside a single-walled carbon nanotube Molecular dynamics study

MARCIN KOŚMIDER, MARIUSZ SOKÓŁ[*], ZBIGNIEW DENDZIK, ZYGMUNT GBURSKI

Institute of Physics, University of Silesia, Uniwersytecka 4, 40-007 Katowice, Poland

Atomically detailed molecular dynamics simulation has been performed to study structural and dynamical properties of the cluster of water molecules $(H_2O)_{80}$ confined inside an open-ended single-walled (10,10) carbon nanotube (SWNT). The structural and dynamical properties of the confined cluster have been compared with the analogous results for an unconfined cluster of water molecules.

Key words: *nanotube; water cluster; molecular dynamics; structural properties; dynamic properties*

1. Introduction

Since Ijima [1] discovered the nanotube, this new material has been studied intensively by many researchers, because of its unique mechanical and electrical properties and also because of its potential as a medium for storing hydrogen and other gases [2–5].

During the last decade, the structural and thermodynamic properties of atoms and molecules adsorbed in the interior end exterior of single nanotubes and nanotube bundles have been widely studied both theoretically [6–8] and experimentally [9–10]. The interior of a SWNT gives new possibilities for investigating the properties of confined fluids which are not seen in the bulk system [11–19]. The behaviour of confined water plays a crucial role in many relevant biological and geological systems. Molecular dynamics simulations [14] show that water confined in CNT formed a new ice phase, not seen in bulk ice. Hummer et al. [15] have observed, in their molecular simulation studies, pulse-like transmission of water through the nanotube. Recently, Kolesnikov et al. [16] have studied the water molecule confined inside an open-ended SWNT. They reported that water molecules form a cylindrical square ice-sheet with a central water chain.

This paper presents the results of fully atomistic molecular dynamics simulation of water deposited inside a (10,10), open-ended carbon nanotube at four different temperatures.

[*]Corresponding author, e-mail: msokol@us.edu.pl

2. Simulation details

The simulated system consists of 80 water molecules confined inside a (10,10) open-ended SWNT. The temperature was controlled by velocity scaling during the equilibration. The thermostat was turned off after the equilibration phase. The same procedure was applied to study a free cluster of water molecules, i.e without the nanotube. The classical equations of motion have been integrated using the velocity Verlet algorithm with the integration time step of 0.2 fs, which ensures sufficient energy conservation. Water molecules were described by the flexible SPC model [20]. This model is described by an intramolecular O–H harmonic stretching and a H–O–H bending term:

$$V\left(r_{ij},\Theta_{ijk}\right) = \frac{1}{2}K_{Wr}\left(r_{ij}-r_{W}\right)^2 + \frac{1}{2}K_{W\Theta}\left(\Theta_{ijk}-\Theta_{W}\right)^2 \tag{1}$$

where r_{ij} is the O–H distance and Θ_{ijk} is the H–O–H angle. The nonbonding interaction between water molecule consists of two terms: the Lennard–Jones potential between oxygen atoms:

$$V(r_{ij}) = 4\varepsilon\left(\frac{\sigma^{12}}{r_{ij}^{12}} - \frac{\sigma^6}{r_{ij}^6}\right) \tag{2}$$

where r_{ij} is the O–O distance, and the Coulomb potential:

$$V\left(r_{ij}\right) = \frac{1}{4\pi\varepsilon_o}\frac{q_i q_j}{r_{ij}} \tag{3}$$

where r_{ij} is the distance between all pair of charges. All constants are listed in Table 1. The intramolecular interactions between the carbon atoms of the nanotubes have been modelled using the potential composed of the components representing the energy of the bonded C atoms and the energy of the van der Waals interaction between the non-bonded C atoms [21, 22] $V = V_{\text{bond}} + V_{\text{vdW}}$. The V_{bond} component is composed of terms representing the energies of the stretching (Morse), bending (harmonic cosine) and twisting (2-fold torsion angle) of the C–C bond:

$$V_{\text{bond}}\left(r_{ij},\Theta_{ijk},\varphi_{ijkl}\right) = K_r\left(e^{-\gamma(r_{ij}-r_C)}-1\right)^2 + \frac{1}{2}K_{\Theta}\left(\cos\Theta_{ijk}-\cos\Theta_C\right)^2$$
$$+ \frac{1}{2}K_{\varphi}\left(1-\cos 2\varphi_{ijkl}\right)^2 \tag{4}$$

where r_{ij} is the distance between a given pair of bonded atoms, Θ_{ijk} is the bending angle between a given three atoms and φ_{ijkl} is the torsional angle between a given four atoms. The values of the K_{γ}, K_{Θ}, K_{φ}, γ, r_C, Θ_C and φ_C parameters [22] are collected in

Table 1. The Van der Waals interaction V_{vdW} between the non-bonded atoms is modelled as a pairwise additive Lennard–Jones (L–J) potential over all pairs of atoms except 1–2 and 1–3 pairs. The values of the ε_{CC} and σ_{CC} parameters are also given in Table 1.

Table 1. Parameters of the H_2O potential

Parameter	Value	Parameter	Value
$K_{W\gamma}$	4637 kJ/mol Å^{-2}	q_H	–0.41 e
$K_{W\Theta}$	382 kJ/mol rad^{-2}	K_γ	478.9 kJ/mol
r_W	1.0 Å	K_Θ	562.2 kJ/mol
Θ_W	109.47°	K_φ	25.12 kJ/mol
ε_{OO}	0.6502 kJ/mol	R_C	1.418 Å
σ_{OO}	3.166 Å	Θ_C	120°
σ_{OC}[a]	0.3126 kJ/mol	γ	2.1867 Å^{-1}
ε_{OC}	3.19 Å	ε_{CC}	0.4396 kJ/mol
q_O	–0.82 e	σ_{CC}	3.851 Å

[a]Ref. [23], and the carbon interactions potentials.

The nanotube–water interaction has been modelled using the L–J potential between oxygen atoms and host C atoms. The parameters for the oxygen–carbon interaction are listed in Table 1.

3. Results and discussion

The nanotube–water interaction in NVE ensemble has been studied. The modelled system was studied at three temperatures: $T_1 = 233$ K, $T_2 = 309$ K, and $T_3 = 344$ K. In all cases 80 water molecules were deposited inside (10,10) a SWNT. For comparison, the properties of the water cluster was studied at $T_1 = 233$ K, $T_2 = 309$ K because, in the case of $T_3 = 344$ K, the free cluster starts to evaporate. Figure 1 gives a snapshot of the simulated system.

The structure of water was analyzed in terms of the radial distribution function, which was computed for all three atomic pairs: oxygen–oxygen $g_{OO}(r)$, oxygen–hydrogen $g_{OH}(r)$, and hydrogen–hydrogen $g_{HH}(r)$. Figure 2a shows the radial distribution function of oxygen–oxygen in studied temperatures for confined water (solid line) and water cluster (dotted line). Figure 2b shows an analogous figure for the oxygen–hydrogen radial distribution function. Two characteristic maxima and one minimum can be discerned. In the case of $g_{HH}(r)$ (Fig. 2c) one characteristic maximum is observed for studied temperatures and small second maximum for $T_1 = 233$ K.

The calculated positions of peaks for all studied cases are listed in Table 2. The confinement of water inside nanotube does not significantly change the structure of water compared to free water cluster.
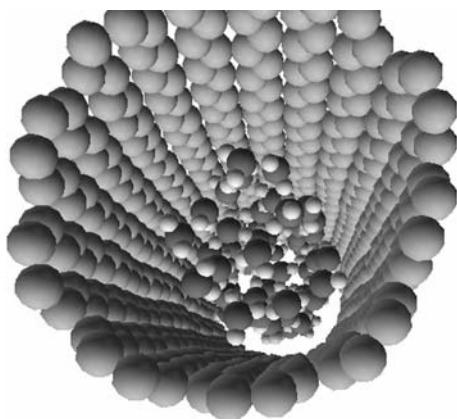
Fig. 1. A snapshot of water cluster deposited inside (10,10) SWNT at the temperature of 298 K
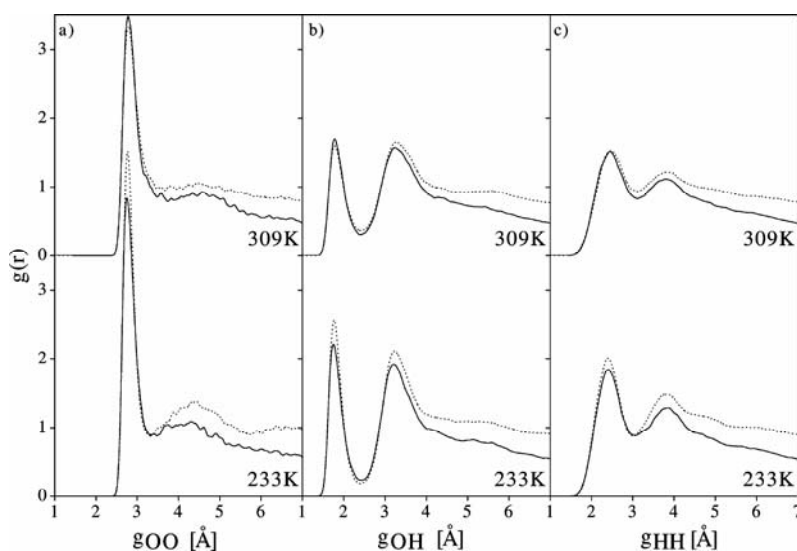
Fig. 2. The oxygen–oxygen (a), oxygen–hydrogen (b) and hydrogen–hydrogen (c) radial distribution functions of water deposited inside carbon nanotube (solid line), and not confined water cluster (dotted line), both at two different temperatures $T_1 = 233$ K and $T_2 = 309$ K

Table 2. The displacement of characteristic peaks in the oxygen–oxygen ($g_{OO}(r)$), oxygen–hydrogen ($g_{OH}(r)$) and hydrogen–hydrogen ($g_{HH}(r)$) radial distribution functions of water deposited inside carbon nanotube (SWNT) and not confined water cluster (H_2O)

SWNT	T [K]	R_1 [Å]	r_1 [Å]	R_2 [Å]	R_1 [Å]	r_1 [Å]	R_2 [Å]
$g_{OO}(r)$	233	2.78	–	–	2.78	3.32	4.39
	309	2.80	–	–	2.80	–	–
$g_{OH}(r)$	233	1.78	2.43	3.23	1.78	2.43	3.24
	309	1.80	2.46	3.28	1.80	2.45	3.28
$g_{HH}(r)$	233	2.41	3.03	3.82	2.41	3.03	3.82
	309	2.46	3.13	3.83	2.46	3.13	3.85
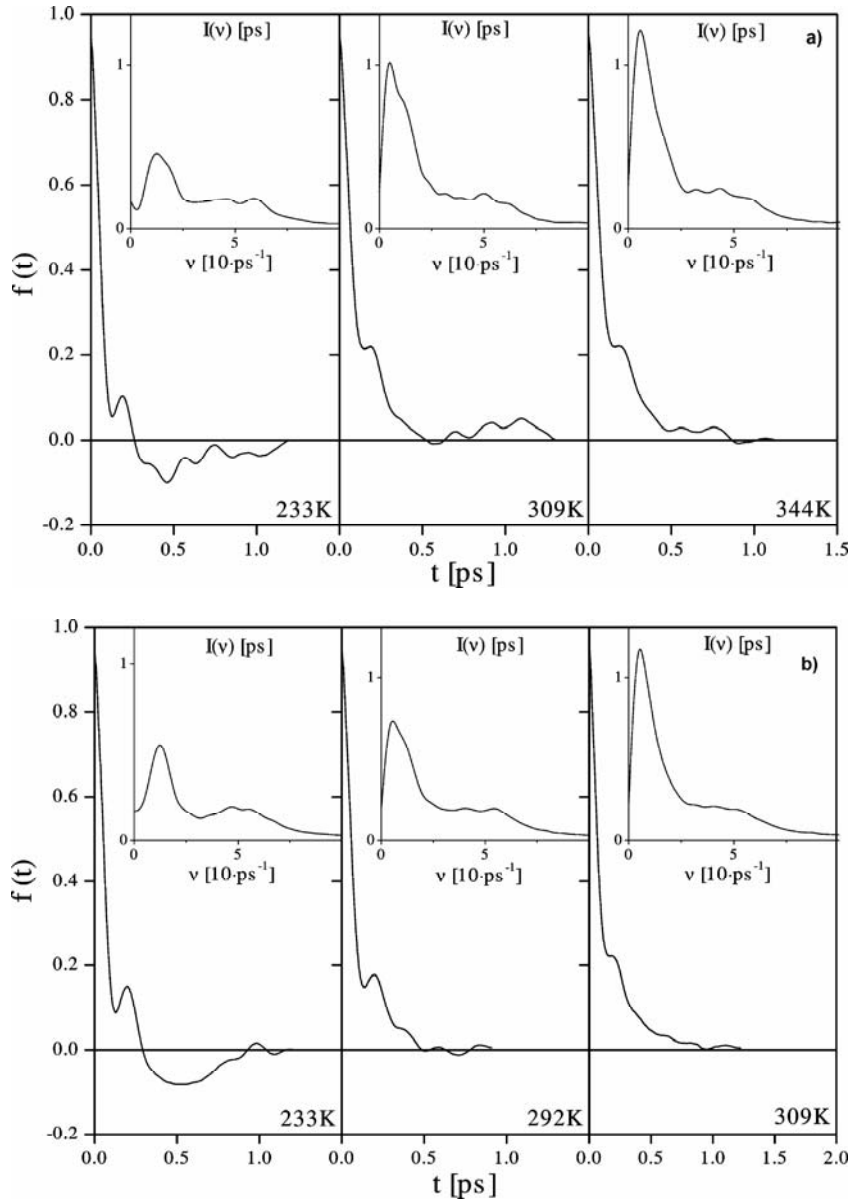
Fig. 3. The normalized centre-of-mass velocity autocorrelation function of water deposited inside carbon nanotube at three different temperatures $T_1 = 233$ K, $T_2 = 309$ K and $T_3 = 344$ K (a), and the normalized centre-of-mass velocity autocorrelation function of not confined water cluster at three different temperatures $T_1 = 233$ K, $T_2 = 292$ K and $T_3 = 309$ K (b)

In contrast to the structural properties, the dynamic properties of confined water significantly differ from those of the free water cluster. The dynamic properties have been studied in terms of the normalized velocity autocorrelation function $C_v(t)$

$$C_v(t) = \frac{\langle \mathbf{v}(0) \cdot \mathbf{v}(t) \rangle}{\langle \mathbf{v}(0) \cdot \mathbf{v}(0) \rangle} \tag{5}$$

and spectral density $I(v)$, computed as the cosine Fourier transform of C_v, which is related to the phonon density of states:

$$I(v) = \int_0^\infty C_v \cos(2\pi v t)\, dt \tag{6}$$

Figure 3a shows the normalized centre-of-mass velocity autocorrelation function for water confinement in SWNT for the considered temperatures. The insets show characteristic frequency of water molecule movements. The same functions are plotted in Fig. 3b for a free water cluster.

To gain deeper insight into the temperature dependencies of dynamic properties, a free water cluster at $T_2 = 292$ K was simulated. The spectral density shows that in the case of water deposited inside a SWNT, the second characteristic frequency strongly depends on temperature. The frequency shifts toward lower values as the temperature is increased. This behaviour is not observed in the case of a free water cluster where the second peak diminishes with increasing temperature. The diminishing of the second peak with increasing temperature in bulk water is also observed experimentally [24, 25].

The diffusion coefficient is also an indicator of differences between the translational mobility of confined water molecule and the free cluster water molecules. The diffusion coefficient has been calculated from the velocity autocorrelation function:

$$D \cong \frac{1}{3} \int_0^t \langle \mathbf{v}_j(0)\, \mathbf{v}_j(t') \rangle\, dt' \tag{7}$$

As anticipated, in all cases studied, it was observed that the diffusion coefficients were lower for the confined water. The calculated diffusion coefficients are given in Table 3.

Table 3. Self-diffusion coefficient D calculated from the present study for water deposited inside a carbon nanotube (SWNT), and not confined water cluster (H_2O) [24, 25]

T [K]	$D \cdot 10^5$ [cm^2/s]		
	SWNT	H_2O	Exper. (T [K])
233	0.77	1.06	0.74 (265)
292	–	3.18	1.80 (289)
309	4.08	5.13	2.90 (308)
344	5.23	–	4.80 (335)

4. Conclusions

In this work, a cluster of water molecules confined inside an open-ended carbon nanotube was studied focusing on the question, of how the geometrical confinement changes the structural and dynamic properties of water. It was observed that the water–nanotube interaction does not significantly change the structural properties of the confined water in contrast to the dynamic properties. In the case of water deposited inside a SWNT, the second frequency in the spectral density shifts considerably towards lower values with increasing temperature. This behaviour is not observed, either in the free water cluster or in bulk water. The determined diffusion coefficients also indicate that both interactions between water and a nanotube, as well as the geometrical confinement, significantly influence the dynamic properties of water.

References

[1] IJIMA S., Nature, 354 (1991), 56.

[2] SKOULIDAS A.I., ACKERMAN D.M, JOHNSON J.K., SHOLL D.S., Phys. Rev. Lett., 89 (2002), 185901-1.

[3] DILLON A.C., JONES K.M., BEKKEDAHL T.A., KIANG C.H., BETHUNE D.S., HEBEN M.J., Nature, 386 (1997), 377.

[4] LIU C., FAN Y.Y., LIU M., CONG H.T., CHENG H.M., DRESSELHAUS M.S., Science, 286 (1999), 1127.

[5] SHIRAISHI M., TAKENOBUA T., YAMADA A., ATA M., KATAURA H., Chem. Phys. Lett. 358 (2002), 213.

[6] ZHAO J., BULDUM A., HAN J., LU J.P., Nanotechnology, 13 (2002), 195.

[7] WEI SHI, JOHNSON J.K., Phys. Rev. Lett. 91 (2003), 015504.

[8] STAN G., et al., Phys. Rev. B, 62 (2000), 2173.

[9] FAN X., et al., Phys. Rev. Lett., 84 (2000), 4621.

[10] MENG-HUNG TSAI, HONG-MIN LIN, WEN-LI TSAI, YEUKUANG HWU, Rev. Adv. Mater. Sci., 5 (2003), 302.

[11] GELB L.D., GUBBINS K.E., RADHAKRISHNAN R., ŚLIWINSKA-BARTKOWIAK M., Rep. Prog. Phys., 62 (1999), 1573.

[12] GOGOTSI Y., LIBERA J.A., GUVENC-YAZICIOGLU A., MEGARIDIS C.M., App. Phys. Lett., 79 (2001), 1021.

[13] WAGHE APARNA, JAYENDRAN C.R., HUMMER G., J. Chem. Phys., 117 (2002), 10789.

[14] KOGA K., GAO G.T., TANAKA H., ZENG X.C., Nature, 412 (2001), 802.

[15] HUMMER G., RASAIAH J.C., NOWORYTA J.P., Nature, 414 (2001), 188.

[16] KOLESNIKOV A.I., ZANOTTI J.M., LOONG C.K., THIYAGARAJAN P., MORAVSKY A.P., LOUFTY R.O., BURNHAM C.J., Phys. Rev. Lett., 93 (2004), 035503.

[17] GORDILLO M.C., MARTI J., Chem. Phys. Lett., 329 (2000), 341.

[18] BEREZHKOVSKII A., HUMMER G., Pys. Rev. Lett., 89 (2002), 064503.

[19] ALLEN R., MELCHIONA S., HANSEN J.P., Phys. Rev. Lett., 89 (2002), 175502.

[20] TELEMAN O., JONSSON B., ENGSTROM S., Mol. Phys., 60(1) (1987), 193.

[21] GUO Y., KARASAWA N., GODDARD W.A., Nature, 351 (1991), 464.

[22] WALTHER J.H., JAFFE R., HALICIOGLU T., KOUMATSAKOS P., J. Phys. Chem. B, 105 (2001), 980.

[23] BOJAN M.J., STEEL W.A., Langmuir, 3(6) (1987), 1123.

[24] STILLINGER F.H., RAHMAN A., J. Chem. Phys., 60 (1974), 1545.

[25] STILLINGER F.H., RAHMAN A., J. Chem. Phys., 55 (1971) 3337.

Simulations of molecular dynamics of cyanoadamantane multilayers between graphite substrates

P. Brol[*], S. Pałucha, M. Skrzypek, Z. Gburski

Institute of Physics, University of Silesia, Uniwersytecka 4, 40-007, Katowice, Poland

Constant temperature molecular dynamic (MD) simulations have been carried out to investigate structural and dynamical properties of the multilayer of cyanoadamantanes ($C_{10}H_{15}CN$) located between the graphite substrates. The velocity autocorrelation function and the second range order parameter, for several numbers of layers and temperatures ranging from 100 to 900 K have been calculated. As the number of cyanoadamantane layers increases, the chain structure of cyanoadamantanes is gradually shown up – the consequence of increasing importance of Coulomb interaction of dipolar cyanoadamantane molecules confined between graphite planes.

Key words: *cyanoadamantane; graphite walls; molecular dynamics; order parameter; simulations; velocity autocorrelation function*

1. Introduction

MD computer simulation techniques have been widely used to study the behaviour of a small quasi two-dimensional molecular system. Knowledge of the structure and dynamics of molecules near the surface is important in the context of assembly, catalysis, lubrication, molecular electronics, thin films and microfluids. Recently, much attention has been focused on the problem of adsorption of gases on planar surfaces such as graphitic material [1–4]. There are several encouraging aspects of this work. Firstly, graphitic materials provide particularly strong attraction compared to other adsorbents [5]. Secondly, corrugated surfaces provide a relatively attractive binding environment which possess the ability to model complex phases, such as plastic molecular solids, in a two-dimensional (2D) system [6]. It would be of interest to study such processes with large molecule as an adsorbate, possibly having a strong dipole moment which can reveal more clearly the process of forming such exciting phases. The molecule which possesses this feature and is currently the subject of much re-

---

[*]Corresponding author, e-mail: brolik@ratnet.pl

search is cyanoadamantane $C_{10}H_{15}CN$ (CNadm). The cyano group (CN) is responsible for the high dipole moment ($\mu = -3.92$ D), which causes that whole CNadm group to create interesting phases, including the plastic phase [7]. With the onset of cooling, a CNadm sample begins to evolve from the fluid phase, which is mainly characterized by translational motion, through the plastic, glassy and solid states. The plastic phase, which is also called the rotatory phase (translations frozen, rotations released), appears between the melting point at $T_m \approx 445$ K and $T_t \approx 238$ K [8,9]. This phase is characterized by the dynamic orientational disorder of molecules and translational order of molecular centres of mass ($Fm3m$ crystalline structure).

In this work, the diffusive motions in multilayer (1–3 near each plane) cyanoadamantane, using molecular dynamics simulations, were studied and how these motions are reflected in the plots of the appropriate correlation functions was explored.

2. Simulation procedure

Modelling of real CNadm molecules is very complex, and simulation, which takes into account detailed molecular structure, is very time consuming. Therefore, the real cyanoadamantane molecule has been simplified by using a three-site model of cyanoadamantane as proposed and previously used by Cathiaux et al. [2] in their study of pure cyanoadamantane. In the diagram below we present the model of the CNadm molecule.
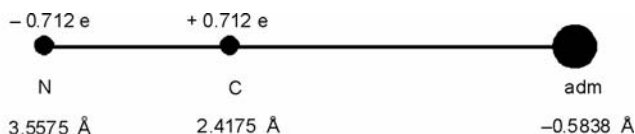
The cyanoadamantane molecule is represented by a rigid, three-site model, instead of the full model with 27 atoms. From the left, the first and second sites correspond to the nitrogen and carbon atoms, respectively, and the third corresponds to the whole adamantane group (supersite or pseudoatom). The interactions between the site atoms and the supersite (adm) have been modelled by Cathiaux et al. [2] in terms of the Lennard-Jones (LJ) potential shown in Equation 1.

$$V_{ij} = 4\varepsilon_{ij}\left[\left(\frac{\sigma_{ij}}{r_{ij}}\right)^m - \left(\frac{\sigma_{ij}}{r_{ij}}\right)^n\right] \qquad (1)$$

where r_{ij} is the distance between the i-th and j-th interacting sites of different molecules, ε_{ij} and σ_{ij} are the corresponding L–J parameters. The usual values for m and n are 12 and 6, respectively, except for the interaction between the supersites which are represented by special values of exponents m and n, 16 and 10, respectively, as deter-

mined by Cathiaux et al. [2]. The values of the interaction energy parameter $\varepsilon_{adm-adm}$ and their minimum distance $\sigma_{adm-adm}$, taken from [2], are given in Table 1.

Table 1. Simulation parameters

ij	ε_{ij} [kJ/mol]	σ_{ij} [Å]
N-N	0.7099	3.25
C-C	0.3089	3.55
N-C	0.4683	3.40
N-adm	2.4290	4.70
C-adm	1.6020	4.90
adm-adm	8.3110	6.30

The interaction between the cyanoadamantane molecule and basal planes of graphite was calculated using a semi-empirical potential approach, where graphite was treated as a static surface providing the external holding potential for the molecules [1].

The CNadm possess a nonzero dipole moment along the cyano group axis with the value $\mu = -3.92D$. Two charges with the value $0.712e$, negative on the nitrogen atom and positive on the carbon atom, were added. In addition, the momentum of inertia of the cyanoadamantane molecule was taken as $I_{xx} = I_{yy} = 580$ au Å^2.

The above models were used to carry out a series of constant temperature ensemble simulations with slab periodic boundary condition along the graphite wall. This means that the system was periodic in the x and y directions, but not in the z direction. That type of boundary condition is particularly useful for simulating surfaces.

The effects of the long-range electrostatic contribution to the intermolecular potential was taken into account using the Hautman–Klein–Ewald method [11], instead of the standard Ewald summation, because of the 2D boundary condition. A series of MD simulations with 64, 128, and 192 molecules of CNadm at several temperatures ranging from 100 to 900 K were carried out. The number of particles were 2496 (2304 graphite C + 64 three site CNadm) for the smallest system up to 2880 (2304 graphite C + 192 three site CNadm) for the largest. The 2304 carbon atoms possess two basal graphite surfaces situated parallel to the *XY* plane of the simulation box. The surface edges lengths were $x = 39.392$ Å and $y = 38.358$ Å, respectively. The CNadm molecules were placed between them, with separation distances of z from 30 Å to 70Å. Each plane was treated as a static surface and models the crystal structure of graphite (Fig. 1).

Two distinct planes of carbon hexagons are stacked with *P63/mmc* symmetry. This structure was described in an earlier work [12]. In Figure 2a one can see a single graphite plane. It is interesting to note that the nearest neighbour spacing in the carbon nanotube is essentially the same as the inter-planar spacing of the graphite (~3.4 Å).

The time step in the simulation was 1 fs, which guarantees fluctuation of the potential energy below ~0.2%. The equilibration runs were about 5×10^5 time steps. The time for evaluating correlation functions was 50 ps after the period of 20 ps required for stabilization of the chosen temperature.
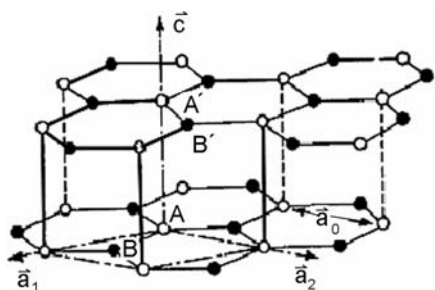
Fig. 1. Structure of graphite planes

3. Results

The cross section of three simulated systems are shown in Fig. 2.
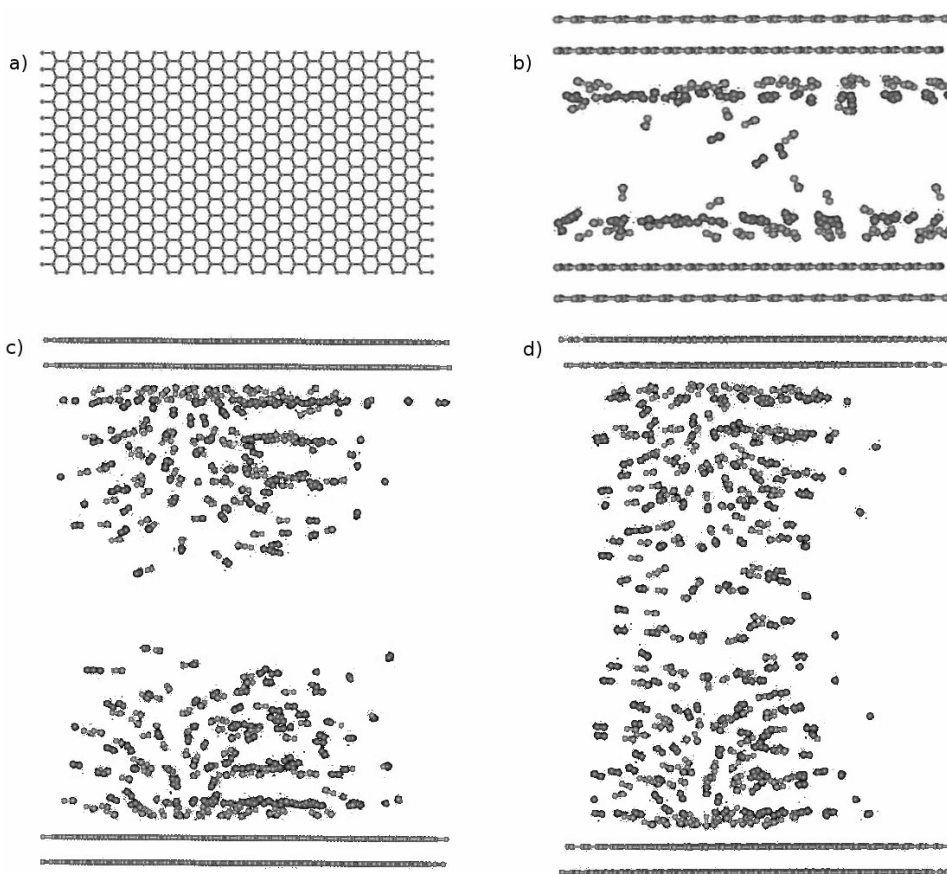
Fig. 2. Sample snapshot of the studied system: a) the structure of a single graphitic layer, b–d) the cross sections of investigated systems with 64, 128 and 192 CNAdm molecules, respectively; black balls – the centre of mass of adamantane group, gray – nitrogen, light gray (same as wall colour) – carbon

One can see in the system with 64 (b), 128 (c) and 192 (d) of CNadm molecules (from one to three layers of CNadm between graphite planes). In the case of two and more layers the formation of chains composed of CNadm molecules is clearly observed (see. Fig. 2c, d). In this situation, the second range order parameter P_2 [10] which indicates the degree of orientational order of a system could be most informative.

In Figure 3, the second-rank-order parameter P_2 calculated for (a) single- and (b) two-layer CNadm systems is presented.
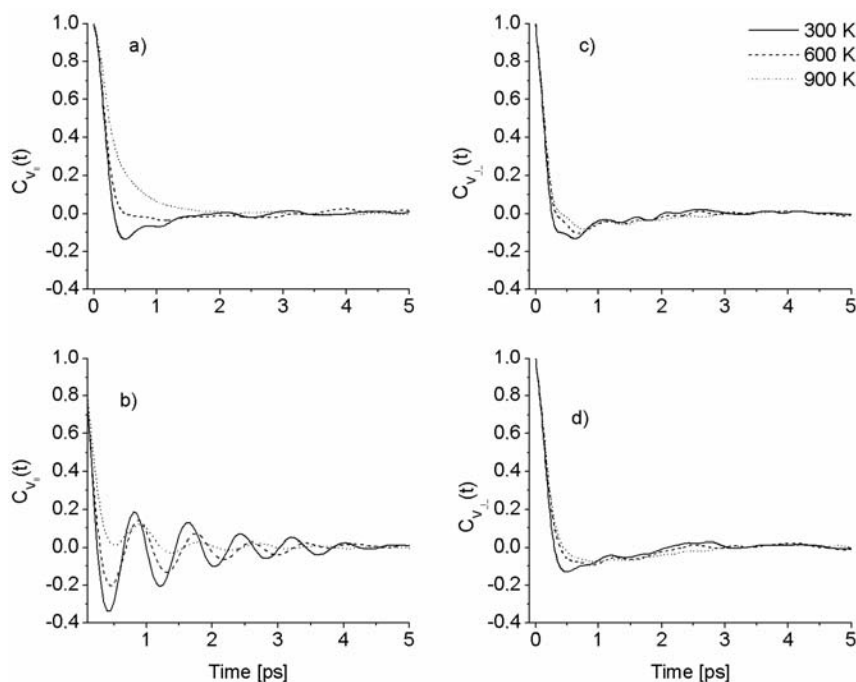
Fig. 3. The velocity autocorrelation functions $C_V(t)$ parallel (a, c) and perpendicular (b, d) to graphite planes calculated in single (b, d) and multilayer (a, b) systems

This parameter P_2 is the largest eigenvalue of the ordering matrix with the elements given by [13]

$$Q_{ij} = \frac{\left\langle 3\cos\theta_i \cos\theta_j - \delta_{ij} \right\rangle}{2} \qquad (2)$$

where $i,j = x, y, z$ are indices referring to the laboratory frame. The brackets <> represent a thermal averaging (over the whole sample and simulation time), θ is the angle between the molecular long axis and the eigenvector of the order tensor Q corresponding to the maximum eigenvalue.

The P_2 parameter was calculated for two cases, namely, parallel and perpendicular to the graphite surfaces. Figure 3 shows that the parallel order parameters are not influenced by increasing temperature, for both one and two layers. However, the distinction between the P_2 value calculated in the parallel and perpendicular direction is clearly seen. In the case of one layer $P_{2(\parallel)}$ has a large value of ~0.7, whereas, in the two-layer system these values are reduced to ~0.25. This was interpreted that in the one-layer system, CNadm molecules are strongly constrained by the appearance of the graphite plane. Moreover, when the second layer was added, molecules which belong to this layer are not strongly influenced by the graphite planes and this causes a reduction of the order parameter in the plane direction. It is interesting that this reduction of the P_2 parameter is not observed in the perpendicular direction. In both cases the values are similar and equal to ~0.5 for all temperatures studied. The explanation is obvious when one remembers the snapshot (see Figs. 2c, d) with the chains composed of CNadm molecules. As a result of the corrugated graphite surface, the interaction potential possesses holes and the cyanoadamantane molecules aggregate around them. After that, in the neighbourhood of CNadm trapped by a hole (in the case of two and more layers), the chain structure of cyanoadamantanes develops because of the strong dipole–dipole interaction of CNadm molecules

Information about the microscopic dynamic is usually provided in MD simulations by means of the velocity autocorrelation function (VAF) $C(t)$ which is calculated from the following expression:

$$C_v\left(t\right) = \frac{\left\langle v(t)\,v(0)\right\rangle}{\left\langle v^2\left(0\right)\right\rangle} \tag{3}$$

where $v(t)$ is the velocity of the centre of mass of the molecule. Depending on the component of the velocity chosen correlations for the parallel, or perpendicular direction ($\parallel$ or $\perp$) could be obtained. As an example, in Fig. 4 the adamantane VAFs calculated for xy and z components of velocity ($\parallel$ and $\perp$) at three temperatures $T = 300$, 600, 900 K are shown.

In Figure 4a, b, the previously mentioned function obtained from simulations with one CNadm layer is given. The distinction between two parallel and perpendicular motions is clear. Planar motions (see Fig. 4a) are similar to fluid at low temperature $T = 300$ K and gaseous at $T = 900$ K. Perpendicular movements, however, are strongly constrained by the graphite planes. As a result of the caging effect, the correlation function falls to a negative value and exhibits dumped oscillations descending to zero value after a long time. Moreover this process is reduced by higher temperatures. When comparing these pictures, with those obtained from two CNadm layers adsorbed on graphite planes, the difference is clearly seen in VAFs for perpendicular velocity component. These functions (see Fig. 4 c, d) are similar to AVFs obtained from fluid like systems as the CNadm molecules can diffuse, not only in the xy plane, but also between the layers in the z direction.
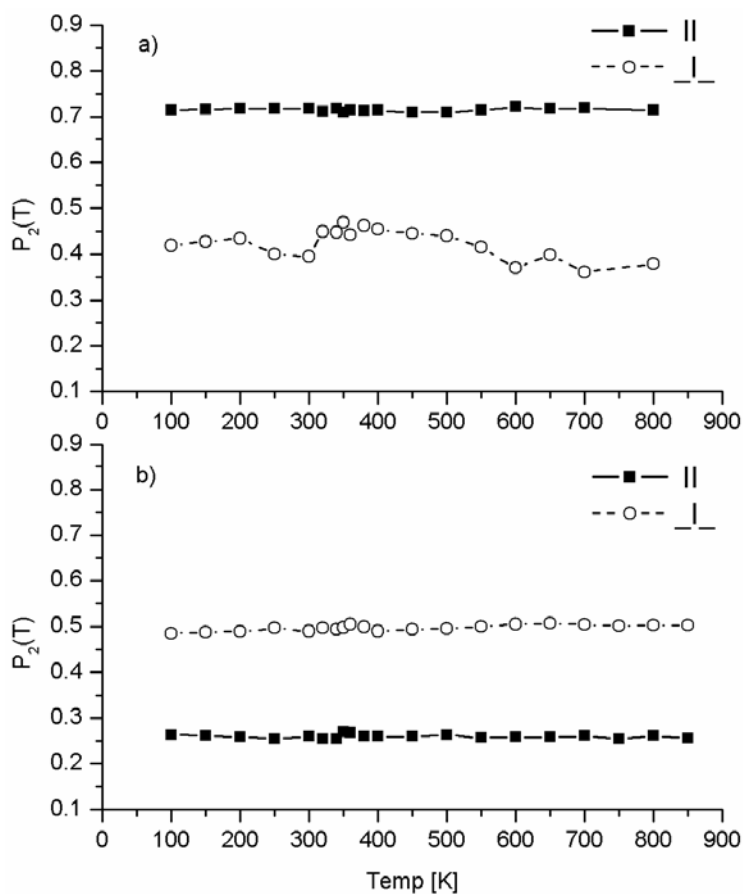
Fig. 4. The temperature dependence of the second-order parameters P_2
for single (a) and multilayer (b) cyanoadamantane systems

4. Conclusion

These computer experiments may contribute to the future "real life" experimental studies of confined nanoscale layers.

References

[1] HANSEN F.Y., BRUCH L.W., Phys. Rev. B, 51 (1995), 2515.
[2] CATHIAUX D., SOKOLIC F., DESCAMPS M, PERERA A., Mol. Phys., 96 (1999), 1033.
[3] KUCHTA B., DESCAMPS M., AFFOUARD F., J. Chem. Phys., 109 (1998), 6753.
[4] HANSEN F.Y., HERWIG K.W., MATTHIES B., TAUB H., Phys. Rev. Lett., 83 (1999), 2362.
[5] BRUCH L., COLE M.W., ZAREMBA E., *Physical Adsorption: Forces and Phenomena*. Intl. Series, Monographs in Chemistry, No. 33, Oxford University Press, Oxford, 1997.

[6] Hansen F.Y., Bruch L.W., Phys. Rev. B, 64 (2001), 045413.

[7] Kaczor K., Kachel K., Gburski Z., Mol. Phys., 100 (2002), 1537.

[8] Willart J.F., Descamps D., Bezakour N., J. Chem. Phys., 104 (1996), 2508.

[9] Moura Ramos J.J., Mol. Phys., 90 (1997), 235.

[10] Allen M.P., Tildesley D.J., *Computer Simulation of Liquids*, Clarendon Press, Oxford, 1989.

[11] Hautman J., Klein M.L., Mol. Phys., 75, (1992), 379.

[12] Brol P., Pałucha S., Skrzypek M., Gburski Z., J. Mol. Struct., 704 (2004) 115.

[13] Hansen J.P., Mcdonald I.R., *Theory of Simple Liquids*, 2nd Ed., Academic Press London, 1986.

[14] Wycko R.W.G., *Crystal Structures*, Interscience, New York, 1964, Vol. 1.

Computer simulation study of solid C_{60} doped by hydrogen cyanide molecules

S. PAŁUCHA[1,2*], P. BROL[2], Z. GBURSKI[2]

[1]Department of Electrotechnology, Division of Computer Methods,
Silesian University of Technology, Krasińskiego 8, Katowice 40-019, Poland

[2]Institute of Physics, University of Silesia, Uniwersytecka 4, Katowice 40-007, Poland

Using the spherically averaged Girifalco potential model of interacting C_{60} fullerenes, the relaxation processes of hydrogen cyanide molecules embedded in a fullerene host has been simulated by the molecular dynamics method. The dynamics of molecules in the system has been studied by inspecting the calculated dipolar absorption spectrum and Arrheniu-like plot. Moreover, the translational and rotational correlation functions of HCN in fullerene environments have been calculated. Comparison with the bulk HCN systems at several temperatures was made.

Key words: *molecular dynamics; hydrogen cyanide; doped fullerene; dielectric relaxation*

1. Introduction

The properties of carbon allotropes with closed cage structures have been an active subject of research since the first experimental discovery in 1985 [1]. Subsequently, the structure and energies of fullerene balls have been intensively studied, both experimentally and theoretically. One of the most important endeavours is to try to change their mechanical and electronic properties by doping. In recent years, exohedrally and endohedrally doped fullerenes have been produced, using a variety of doping atoms or even small molecules. In the endohedral case, the molecule encloses the dopant species, isolating them from the outside. Many possible applications, for example the recently proposed electron-spin quantum computer [2], have been envisaged using these new systems. In the exohedral case, the dopant atoms (or molecules) are external, attached to the fullerene, as in the case of superconducting fullerides. The recently reported high-temperature superconducting fullerides [3] have turned scientists' attention to problems concerned with the stability of a doped fullerite matrix. The results obtained could be of value in areas of developing technology for the storage of poisons, such as HCN, inside fullerites.

---

*Corresponding author, e-mail: palucha@us.edu.pl

2. Potential model and the simulation performed

MD calculations for 216 HCN molecules doped inside 856 C_{60} molecules arranged in an FCC structure at the temperatures from 100 K to 1400 K and $\rho = 1.73$ g/cm^3 were carried out. The equation of motion was integrated with a leapfrog Verlet integration algorithm with coupling to the thermal bath (ensemble NVT) [4]. Because of the high frequency of the intramolecular vibrations, a small integration time step of 0.2 fs was employed which guarantees fluctuation of the potential energy of ~ 0.1%. A long MD run of 1×10^6 time steps (200 ps) was performed after an equilibration period of 20 ps. The HCN potential model is a three-point interaction site model with charges placed at the atomic centres of H, C, and N with the values of 0.119e, –0.333e, and 0.214e, respectively. In a classical mechanics approximation of intramolecular motion, the internal degrees of freedom are modelled by bond and angle potentials. The bonds and angles are normally constrained to fluctuate around some equilibrium value to avoid dissociation of the molecule. Such molecules allow the study of environmental effects on the intramolecular structure and vibrational frequency shifts can be determined, etc. As these are experimentally measurable data, potential models can be critically tested and new insights gained on the molecular nature of the phenomena. Molecular flexibility was introduced in the HCN potential by assuming that C–H and C–N vibrations were modelled by harmonic [4] potentials $V(r_{ij}) = 1/2k(r_{ij} - r_0)^2$ with stretching force constants $k_{CH} = 580$N·m^{-1} ($\nu_{CH} = 3312$ cm^{-1}) and $k_{CN} = 1790$ N·m^{-1} ($\nu_{CN} = 2089$ cm^{-1}). The interatomic distances were $r_0 = 1.06$ Å and $r_0 = 1.15$ Å, respectively [5]. Periodic boundary conditions were used, and the long-ranged Coulombian interactions were computed with the Ewald summation method [4]. Samples of the trajectory were stored every 0.002 ps.

The interactions between HCN molecules have been modelled in terms of the Lennard–Jones potentials of the form $V(r_{ij}) = 4\varepsilon[(\sigma/r_{ij})^{12} - (\sigma/r_{ij})^6]$, where r_{ij} is the distance between the i-th and j-th atoms, ε is the minimum of the potential at the distance $2^{1/6}\sigma$. The following ε (in KJ/mol) and σ (in Å) have been taken [4]:

$$\varepsilon_{H-H} = 0.0715, \ \sigma_{H-H} = 2.81, \ \varepsilon_{N-N} = 0.3102,$$

$$\sigma_{N-N} = 3.35, \ \varepsilon_{C-C} = 0.4257, \ \sigma_{C-C} = 3.55.$$

The cross interactions were modelled with the Berthelod rules [4]. The interaction between two C_{60} molecules (Eq. (1)) was described according to the potential proposed by Girifalco [6], with the interactions values α and β equal 4.4775 kJ/mol and 0.0081 kJ/mol, respectively (the α and β coefficients being as in [6])

$$V_{C_{60}-C_{60}}(r) = -\alpha\left[\frac{1}{s(s-1)^3} + \frac{1}{s(s+1)^3} - \frac{2}{s^4}\right] + \beta\left[\frac{1}{s(s-1)^9} + \frac{1}{s(s+1)^9} - \frac{2}{s^{10}}\right] \quad (1)$$

where $s = r/\sigma_{C_{60}}$, with the diameter of the fullerene molecule $\sigma_{C_{60}} = 7.1$ Å.

Similarly, the interaction between C$_{60}$ and HCN molecules has been taken into account, describing the interaction between a single atomic member of a C$_{60}$ molecule and a gas atom in terms of the Lennard–Jones potential. Subsequent integration of the latter over the entire fullerene sphere results in the overall potential between the molecules given in [7].

$$V_{C_{60}\text{-site}}(r) = 60\left(\frac{c_6}{R^6}F_6(s) + \frac{c_{12}}{R^{12}}F_{12}(s)\right) \tag{2}$$

where

$$F_n = \frac{1}{s(n-2)}\left[(1-2s)^{2-n} - (1+2s)^{2-n}\right], \qquad 2R = \sigma_{C_{60}}, \qquad c_6 = -4\varepsilon_{\text{site-C}}\sigma_{\text{site-C}}^6$$

and

$$c_{12} = 4\varepsilon_{\text{site-C}}\sigma_{\text{site-C}}^{12}$$

with ε and σ presented previously (site $\equiv$ H, C, N).

3. Results and discussion

Information about microscopic dynamics is usually provided in MD simulations by means of the atomic velocity autocorrelation function (VAF) $C_v(t)$ [4]. The expression for calculating VAF is

$$C_V(t) = \frac{\langle v(t)v(0)\rangle}{\langle v^2(0)\rangle} \tag{3}$$

Depending on the velocities chosen, any correlation function, i.e., for a particular direction (x, y, or z) or for a given species (hydrogen, carbon, or nitrogen) may be obtained. Here that for the C atom of the HCN molecule is presented. From the VAF we can compute the spectral densities which will be associated with the experimental Raman and infrared spectra. As an example in Fig. 1 the carbon VAFs for pure HCN and HCN doped in C$_{60}$ at two temperatures 200 and 400 K is shown.

The shapes of the functions for the case of bulk HCN and C$_{60}$ doped with HCN are noticeably different. In the doped case (Fig. 1b), the VAF decays to a negative value and reveals an oscillating long tail behaviour which is not observed in unconstrained HCN as shown in Fig 1a. Increasing the temperature in both systems shifts the VAFs to shorter times. The observed oscillation can be interpreted as a caging effect of the C$_{60}$ host on HCN molecules. The spectral density $S(\omega)$ was analysed by

$$S(\omega) = \int_0^\infty dt\,\langle v(t)v(0)\rangle\cos(\omega t) \tag{4}$$
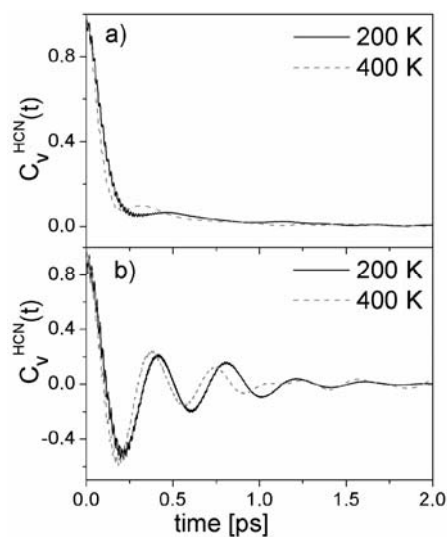
Fig. 1. Velocity autocorrelation function $C_v(t)$ calculated for two systems:
a) bulk HCN, b) HCN–C_{60} mixture
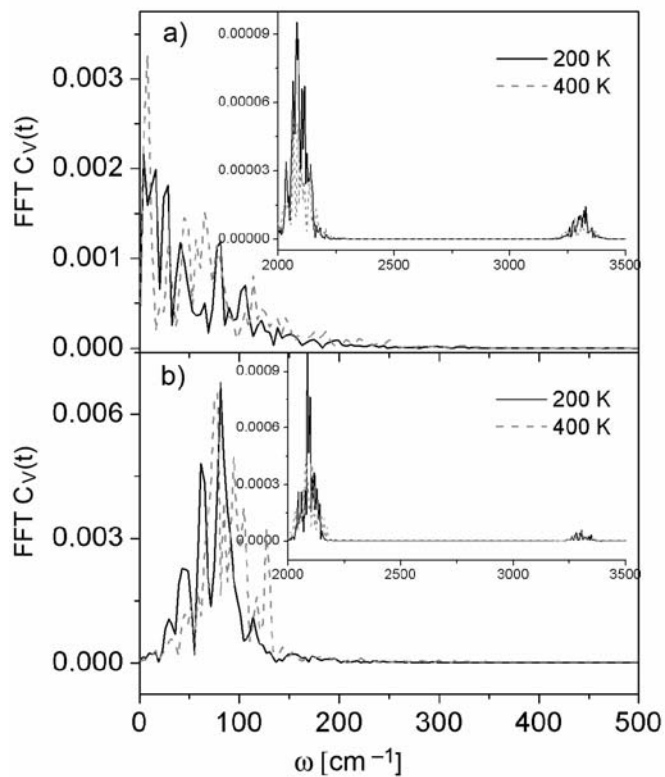
Fig. 2. Fourier transform of velocity correlation function $C_v(t)$ of HCN molecules
obtained from: a) bulk HCN and b) HCN–C_{60} mixture at two temperatures 200 K and 400 K,
respectively. The insets show the spectral densities at higher frequencies
(mid-infrared) of stretching vibrations H–C and C–N, respectively

   The Fourier transforms of the velocity autocorrelation functions for the hydrogen, carbon and nitrogen are related to the infrared spectrum [8]. The $S(\omega)$ have been calculated by numerical integration of the velocity autocorrelation functions calculated from MD simulations using standard FFT routines [9]. When generating spectra, a Hanning window was used and its width was the same as the sampling interval (20 fs). This choice of sampling interval corresponds to a Nyquist critical frequency of 8333 cm^{-1} and sets an upper bound on the frequency range over which the power spectra can be obtained. It is well known that the experimental frequency bands cannot be fully reproduced by classical simulations and this paper is restricted to a qualitative analysis mainly focused on the frequency shifts. The nitrogen spectral densities (far-infrared) found for two temperatures are plotted in Fig. 2 and are compared for the doped C$_{60}$ and bulk HCN case.

   In general, the rise of temperature produces a weakening in the intensity of frequency modes. The low frequency spread around 50 cm^{-1} in bulk HCN changed to narrower features shifted to higher frequencies around 80 cm^{-1}. This behaviour is associated with the restricted cage motions typical for dense liquids. In both cases, the intramolecular vibrational (mid-infrared) modes for HCN corresponding to stretching frequencies around 2089 cm^{-1} (H-C) and 3312 cm^{-1} (C-N), are clearly seen (see insets in Fig. 2a, b).
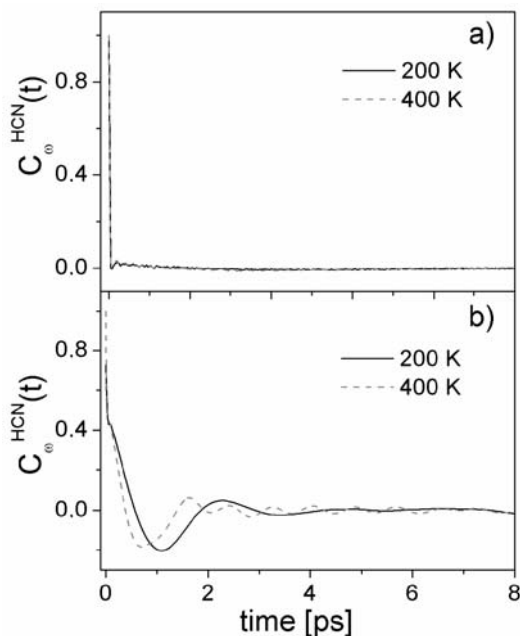
Fig. 3. Angular velocity autocorrelation function
$C\omega(t)$ calculated for two systems:
a) bulk HCN, b) HCN–C$_{60}$ mixtures

   Insight into rotational motion is given by the rotational relaxation functions. One of them is the angular velocity autocorrelation function (AVAF) $C\omega(t)$ which is presented in Fig. 3. The expression for calculating AVAF is

$$C_\omega(t) = \frac{\langle \omega(t)\omega(0) \rangle}{\langle \omega^2(0) \rangle} \tag{5}$$

Firstly it must be noted that at very short times AVAF in bulk HCN (Fig. 3a) decays rapidly to values near zero and remains in a long-time tail. The main difference arising from doping C_{60} with HCN is the occurrence of negative values in AFAF at short-times (up to 2 ps). The corresponding Fourier transforms are presented in Fig. 4.
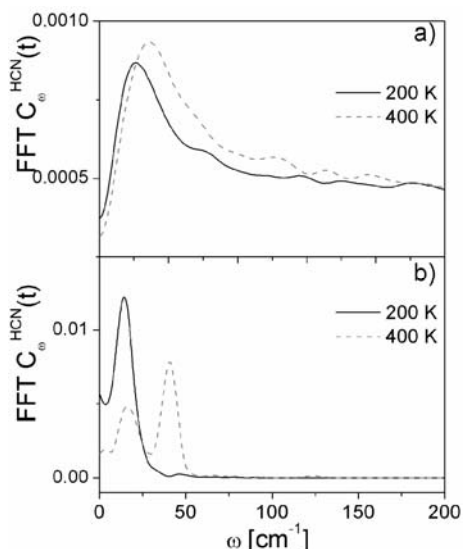
Fig. 4. Fourier transform of angular velocity correlation function $C\omega(t)$ obtained from: a) HCN and b) HCN–C_{60} mixture at two temperatures 200 K and 400 K, respectively

In both cases the influence of increasing temperature shifts the peaks to higher frequency values. The fast unconstrained reorientation located near 52 cm^{-1} at $T = 200$ K moves to 73 cm^{-1} at $T = 400$ K in bulk HCN. However, in HCN doped C_{60} the well pronounced maximum at 15 cm^{-1} shifts its location to 17 cm^{-1} and diminishes at higher temperatures. Moreover, at $T = 400$ K new maxima are developed at 41 cm^{-1}.

Now consider the relaxation processes of polar impurities (HCN) in the fullerene environment in terms of the dielectric formalism. In experiments one can measure the frequency dependency of permittivity $\varepsilon'(\omega)$ and loss $\varepsilon''(\omega)$, which are the real and imaginary parts of the dielectric function $\varepsilon(\omega) = \varepsilon'(\omega) + i\varepsilon''(\omega)$. The data obtained can be compared to many theoretical models. For example, the single-relaxation-time Debay model [10] described by the following equation for a complex dielectric function:

$$\frac{\varepsilon^*(\omega) - \varepsilon_\infty}{\varepsilon_0 - \varepsilon_\infty} = \frac{1}{1 + (i\omega\tau_D)^2} \tag{6}$$

where $\omega = 2\pi\nu$ is the angular frequency, ε_∞ is the intrinsic permittivity, ε_0 is the static permittivity and τ_D is the relaxation time parameter. Moreover, there are empirical expressions such as that originally proposed by Havriliak and Negami [11]:

$$\frac{\varepsilon^{*}(\omega)-\varepsilon_{\infty}}{\varepsilon_{0}-\varepsilon_{\infty}}=\left(1+\left(i\omega\tau_{D}\right)^{m}\right)^{-n/m} \tag{7}$$

where the parameter ω, ε_{∞}, ε_{0}, and τ_{D} have the same meaning as stated earlier. Dissado and Hill [12] developed the concept of clusters and the various charge or dipolar transitions being divided into intra-cluster ones occurring within clusters and inter-clusters transitions occurring between the clusters. A cluster is defined as an assembly of molecules surrounding a defect which vibrates coherently with slightly modified frequencies with respect to the frequencies of the perfect lattice. The degree of coherence of these motions is measured by an index $1-n$. The case of $1-n$ approaching unity implies a high degree of coherence, similar to that which might arise in strongly interacting defects/lattice systems. Similarly, the case of $1-n$ approaching zero denotes incoherent cluster oscillations with slight distortion of the lattice by the defect. The evolution of cluster relaxations now proceeds through what is termed inter-cluster transitions, where adjacent clusters exchange oscillating molecules. This process is characterized by a parameter m which, in relation to this process, plays a role analogous to that of n for the intra-cluster transitions. The shape of the dielectric response depends on the long-range inter-cluster correlations at low frequencies ($\omega<<\omega_{D}$) and on the short-range intra-cluster dynamics at high frequencies ($\omega>>\omega_{D}$). The basic assumption of the Dissado–Hill approach is the self-similarity in the energy redistributions within and among clusters (short-range and long-range interactions). The parameter m is related to the degree of inter-cluster correlation, while the parameter n reflects the local intra-cluster dynamics.

A connection between the measurable quantity $\varepsilon(\omega)$ and the relaxation function $C_M(t)$ can be introduced. Using the Fröhlich theory of dielectrics [13], the permittivity and dielectric loss can both be connected with this relaxation function:

$$\varepsilon'(\omega)=\varepsilon_{0}-(\varepsilon_{0}-1)\omega\int_{0}^{\infty}C_{M}(t)\sin(\omega t)dt$$

$$\varepsilon''(\omega)=(\varepsilon_{0}-1)\omega\int_{0}^{\infty}C_{M}(t)\cos(\omega t)dt \tag{8}$$

where $C_{M}(t)=\left\langle\mathbf{M}(t)\cdot\mathbf{M}(0)\right\rangle\cdot\left\langle\mathbf{M}(0)\cdot\mathbf{M}(0)\right\rangle^{-1}$ is a correlation function of macroscopic dipole moment $\mathbf{M}(t)=\sum_{i=1}^{n}\mathbf{m}_{i}(t)$; $\mathbf{m}_{i}$ is dipole moment of i-th molecule and n is the total number of HCN molecules.

In Figures 5a, b, the imaginary part of the dielectric response of pure HCN and HCN in a fullerene environment in log scale is presented.

The $\varepsilon''(\omega)$ peaks are located between 1 and 30 cm^{-1}. In the case of HCN doped C$_{60}$ the dielectric loss peaks change their magnitude and alter slightly the shape and fre-

quency positions from 20 cm^{-1} to 3 cm^{-1}. These features depend on temperature. The obtained data were fitted using Eq. (7). The fitted parameter m and $1 - n$ for the high- and low-frequency exponents are also presented in Fig. 5. These values are typical of polar interaction. Note, that doping HCN into C$_{60}$ results in an increase of the $1 - n$ value, which suggests more coherent cluster oscillations following the interpretation of the Havriliak and Negami model. An Arrhenius plot of the frequency position of the dielectric loss peaks shown in Fig. 5 is presented in Fig 6.
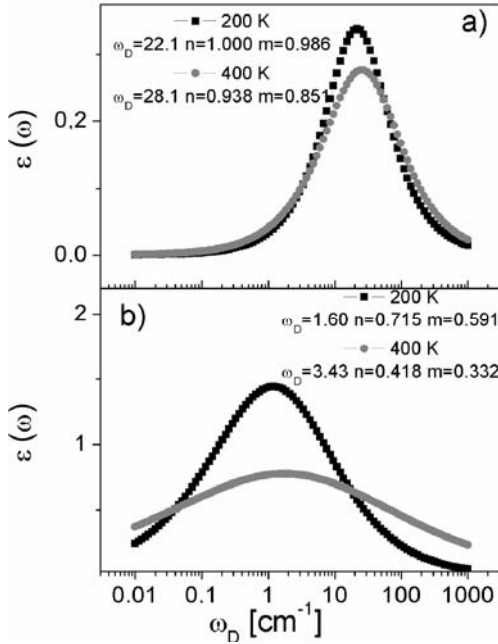
Fig. 5. Frequency dependence of the imaginary part of dielectric function obtained from: a) HCN, b) HCN–C$_{60}$ mixture at two temperatures 200 K and 400 K, respectively
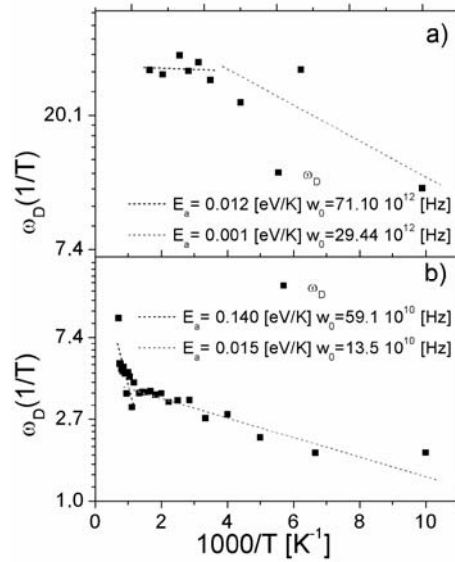
Fig. 6. Arrhenius plot of the position of the dielectric loss peak frequency obtained from a) HCN system and b) C$_{60}$–HCN mixtures

It was found that the peaks are indeed temperature activated with a functional dependence:

$$\omega_D = \omega_0 \exp\left(-\frac{E_a}{k_B T} \right) \qquad (9)$$

where E_a is the activation energy, and ω_0 is the frequency prefactor. In general, two regions connected with low- and high-temperature behaviour of ω_D could be approximated. From Fig. 6a (pure HCN) it was found that the activation energy of the loss peak below the phase transition at $T = 260$ K is 0.001 eV, whereas the activation energy E_a above the phase transition is 0.012 eV. In the HCN–C$_{60}$ mixture, the activa-

tion energies E_a are 0.015 eV/K and 0.14 eV/K with the phase transition at $T = 700$ K. In the pure HCN molecules the activation energy is an order of magnitude smaller than the one for HCN located inside the fullerene matrix. This means that in the former system the HCN molecules start rotating freely, while in the latter the rotation of HCN in C$_{60}$ system is constrained. In both analyzed systems the frequency prefactor ω_0 is within the phonon frequency range 10^{10}–10^{12} Hz.

4. Conclusion

In this study, the molecular dynamics technique was used to simulate the C$_{60}$–HCN system. This system has been systematically investigated and the rotational behaviour was analysed. Two areas were found (see Fig. 6); below 700 K the rotation of HCN is hindered, for higher temperatures it is almost undisturbed. Substantial differences in the dynamics of pure HCN and HCN doped C$_{60}$ are reported.

References

[1] KROTO H.W., HEATH J.R., O'BRIEN S.C., CURL R.F., SMALLEY R.E., Nature, 318 (1985), 162.

[2] HERNEIT W, Phys. Rev. A, 65 (2002), 032322.

[3] DRESSELHAUS M.S., DRESSELHAUS G., EKLUND P.C., *Science of Fullerenes and Carbon Nanotubes*, Academic Press, New York, 1996.

[4] ALLEN M.P., TILDESLEY D.J., *Computer Simulations of Liquids*, Oxford University Press, Oxford, 1989.

[5] HERZBERG G., *Molecular Spectra and Molecular Structure*, Vol. II, p. 173, D. van Nostrand, New York, 1966.

[6] GIRIFALCO L.A., J. Phys. Chem., 95 (1992), 5370.

[7] BRETON J., GONZALES-PLATAS J., GIRARDET C., J. Chem. Phys., 99 (1993), 4036.

[8] MARTÍ J., GUÀRDIA E., PADRÓ J.A., J. Chem. Phys., 101, (1994), 10883.

[9] PRESS W.H., FLANNERY B.P., TEUKOLSKY S.A., VETTERLING W.T., *Numerical Recipes in Fortran*, Cambridge University Press, Cambridge, 1992.

[10] JONSCHER A.K., *Dielectric Relaxation in Solids*, Chelsea Dielectrics, London, 1983.

[11] HAVRILIAK S., NEGAMI S., Polymer 8 (1967), 161.

[12] DISSADO L.A., HILL R.M., Chem. Phys., 111 (1987), 193.

[13] FRÖHLICH H., *Theory of Dielectrics*, Oxford University Press, London, 1958.

Ceramic hydration with expansion.
The structure and reaction of water layers
on magnesium oxide. A cyclic cluster study

Bettina Heidberg[1,2], Thomas Bredow[1], Klaus Littmann[2], Karl Jug[1*]

[1]Universität Hannover, Fachbereich Chemie, Fachgebiet Theoretische Chemie,
Am Kleinen Felde 30, Hannover 30167, Germany

[2]Universität Hannover, Fachbereich Architektur, Fachgebiet für Beschichtungstechnik
und Werkstoffchemie, Herrenhäuser Straße 8, Hannover 30419, Germany

MgO hydration is an expansive process. It is used in cement to compensate for shrinkage, but it can be harmful at higher concentrations. In this quantum-chemical study, the first steps of the hydration of MgO have been explored. The semiempirical MO method MSINDO with the cyclic cluster model, including long-range electrostatic interactions, has been applied to investigate water adsorption on the (001) surface of MgO. Both molecular adsorption and dissociative adsorption have been found to occur. The latter is stabilized by hydrogen bonding from neighbouring water molecules and surface oxygen. Several energy minima exist for the experimentally low temperature $p(3\times2)$ monolayer H_2O observed on the MgO (001) surface which consists of a mixture of dissociated and molecular water. One third of the water molecules were dissociated, which is consistent with previous DFT studies. A stable fully hydroxylated MgO (001) surface with OH bridging two Mg ions and the hydrogen bound to the surface oxygen was discovered. This structure appears to promote the expansive, topotactic nucleation of brucite on the MgO (001) surface.

Key words: *magnesium oxide; brucite; water; hydration; adsorption*

1. Introduction

The hydration of magnesium oxide provides an interesting example for studying the surface structure and chemical reactions of ceramic oxides. Its simple crystallographic and electronic structure makes MgO known by its mineral name, periclase, a prototype for investigating the surface chemistry of ceramics, and in particular, for ceramic hydration. The final product of MgO hydration is $Mg(OH)_2$, brucite, which is

_____

a layered mineral of hexagonal symmetry with the crystallographic space group $P\bar{3}m1$. The relation

$$MO\{Fm\bar{3}m\} + H_2O \rightarrow M(OH)_2 \{P\bar{3}m1\} \tag{1}$$
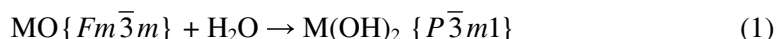
holds not only for M = Mg but for a whole group of divalent metals: Mg, Ca, Mn, Fe, Co, Ni, and Cd. Their oxides MO have a rock-salt structure and their hydroxides $M(OH)_2$ have brucite structure. Thus the hydration of MgO can be considered as representative of the whole group. A particular feature of the hydration is the volume expansion associated with the reaction. The MgO hydration increases the solid volume by a factor of 2.2.

The expansion associated with periclase hydration is significant for ceramics engineering in at least two aspects. Although it is useful it can also be hazardous.

1. The long-term expansion produced by periclase hydration compensates in part for the thermal and autogenous shrinkage in concrete. Because of its high durability, concrete made from Portland slag cement which has a slight expansion is used for huge dam constructions. Much research has been carried out to achieve shrinkage -compensating cement by increasing the amount of MgO and determining the proper hydration conditions. Due to the heat produced by cement hydration, the temperature in an uncooled mass of concrete may reach more than 50 °C. Without appropriate and costly temperature-controlling measures the tensile thermal stress caused by mass concrete shrinkage during the cooling may exceed the tensile strength and the concrete may crack. The cooling generally lasts six months or more. The amount and rate of shrinkage compensating MgO expansion has to be controlled in practice by adjusting the calcinating conditions of MgO, its fineness, the amount in the cement and other parameters [1, 2].

2. However, periclase is generally regarded as a harmful component in cement because of its very slow hydration with significant volume expansion, which generates unsoundness in concrete and even causes cracking (Fig. 1). Up to 2 weight per cent of magnesium oxide is incorporated into clinker phases by building magnesium ions into the crystal lattice [3]. Excess MgO exists in industrially produced Portland cement clinkers as primary or secondary periclase at room temperature. The permitted limit for the total MgO content for Portland cement is 5% by mass in Germany, 6% in USA.
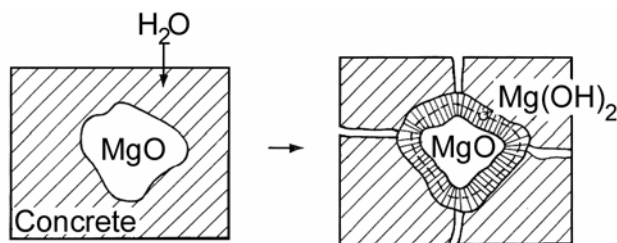

Fig. 1. Scheme of MgO hydration with volume expansion in concrete

Furthermore, the MgO hydration has to be considered in the processing of widely used industrial products such as fused periclase, refractory (chemically inert) magnesia and calcinated (chemically active) magnesia.

In view of the wide range of applications an understanding of the hydration process of MgO at an atomic and nanometer scale is desirable. This paper describes the quantum-chemical modelling of the magnesia hydration on a scale ranging from the atom to the nanometer cluster.

2. Quantum chemical modelling. MSINDO CCM

In this work, the semiempirical molecular orbital method MSINDO [4] is used. This method is based on the intermediate neglect of the differential overlap (INDO) approximation. This reduces the total number of integrals for a n-electron system to n^2 compared to n^4 in the case of ab initio Hartree–Fock calculations, or n^3 for calculations based on the density-functional theory (DFT). The remaining two-centre integrals are Coulomb integrals of the form $(\mu_I \mu_I | \nu_J \nu_J)$ with basis function μ_I on atom I and ν_J on atom J, nuclear attraction integrals $-(\mu_I | Z_J / r_{IJ} | \mu_I)$, overlap integrals $S_{\mu\nu}$ and the two-centre one-electron integrals $L_{\mu\nu}$ and $\Delta H_{\mu\nu}$ for the kinetic energy and the orthogonalization correction, respectively [5]. The striking feature of MSINDO is the use of a symmetrically orthogonalized valence basis with 6-31G and 6-31G* quality. The atomic basis set is augmented by 2p functions on hydrogen to account for hydrogen bonding. Core electrons are included by Zerner's pseudopotential [6].

The cyclic cluster model (CCM) [7] implemented in MSINDO has been applied to investigate the first steps of the reaction (Eq. 1) with M = Mg. Since the Coulomb interactions in these systems with partial ionic character decrease slowly, large clusters are considered and the effects of long-range electrostatic interactions are calculated [8] based on the Ewald summation technique. Within the CCM, the interactions of each atom with all other atoms of its Wigner–Seitz cell are calculated. To retain the proper symmetry, weighting factors are used for the interaction integrals with atoms at the border of the Wigner-Seitz cells. The deficiencies of the free cluster model, such as the loss of local symmetry and the occurrence of boundary effects at the borders of free clusters are overcome by employing the CCM [7]. The dimension of the Coulomb matrix **G**, the density matrix **P** and the Fock matrix **F** is given only by the basis functions of the original cluster atoms I in MSINDO CCM.

The work involved the exploration of a multidimensional potential energy surface and considered the interplay between several competing interactions: substrate–water, water–water–hydrogen bonding, partial and complete dissociation of water, surface hydroxylation as well as covalent, ionic, and dispersive interactions. This complexity of the pertinent bulk and surface phases precluded the systematic application of the more common ab initio or DFT methods. The method MSINDO has been successfully used to study the bulk and surface properties of various oxides [9–12] and provided

the theoretical framework to systematically explore the energetic, structural and elastic properties of the MgO–water system with models containing up to 1000 atoms.

In all the simulations, the magnesium oxide surface was modelled by a $Mg_{96}O_{96}$ slab containing four layers of (001) crystal planes with 48 atoms each, of which the bottom three were fixed in the optimized bulk structure, while the water molecules were optimized together with a relaxation of the atoms of the first layer of MgO. In this way, structures denoted as "relaxed" were obtained. In order to determine the effects of surface relaxation all atoms of the MgO slab were fixed at their optimized bulk positions while the positions of the adsorbed water molecules were optimized. These structures were denoted as "unrelaxed".

3. Results and discussion

3.1. Energetics of MgO

The binding energy E_B per MgO unit for the perfect crystal was calculated using cyclic clusters of increasing size. The results for E_B show fast convergence to the bulk limit with increasing cluster size. The Madelung term does converge rapidly in CCM due to the cubic symmetry of MgO. The result of $E_B^{CCM} = 1023$ kJ/mol is close to the experimental value of 990 kJ/mol [13]. The same rapid convergence occurs also for the lattice parameter a of MgO in the cyclic cluster model. In principle, the same trends are found for the (001) surface energy and the (001) surface relaxation energy. The surface energy E_s was calculated using the equation:

$$E_s = \frac{E_{2D} - E_{3D}}{n_s} \qquad (2)$$

The converged value of E_s is 76 kJ/mol, compared to the experimental range of 55–63 kJ/mol [14]. E_{3D} denotes the energy of the optimized periodic bulk structure, in three dimensions. E_{2D} is the energy of the slab model obtained by using the same cluster and geometry as for the calculation of E_{3D} but with the periodicity in only two dimensions in the (001) plane. n_s is the number of MgO units in the surface.

3.2. Adsorption of water on MgO (001) and surface hydroxylation

All theoretical models agree that dissociative water adsorption occurs at surface defects such as steps, kinks or vacancies. Systematic optimization of the geometry of the water monolayer adsorbed on MgO (001) using MSINDO CCM yields several types of stable structures including physisorbed structures with undissociated water molecules; chemisorbed structures with a part of the water molecules dissociated due to lateral hydrogen bonding; and structures with a fully hydroxylated surface. In Ta-

ble 1 the results for the adsorption energies of various configurations of water monolayers on MgO (001) are given. The adsorption energy E_{ads} per water molecule was calculated for a cluster adsorbate structure of n water molecules on MgO according to:

$$E_{ads} = \frac{E_{MgO/water} - E_{MgO} - nE_{water}}{n} \tag{3}$$

Table 1. Adsorption energy [kJ/mol] per H_2O molecule of different monolayer structures

Structure	Remarks	Unrelaxed	Relaxed	Experimental
$p(3\times2)$				−85 [16]
A	No dissociation	−60		
B	1/3 dissociated	−79	−111	
C	1/3 dissociated	−72	−100	
(1×2)				−
D	Dissociated OH bridge	− 69		
(1×1)				−
E	No dissociation	− 6	− 6	
F	Dissociated OH on top of Mg	−24	−24	
G	Dissociated OH bridge		−99	

Polarization infrared spectroscopy detected a stable ordered H_2O MgO (001) adsorbate at temperatures between 185 and 220 K [15]. Diffraction indicated its $p(3\times2)$ symmetry and its adsorption energy was measured as −85 kJ/mol [16]. The model calculations found the lowest energy minimum for the $p(3\times2)$ structure consisting of a mixture of dissociated and molecular water, one third of the molecules being dissociated. OH is stabilized by three hydrogen bonds, one from the dissociated proton and two from undissociated water molecules (Fig. 2, structure **B**). Less stable is the physisorbed $p(3\times2)$ structure **A** on the unrelaxed MgO(001) surface. A complete network of hydrogen bonds connects the undissociated water molecules. Upon surface relaxation, structure **A** forms a chemisorbed layer with one third of the molecules dissociated. In the similar $p(3\times2)$, structure **C**, with the second lowest energy, one third of the molecules are also dissociated. OH is again stabilized by three hydrogen bonds, but in this case from three undissociated water molecules.

Both the physisorbed and chemisorbed states of water on MgO (001) have recently been reported in theoretical studies by DFT [17, 18] and spectroscopic work [19]. According to earlier DFT work, water chemisorption on MgO(001) involves a reconstruction and protonation to form a stable (111) hydroxyl surface [20]. Experimentally, using x-ray standing waves, a (1×1) H_2O overlayer on MgO (001) at 300 K was observed and a fully hydroxylated surface was postulated [21, 22]. In contrast, the

fully hydroxylated surface with OH placed over the Mg ion was found to be unstable by correlation corrected periodic Hartree–Fock calculations [23] and self-consistent tight-binding studies of embedded clusters [24], in accordance with DFT based molecular dynamics calculations [25].
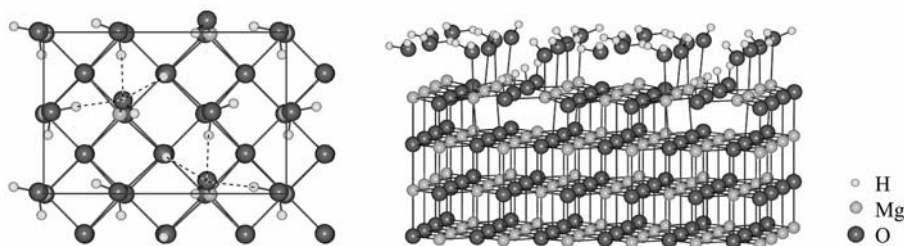
Fig. 2. Most stable structure **B** of the water monolayer on MgO (001). One third of the water molecules dissociated, $p(3\times2)$ symmetry. OH stabilized by three hydrogen bonds. (see Table 1). Top view, section (left). Side view (right)

In a more complete study of the potential energy surface this result was confirmed for the on-top adsorption of OH (structure **F**), but a stable fully hydroxylated MgO (001) surface was discovered. The OH group is placed in a bridging position over two Mg ions and the hydrogen atom is bound to the surface oxygen, the adsorption energy being $E_{ads} = -99$ kJ/mol (Fig. 3, structure **G**). This (1×1) structure is consistent with diffraction measurements at 300 K. It is slightly less stable than the $p(3\times2)$ structure **B**, with only one third of the water molecules dissociated, and $E_{ads} = -111$ kJ/mol. The (2×1), structure **D**, consists of a completely dissociated water monolayer characterized by a tilted OH group, bridging the Mg ions, with antiparallel ordering of OH chains (antiferroelectric order). The (1×1), structure **E**, is an undissociated monolayer.
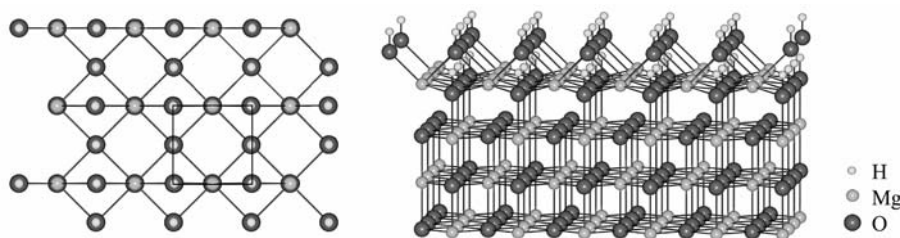
Fig. 3. Fully hydroxylated MgO (001) surface with (1×1) symmetry, with relaxation of the first layer of the MgO cluster. (see Table 1, structure **G**). Top view, section (left). Side view (right)

This fully hydroxylated structure **G** promotes the topotactic nucleation and growth of brucite. The (111) planes of the reactant periclase are typically observed parallel to the (0001) planes of the product brucite [26]. The development of brucite-like layers from the MgO (001) surface occurs perpendicularly to the brucite [0001] axis (Fig. 4). This reaction, including the elastic behaviour, will be modelled in a subsequent study based on the results obtained for the MgO surface hydration.
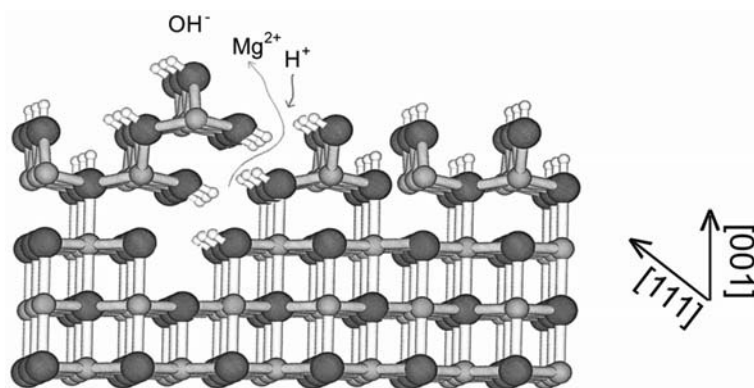
Fig. 4. Schematic picture of the expansive,
topotactic nucleation of brucite on the MgO (001) surface

4. Summary and conclusions

The cyclic cluster model with the Madelung potential implemented in the semiempirical SCF-MO method MSINDO is applied in a study of the periclase hydration.

The calculations reveal several types of stable water monolayer structures on MgO (001) including special physisorbed species. These form a hydrogen-bonded network of undissociated water molecules and chemisorbed water with part of the water molecules dissociated, mainly due to lateral interactions. A stable fully hydroxylated MgO (001) surface with OH bridging two Mg ions and hydrogen bound to the surface oxygen was discovered. This structure promotes the expansive, topotactic nucleation of brucite and provides the basis for future studies of periclase to brucite transformation reactions including the elastic behaviour of the product.

References

[1] QING Y., CHEN H.X., WANG Y.Q., LOU Z.G., Cement and Concrete Comp., 26, (2004), 331.
[2] ZHENG L., CUI X.H., TANG M.S., Cement and Concrete Research, 21 (1991), 1049; ZHENG L., XUEHUA C., MINGSHU T., Cement and Concrete Research, 22 (1992), 1.
[3] DREIZLER I., KNÖFEL D., Zement Kalk Gips, 35 (1982), 537.
[4] AHLSWEDE B., JUG K., J. Comp. Chem., 20 (1999), 563.
[5] NANDA D.N., JUG K., Theor. Chim. Acta, 57 (1980), 95.
[6] ZERNER M.C., Mol. Phys., 23 (1972), 963.
[7] BREDOW T., GEUDTNER G., JUG K., J. Comp. Chem., 22 (2001), 89.
[8] JANETZKO F., BREDOW T., JUG K., J. Chem. Phys., 116 (2002), 8994.
[9] AHLSWEDE B., HOMANN T., JUG K., Surf. Sci., 445 (2000), 49.

[10] TIKHOMIROV V.A., JUG K., J. Phys. Chem. B, 104, (2000), 7619.

[11] HOMANN T., BREDOW T., JUG K., Surf. Sci., 515 (2002), 205.

[12] HOMANN T., BREDOW T., JUG K., Surf. Sci., 555 (2004), 135.

[13] LIDE D.R., *CRC Handbook of Chemistry and Physics*, CRC Press, Boca Raton, FL, 79th Ed., 1998/1999.

[14] TOWLER M.D., HARRISON N.M., MCCARTHY M.I., Phys. Rev. B, 52 (1995), 5375.

[15] HEIDBERG J., REDLICH B., WETTER D., Ber. Bunsenges. Phys. Chem., 99 (1995), 1333.

[16] FERRY D., GLEBOV A., SENZ V., SUZANNE J., TOENNIES J.P., WEISS H., Surf. Sci., 377 (1997), 634.

[17] LYNDEN-BELL R.M., DELLE SITE L., ALAVI A., Surf. Sci., 496 (2002), L1.

[18] GIORDANO L., GONIAKOWSKI J., SUZANNE J., Phys. Rev. Lett., 81 (1998), 1271.

[19] KIM Y.D., LYNDEN-BELL R.M., ALAVI A., STULZ J., GOODMAN D.W., Chem. Phys. Lett., 352 (2002), 318.

[20] REFSON K., WOGELIUS R.A., ERASER D.G., PAYNE M.C., LEE M.H., MILMAN V., Phys. Rev. B, 52 (1995), 10823.

[21] LIU P., KENDELEWICZ T., NELSON E.J., BROWN G.E., Surf. Sci., 415 (1998), 156.

[22] DANIELS B.G., LINDSAY R., THORNTON G., Surf. Rev. Lett., 8 (2001), 95.

[23] SCAMEHORN C. A., HARRISON N.M., MCCARTHY M.I., J. Chem. Phys., 101 (1994), 1547.

[24] GONIAKOWSKJ J., BOUTTE-RUSSO S., NOGUERA C., Surf. Sci. 284 (1993), 315.

[25] LANGEL W., PARRINELLO M., J. Chem. Phys., 103 (1995), 3240.

[26] GIOVANOLI R., FEITKNECHT W., FAHRER W., J. Microscopie, 7 (1968), 177.

Coupled space-time multiscale simulations
of dynamic delamination tests

Stefano Mariani [1*], Anna Pandolfi[1], Raffaella Pavani[2]

[1]Dipartimento di Ingegneria Strutturale, Politecnico di Milano,
Piazza L. da Vinci 32, 20133 – Milano, Italy

[2]Dipartimento di Matematica "Francesco Brioschi", Politecnico di Milano,
Piazza L. da Vinci 32, 20133 – Milano, Italy

The aim of this work was to numerically investigate the dynamic debonding of a thin composite laminate from a rigid substrate. The laminate is elastic and the separation surface behaviour is governed by a cohesive softening law. By way of simplification, the bending dominated deflection of the free part of the laminate is described through the Euler–Bernoulli kinematics. In this context, the partial differential equation governing the laminate motion is characterized by two length scales and two time scales. To accurately simulate the growth of delamination, a coupled space-time multiscale integration was used. The qualifying features of such an approach are: i) a fine spatial discretization across the process zone, where the evolution of the cohesive tractions demands a detailed description; ii) a high order accurate time integration algorithm, capable of damping spurious high frequency oscillations of the solution. The results of a two-stage peel test testify to the good performance of the approach applied.

Key words: *non-linear dynamic fracture mechanics*; *delamination*; *heterogeneous multiscale method*

1. Introduction

The failure of composite structures under dynamic loading is in need of deep investigation, as the recently published literature testifies (see, e.g., [1–6]). The research has two main objectives: i) the development of ad-hoc constitutive models for the process zone (the region ahead of the crack tip where most of the dissipative events occur), which possibly includes rate and temperature dependence; ii) the definition of accurate numerical schemes for the simulation of fracture propagation, crack tip velocity fluctuation, and material fragmentation.

---

*Corresponding author, e-mail: stefano.mariani@polimi.it

In both cases, a fully macroscopic approach – where the microstructural features of the delamination are accounted for solely by using phenomenological models – could introduce a severe limit on the a'' methods represent a promising tool, since they are specifically built to capture the details of all the time/space scales involved in the description of the problem.

In the simple cases of linear and nonlinear elasticity, wave propagation in heterogeneous materials has been simulated through asymptotic analysis (see, e.g., [7]). However, when dissipative processes are involved, as is the case with delamination in composites, analytical and numerical results are seldom available.

This paper reports on the simulation of the propagation of interlaminar debonding in composite laminates under dynamic loading by applying a coupled space-time multiscale scheme. The computational convenience of the multiscale method derives from the fine space/time scale resolution of the traction distribution in the process zone and the coarse resolution in the remaining domain. Annoying spurious problems often introduced by fine space discretization are the high frequency oscillations of the solution. The accuracy of the numerical solution was ensured by adopting a time integration algorithm (α-method [8]) able to damp spurious oscillation modes.

As the purpose was the presentation and assessment of the multiscale method performance, only tests concerning a single lamina which separates from a rigid substrate were considered. In particular, a two-stage peel test described in [1, 9, 10] was analysed: a thin lamina partially debonded from a substrate is statically deformed at fixed crack length; thus the constraints are relaxed and the stored elastic energy induces dynamic delamination growth. The results demonstrate that the proposed multiscale scheme accurately resolves the nonlinearities characterizing the process zone at a much reduced computational cost compared to full scale finite element simulations.

2. Problem formulation

Polymer matrix laminates used in standard delamination tests are assembled by bonding with resin-enriched interlayers a stacking sequence of laminae. Interlayers have small, although not totally negligible, thickness in comparison with one of the assembled laminate. Referring to a standard laminate used in the experiments, in the simulations a single pre-existing interlaminar crack (at the topmost level) is allowed to propagate, while the rest of the composite is assimilated to a rigid substrate. The mechanical properties of the separating interlayer are accordingly lumped to the zero-thickness surface Γ.

The problem at hand is described in Fig. 1. A thin layer is partially bonded to a rigid substrate through a cohesive surface Γ. The lamina small thickness allows to disregard shear deformations with respect to bending deflections. Thus, the motion of the thin layer under dynamic loadings in the small displacement regime is accurately modelled by the Euler–Bernoulli beam theory:

$$\rho A u_{,tt} + E I u_{,xxxx} + b \sigma(u) = 0 \tag{1}$$

where t is time, x is the lamina longitudinal axis coordinate; ρ is the material mass density, E the effective material's Young's modulus depending on the out-of-plane confinement of the displacement field, $A = bh$ and $I = bh^3/12$ the area and the moment of inertia of the lamina cross-section respectively, $u = u(x; t)$ the transversal displacement of the longitudinal axis, and the $\sigma(u)$ the normal cohesive traction between lamina and substrate.
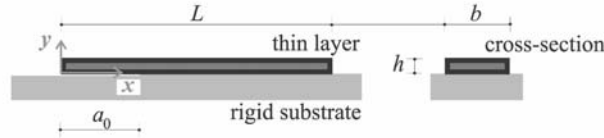
Fig. 1. Geometry of the lamina bonded to the rigid substrate

The loading conditions in a first stage are imposed by assigning the displacement history of the free end of the beam, $\bar{u}(t) = u(0; t)$. The imposed displacement $\bar{u}$ grows smoothly with time, to avoid the activation of higher order oscillation modes in the specimen. In this way, the adopted kinematics adequately describes the motion of the beam (see also [10]).

The test configuration is characterized by an initial crack of length a_0 (see Fig. 1). For $x \in [0; a_0)$ the vertical displacement must be positive on null, as a consequence of the impenetrability constraint given by the substrate. In the debonding region $x \in [a_0; L]$, the crack growth is modelled by a softening $\sigma = \sigma(u)$ relationship. According to classical cohesive theories in nonlinear fracture mechanics, a piecewise linear model is assumed (see Fig. 2):

$$\sigma(u) = \begin{cases} \sigma_M \dfrac{u/u_c}{\delta} & \text{if} \quad \le \delta u_c \\[2mm] \sigma_M \dfrac{1 - u/u_c}{1 - \delta} & \text{if} \quad \delta u_c \le u \le u_c \\[2mm] 0 & \text{if} \quad u \ge u_c \end{cases} \tag{2}$$

where σ_M is the cohesive strength, u_c the critical opening displacement (beyond which the tensile response of the material vanishes), and δ a constitutive parameter defining the opening displacement at the stress peak. The parameter δ can be thought as an expedient to introduce an initial "elastic" stiffness.

The elastic branch of the cohesive law, for $u \le \delta u_c$, is representative of the response of the interlayer prior to the localization of microscopic damage mechanisms, eventually leading to the formation of a well-defined macrocrack.
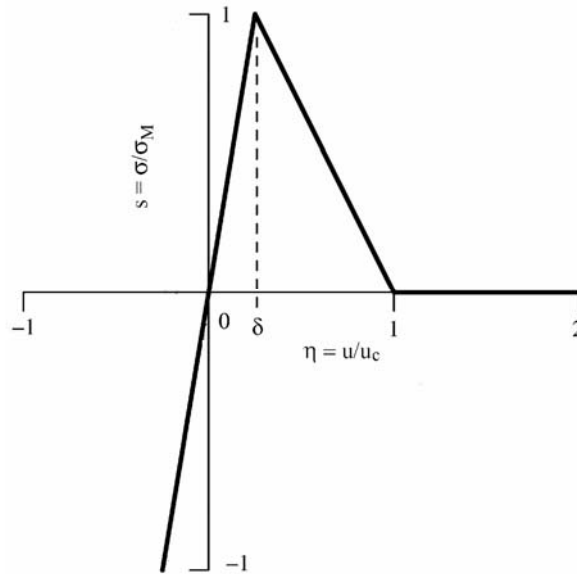
Fig. 2. Adopted piecewise linear cohesive law

The interface law (2) is path-independent or holonomic for $u < u_c$. Rate sensitive cohesive laws $\sigma(u; \dot{u})$, which explicitly include the dependence on the opening velocity, thus more suitable to describe rate-dependent experimental results in the low velocity crack growth regime [10] are not considered in this work.

As already pointed out [9, 4], cohesive models of fracture introduce characteristic length- and time scales into the material description.

The characteristic length l_c is defined as:

$$l_c = \frac{EG_c}{\sigma_M^2} \tag{3}$$

where $G_c = \int_0^\infty \sigma(u)\,du$ is the critical energy release rate, i. e. the energy spent for a unit increase of the extension of the crack surface Γ. The intrinsic length l_c roughly estimates the size of the process zone, where the crack opening takes place.

The characteristic (cohesive) time t_c is:

$$t_c = \frac{\rho c_L u_c}{2\sigma_M} \tag{4}$$

where c_L is the longitudinal wave speed, $c_L = \sqrt{E/\rho}$. The intrinsic time t_c arises from the interplay between material inertia and cohesive properties under dynamic conditions.

An additional time scale characterizes the problem in Fig. 1. The geometric time t_g is the time spent by a longitudinal wave to travel along the initially free part of the specimen, i.e.:

$$t_g = \frac{a_0}{c_L} \tag{5}$$

Equation (1) can be conveniently written in a more manageable form, pointing out the two time scales, by introducing the following non-dimensional time, space, displacement, and traction variables:

$$\tau = \frac{t}{t_g}, \qquad \xi = \frac{x}{a_0}, \qquad \eta = \frac{u}{u_c}, \qquad s = \frac{\sigma}{\sigma_M} \tag{6}$$

Thus the normalized equation of motion reads:

$$\eta_{,\tau\tau} + \frac{1}{12\lambda^2} \eta_{,\xi\xi\xi\xi} + \frac{1}{2} \frac{t_g}{t_c} \lambda s(\eta) = 0 \tag{7}$$

where $\lambda = a_0/h$ is the slenderness of the free part of the specimen at $t = 0$. Eq. (7) explicitly shows that the cohesive law $s(\eta)$ couples the two time scales t_c and t_g, which, in the case of standard composite materials, can differ by several orders of magnitude. This peculiarity must be accurately considered in devising numerical algorithms for the time integration of Eq. (7).

It should be emphasized that Eq. (7) additionally depends on two length scales. Besides the microstructural length scale l_c (Eq. (3)), measuring the extension of the active delamination zone, a macroscopic length scale, l_g, linked to the lengths a_0 and L can be introduced. In practice, the macroscopic scale l_g represents the actual size of the specimen, and, possibly, the scale of variation of the applied loading conditions. Depending on the material properties, the two space scales can also differ by several orders of magnitude.

3. Space-time multiscale approach

In spite of the simplicity of the problem at hand, the space-time multiscale nature of Eq. (7) is a challenging issue. In order to obtain an accurate numerical result one is compelled to use space and time discretization fine enough to capture the variation of the cohesive tractions within the smallest space and time scale. By making recourse to obvious uniformly fine space and time subdivisions, the analysis can quickly reach prohibitive computational costs. Additionally, the use of a fine discretization pushes the accumulation of numerical errors which inevitably spoil the quality of the solution.

As an alternative, a multiscale approach was used. Following the format typically employed by the heterogeneous multiscale method (HMM) for evolutionary problems [11], the method was cast into a two-step algorithm:

1. Force (residual) estimation:

a) reconstruction of the displacement field at the microscale;

b) solution of the governing equation at the microscale;

c) averaging the microscale solution into the macroscale variables.

2. Evolution of the displacement field at the macroscale.

The algorithm requires a double spatial discretization of Eq. (7). Two grids were introduced, with different spacing and location. The background, macroscopic grid is coarse and fixed, with node spacing $\Delta\xi_M$. The coarse grid covers the whole length of the specimen. The foreground, microscopic grid is much finer, with node spacing $\Delta\xi_m$, and moves with the crack tip. The fine discretization covers the region of Γ surrounding the process zone for an extension of 4–5 times the cohesive length scale l_c.

Adopting a classical finite difference scheme, the spatial derivative $\eta_{,\xi\xi\xi\xi}$ of the transversal displacement at the i-th node is second-order approximated as:

$$\eta_{,\xi\xi\xi\xi}^i = \frac{\eta^{i-2} - 4\eta^{i-1} + 6\eta^i - 4\eta^{i+1} + \eta^{i+2}}{\Delta\xi^4} \tag{8}$$

where $\Delta\xi$ takes the value $\Delta\xi_M$ or $\Delta\xi_m$, depending on the active grid. To link together the two approximations, continuity on displacement and rotations at the boundaries of the microscopic grid was imposed. This excludes the presence of kinks in the discrete solution.

The semi-discrete form of the original partial differential equation is given by the following system of ordinary differential equations:

$$\eta_{,\tau\tau}^I + \frac{1}{12\lambda^2} \frac{\eta^{I-2} - 4\eta^{I-1} + 6\eta^I - 4\eta^{I+1} + \eta^{I+2}}{\Delta\xi_M^4} + \frac{1}{2}\frac{t_g}{t_c}\lambda s(\eta^I) = 0, \quad I = 1, ..., I_M$$

$$\eta_{,\tau\tau}^i + \frac{1}{12\lambda^2} \frac{\eta^{i-2} - 4\eta^i + 6\eta^i - 4\eta^{i+1} + \eta^{i+2}}{\Delta\xi_m^4} + \frac{1}{2}\frac{t_g}{t_c}\lambda s(\eta^i) = 0, \quad i = 1, ..., I_m \tag{9}$$

where I_M and I_m are the number of nodes in the macroscopic and microscopic grids, respectively.

The initial conditions for Eq. (9) are:

$$\eta^I(\tau = 0) = \eta^{I(0)} \qquad \eta_{,\tau}^i(\tau = 0) = \eta_{,\tau}^{I(0)}, \qquad I = 1, ..., I_M$$

$$\eta^i(\tau = 0) = \eta^{i(0)} \qquad \eta_{,\tau}^i(\tau = 0) = \eta_{,\tau}^{i(0)}, \qquad i = 1, ..., I_m \tag{10}$$

It is well known [12] that the Euler–Bernoulli equation is dispersive, i.e., every frequency of the solution propagates with its own velocity. The fine space grid allows the local capture of high frequency oscillations, characterized by increasing propagation speeds as the node spacing $\Delta\xi_m$ reduces.

The initial value problem (9)–(10) is thus integrated in time with the explicit α-method [8]. The α-method possesses the positive feature to numerically filter out of the solution high frequency oscillations, thus conserving the order of accuracy of the scheme.

The multiscale solution in the time step $[\tau^{(n)},\tau^{(n+1)}]$, with $\tau^{(n+1)}=\tau^{(n)}+\Delta\tau_M$, is described in Table 1. The constants α, β, and γ are algorithmic coefficients.

Table 1. Explicit time integration algorithm

(1) Microscopic fields $(i=1,...,I_m)$, for $k=0,K-1$:

- predictor phase:

$$\bar{\eta}^{i(n+1,k+1)} = \eta^{i(n+1,k)} + \Delta\tau_m \eta_{,\tau}^{i(n+1,k)} + \frac{\Delta\tau_m^2}{2}(1-2\beta)\eta_{,\tau\tau}^{i(n+1,k)}$$

$$\bar{\eta}_{,\tau}^{i(n+1,k+1)} = \eta_{,\tau}^{i(n+1,k)} + \Delta\tau_m(1-\gamma)\eta_{,\tau\tau}^{i(n+1,k)}$$

- solution phase:

$$\eta_{,\tau\tau}^{i(n+1,k+1)} = -\frac{1}{12\lambda^2}\frac{\tilde{\eta}^{i-2}-4\tilde{\eta}^{i-1}+6\tilde{\eta}^{i}-4\tilde{\eta}^{i+1}+\tilde{\eta}^{i+2}}{\Delta\xi_m^4} - \frac{1}{2}\frac{t_g}{t_c}\lambda\, s(\tilde{\eta}^i)$$

where:

$$\tilde{\eta}^i = (1+\alpha)\bar{\eta}^{i(n+1,k+1)} - \alpha\,\eta^{i(n+1,k)}$$

- corrector phase:

$$\eta^{i(n+1,k+1)} = \bar{\eta}^{i(n+1,k+1)} + \Delta\tau_m^2\beta\,\eta_{,\tau\tau}^{i(n+1,k+1)}$$

$$\eta_{,\tau}^{i(n+1,k+1)} = \bar{\eta}_{,\tau}^{i(n+1,k+1)} + \Delta\tau_m\gamma\,\eta_{,\tau\tau}^{i(n+1,k+1)}$$

(2) Macroscopic fields $(I=1,...,I_M)$:

- predictor phase:

$$\bar{\eta}^{I(n+1)} = \eta^{I(n)} + \Delta\tau_M \eta_{,\tau}^{I(n)} + \frac{\Delta\tau_M^2}{2}(1-2\beta)\eta_{,\tau\tau}^{I(n)}$$

$$\bar{\eta}_{,\tau}^{I(n+1)} = \eta_{,\tau}^{I(n)} + \Delta\tau_M(1-\gamma)\eta_{,\tau\tau}^{I(n)}$$

- solution phase:

$$\eta_{,\tau\tau}^{I(n+1)} = -\frac{1}{12\lambda^2}\frac{\tilde{\eta}^{I-2}-4\tilde{\eta}^{I-1}+6\tilde{\eta}^{I}-4\tilde{\eta}^{I+1}+\tilde{\eta}^{I+2}}{\Delta\xi_M^4} - \frac{1}{2}\frac{t_g}{t_c}\lambda\, s(\tilde{\eta}^I)$$

where:

$$\tilde{\eta}^I = (1+\alpha)\bar{\eta}^{I(n+1)} - \alpha\,\eta^{I(n)}$$

- corrector phase:

$$\eta^{I(n+1)} = \bar{\eta}^{I(n+1)} + \Delta\tau_M^2\beta\,\eta_{,\tau\tau}^{I(n+1)}$$

$$\eta_{,\tau}^{I(n+1)} = \bar{\eta}_{,\tau}^{I(n+1)} + \Delta\tau_M\gamma\,\eta_{,\tau\tau}^{I(n+1)}$$

It is assumed that at the beginning of the time step the solution is completely known in terms of the displacement, velocity and acceleration fields. The time steps $\Delta \tau_M$ and $\Delta \tau_m = \Delta \tau_M / K$ are chosen to satisfy the Courant, Friedrichs and Lewy numerical stability conditions for the propagation of stress waves in solids. In particular, to ensure that in the solution the waves do not propagate faster than the actual longitudinal wave speed

$$\Delta \tau_M = \frac{1}{\vartheta} \frac{\Delta \xi_M}{\gamma_L}, \qquad \Delta \tau_m = \frac{1}{\vartheta} \frac{\Delta \xi_m}{\gamma_L} \tag{11}$$

were set, where $\gamma_L = t_g c_L / a_0$ is the normalized speed of longitudinal waves, ϑ a reducing factor, typically assumed $\vartheta = 10$–20. The integer ratio K is kept constant along the whole analysis. According to Table 1, the HMM scheme repeats the step (1) K times in order to cover a single macroscopic step $\Delta \tau_M$. The macroscopic solution can be advanced in time only when the sequence of K microscopic steps is accomplished.

4. Numerical results

The two-stage test described in section 1 has been previously analyzed with finite elements in [9]. The results of those calculations pointed out that during the initial, transient phase of the second stage transversal waves emitted from the crack tip are reflected on the top surface of the layer, affecting the crack growth speed. Once the transient phase is completed, the lamina behaves as a beam, and its response is mainly governed by longitudinally propagating waves.

The macroscopic boundary conditions imposed in the second phase of the analysis are:

$$\eta = \bar{\eta}, \qquad \eta_{,\xi\xi} = 0 \quad \text{at} \quad \xi = 0, \forall \tau$$

$$\eta_{,\xi\xi} = \eta_{,\xi\xi\xi} = 0 \quad \text{at} \quad \xi = \frac{L}{a_0}, \forall \tau \tag{12}$$

i.e., at the left end, the transversal displacement is held fixed, the rotation is free, and the bending moment is null; at the right end, both displacement and rotation are free, while shear and bending moment are null.

The material of the lamina is alumina, characterized by the density $\rho = 3690$ kg/m^3, Young's modulus $E = 260$ GPa, cohesive strength $\sigma_M = 400$ MPa, critical energy release rate $G_c = 34$ J/m^2, and longitudinal wave speed $c_L = 8394$ m/s. In the calculation $\delta = 0.01$ was assumed. A higher value of δ could allow better matching to the finite element simulation results [9], but it would also spoil the solution by introducing severe numerical instabilities.

The dimensions of the specimen are $a_0 = 0.4$ mm, $L = 12$ mm, and $h = 0.2$ mm (b assumed unitary). The ratio L/a_0 is high enough to exclude, in the time interval of interest, wave reflection effects on the crack propagation.

The values of the characteristic times and lengths thus are t_c = 0.0066 μs, t_g = 0.0477 μs, l_c = 55.25 μm, and l_g = 400 μm. The nodal spacings adopted in the simulations are Δx_M = 50 μm for the background grid, and $\Delta x_M \leq 11.05$ μm (at least 5 elements to cover l_c) for the process zone.

Figure 3 shows the crack tip history for two different values of the initially imposed displacement $\bar{u}$.
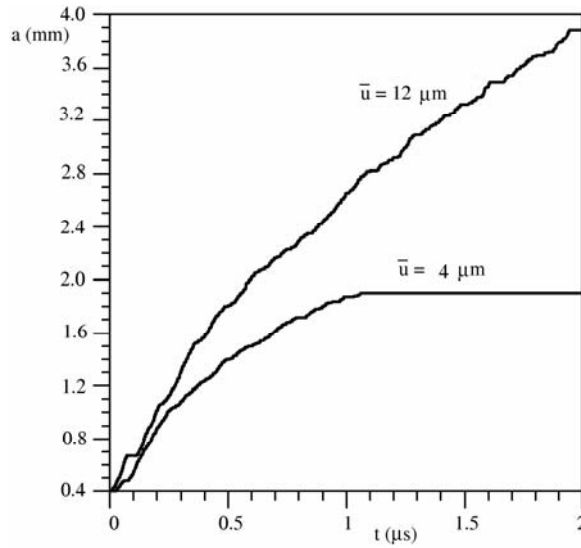

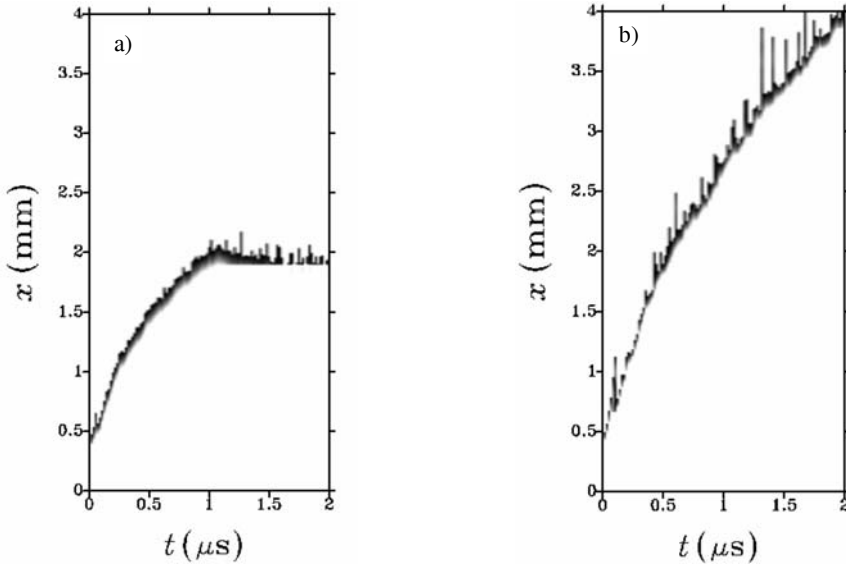Fig. 3. Peel test: effect of the imposed displacement $\bar{u}$ on crack growth

Fig. 4. Peel test: space-time map of the active process zone: a) $\bar{u}$ = 4 μm, b) $\bar{u}$ = 12 μm

Assigning a small initial displacement as $\bar{u} = 4$ μm, the specimen stores a small amount of elastic energy, sufficient to start the dynamic delamination, but not to complete the separation process. In fact, after about 1 μs the crack speed drastically reduces and finally the crack arrests at $a_f = 1.9$ mm. For a bigger initial displacement, as $\bar{u} = 12$ μm, the stored elastic energy is big enough to start and maintain crack growth, although the crack speed monotonically reduces with time.

Figure 4 shows (for the small and large initial displacements), space-time maps of the active process zone location. The dark regions in the plots indicate the region (ahead of the current crack tip), where $u \geq u_c$ and $u_{,t} > 0$. Sudden variations of the process zone length are a consequence of the interaction between the transversal waves released from the crack tip and the layer deformation due to the elastic branch of the cohesive law. Such variation should disappear for high elastic slopes, i.e. for $\delta \rightarrow 0$. It is interesting to observe that, for a given imposed displacement, the extension of the active process zone is generally constant, independent of the effective crack speed, except for the mentioned peaks.

5. Concluding remarks

A simple space-time coupled multiscale approach for the solution of an interesting and difficult problem in composite fracture mechanics, i.e. the delamination under dynamic loading, has been presented. The approach is based on a double discretization of the model, with a coarse grid in the structure and a fine grid, moving with the crack tip location, surrounding the process zone. Time discretization follows the space grids, in order to satisfy Courant's stability requirement. Overall the method is second order accurate. The advantages of such a multiscale method could be exploited for more complicated problems, as in the case of rate-dependent or temperature-dependent materials, where more than two time scales are involved. In future works, concerning rate-dependent material models, it is intended to apply the proposed multiscale methodology to a finite element discretization of the continuum.

References

[1] FREUND L.B., *Dynamic Fracture Mechanics*, Cambridge University Press, 1990.
[2] XU X.-P., NEEDLEMAN A., J. Mech. Phys. Solids, 42 (1994) 1397.
[3] YANG B., RAVI-CHANDAR K., J. Mech. Phys. Solids, 44 (1996), 1955.
[4] PANDOLFI A., KRYSL P., ORTIZ M., Int. J. Fracture, 95 (1999), 1.
[5] ROSAKIS A.J., Adv. Phys., 51 (2002),1189.
[6] COSTANZO F., WALTON J.R., J. Mech. Phys. Solids, 50 (2002),1649.

[7] Yᴜ Q., Fɪsʜ J., Int. J. Solids Struct., 39 (2002), 6429.

[8] Hɪʟʙᴇʀ H.M., Hᴜɢʜᴇs T.J.R., Tᴀʏʟᴏʀ R.L., Earthquake Eng. Struct. Dynamics, 5 (1977), 283.

[9] Cᴀᴍᴀᴄʜᴏ G.T., Oʀᴛɪᴢ M., Int. J. Solids Struct., 33 (1996), 2899.

[10] Cᴏʀɪɢʟɪᴀɴᴏ A., Mᴀʀɪᴀɴɪ S., Pᴀɴᴅᴏʟꜰɪ A., Compos. Sci.e Technol., to appear, 2005.

[11] E W., Eɴɢǫᴜɪsᴛ B., Commun. Math. Sciences, 1 (2003), 87.

[12] Sᴛʀɪᴋᴡᴇʀᴅᴀ J.C., *Finite Difference Schemes and Partial Differential Equations*, Chapman & Hall, 1989.

Influence of the dislocation structure
on the crack tip in highly deformed iron

K. Borysovska[1], V. Slyunyayev[1], Yu. Podrezov[1*],
Z. Pakiela[2], K. Kurzydłowski[2]

[1] Institute for Problems of Materials Science, 3 Krzhizhanovsky, Kiev 03142, Ukraine

[2] Warsaw University of Technology, Faculty of Materials Science and Engineering,
Wołoska 141, 02-507 Warsaw, Poland

Plastic deformation can produce materials with different structural states. Strained BCC-metals have been shown to undergo internal structural developments during plastic deformation. The interaction between quasi-cleavage crack and substructure was studied. The details of the influence of substructure on stress near the crack tip, structure rebuilding near the crack tip and the energy of dislocation movement were analyzed. The essential influence of the deformation substructure on the force and energy parameters of fracture processes was established.

Key words: *structural sensitivity; deformation structure; edge dislocation*

1. Introduction

Both strain hardening and fracture toughness reveal structural sensitivity depending on the interaction of a crack with the dislocation substructure. The hardening curve of each structural state can be approximated by straight lines in $\sigma-e^{0.5}$ true stress, e – true deformation coordinates as shown in Fig. 1. The structural sensitivity of fracture toughness was analyzed in the previous paper [1] as shown in Fig. 2. The main task of modelling is to analyze the interaction of a crack tip and an edge dislocation in the plastic zone with a dislocation substructure (forest of dislocations, cell walls and boundary of nanograin).

The assumption made for model proposed are:

• Fracture mechanism is quasi-cleavage.

• The size of the plastic site created by a dislocation source near the crack tip is not less than the grain size.

_____

* Corresponding author, e-mail: podrezov@materials.kiev.ua

• The external stress is constant, and the evolution of the structure occurs in the real time.
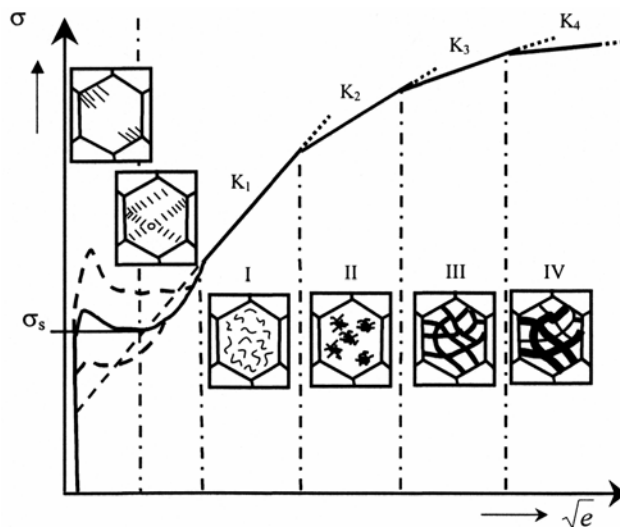
Fig. 1. Deformation hardening curve in σ–$e^{0.5}$ coordinates: I – single dislocations, II – dislocation loops and pile-up, III – low angle cells; IV – high angle cells
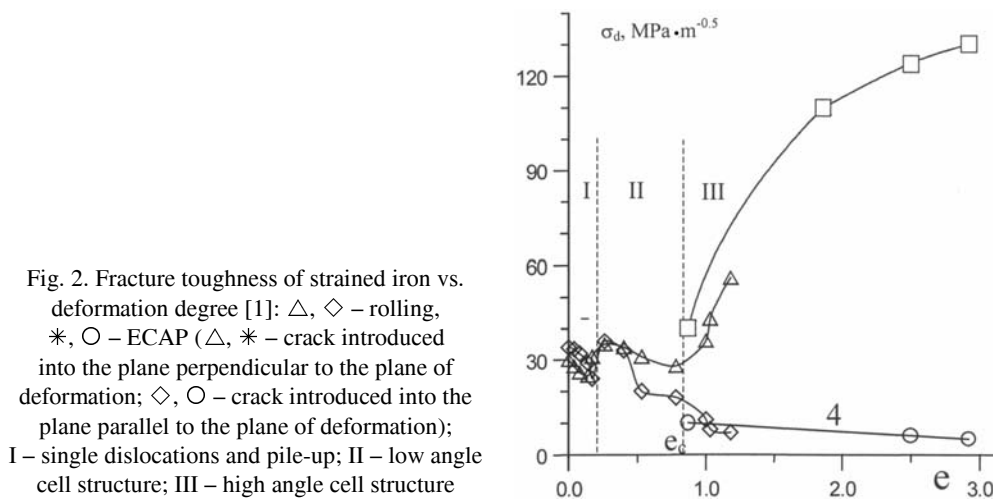
Fig. 2. Fracture toughness of strained iron vs. deformation degree [1]: △, ◇ – rolling, ✳, ○ – ECAP (△, ✳ – crack introduced into the plane perpendicular to the plane of deformation; ◇, ○ – crack introduced into the plane parallel to the plane of deformation); I – single dislocations and pile-up; II – low angle cell structure; III – high angle cell structure

The stress effects on the dislocation near the crack tip are calculated in accordance with Ohr's model [2], and are shown in Fig. 3.

The total stress is obtained by adding the crack stress, which is repulsive, and the image stress which is attractive. The crack stress components are:

$$
\left\{
\begin{array}{l}
\sigma_{22} = \sigma \sqrt{\dfrac{a}{2r}} \cos\dfrac{\Theta}{2}\left(1 + \sin\dfrac{\Theta}{2}\sin\dfrac{3\Theta}{2}\right) \\[3ex]
\sigma_{11} = \sigma \sqrt{\dfrac{a}{2r}} \cos\dfrac{\Theta}{2}\left(1 - \sin\dfrac{\Theta}{2}\sin\dfrac{3\Theta}{2}\right) \\[3ex]
\sigma_{12} = \sigma \sqrt{\dfrac{a}{2r}} \sin\dfrac{\Theta}{2}\cos\dfrac{\Theta}{2}\cos\dfrac{3\Theta}{2}
\end{array}
\right.
$$

where a – length of the crack, r – distance between dislocation and crack tip, Θ – angle between *x*-axis and the line which connects the crack tip.
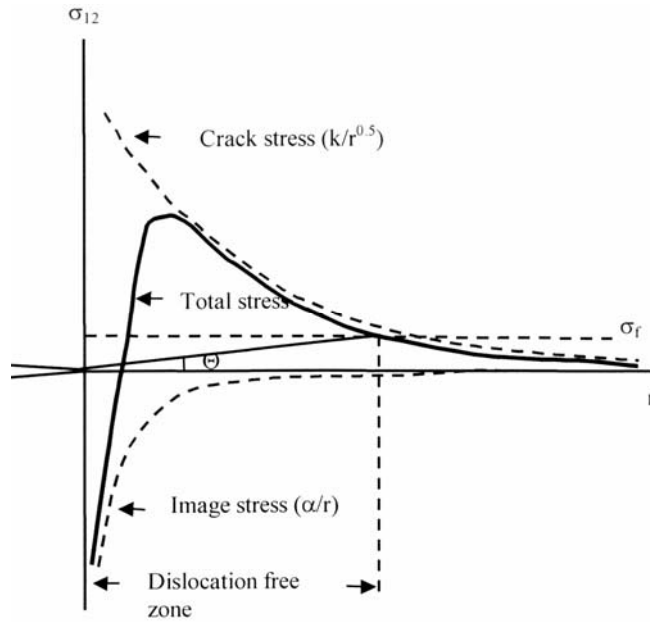
Fig. 3. Stress effects on the dislocation near crack tip [2]

The dislocation can glide if the stress is greater than the friction stress σ_f. In the case, when more than one dislocation remains near the crack tip, the total stress consists of the crack stress, the self-image stress, the image stress from other dislocations [4–6]. The stress component on an edge dislocation 2 (x, y) from edge dislocation 1 can be found from the following expression (Fig. 4):

$$
\sigma_{12} = -\sigma_{11}\cos\beta\sin\beta + \sigma_{22}\sin\beta\cos\beta + \sigma_{12}(\cos^2\beta - \sin^2\beta)
$$

$$
\sigma_{11} = \sigma_{11}\cos^2\beta + \sigma_{22}\sin^2\beta + 2\sigma_{12}\cos\ \beta\sin\beta
$$

$$
\sigma_{22} = \sigma_{11}\sin^2\beta + \sigma_{22}\cos^2\beta - 2\sigma_{12}\cos\ \beta\sin\beta
$$

where

$$\sigma_{11} = \frac{Gb}{2\pi(1-\nu)} \frac{y(3x^2 + y^2)}{(x^2 + y^2)^2}$$

$$\sigma_{22} = \frac{Gb}{2\pi(1-\nu)} \frac{y(x^2 - y^2)}{(x^2 + y^2)^2}$$

$$\sigma_{11} = \frac{Gb}{2\pi(1-\nu)} \frac{x(x^2 - y^2)}{(x^2 + y^2)^2}$$

and b is the Burgers vector, G – shear module, β – angle between x and line, which connects dislocation 1 and dislocation 2.
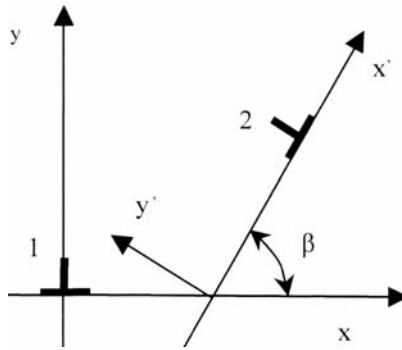
Fig. 4. Edge dislocations located in parallel slip planes

The interaction of a cleavage crack and dislocations emitted from the crack tip with the deformation substructure was calculated. In this paper the following cases of substructures are considered: no wall; chaotic distribution of dislocation; a moving dislocation wall; a non-moving penetrable by a lattice dislocation; and a substructure not penetrable by a lattice dislocation.

The calculated algorithm was achieved as follows:

1 step: to calculate total stress on all moving dislocations at the time t and at a given internal stress (100 MPa.).

2 step: to calculate the speed of each moving dislocation.

3 step: to calculate the new position of each moving dislocation.

4 step: to calculate the stress (σ_{22}) from all the dislocations at the distance $2b$ from the crack tip (σ_d).

5 step: to calculate the movement energy (E) (the increase of movement energy is $\sigma bvdt$) of all moving dislocations (v – rate of dislocation, dt – time step).

6 step: to calculate the stress on the source located at the distance $2b$ from crack tip; if this stress is higher than the yield stress then two dislocations are emitted.

7 step: $t = t + dt$ ($dt = 3\times10^{-13}$ sec) $\Rightarrow$ 1 step.

In this work, the dislocation wall consists of 100 dislocations at the distance $100b$ from the crack tip and has a length of $500b$. The parameters of the material (iron) are: Shear modules $G = 84$ GPa, Burger vector $b = 2.8 \times 10^{-10}$ m, Poisson ratio $\nu = 0.29$, yield stress $\sigma_{yi} = 100$ MPa.

2. Results

The results of our calculation are shown in Figs. 5–9.
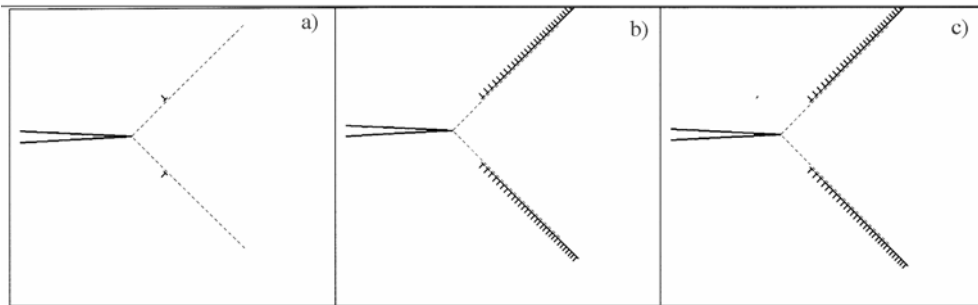
Fig. 5. Movement of dislocations emitted from crack tip in ironcrystal of iron without deformation substructure (case I): a) $t = 1 \times 10^{-13}$ sec, $E = 3 \times 10^{-6}$ J, $\sigma_d = -3 \times 10^3$ MPa, b) $t = 50 \times 10^{-13}$ sec, $E = 1.74 \times 10^{-4}$ J, $\sigma_d = -8.1 \times 10^3$ MPa, c) $t = 100 \times 10^{-13}$ sec, $E = 3.62 \times 10^{-4}$ J, $\sigma_d = -1.37 \times 10^5$ MPa
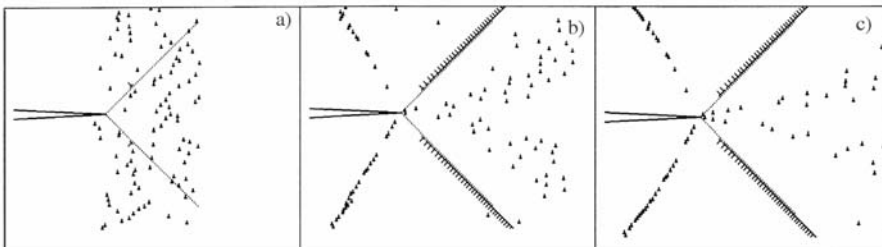
Fig 6. Movement of dislocation near crack tip on monocrystal of iron with chaotic distribution of dislocation (case II): a) $t = 1 \times 10^{-13}$ sec, $E = 3 \times 10^{-6}$ J, $\sigma_d = -3 \times 10^3$ MPa, b) $t = 50 \times 10^{-13}$ sec, $E = 1.60 \times 10^{-4}$ J, $\sigma_d = -9.1 \times 10^4$ MPa, c) $t = 100 \times 10^{-13}$ sec, $E = 3.18 \times 10^{-4}$ J, $\sigma_d = -1.47 \times 10^5$ MPa
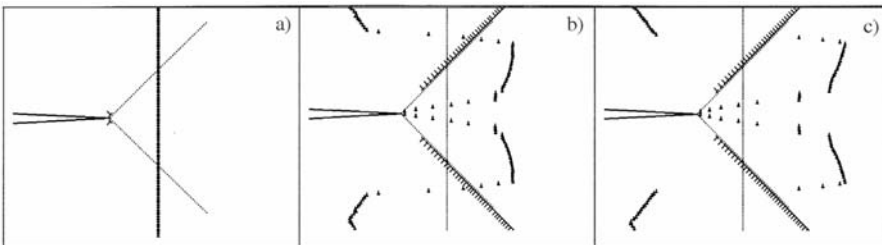
Fig. 7. Movement of dislocation near crack tip in iron crystal with moving dislocation wall (case III): a) $t = 1 \times 10^{-13}$ sec, $E = 2.7 \times 10^{-6}$ J, $\sigma_d = -6 \times 10^3$ MPa, b) $t = 50 \times 10^{-13}$ sec, $E = 1.60 \times 10^{-4}$ J, $\sigma_d = -9.5 \times 10^4$ MPa, c) $t = 80 \times 10^{-13}$ sec, $E = 2.522 \times 10^{-4}$ J, $\sigma_d = -1.28 \times 10^5$ MPa
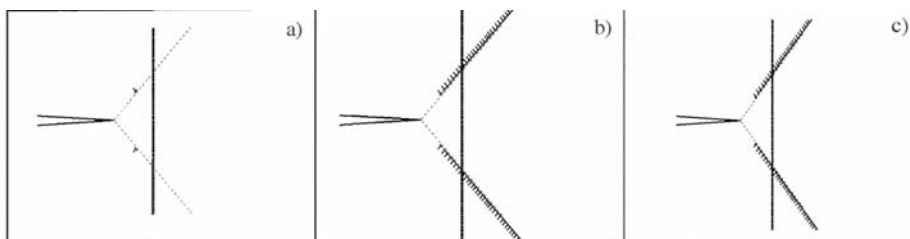
Fig. 8. Movement of dislocation emitted from crack tip in iron crystal with nonmoving wall, penetrable by dislocation (case IV): a) $t = 1\times10^{-13}$ sec, $E = 2\times10^{-6}$ J, $\sigma_d = -10\times10^3$ MPa, b) $t = 50\times10^{-13}$ sec, $E = 1.40\times10^{-4}$ J, $\sigma_d = -8.9\times10^4$ MPa, c) $t = 100\times10^{-13}$ sec, $E = 3.006\times10^{-4}$ J, $\sigma_d = -1.47\times10^5$ MPa
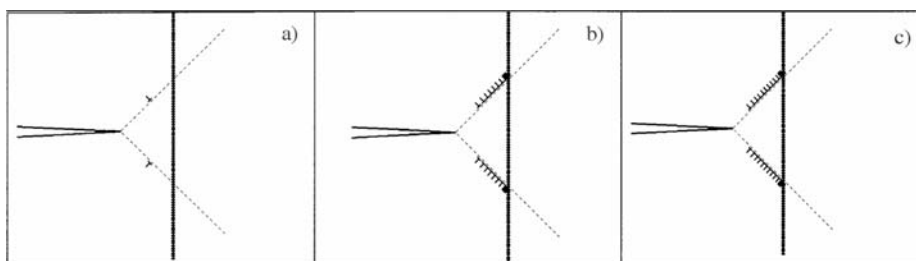
Fig. 9. Movement of dislocation emitted from crack tip in iron crystal with nonmoving wall, nonpenetrable for dislocation (case V): a) $t = 1\times10^{-13}$ sec, $E = 2\times10^{-6}$ J, $\sigma_d = -10\times10^3$ MPa, b) $t = 50\times10^{-13}$ sec, $E = 1.19\times10^{-4}$ J, $\sigma_d = -1.16\times10^4$ MPa, c) $t = 1\times10^{-11}$ sec, $E = 2.02\times10^{-4}$ J, $\sigma_d = -2.26\times10^5$ MPa

The dependence of movement energy on time is shown in Fig. 10.
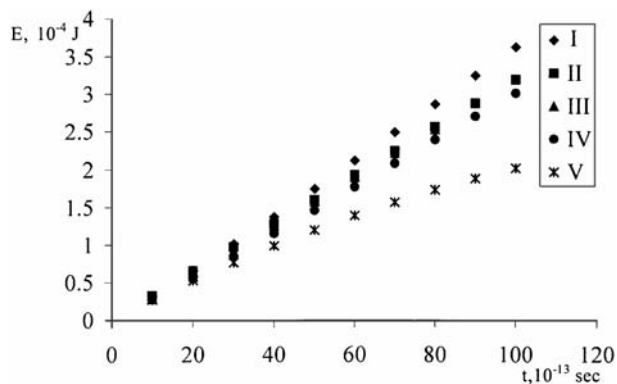
Fig. 10. The dependence of movement energy on time

The faster growth of energy is observed in case I (no substructure); in this case the substructure does not block the dislocation movement, which leads to energy growth. In case II (chaotic distribution) the substructural influence is weak, so energy growth in this case is higher than in case III (moving wall). Dislocations emitted from the crack tip mainly influence the energy in the selected parameters (high external stress), because it is located near the crack tip. Therefore, there is no essential difference be-

tween the energy in case III (movement wall) and case IV (non moving penetrable wall). In case V (non moving non penetrable wall) the energy is the lowest, because in this case the movement of dislocations is limited.

The dependence of σ_d (with inverse sign) on time is shown in Fig. 11.
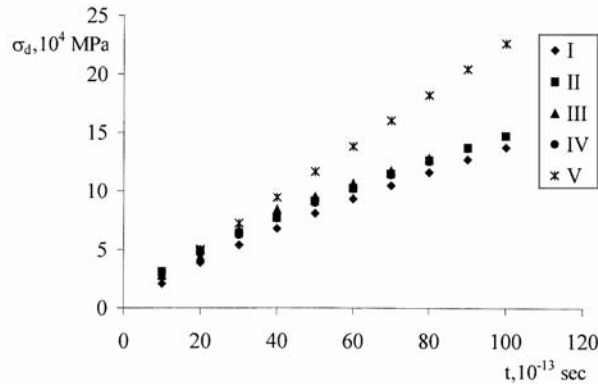
Fig. 11. The dependence of σ_d (with inverse sign) on time

The lower growth of σ_d is observed in case I (no substructure), in this case the substructure does not block the emitted dislocations and its movement away from the crack tip. There is no large difference between case II (chaotic distribution), case III (moving wall) and IV (nonmoving penetrable wall). Therefore, the wall cannot block the emitted dislocations at high external stress. In case V (nonmoving nonpenetrable wall) the σ_d growth is the faster, because in this case emitted dislocations are blocked and interact with the crack tip, causing blocking the emission of dislocation and suppression of crack development.

3. Conclusions

The interaction between a quasi cleavage crack and the substructure was studied. The details of the influence of substructure on the stress near crack tip, structure rebuilding near the crack tip and the energy of dislocation movement were analyzed. There is an essential influence of the deformation substructure on the force and energy parameters of the fracture processes. In this case the influence of a number of dislocations is lower than the influence of the substructure tip.

In case V (nonmoving nonpenetrable wall) the value of stress is essentially higher than in penetrable walls case, though the movement energy is lowest in this case. In cases II (chaotic distribution), III (moving wall) and IV (nonmoving penetrable wall) the difference between current movement energy or force parameter σ_d is not high, which is similar to the fracture toughness shown in Fig. 2.

References

[1] PODREZOV YU.N., DANILENKO N.I ., KOPYLOV V.I., FIRSTOV S.A, Phys. High Pressure, 11 (2001), 33.

[2] OHR S.M., Mater. Sci. Eng., 72 (1985), 1

[3] NOTT J., *Fundamentals of Fracture Mechanics*, Butterworths, London,1978.

[4] FERNEY B.D., HSIA K.J., Mater. Sci. Eng., A260 (1999), 1.

[5] HIRSCH P.B., ROBERTS S.G., SAMUELS J., Proc. R. Soc. London, A421 (1989), 25.

[6] BORYSOVSKA K.M., PODREZOV YU.M., SLYUNYAYEV V.M., Electron microscopy and material strength, (In Russian), (2002), 3

Finite element modelling of the residual stresses in the ceramic-elastomer composites

Anna Boczkowska[1*], Katarzyna Konopka[1], Kamil Babski[1],
Grzegorz Krzesiński[2], Krzysztof J. Kurzydłowski[1]

[1]Warsaw University of Technology, Faculty of Materials Science and Engineering,
Woloska 141, 02-507 Warsaw, Poland

[2]Warsaw University of Technology, Institute of Aeronautics and Applied Mechanics,
Nowowiejska 24, 00-665 Warsaw, Poland

Ceramic-elastomer composites are obtained by the infiltration of porous ceramics by an elastomer prior to the curing reaction at elevated temperatures. Because the elastomer and the ceramic have different expansion coefficients thermal stresses are generated during cooling to ambient temperature. In addition the elastomer contracts as it transforms from a mixture of the substrates in the liquid state to the solid state polymer with a covalently bonded network structure. These two phenomena result in the development of residual stresses in the composite. Residual stresses are of significant concern because they can cause damage in the form of cracks in the ceramic and delamination between the ceramic and the elastomer. They can also have an effect on the mechanical properties of the composite. The aim was to model in 3D space the residual stresses in the composites with two different interpenetrating phases. The Finite Element Method (FEM) was used to calculate the stresses

Key words: *ceramic-elastomer composites; residual stresses; Finite Element Method; infiltration*

1. Introduction

Ceramic-elastomer composites are obtained by infiltrating porous ceramics with urea-urethane elastomers [1]. As a result composites of two interpenetrating phases are obtained [2, 3]. They possess hardness and stiffness of ceramics with the rubbery entropy-elasticity of elastomers. Such composites are distinguished by high compression strength and the ability to achieve large deformations [4–6] as well as the ability to absorb impact energy.

---

[*]Corresponding author, e-mail: abocz@meil.pw.edu.pl

The infiltration of the ceramic with the elastomer is made before it undergoes its curing reaction. The elastomer is synthesized by a one-shot method. The liquid mixture of the substrates is incorporated into ceramics pores using vacuum pressure at a temperature of 120 °C. Then the addition reaction is conducted at this temperature [7, 8]. Because the thermal expansions of the elastomer and ceramics are different, cooling to ambient temperature results in the buildup of residual stresses in the composite. Additional residual stresses arise due to the elastomer's shrinkage as a consequence of the transformation from the liquid mixture of the substrates to the solid state polymer with a covalently bonded network structure. The adhesion between SiO_2 ceramics and urea-urethane elastomer is fairly good and could be improved by the addition of coupling agents. Good adhesion between the components of the composite is very important from the mechanical point of view [9–11].

The residual stresses developed in the composite by the thermomechanical mismatch between the ceramic and the elastomer during cooling from the fabrication temperature are of significant concern because they can cause damage in the form of ceramics cracks and delaminations between the ceramic and the elastomer as well as affect mechanical properties of the composite [12, 13].

The aim of the studies was to develop a 3D numerical model describing the residual stresses in composites with two different interpenetrating phases. The residual stresses were calculated using the Finite Element Method (FEM). Scanning Electron Microscopy (SEM) was used to determine the microstructure and stereological methods for its quantitative analysis [14].

2. Experimental

Cylindrical porous SiO_2 samples of the diameter of 20 mm and 20 mm high were obtained. The average open porosity measured by the Archimedes method was 40%. The average pore size measured using the mercury porosimeter was 145 µm. The average apparent density of the samples was 1.43 g/cm^3.

Cast segmented polynitrile-urea-urethane elastomer (PNUU) with linear macromolecules structure was used for the infiltration of the SiO_2. It was obtained from 4,4′-diphenylmethane diisocyanate (MDI), ethylene oligoadipate (OAE) and dicyandiamide (DCDA). The PNUU elastomer was synthesized by a one-shot method. Subsequently, the mixture was cast into special moulds with the porous ceramic samples inside and heated to 120 °C. Next the infiltration process was carried out [1]. The elastomer was cured for 10–14 hours at 120 °C. The samples were then cooled to room temperature and conditioned for two weeks.

Observations of the microstructure of the composites were carried out using a scanning electron microscope (SEM) HITACHI S-3500N, equipped with a low -vacuum mode. Quantitative analysis of the microstructure of the composites was carried out using the stereological methods [14]. MicroMeter software was used to

estimate the following parameters: volume fraction of elastomeric phase (V_V) and specific surface of the boundaries of elastomer (S_V). FEM analysis was conducted using the ANSYS software, version 6.1.

3. Results and discussion

Observations of the microstructure of ceramic-elastomer composite were carried out using a scanning electron microcsope. A typical image of the microstructure and its binary form are shown in Fig. 1.
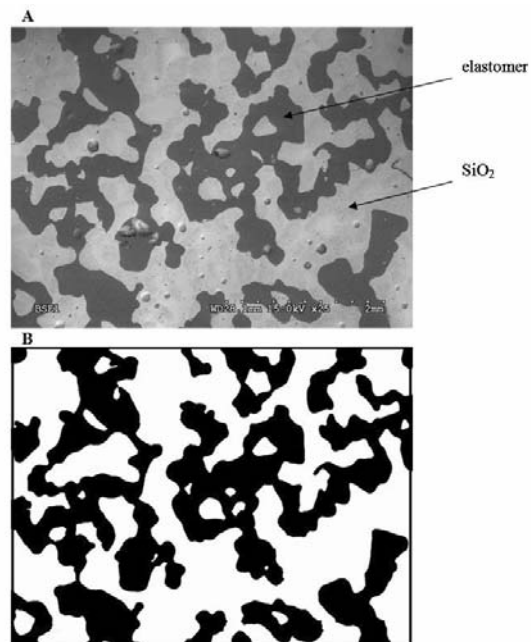
Fig. 1. SEM image of the ceramic-elastomer microstructure (A) and its binary form (B)

It can be seen that the elastomer has infiltrated into the pores of ceramic matrix. Quantitative analysis of the composite's microstructure was carried out to estimate the volume fraction of the elastomeric phase and the specific surface of the boundaries of the elastomer, using stereological methods. The results are shown in Table 1.

Table 1. Results of stereological analysis of ceramic-elastomer composite microstructure

Sample	V_V	S_V [mm^{-1}]
III 29	0.40	3.92
III 37	0.40	4.38
III 41	0.32	3.94
III 33	0.38	4.41

Materials data for the PNUU elastomer and SiO_2 ceramics which were used for the residual stress calculations, are given in table 2. It can be seen that the ceramics and elastomer possess significantly different stiffness and thermal expansion characteristics.

Table 2. Selected properties of PNUU and SiO_2

Properties	PNUU	SiO_2
Elastic modulus, MPa	27	47000
Poissons ratio	0.23	0.49
Thermal expansion coefficient, 1/K	2.1×10^{-4}	0.5×10^{-6}

3-D unit cell Finite Element Models were developed for the ceramic-elastomer composite material. It was assumed that the microstructure presented in Fig. 1 could be described as a composite consisting of a ceramic matrix filled with elastomer particles. The representative unit cell, shown in Fig. 2, is hexahedral and includes the elastomer particles in three corners.
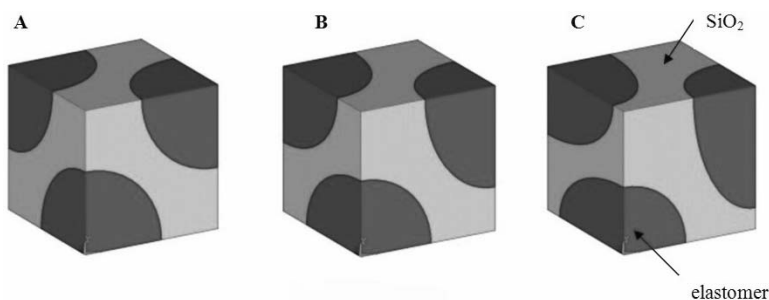
Fig. 2. The 3-D representative unit cell FE models of ceramic-elastomer
microstructure: A) model 1, B) model 2, C) model 3

Figure 2 shows that the shape of the particles changes from spherical to ellipsoidal, but the volume fraction of elastomeric phase is constant at 0.40. 3D FE models were chosen for their advantages over axisymmetric and two-dimensional versions. It was assumed that all the particles in each model have the same dimensions and orientation and are uniformly distributed. The ceramic and elastomer are isotropic in stiffness and thermal expansion. Perfect bonding between the ceramic and the elastomer was also assumed. The temperature in the composite was assumed to be homogeneous at all times.

The unit cells were subjected to a thermal load simulating the cooling from the fabrication (120 °C) to room temperature (20 °C). The distributions of principal stresses in the dual phase composite material, obtained by infiltration of the porous skeleton, calculated for each assumed model with the ANSYS 6.1 software, are shown in Figs. 3 and 4.
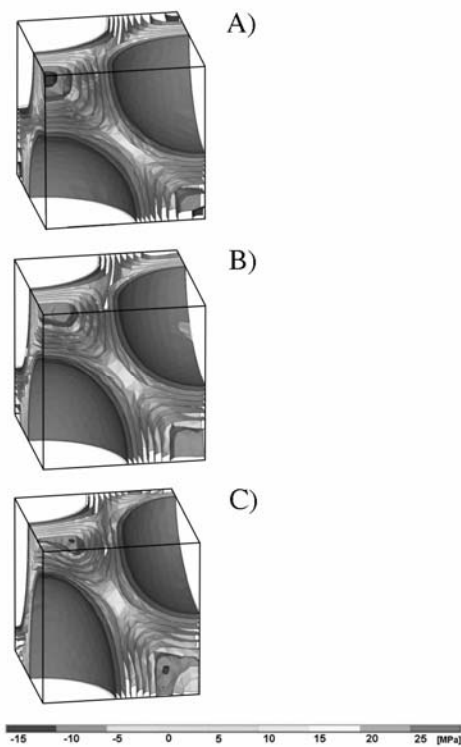
Fig. 3. The maximum principal stresses distribution σ_1 in: A) model 1, B) model 2, C) model 3
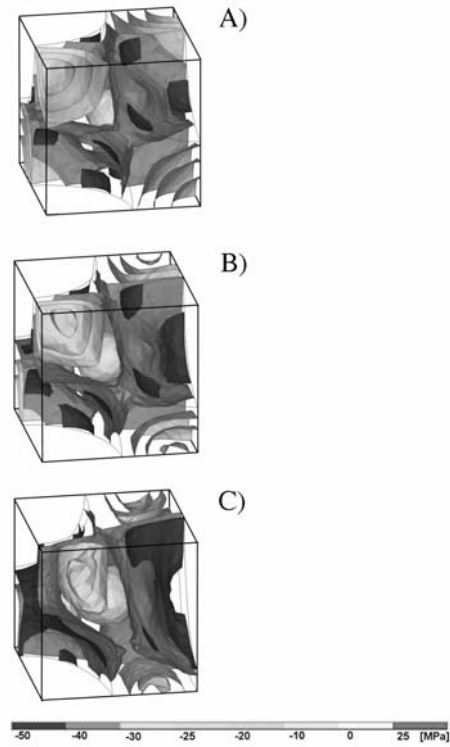
Fig. 4. The minimum principal stresses distribution σ_3 in: A) model 1, B) model 2, C) model 3

4. Conclusions

Residual stresses are often induced in composite materials when they cool from the fabrication temperature to room temperature. This is mainly due to the difference in the coefficients of thermal expansion of the components. The induced stresses were studied using a fully three-dimensional termomechanical model for ceramic-elastomer composites obtained by infiltration of porous ceramics by an elastomer. It was found that elastomeric phase is characterized by an almost uniform tensile stresses. The maximum principal stress distribution σ_1 is weakly dependent on the shape of the elastomeric particles and is more uniform than the minimum principal stresses distribution σ_3. The σ_3 values in the ceramics are mainly compressive. The change of the shape of elastomeric particles from spherical to ellipsoidal leads to a growth of compressive stresses in tangential directions in the ceramic phase which is mechanically advantageous. However, these stresses could also cause debonding between the ceramic and elastomer phases. Further analysis of the results and their interpretation for understanding the mechanical properties of the composites are in progress.

References

[1] SZAFRAN M., BOCZKOWSKA A., KONOPKA K., KURZYDŁOWSKI K., ROKICKI G., BATORSKI K., PL patent No. P.353130 (2002).

[2] KONOPKA K., BOCZKOWSKA A., BATORSKI K., SZAFRAN M., KURZYDŁOWSKI K.J., Mater. Lett., 58 (2004), 3857.

[3] KONOPKA K., BOCZKOWSKA A., SZAFRAN M., KURZYDŁOWSKI K.J., Kompozyty, 7 (2003), 216.

[4] KONOPKA K., BOCZKOWSKA A., BATORSKI K., KURZYDŁOWSKI K.J., SZAFRAN M., Kompozyty, 3 (2002), 108.

[5] BOCZKOWSKA A., KONOPKA K., KURZYDŁOWSKI K.J., 12th Achievements in Mechanical & Materials Engineering, AMME 2003, Zakopane, Conference Proceedings, p. 111.

[6] KONOPKA K., BOCZKOWSKA A., SZAFRAN M., KURZYDŁOWSKI K.J., European Congress and Exhibition on Advanced Materials and Processes Euromat 2003, Lozanna.

[7] PL Patent 148 671 (1990).

[8] PL Patent 150 154 (1991).

[9] BOCZKOWSKA A., KAPUŚCIŃSKI J., LINDEMANN Z., WITEMBERG-PERZYK D., WOJCIECHOWSKI S., *Kompozyty*, II Ed., Oficyna Wydawnicza PW, Warszawa, 2003.

[10] BOCZKOWSKA A., KONOPKA K., KURZYDŁOWSKI K.J., Materiały polimerowe Pomerania-Plast, 2004, Szczecin, Conference Proceedings, 65.

[11] BOCZKOWSKA A., KONOPKA K., SCHMIDT J., KURZYDŁOWSKI K.J., Kompozyty, 9 (2004), 41.

[12] GOLAŃSKI D., Kompozyty, 2 (2002), 5.

[13] CHOO H., BOURKE M.A.M., *Evolution of thermal residual stress in intermetallic matrix composites during heating*; Ceramic Engineering and Science Proc. ACerS, 21 (2000), 627.

[14] KURZYDŁOWSKI K.J., RALPH B., *Quantitative Description of Microstructure of Materials*, CRC Press, Boca Raton, FL, 1995

Percolation threshold model and its application to the electrical conductivity of layered BaTiO$_3$–Ni

M. AMBROŽIČ[*], A. DAKSKOBLER, M. VALANT, T. KOSMAČ

Jožef Stefan Institute, Jamova 39, 1000 Ljubljana, Slovenia

The electrical conductivity percolation threshold of the materials composed of conducting particles embedded in a non-conducting host matrix has been investigated. A statistical, numerical method was used, in which the particles are randomly placed, one by one, into the non-conducting host, and the conducting path is searched. The influence of different particle shapes on the percolation threshold is considered. It has been found that, in addition to the anisotropy in the dimensions of particles, the angular distribution of their long axes plays a dominant role in the calculations of the conductivity percolation threshold. Finally, the non-uniform space distribution of positions of particles is taken into account and the model is used to analyze the percolation threshold of the AC conductivity of layered BaTiO$_3$–Ni composites.

Key words: *conductivity percolation threshold; particle shape; orientational order; layered structure*

1. Introduction

When electrically conducting particles are randomly distributed within an insulating matrix such as metal-ceramic matrix composites, the sample is non-conducting, until the volume fraction of the conducting phase reaches the so-called percolation threshold. In addition, close to the percolation threshold, the electrical properties show a nonlinear (critical) behaviour: small variations in the physical parameters, such as composition, voltage or temperature, result in large variations of electrical properties [1–4]. In order to control the electrical characteristics of such systems, it is very important to have exact knowledge of the percolation threshold. Models using particles of different shapes, mostly spheres, rods and fibres, were employed for the reported calculations of the percolation threshold, not only for electrical conductivity but also for other characteristics of interest. Different models are applied for different particle size distributions [5–9]. Barberg et al. [8] and De Bondt et al. [9] studied the important and more realistic systems of capped cylinders.

---

[*]Corresponding author, e-mail: milan.ambrozic@ijs.si

The percolation-threshold volume fraction when the morphology of the conducting phase develops from a spherical to a brick-like shape was studied. The application of the developed model for a rough explanation of the electrical conductivity percolation threshold of a layered $BaTiO_3$–Ni composite with ribbon-like microstructures, in the direction perpendicular to the layers [10–12] was required. The rolling-and-folding technique was applied to produce a layered $BaTiO_3$–Ni composite with a ribbon-like microstructure. Laminates were obtained by rolling an initial stack of two layers: an insulating one of pure $BaTiO_3$ and a conducting one in which the volume fraction of doped Ni in $BaTiO_3$ was 50%, i.e., above the percolation threshold for the layer itself. By repeated folding and rolling several alternating conducting and insulating layers were produced. The width of the laminate at the end of this procedure was the same as the initial pair of layers, so that any single layer was much thinner than at the beginning of the process. The sintered samples with different numbers of foldings were prepared in order to compare the **AC** electrical conductivity after sintering. The microstructures of the sintered composites were observed using an optical microscope.
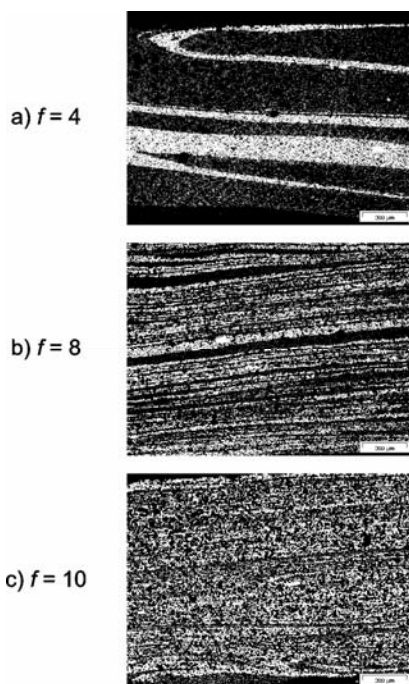
Fig. 1. Microstructure of layered $BaTiO_3$–Ni composite
after 4 (a), 8 (b) and 10 (c) foldings

One of the interesting features of such composites is the enormous change of the electrical conductivity in the direction perpendicular to the layers, clearly resulting from the development of their microstructure after a sufficient number of foldings f. After $f = 4$ or 5 the layers start to undulate with random phase shifts. This makes it

possible for the nearest conducting layers to adhere and make an electrical contact. Furthermore, the conducting layers even start to disintegrate after $f = 10$. Figure 1 shows the development of microstructure when $f = 4$, 8 and 10. For $7 < f < 10$ the layers seem to stick together at individual contact points, and this produces the conductivity threshold. After $f = 10$ the conductivity drops as the system is below the percolation threshold.

2. The model

A rectangular cell with dimensions L_x, L_y and L_z, was taken with the plates at $z = 0$ and $z = L_z$, as the electrodes as shown in Fig. 2. Thus the conductivity in the z-axis direction was investigated. Conducting particles in three dimensions with three different shapes: a) spherical (called *spheres*), b) cylindrical rods with half-spheres at the ends (capped cylinders, also called *sticks*), and c) cuboids rounded by half-cylinders and quarter-spheres (called *bricks*) were considered. Mathematical details of the computational procedure are given in [13]. The procedure consists of randomly inserting particles, one by one, into the cell, and checking for the conducting path between the electrodes.

Going from spheres to rounded bricks more parameters and degrees of freedom are needed. For a particular sphere we need three coordinates for the position of its centre and the diameter d of the sphere. The dimensions of a particular stick are given by two variable parameters: the diameter d of the cylinder and spherical caps, and the length-to-diameter aspect ratio: $L/d \geq 1$. In contrast to the spheres, the sticks have two additional degrees of freedom: two angles, θ and φ, defining the direction **k** of the particle long axis with respect to the z-axis of the system (Fig. 2).

Fig. 2. Coordinate system of rectangular cell and three types of particles.
Definition of the directional vectors for non–spherical particles

The dimensions of a particular brick are given by three variable parameters: the width, W, and two aspect ratios: the length-to-width aspect ratio, L/W, and the height-to-width aspect ratio, H/W. $H \leq W \leq L$ was always applied. The bricks have another degree of freedom, the spin angle ψ, which measures the rotation 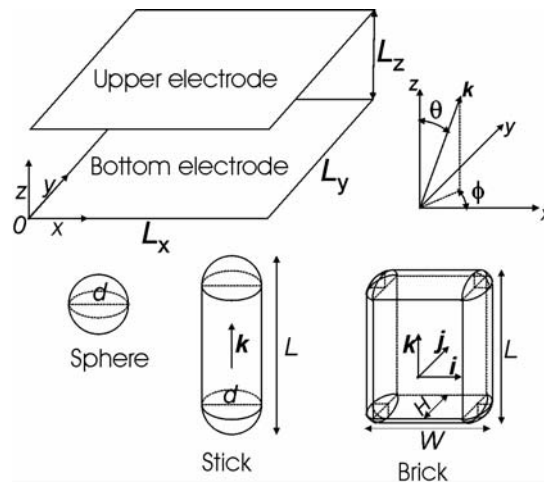of the particle around its long axis. For computational purposes the three unit directional vectors $\boldsymbol{i}$, $\boldsymbol{j}$ and $\boldsymbol{k}$, defining the directions of the edges of the rectangular part of the brick were used (Fig. 2).

In layered composites the distributions of the centres of gravity of particles are non-uniform in the direction perpendicular to the layers. In the simple model, the undulation of layers and study of the "layers" after disintegration were disregarded. An even number of equally thick layers, regarding the odd ones as "conducting" and the even ones as "non-conducting" were taken. When the conducting layers break apart, they are split into smaller conducting objects (rounded bricks, which were taken as the simulation particles), which can rotate in space to some degree and their centres of gravity get redistributed.

3. Results and discussion

The percolation volume v_p for spherical particles was calculated mainly to compare the results with the literature data, to test the reliability of the method, and to adjust some parameters, e.g. the appropriate sizes of particles with respect to the cell dimensions. In the calculations, a typical absolute statistical deviation of the results is 1%. The percolation volume for the sticks depends strongly on the L/d aspect ratio and on the distribution of the long-axis orientation of the particles. The results agree, within the numerical error, with published results [8, 9]. It is believed that this was the first study using rounded bricks. The main conclusions are similar to those for sticks, where for obtaining lower percolation thresholds, larger aspect ratios between dimensions of the bricks are generally advantageous. Also, regarding the distribution of long axes of particles in space (**k**-vectors), the results are similar to those for sticks.

It was found that once the particles were long enough (of the order of the layer thickness), the position order/disorder (e.g. the number and thickness of layers, etc.) is not crucial for the percolation volume. What is important, are the aspect ratios of dimensions of particles and their orientational distribution in space as is the case with the non-layered structures. The average orientation of long axes of particles parallel to x-axis was taken, allowing different deviations of individual long axes of particles from this direction. In addition, the spin angle rotations were allowed. For reasonable values of parameters (aspect ratios, etc.) the percolation volumes for bricks are well below 50%, which is enough for conduction, because conducting layers gave 50% of the total layers.

It is concluded that it is quite probable that the electrical conductivity is preserved in the z-axis direction as soon as the layers disintegrate. This contradicts the observation that the percolation threshold is not established after the disintegration of the layers. The most probable answer to this contradiction is that after disintegration of

the conducting layers their pieces also slowly "dissolve". This means that nickel spherical precipitates diffuse out of BaTiO$_3$–Ni groups into the pure BaTiO$_3$ phase. Thus, the pieces of the broken conducting layers themselves become nonconducting. On the other hand, the layers after undulation and before complete disintegration ($7 < f < 10$) may be roughly treated as the sticking groups of still-conducting bricks, which also touch the bricks from neighbouring conducting layers, so that the conductivity is established in all directions.

4. Conclusions

Typical percolation volumes for spherical conducting particles in an insulating matrix, obtained with the calculations and reported in the literature (calculations and experiments [6–9]), are between 30% and 40%. With non-spherical particles with a relatively large aspect ratio, much smaller percolation thresholds and, if the particles are at least partially orientationally ordered, anisotropic electric properties are obtained. An alternative and perhaps easier method for achieving similar behaviour is by producing layered composites, including conducting particulate and pure ceramic insulating layers. In this case, the layered BaTiO$_3$–Ni composite, containing only 25 vol. % of nickel, is considered. By using percolation-threshold numerical method a possible explanation for the behaviour of the electrical conductivity of materials in the direction perpendicular to the layers has been found.

References

[1] EFROS A.L., SHKLOVSKII B., Phys. Stat. Sol., 76 (1976), 475.
[2] LISJAK D., DROFENIK M., KOLAR D., J. Mater. Res., 15 (2000), 417.
[3] GUSEV A.A., GUSEVA O.A., Adv. Eng. Mater., 5 (2003), 713.
[4] GRANNAN D.M., GARLAND J.C., TANNER D.B., Phys. Rev. Lett., 46 (1981), 375.
[5] LUX F., J. Mater. Sci., 28 (1993), 285.
[6] LORENZ C.D., ZIFF R.M., J. Chem. Phys., 114 (2001), 3659.
[7] PIKE G.E., SEAGER C.H., Phys. Rev. B, 10 (1974), 1421.
[8] BALBERG I., BINENBAUM N., WAGNER N., Phys. Rev. Lett., 52 (1984), 1465.
[9] DE BONDT S., FROYEN L., DERUYTTERE A., J. Mater. Sci., 27 (1992), 1983.
[10] MENON M., CHEN I-W., J. Am. Ceram. Soc., 82, (1999), 3413.
[11] CHEN I-W., WINN E.J., MENON M., Mat. Sci. Eng. A, 241 (2001), 226.
[12] DAKSKOBLER A., KOSMAČ T., CHEN I-W., J. Am. Ceram. Soc., 85, (2002), 1013.
[13] AMBROŽIČ M., DAKSKOBLER A., VALANT M., submitted to Eur. Phys. J., Appl. Phys.

Influence of the packing effect
on stability and transformation of nanoparticles
embedded in random matrices

HELMUT HERMANN[*], ANTJE ELSNER, THOMAS GEMMING

Institute for Solid State and Materials Research, IFW Dresden, PF 260116, D-01171 Dresden, Germany

The compression of random hard sphere systems does not lead to the formation of iscosahedral short-range order. Instead, icosahedral clusters embedded in a hard sphere system with a medium packing fraction are not stable against densification and they dissolve with an increasing packing fraction. Random homogeneous hard sphere models with equal spheres transform into nanometre scale composites of face-centred cubic nanocrystals embedded in a dense random packed matrix when the mean packing fraction of 0.64 is exceeded

1. Introduction

There are experimental indications for the existence of clusters embedded in the matrix of the material in liquid and amorphous metallic alloys where the clusters and matrix differ with respect to their short-range order. Five-fold local symmetry [1] and icosahedral short-range order [2] have been recently detected in liquid metals. These experimental results re-activated the discussion about the classical icosahedron as a possible characteristic of the structure of simple liquids [3, 4]. Amorphous metallic alloys prepared from the liquid are often believed to retain some form of structural elements preformed in the melt. The formation of quasicrystalline particles observed in several metallic glasses could be a consequence of frozen-in icosahedral clusters. On the other hand, ultrafine crystalline particles of size about 1nm were detected in a series of amorphous metallic alloys [5–9]. The question of the existence or absence of clusters in liquids is relevant to the basic understanding of the structure of liquids.

_____

[*] Corresponding author, e-mail: h.hermann@ifw-dresden.de

With respect to amorphous metallic alloys it is known that nanometre scale precipitates may have considerable influence on the properties of the material.

The experimental observation of clusters or particles with diameters of the order of magnitude of 1nm is difficult and in most cases it is necessary to compare experimental data with model calculations in order to obtain reliable information. Important methods for this purpose are the simulation of high-resolution electron microscopy images [10] and the calculation of the scattering data [11].

There is a rich body of theoretical work on structure optimization and stability of isolated clusters. Frank [3] showed that a cluster consisting of 13 atoms interacting through a Lennard–Jones potential is most stable if there is a central atom surround by 12 neighbours situated on the vertices of an icosahedron. Detailed recent cluster calculations investigated the role of the interatomic potential and the dependence of structure and stability on the number and the type of atoms forming the cluster [12–14]. The problem of the formation of clusters with icosahedral order in extended systems of the order of 1000 atoms with periodic boundary conditions was studied [15–19] for different interaction potentials. While the simulations [15–19] led to local arrangements of atoms showing features of icosahedrality, the ab-initio calculations for liquid iron [20] resulted in structures characterized by pair distribution functions, which did not show the specific shape characteristic of icosahedral order. The ab-initio calculations are, of course, most accurate with respect to the interaction of atoms. They are, however, restricted to about one hundred atoms and are therefore not well suited to study the properties of clusters embedded in a liquid or amorphous matrix since a single cluster may already consist of about one hundred atoms.

The simplest approach to study systems of many particles is the hard sphere model. A review of the statistical theory of the packing of hard spheres is given in [21]. Both the quality of the algorithms and the range of applications of the hard sphere model have been developed continuously. Systematic investigations of binary mixtures of hard spheres [22] and continuous (truncated log-normal) distributions of radii [23], and the generalization of the so-called force-biased algorithm [24, 25] are important steps during this development. General problems of hard-sphere structures such as the question of whether or not random close packing of spheres is mathematically well-defined were also considered [26]. Investigations using packing algorithms are accompanied by molecular dynamics studies with hard spheres considering metastability and crystallization behaviour in hard-sphere glasses [27, 28].

In this paper, the model of hard spheres is used to study the behaviour of icosahedral and crystalline clusters in liquid and amorphous metals and metallic alloys. The repulsive interaction of two atoms is controlled by the hard core radii of the atoms which is the only parameter discriminating between different types of atoms. The attractive interaction is simulated by compressing the system of spheres using the described force-biased algorithm [25]. Periodic boundary conditions are applied to avoid surface effects.

2. Method

The first step in the simulation process is the preparation of an initial set of coordinates for the centres of the spheres. Two initial structures were considered: A random uncorrelated homogeneous distribution of coordinates (type 1) and icosahedral clusters embedded in a matrix of random uncorrelated coordinates (type 2). Each coordinate marks the centre of a sphere but the radii of the spheres may vary.

The second step is the densification of the system. The size of the systems analyzed ranged from 10 000 to 100 000. Systems with equal spheres and binary models are studied. In the latter case, the ratio of the diameters was 0.90 which corresponds to the ratio of the diameters of the central sphere to that of the outer spheres in an ideal icosahedral cluster.

The concept of a local packing fraction is used to characterize a given model. This structure parameter characterized the local environment of a sphere and is defined by the ratio of this sphere volume to the volume of its S-Voronoi cell. This cell was defined as follows: Select a sphere A and choose a random test point in the neighbourhood of sphere A. Calculate the distance d_A of the test point to the surface of sphere A and the distances of the test point to the surface of each other sphere situated in the neighbourhood A. If d_A is the smallest one of all distances then the test point belongs to the cell of sphere A. This procedure leads to a space-filling mosaic.

The neighbourhood of sphere A must be chosen in such a way that all spheres are included which may have an influence on the shape and volume of the mosaic cell of sphere A. The dimensions of the neighbourhood of a sphere and the number of test points determine the statistical accuracy of the calculated value for the local packing fraction. In these simulations, the statistical error was always below 0.3%. In a face-centred cubic crystal, the local packing fraction 0.74 is equal for all spheres. The central sphere of an ideal icosahedron is characterized by a local packing fraction of 0.76. The local packing fraction of a dense random packing model with equal spheres follows a monomodal distribution, and the global packing fraction (i.e. the total volume of the spheres divided by the volume of the box containing the spheres) is 0.64.

The distribution of the local packing fraction gives the basic information for discussing the structure of simulated hard sphere systems and the structural changes within them, especially for the identification of icosahedral and crystalline clusters in randomly packed matrices. Additionally, high-resolution transmission electron microscopy images can be simulated using the multi-slice method [10], and diffraction curves calculated by means of the well-known Scherrer formula.

3. Results

Figure 1 gives an impression of how a hard sphere model looks like. The model shown in Fig. 1was generated from a random initial distribution (type 1) of a binary mixture of hard spheres (size ratio 0.90 with a concentration of small spheres of 1/13).

The arrangement (global packing fraction: 0.65) is clearly non-crystalline but at several places the tendency to form local ordered clusters is visible. Fig. 2 shows the result of a simulation for a system of equal spheres (type 1). The global packing fraction of 0.66 is above the value for the classical dense random packing model (0.64) which points to partial crystallization.
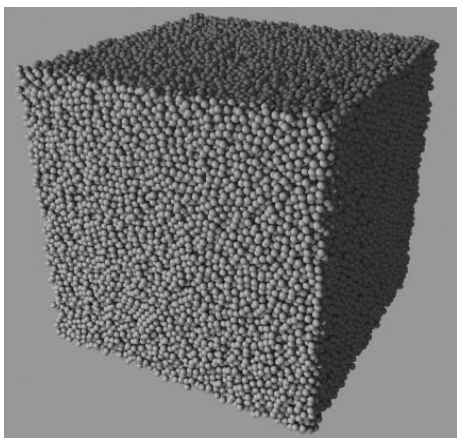
Fig. 1. Hard sphere structure consisting
of 100 000 spheres
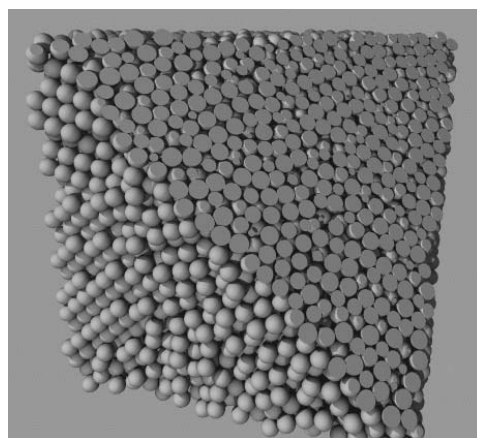
Fig. 2. Cross-section of a partially crystallized
system of 10 000 equal spheres

Nanocrystalline regions are visible at the (internal) surface of the model whereas the cross-section does not make the crystalline clusters visible. The model shown in Fig. 2 is a part of a systematic series of simulations. The following question was considered: Do clusters with a high local packing fraction appear when a dilute system of randomly arranged equal hard spheres is compressed? The answer is given in Fig. 3, showing typical frequency distributions of two highly compressed models: There is not one sphere with a local packing fraction of 0.76, i.e. icosahedral clusters are not created. Instead, a second maximum at 0.74 appears which points to the formation of face-centred cubic (fcc) or hexagonal crystallites.

Figure 4 shows the corresponding HREM images. The model with global packing fraction of 0.65 is still amorphous (or liquid) but for 0.66 the crystallites are visible and are shown to have cubic symmetry.

The diffraction patterns given in Fig. 5 are quite different, especially the splitting of the second peak. The maximum appeared at $2qR = 14.4$ which corresponds to the (220) reflection of fcc crystals and points to the transition from a homogeneous disordered state to a nanometre scale composite consisting of fcc crystallites embedded in an amorphous matrix.

In order to improve the conditions for the formation of icosahedral clusters binary models with size ratio of 0.90 (i.e., the diameter ratio of central and peripheral spheres in ideal icosahedra) were considered. The composition was also chosen as it occurs in a single icosahedron: 1 small central sphere and 12 large peripheral ones. Initial struc-

tures of types 1 and 2 were used. The type 2 structures are generated in the following way. Ternary hard sphere models are simulated with sphere radii of 0.90, 1, and 3. Then, the spheres with diameter 3 are replaced by icosahedral clusters each consisting of one central sphere of diameter 0.90 and 12 spheres of diameter 1. This procedure is illustrated in Fig. 6. The result is a binary system consisting of icosahedral clusters embedded in a binary system of hard spheres.
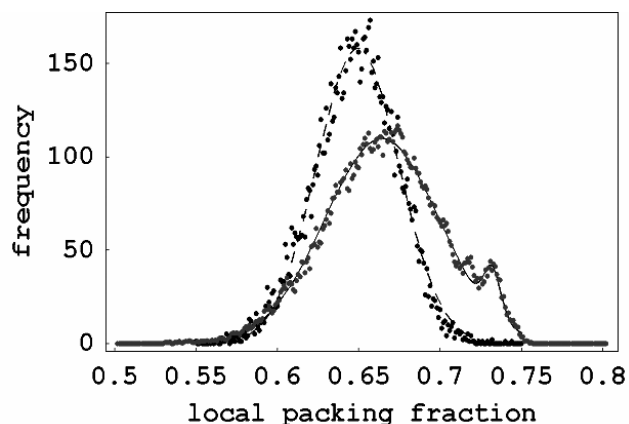
Fig. 3. Frequency distribution of local packing fraction and least-squares
fit by Gaussian functions; mean packing fraction 0.65 (dashed line) and 0.66 (solid line)
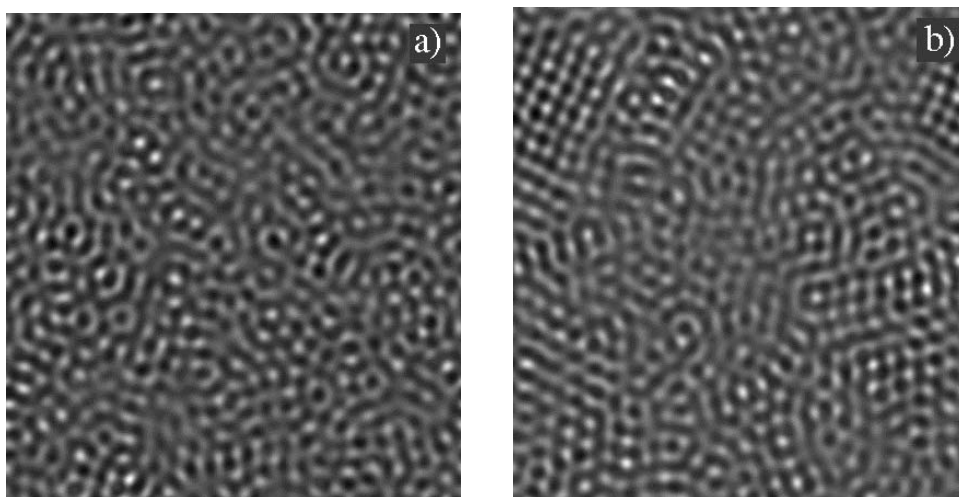
Fig. 4. HREM images of models with mean packing fraction of 0.65 (a) and 0.66 (b)
simulated for a Tecnai F30 microscope operated at 300 kV

Both systems were subjected to the compression routine, and for a sequence of global packing fractions the S-Voronoi analysis was carried out. Figure 7 shows the distribution of local packing fraction for the small spheres for representative steps.
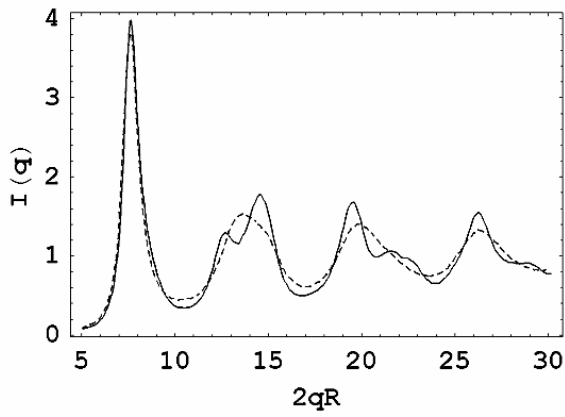
Fig. 5. Diffraction patterns of the model
with mean packing fraction
0.65 (dashed line) and 0.66 (solid line)
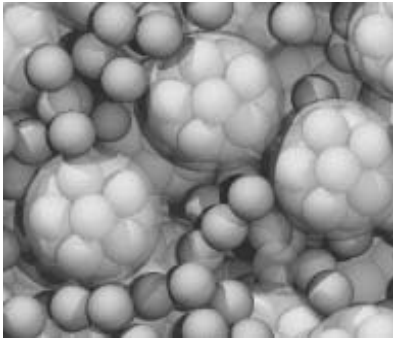
Fig. 6. Preparation of initial structures
including icosahedral clusters
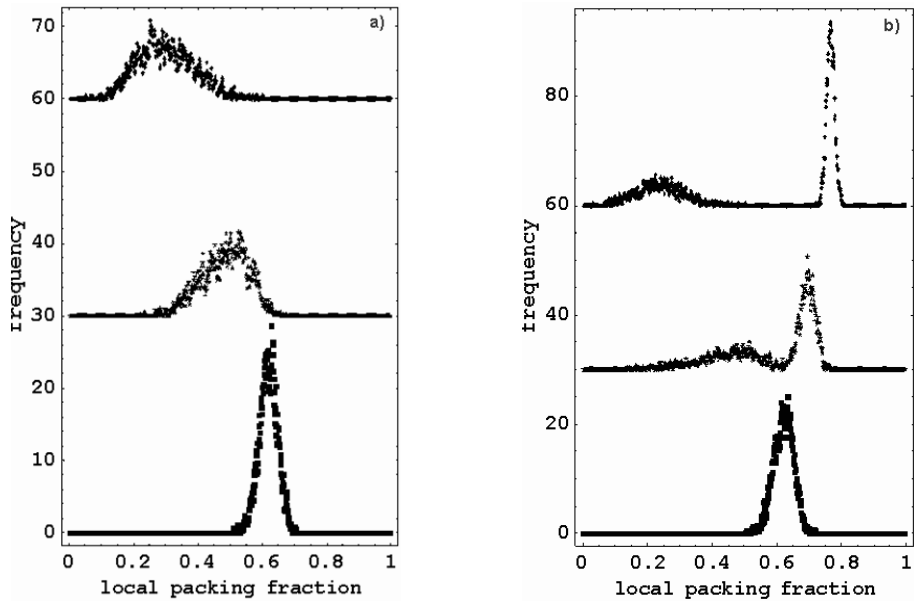
Fig. 7. Frequency distribution of local packing fraction of small spheres
for random initial structure (a) and with icosahedra embedded in the initial state (b). Initial state,
mean packing fraction 0.30 (top), mean packing fraction of 0.50 (middle) and 0.64 (bottom)

The distribution for the initial type 1 structure is monomodal and centred at the mean value of 0.3. The width decreases during densification and the maximum is shifted to higher values. The distribution is zero above 0.70 which means that no icosahedral clusters appear in the non-crystalline state. The distribution of the system containing icosahedral clusters in the initial state shows different behaviour. The icosahedra are clearly detected by the sharp maximum at 0.76 whereas the small spheres distributed in the random matrix give rise to the broad maximum situated at a low local packing fraction. During densification, the broad maximum characterizing the small spheres in the random matrix is shifted to a higher local packing fraction, but the icosahedral peak moves towards lower values. Both distributions overlap and form a common distribution in the final state. No residue of the initial icosahedral order can be detected and no significant difference of the distributions of local packing fraction for type 1 and type 2 structures can be observed in the final state.

The diffraction patterns (Fig. 8) show the same tendency. The random and the icosahedral initial state can be distinguished by the diffraction curves.
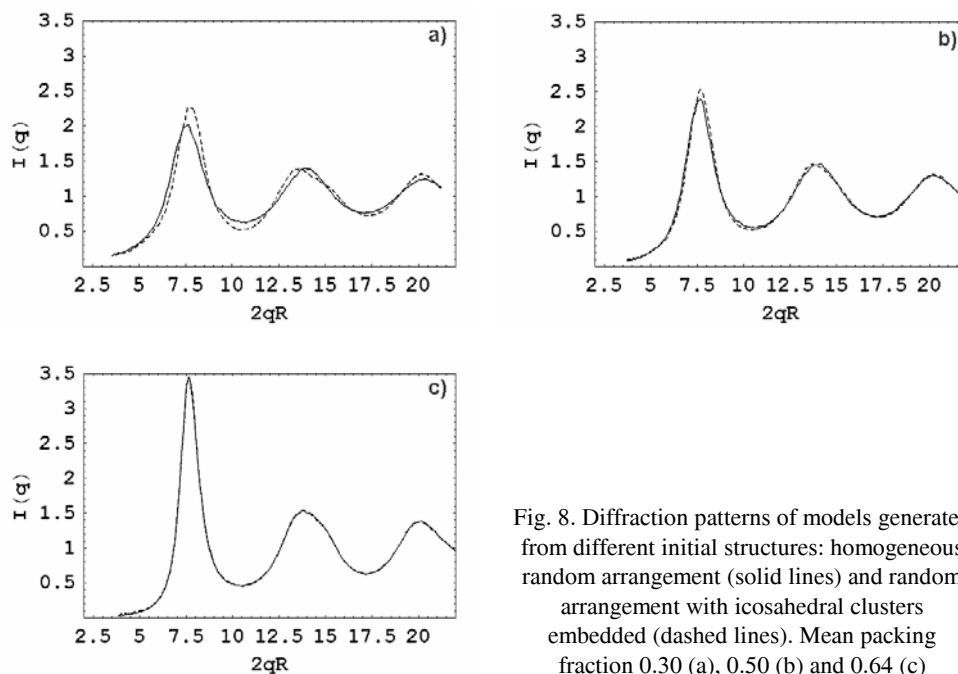
Fig. 8. Diffraction patterns of models generated from different initial structures: homogeneous random arrangement (solid lines) and random arrangement with icosahedral clusters embedded (dashed lines). Mean packing fraction 0.30 (a), 0.50 (b) and 0.64 (c)

The shoulder of the second maximum is well developed for the icosahedral system. This shoulder was discussed in [11] as a feature which is characteristic of structures with icosahedral short-range order and it was used in [2] for the interpretation of experimental curves obtained from liquid metals. The present model with icosahedral clusters in the initial structure still shows a bimodal distribution of local packing fraction at the mean packing fraction of 0.50 (Fig. 7b), but the difference of the corre-

sponding diffraction curve to that for the random system is very weak (Fig. 8b). At the mean packing fraction of 0.64 the diffraction curves of the two systems cannot be distinguished (Fig. 8c).

4. Discussion and conclusions

The simulations with equal spheres show that crystallization appears in hard sphere systems during densification above the global packing fraction of 0.64, which is characteristic of the standard dense-random packing model (for equal spheres). This confirms that there is no homogeneous random arrangement of hard spheres possible above 0.64, and models with higher values must be heterogeneous. The heterogeneity was realized in these simulations by mixtures of face-centred cubic nanocrystals of local packing fraction of 0.74 and the disordered (i.e., liquid or amorphous) matrix.

It was also expected that mixtures of amorphous matrix and icosahedral clusters would appear during densification but this was not the case. In previous papers [29, 30], the authors proposed the existence of icosahedral order with hard-sphere packing. However, the common-neighbour analysis done in [29] does not give an exact measure for icosahedrality and, furthermore, the amount of 13-sphere clusters having a central atom was negligible. In [30], a Voronoi analysis was carried out and the authors concluded that *the system approaches icosahedral order when increasing the density…* Indeed, they did not found any sphere in the systems analysed with the Voronoi cell volume required for local icosahedral order.

In the binary systems considered, the value 0.90 was chosen for the ratio of small to large spheres in order to favour and to stabilize local icosahedral arrangements. The result was that no icosahedra were formed during densification up to a mean packing fraction of 0.64. Instead, systems containing icosahedral clusters (13 atoms) in the initial state transform into a homogeneous disordered state without any icosahedron. It might be that there is a critical size of icosahedral arrangements which is above the size of the13-atoms clusters considered in the simulation. Such a critical size, which seems to exist for the fcc crystallites observed, may be controlled by the packing misfit at the interface between the cluster and the amorphous or liquid matrix.

The present study also showed that simulations of structural fluctuations on the nanometre scale are of interest for the interpretation of related experimental data.

References

[1] REICHERT H., KLEIN O., DOSCH H., DENK M., HONKIMÄKI V., LIPPMANN T., REITER G., Nature, 408 (2000), 839.
[2] SCHENK T., HOLLAND-MORITZ D., SIMONET V., BELLISENT R., HERLACH D.M., Phys. Rev. Lett., 89 (2002), 075507.
[3] FRANK F.C., Proc. Roy. Soc. London A, 215 (1952), 43.
[4] SPAEPEN F., Nature, 408 (2000), 781.

[5] MATTERN N., KÜHN U., NEUEFEIND J., ECKERT J., Appl. Phys. Lett., 77 (2000), 1153.

[6] FAN C., INOUE A., Appl. Phys. Lett., 77 (2000), 46.

[7] FAN C., LI C., INOUE A., HAAS V., Phys. Rev. B, 61 (2000), R3761.

[8] HERMANN H., HEINEMANN A., BAUER H.-D., MATTERN N., KÜHN U., WIEDENMANN A., J. Appl. Cryst., 34 (2001), 666

[9] HERMANN H., MATTERN N., KÜHN U., HEINEMANN A., LAZAREV N.P., J. Non-Cryst. Solids, 317 (2003), 91.

[10] STADELMANN P.A., Ultramicroscopy, 21 (1987), 131.

[11] VAN DE WAAL B., J. Non-Cryst. Solids, 189 (1995), 118.

[12] DOYE J.P.K., WALES D.J., ZETTERLING F.H.M., DZUGUTOV M., J. Chem. Phys., 118 (2003), 2792.

[13] DOYE J.P.K., J. Chem. Phys., 119 (2003), 1136.

[14] COZZINI S., RONCHETTI M., Phys. Rev. B, 53 (1996), 12040.

[15] DZUGUTOV M., Phys. Rev. A, 46 (1992), R2984.

[16] DZUGUTOV M., Phys. Rev. Lett., 70 (1993), 2924.

[17] HUI L., GUANGHOU W., XIUFANG B., FENG D., Phys. Rev. B, 65 (2001), 035411.

[18] HUI L., XIUFANG B., GUANGHOU W., Phys. Rev. B, 67 (2003), 094202.

[19] WANG L., XIUFANG B., YANG H., Physics Lett. A, 302 (202), 318.

[20] ALFE D., KRESSE G., GILLAN M. J., Phys. Rev. B, 61 (2000), 132.

[21] SACHDEV S., *Icosahedral Ordering in Supercooled Liquids and Metallic Glasses*, [in:] K. J. Strandburg (Ed.), *Bond Orientational Order in Condensed Matter Systems*, Springer-Verlag, New York, 1992.

[22] CLARKE A.S., WILEY J.D., Phys. Rev. B, 35 (1987), 7350.

[23] YANG A., MILLER C.T., TURCOLIVER L.D., Phys. Rev. E, 53 (1996), 1516.

[24] JODREY W.S., TORY E.M., Powder Technol., 30 (1981), 111; Phys. Rev. A, 32 (1985), 2347; A 34 (1986), 675.

[25] BEZRUKOV A., BARGIEL M., STOYAN D., Part. Syst. Charact., 19 (2002), 111.

[26] TORQUATO S.,TRUSKETT T.M., DEBENEDETTI P.G., Phys. Rev. Lett., 84 (2000), 2064.

[27] WILLIAMS S.R., SNOOK I.K., VAN MEGEN W., Phys. Rev. E, 64 (2001), 021506.

[28] RINTOUL M.D., TORQUATO S., Phys. Rev. Lett., 77 (1996), 4198.

[29] CLARKE A.S., JONSSON H., Phys. Rev. E, 47 (1993), 3975.

[30] JULLIEN R., JUND P., CAPRION D., QUITMANN D., Phys. Rev. E, 54 (1996), 6035.

Digital image analysis and visualization of early caries changes in human teeth

Elżbieta Kaczmarek[1*], Anna Surdacka[2],
Teresa Matthews-Brzozowska[2, 3], Bogdan Miśkowiak[4]

[1]Laboratory of Morphometry & Medical Image Processing at Chair of Pathology,
University of Medical Sciences in Poznań, Poland

[2]Department of Conservative Dentistry and Periodontology,
University of Medical Sciences in Poznań, Poland

[3]Department of Orthodontics, Wrocław Medical University, Poland

[4] Department of Optometry and Visual System, University of Medical Sciences in Poznań, Poland

The primary aims were the visualization, digital image analysis and X-ray EDS microanalysis to evaluate caries lesions in human premolars, with and without resin sealants, and light and scanning electron microscopic observations of hard dental tissues before and after the use of experimental protective strontium-fluoride toothpaste. The material consisted of healthy premolars extracted for orthodontic reasons, sectioned into slices. Sections of tooth crowns were digitized with a light microscope. The area of enamel demineralization was then measured. The in situ model was developed by placing the samples on the buccal surfaces of the first molars in healthy subjects, and exposing them to the use of the experimental toothpaste for 3 or 6 months. X-ray EDS microanalysis was undertaken to examine the Ca and Sr content on the enamel surface and at 15, 30, 60 and 100 microns depth. The results showed that the toothpaste induces an increased deposition of Ca in sub-superficial layers of the damaged enamel. The role of digital imaging needs to be defined with the diagnostic problem of the patient to plan an effective prophylaxis and treatment of early caries.

Key words: *digital image analysis; EDS microanalysis; dental hard tissue restoration; enamel demineralization; fissure sealants.*

1. Introduction

Human tooth enamel is a hard tissue structure which can lose mineral substances due to unfavorable long term conditions involving low pH and the presence of carbo-

---

[*]Corresponding author, e-mail: elka@amp.edu.pl

hydrates and microorganisms which cause caries changes. To prevent demineralization of dental hard tissues, the enamel structure needs to be remineralized by supplementing fluoride, phosphorus, calcium, and other ions into the enamel apatites, for example strontium. It can be performed by application of toothpastes supplemented with cariostatic ions and/or placing fissure sealants or varnishes on the total enamel surface.

Pit and fissure sealing aims at providing a good protection against caries. To achieve the best benefit, sealants and varnishes should bond appropriately to the enamel surface. However, sealant retention depends on the sealant quality and procedures used for fissure preparation. Small fractures of sealant indicating failure or degradation of adhesion in pits, fissures and their environs were shown by scanning electron microscopy observations [4]. Penetration of sealant into fissures was reported to be significantly greater when a drying agent was used [1]. An assessment of microleakage around pit and fissure sealant with and without the use of pumice prophylaxis was recently reported [2]. Pumice cleaning prior to enamel etching removes plaque and debris from the enamel surface and improves sealant retention which reduces microleakage. These studies show applications of biomaterial science to induce remineralization of dental hard tissues through modelling and restoring enamel structures.
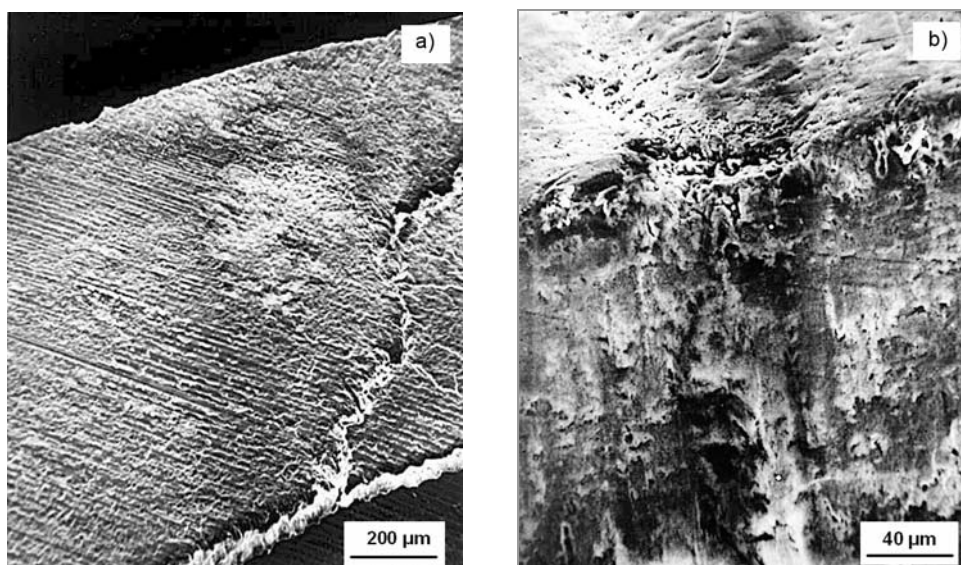
Fig. 1. SEM images of enamel lamellae, with demineralization,
at 100 microns of depth (a) and at sub-superficial layer (b)

The authors' previous works were developed to quantitatively assess caries changes [5, 8, 9]. The aim of this in vitro study was the use of digital image analysis and X-ray EDS microanalysis for evaluation of quantitative differences between car-

ies lesions in human premolars with and without resin sealants before and after the use of experimental strontium-fluoride toothpaste protecting hard dental tissues observed in light and scanning electron microscopy (Fig. 1).

2. Experimental

The material of the in vitro study consisted of seventy cavity free first premolars extracted for orthodontic reasons from twenty healthy young men and women of 16–19 years of age. Thirty teeth had fissures protected with sealant a year before extraction and formed the "fissure sealant premolar" group (Fig. 2). The remaining teeth established the "premolar" group (Fig. 3).
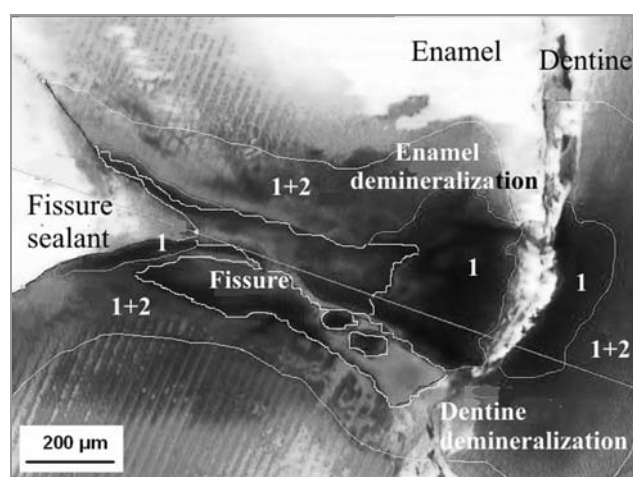
Fig. 2. Caries lesions in a fissure sealant premolar – a light micrograph
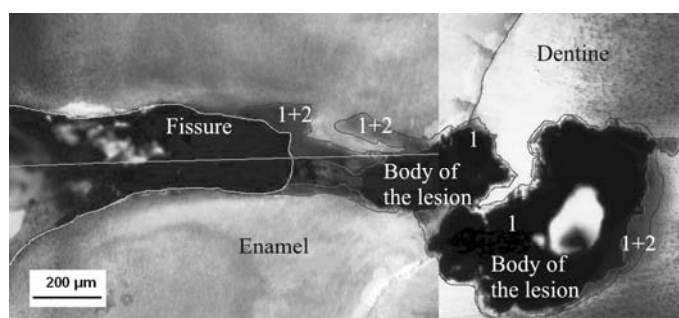
Fig. 3. Caries lesions in an unprotected premolar

Crowns of teeth were sectioned along the vertical axis of tooth using a low speed Buehler diamond disc, 0.1 mm thick, cooled with distilled water to obtain four sections each approximately 2 mm thick. Selected sections were smoothed out on both

sides to remove the smeared layer. Next, the sections were Mallory stained and digitized with a computer-assisted Nikon Optiphot-2 light microscope, running with the MicroImage v 4.0 for Windows image analysis system. Dark areas representing the main demineralization of enamel were segmented by colour sampling and thresholding in HSB colour space. Brightness of pixels was introduced as the third dimension expanding 2D images into 3D space. The scenery behind objects of interest was reduced to a background by sets of threshold levels for hue, brightness and saturation of colours. The orthogonal projection of spatial objects of interest (Fig. 4) allowed us to determine their planar area [6].
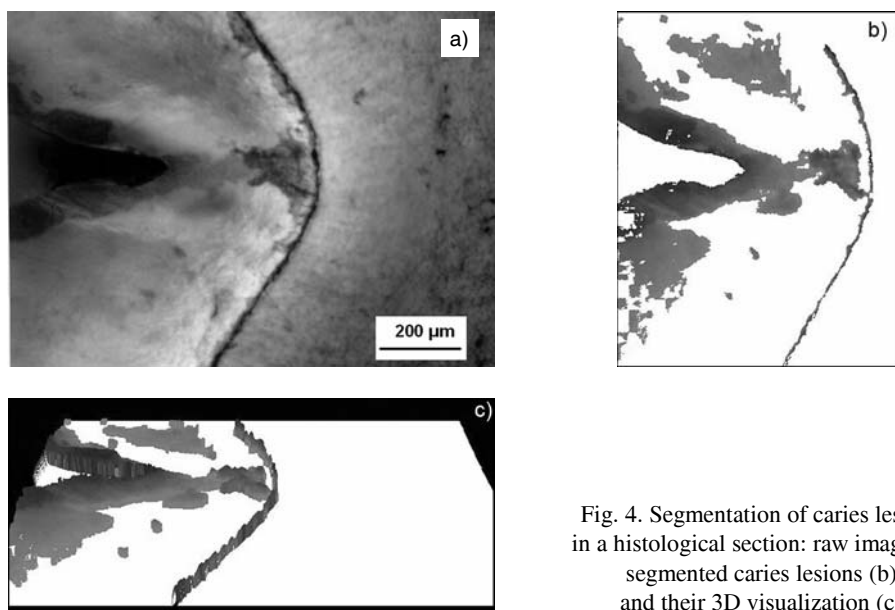
Fig. 4. Segmentation of caries lesions in a histological section: raw image (a), segmented caries lesions (b) and their 3D visualization (c)

Smooth smears surrounding the main demineralized areas of enamel and/or located around the fissure were also segmented in the same way. These areas, together with the main demineralized area, represented the area of total demineralization of enamel (Figs. 2, 3). The area of segmented main and total demineralization was then determined.

The in situ model was developed for twelve volunteers selected from the same group of young people. The remaining samples of 4 mm^2, prepared from selected sections were placed on the buccal surfaces of the first molars in the same subjects, and exposed for 3 or 6 months to use of the experimental strontium-fluoride (F$^-$ and Sr^{2+}) toothpaste. The quantitative X-ray EDS microanalysis was performed to examine the Ca and Sr content on the enamel surface and layers at 15, 30, 60 and 100 microns deep (Figs. 5, 6).

The collected results were subjects of statistical analysis by using the Mann–Whitney test.
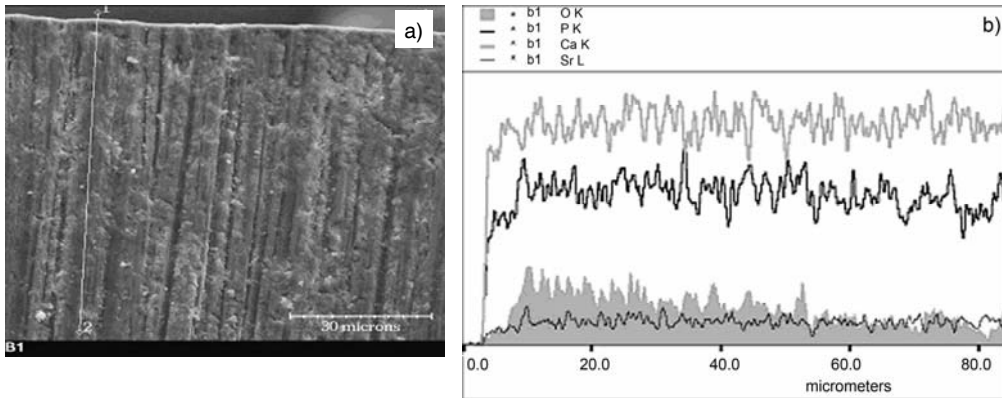
Fig. 5. A SEM image of enamel lateral wall after demineralization (a)
and spectra of the examined elements on the enamel lateral wall (b)
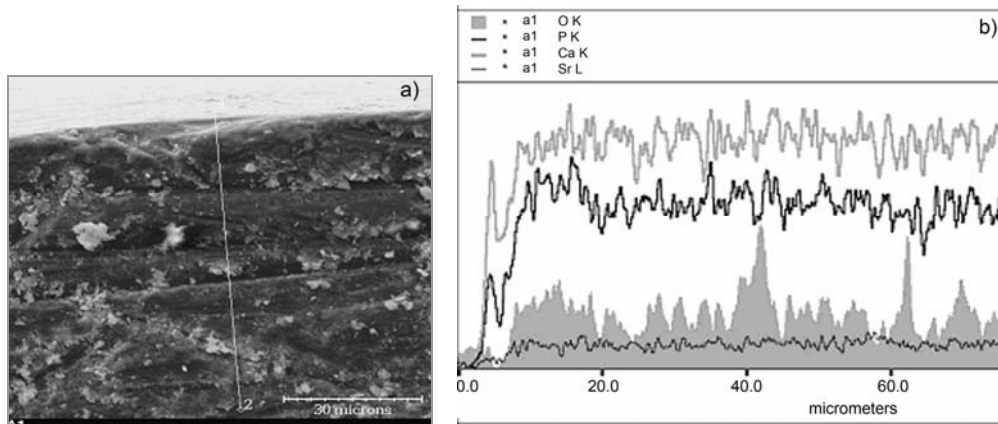
Fig. 6. A SEM image of enamel lateral wall after 3-months application of strontium-fluoride
toothpaste (a) and spectra of the examined elements on enamel lateral wall (b)

3. Results

In the light microscopy images, the area of total demineralization was significantly greater in fissure sealant premolars than in unprotected premolars ($p < 0.05$), whereas the area of the main demineralization was not significantly different between the groups of teeth compared (Table 1).

The results of studies on the in situ model showed that the experimental strontium-fluoride toothpaste induces calcium deposition in sub-superficial layers of the demin-

eralized enamel, thus inducing the recovery of its injury (Tables 2–4). The toothpaste significantly promotes the remineralization of deeper layers of damaged enamel.

Table 1. Evaluation of enamel demineralization in light microscopy observations

Quantitative assessment of enamel demineralization		Mean ± std. dev.	Significance level p
Area of the main demineralization (mm^2)	Premolars	0.09 ± 0.21	non significant
	Fissure sealant premolars	0.04 ± 0.02	
Area of the total demineralization (mm^2)	Premolars	0.27 ± 0.35	
	Fissure sealant premolars	0.29 ± 0.15	$p < 0.05$

Table 2. Enamel surface microanalysis of Ca and Sr
at baseline and after 3 and 6 months of the experiment

Trace element (wet %)	At baseline	After 3 months	After 6 months
Ca	20.80 ± 3.84	21.36 ± 4.16	22.11 ± 2.05
Sr	0.71 ± 0.11	0.68 ± 0.08	0.72 ± 0.02

Table 3. Enamel lateral wall microanalysis of calcium at baseline,
after 3 and 6 months of the experiment

Enamel depth (μm)	Ca (wet %) at baseline	After 3 months	After 6 months
15	15.70 ± 0.22	28.23 ± 0.38[3]	28.22 ± 2.49[1]
30	15.55 ± 0.25	28.54 ± 0.38[3]	28.50 ± 1.55[2]
60	15.76 ± 0.32	28.57 ± 0.48	29.04 ± 0.37
100	15.45 ± 0.31	28.68 ± 0.32[2]	29.65 ± 2.09[1]

[1]$p < 0.05$, [2]$p < 0.01$, [3]$p < 0.0001$ (the results after 3 and 6 months compared with the results at baseline).

Table 4. Enamel lateral wall microanalysis of strontium at baseline,
after 3 and 6 months of the experiment

Enamel depth (μm)	Sr (wet %) at baseline	After 3 months	After 6 months
15	0.02 ± 0.01	0.44 ± 0.55	0.02
30	0.00	0.48 ± 0.19	0.16 ± 0.22
60	0.00	0.06 ± 0.05[1]	0.56 ± 0.26[1]
100	0.00	0.00	1.07 ± 0.21

[1]$p < 0.01$ (the results at 60 μm significantly different from the results at 15 and 30 μm).

4. Discussion and conclusions

Image analysis of histological sections of human premolars showed that caries changes can be present in teeth protected with fissure sealants [2, 5]. To prevent lesions progressing, teeth should be appropriately diagnosed and prepared before introducing the sealant. The quality of sealant and its placement can be assessed in in vitro studies by examining microcracks or a range of microleakage (if appeared) in light and/or scanning electron microscopy. The results presented in this paper, showed the usefulness of digital image analysis for this kind of data. SEM topographic analysis of the enamel surface revealed smoothing probably caused by mineral compound deposition and associated with caries incipience [9]. Early caries lesions are reversible and may heal. To induce enamel remineralization, sealants, varnishes, toothpastes and other agents of oral hygiene should be supplemented with the most efficient cariostatic ions. Fluoride has substantial benefits in the prevention of tooth decay, depending on the level and source of exposure. Fluorides also have adverse effects on human tissue [3]. The most common adverse effect of excess exposure to fluoride is dental fluorosis, a permanent hypomineralization of enamel, which shows unfavorable modelling of the structure. The role of trace elements with cariestatic potential, other than fluoride, in caries prophylaxis has long been investigated. Strontium has been one of the leading trace elements applied to induce remineralization of dental tubules in cases of dentine hypersensivity [7, 10]. Therefore, the idea arose to limit fluoride content by supplementing with strontium for remineralization of dental enamel. In the studies, after 6-months application of strontium-fluoride toothpaste, the level of calcium and strontium increased in the deeper layers of the enamel. It confirms a usefulness of Sr^{2+} for enamel remineralization and healing of early caries changes. Concluding, the increasing role of digital imaging needs to be defined with the diagnosis of further problems for the patient in mind in order to plan an effective prophylaxis and treatment of early caries changes.

References

[1] ADAMS T.J., FRAZIER K.B., BROWNING W.D., J. Dent. Res., 79 (2000), 189.

[2] ANSARI G., OLOOMI K., ESLAMI B., Int. J. Paed. Dent., 14 (2004), 272.

[3] BILLINGS R.J., BERKOWITZ R.J., WATSON G., Pediatrics 113 (2004), 1120.

[4] HIRAYAMA A., Shikwa Gakuho, 90 (1990), 1019.

[5] KACZMAREK E., MATTHEWS-BRZOZOWSKA T., MIŚKOWIAK B., Ann. Biomed. Eng., 31 (2003), 931.

[6] KACZMAREK E., STRZELCZYK R., *From two to three-dimensional visualisation of structures in light and confocal microscopy – applications for biomedical studies. Current Issues on Multidisciplinary Microscopy Research and Education*, FORMATEX Microscopy Book Series No. 2, in press.

[7] KODAKA T., KUROIWA M., KUROIWA M., OKUMURA J., MORI R., HIRASAWA S., KOBORI M.J., Electron Microsc., 50 (2001), 57.

[8] MATTHEWS-BRZOZOWSKA T., STOPA J., MIŚKOWIAK B., CHMIELNIK M., SURDACKA A., JÓŹWIAK K., MESMACQUE G., CELLARY A., KACZMAREK E., PARTYKA M., Ann. Acad. Med. Silesiensis, Suppl., 26 (1998), 145.

[9] STOPA J., MATTHEWS-BRZOZOWSKA T., MIŚKOWIAK B., SURDACKA A., CHMIELNIK M., JÓŹWIAK K., MESMACQUE G., KACZMAREK E., CELLARY A., *Determination of qualitative and quantitative carietic lesions in the enamel using various measuring techniques*, [in:] *Biomedical Measurement and Instrumentation*, Proceedings of the 8th International IMEKO Conference on Measurement in Clinical Medicine, Dubrovnik, Croatia, September 16–19, 1998., Zagreb, 1998, pp. 5-46–5-49.

[10] TOPBASI B., TURKMEN C., GUNDAY M., Quintessence Int., 29 (1998), 197.

New possibilities of light microscopy research resulting from digital recording of images

AGNIESZKA SZCZOTOK[*], STANISŁAW ROSKOSZ

*Silesian University of Technology, Department of Materials Science,
Krasińskiego 8, 40-019 Katowice, Poland*

New research possibilities related to recent improvements in light microscopy are discussed. New research microscopes are fully automated and motorized. All functions, such as those connected with focusing or stage positioning, can be controlled with a PC. Techniques which combine images recorded at different locations on *X*, *Y* and *Z* axes are presented. The first technique – combining high resolution single images, made in *X* and *Y* axes on the surface of a specimen, creates overview images of specimens. This is particularly important in quantitative materialography because the technique produces a significant decrease in the edge effect. Examples of applications of PC controlled *X-Y* stage and stage management software in the study of a duplex steel, made from Ni-base superalloy and welding are presented. Automatic alignment of images made in applications of this technique in the study of a zinc layer on cast iron and thermal barrier coatings on a heat-resisting alloy are shown.

Key words: *digital imaging; extended focal imaging; motorized stage; image analysis software*

1. Introduction

Progress in light microscopy has been made since the invention of the first simple microscope in 16th century. The main improvements made in recent decades have had a great influence on obtaining images rich in detail. The most important examples are: refinement of microscope illuminators; introduction of new lenses and multilayer non-reflective coatings; study of a new generation of universal objectives for passive light and reflection for greater fields of vision and working distances. These achievements have an influence on more effective correction of optical system defects. Thus, obtaining a sharp image with more contrast and constant beam intensity over the whole

---

[*]Corresponding author, e-mail: agnieszka.szczotok@polsl.pl

field of vision becomes possible [1]. Moreover, the application of systems for changing magnification, zoom systems, and enriching a microscope with a number of useful devices for sharp images in all observation outputs, i.e. infinity-corrected optics [2, 3], is conducive to digital image recording. In addition, improvements to all mechanical systems and increasing the rigidity of microscopes is of significance, because these all affect ease of use and are propitious for the introduction of automatization and management of the stage.

It is important to emphasize that all the described changes have significance for the digital recording of images. The latest digital cameras, combined with powerful computer software, offer image quality that is comparable with traditional silver halide film photography. Moreover, digital cameras are also easier to use and offer greater flexibility of image manipulation and storage. Digital imaging is increasingly applied to image capture for microscopy – an area demanding high resolution, colour fidelity and careful management of, often, limited light conditions [4]. The quality of the final image, both digital and film, is dependent on the quality of the original microscopic image.

2. Experimental

All digital images presented in this paper have been produced using an Olympus DP70 digital camera system coupled to an inverted stage metallurgical microscope Olympus GX71 with infinity-corrected optics. The microscope has a mechanical z-drive and mechanically operated stage. It characterises by super-wide field, zooming and a mirror cube turret for BF, DF, DIC and polarized light. Combining the microscope with the DP70 Olympus digital camera enables sharp images to be recorded, because the DP70 can gather extremely high resolution images, equivalent to 12.5 million pixels in only 3 seconds [5] as well as high sensitivity coupled with high-speed processing. The images obtained can have 36-bits of RGB colour depth which is essential for recording subtle colour gradations and intensities, and, as a result true, the natural colours of images.

The microscope is equipped with image analysis software analySIS supplied by the German company Soft Imaging System GmbH. The software offers image acquisition, evaluation and analysis, data archiving and the generation of professional reports. The motorized stage of the microscope enables analySIS modules to automate the processing. The microscope stage can be correctly controlled by the image analysis software. The Stage is a module for automatic service of the microscope stage which results in the operator having full control of all three axes: x, y and z. Two modules of this software using the motorized stage and the appropriate software represented here to give evidence of the possibilities of modern microscopy.

3. Results

3.1. Application of combining single images made in *X-Y* axes

The Stage Manager module from the analySIS provides the following possibilities:
- creating an overview image of the specimens by combining single images with high resolution – the resolution of the overview image can be adjusted (Fig. 1);
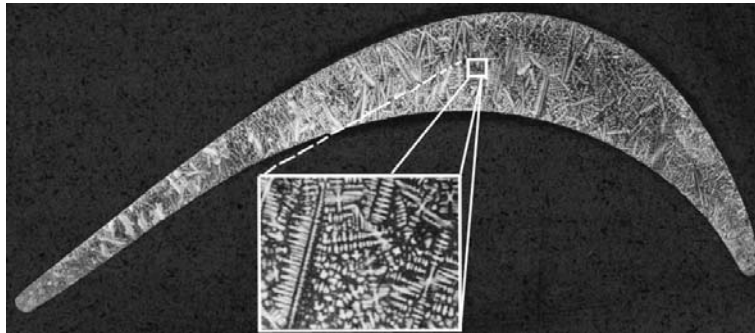
Fig. 1. An overview image of a dendritic microstructure turbine blade
made from Ni-base superalloy René 77 (magnification 50×)

- defining individual stage positions for the acquisition of the series of images – the motorized microscope stage can be executed at the different positions (the positions and travel paths of the stage are defined in the Stage Manager – integrated into the analySIS [6]);
- making an estimation of inhomogeneity structure on the cross-section and longitudinal view of products (Fig. 2);
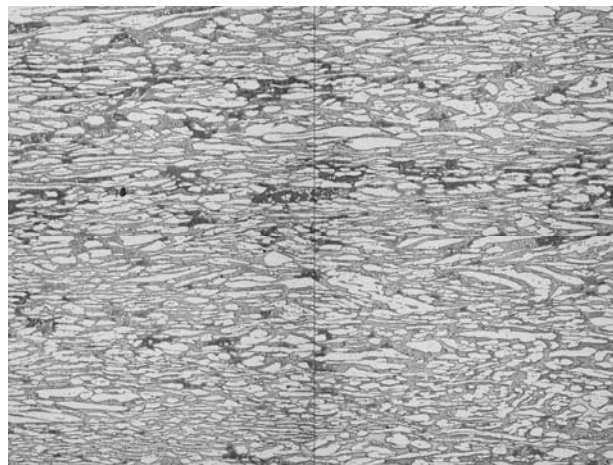
Fig. 2. A fragment of the overview image of duplex steel 2205 (magn. 200×)

- quantitative evaluation of materials microstructure;
- carrying out researches of materials macrostructure; the overview image is a high resolution image of a larger object (Fig. 3).
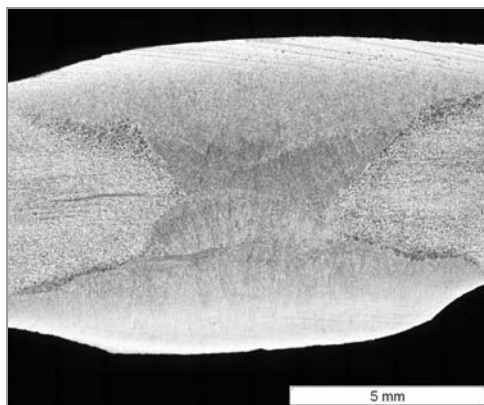
Fig. 3. Double-sided headwave weld of duplex steel made by welding
with coated electrode Avesta 2205 AC/DC (magnification 1:1)

In the overview image only the object areas which have already been scanned can be displayed. The system positions individual images from which the overview image is composed in edge to edge mode. All individual images which belong to the current stage path are represented by frames.

A resulting digital overview image of the duplex steel is illustrated in Fig. 2. The importance of being able to combine single images is worth emphasizing in this case, for the reason that the duplex steel microstructure is characterized by two basic grain sizes. Using a higher magnification revealed fine grey grains of ferrite, but the measuring frame will cut long bright grains of austenite which were not taken into consideration in the analysis and evaluation. However, if one wants to avoid cutting grains of austenite by frame and use a smaller magnification, grains of ferrite are not visible. Thus an overview image avoids an edged effect and to observe through a microstructure both kinds of grains [7].

Figure 3 shows an example of weld overview made with the Stage Manager. It is an image consisting of 4 (2×2) single frames. An auxiliary grid has been removed to show the whole weld.

A MosaiX and a Panorama image acquisition module from Axio Vision Carl Zeiss [8] appears to be similar to the Stage Manager module.

3.2. Application of automatically aligning images made in *Z* axis direction

In many cases Extended Focal Imaging eliminates a restricting problem of light microscopy – limited depth of focus. The microscope's own depth of focus is only

capable of focusing a limited range of height. The remaining parts of the image are then blurred, i.e. details which are visible on images taken with different focus settings are normally not visible in sharp details on a single image. Electronic image processing gives the solution to this problem. A series of individual images of the specimen is needed, which are obtained by adjusting the microscope focus for each image, i.e. separately focusing each image at different height. The module extracts the sharp details from each individual shot to determine a final image that is rich and sharp in all details, i.e. it seems to have unlimited depth of focus. To generate an EFI image from a focused series, the EFI software goes through the whole image series pixel by pixel. EFI determines which the image which contains the best focused pixel(s) of every image in the series [6]. Moreover, the EFI module can automatically align images that show a lateral displacement, for example if the images were taken with a stereo microscope.

Selected digital images with limited depth of focus at different locations of the images recorded at varying focus levels are shown in Figs. 4a–c, and in Fig. 4d – the reconstructed image which is of better quality and sharpness than the primary images.
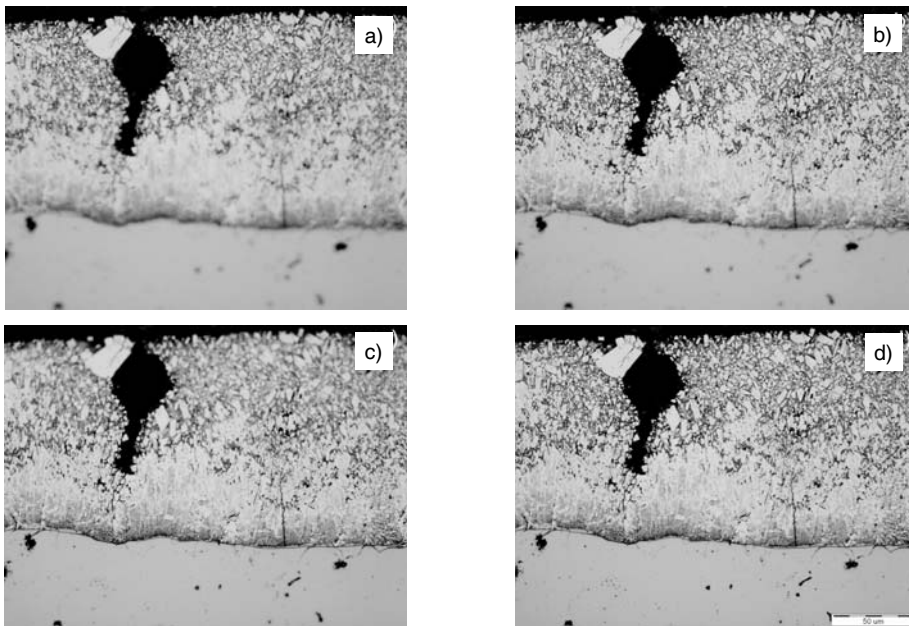
Fig. 4. Example EFI procedure – zinc layers on the cast iron (magnification 50×)

When used in a live mode, the EFI module provides both a live image as well as a partially reconstructed one. The program is able to focus interactively the missing details of the image which are not yet in focus and then add them to the current image.

The EFI has greater importance at higher magnifications. In spite of correct preparation of specimens to be examined at high magnification it is difficult to obtain

a sharp image of the microstructure over the whole field of vision. The EFI module is very useful for observing surface layers of products and materials with phases having different properties which make it difficuot to obtain a structure without relief. Figures 5a–c present selected digital images with a limited depth of focus and Fig. 5d – a reconstructed image of another inhomogeneous material, a thermal barrier coating on a heat-resisting alloy, René 77.
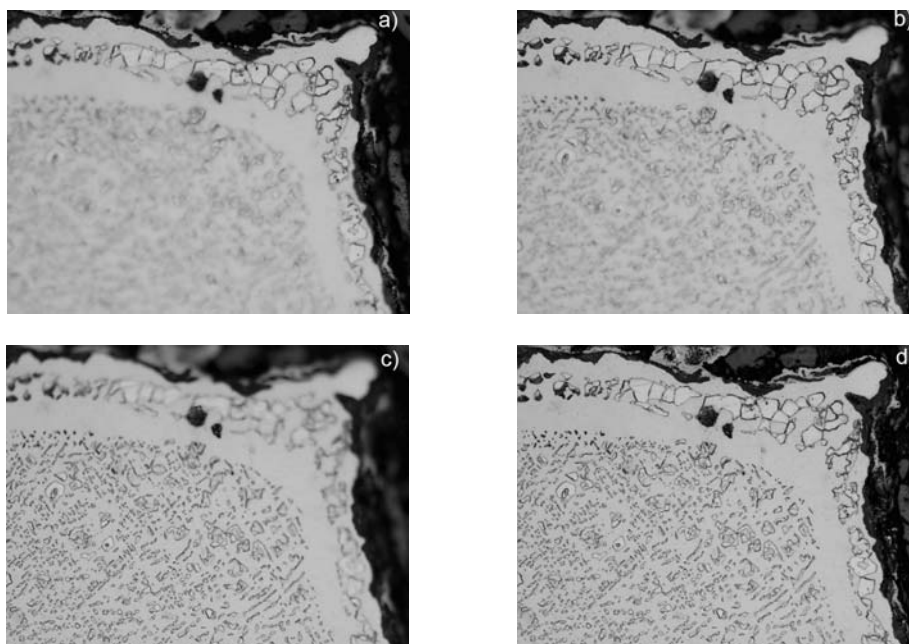
Fig. 5. Acquisitions of images at various focus levels and the reconstructed image following EFI procedure – Ni-based superalloy René 77 after aluminizing and oxidation (magnification 1:1)

On the basis of the whole series of images the EFI module provides an option to determine a height map. The height map can be used to create a 3-dimensional representation of the object's surface. The described module enables precise measurements of the roughness of the surface [6]. This is important for fracture surfaces permitting quantitative fractography research and in wear mechanism research. Moreover, creating a height map makes light microscopy similar to a confocal laser microscopy because of the reconstruction abilities. The latter also provides height maps of an object's surface. Classical light microscopy does not permit the construction of a single objective with a large depth of focus coupled with high resolution of the specimen details, i.e. true colour, high-quality images rich in detail, because the depth of focus is inversely proportional to the numerical aperture.

The appropriate software and microscopic equipment, i.e. the digital camera and motorized stage, can solve the problem of the limited depth of focus. A DeepView

technique, Axiovert 200 MAT from Carl Zeiss company [9, 10] seems to be similar to the EFI module.

4. Conclusions

The examples presented show that digital recording of high resolution images increases the range of possible image analysis and accuracy of microstructural evaluation; without these techniques complete investigations practically are not possible.

The analysis of digital images essentially increases the possibilities of quantitative materialography and fractography applications. Thus the digital microscope ensures high performance and a diverse programme of examination.

Moreover, the digital form of images stored in the computer memory makes them especially suitable for various numerical transformations. The recorded images are immediately available and ready to be processed electronically, by e-mail or archive. Thus, the perfect complement to a digital camera for image archiving, measuring, analyzing or direct reporting is network-compatible image management software.

References

[1] CWAJNA J., *Metody badawcze współczesnej metalografii*, [in:] M. Hetmańczyk (Ed.), *Postępy nauki o materiałach i inżynierii materiałowej*, Wydawnictwo Politechniki Śląskiej, Gliwice, 2002, p. 15.

[2] WOJNAR L., Laboratoria, Aparatura, Badania, 2 (2000), 11.

[3] WOJNAR L., *Modern approach to microstructure image analysis*, [in:] L. Wojnar, K. Rożniatowski, K.J. Kurzydłowski (Eds.) *Proceedings of International Conference on the Quantitative Description of Materials Microstructure* Q-MAT '97, Kraków, 1997, p. 103.

[4] DRENT P., Imaging & Microscopy, 1 (2001), 2.

[5] G.I.T. Imaging and Microscopy 4 (2003), 17 (I&M show case: cameras).

[6] *AnalySIS User's Guide*, Soft Imaging System GmbH, Germany, 2000, 87.

[7] SZCZOTOK A., Wiad. Stereolog., 10 (2004), 44.

[8] Axiovert 200 MAT (company brochure www.zeiss.de/mat).

[9] Axioskop 2 MAT (company brochure www.zeiss.de/mat).

[10] AxioVision (company brochure www.zeiss.de/axiovision).

Multifractal description of fracture morphology: Quasi-3D analysis of fracture surface

SEBASTIAN STACH[1*], JAN CWAJNA[2], STANISŁAW ROSKOSZ[2], JERZY CYBO[1]

[1]Department of Materials Science, Silesian University, ul. Snieżna 2, 41-200 Sosnowiec, Poland

[2]Department of Materials Science, Silesian University of Technology, ul. Krasińskiego 8, 40-019 Katowice, Poland

The paper presents a verification of the multifractal analysis proposed in other papers. It has been found that the analysis of simulated profiles formed by removing overlaps and secondary cracks from a real profile (which corresponds to a file obtained from a profilographometer) ensures proper diversity of fractal characterization, adequate for the degree of fracture surface development of the investigated grades of sintered carbide measured with a Taylor–Hobson's Talysurf 2 profilographometer.

Key words: *fracture; surface; stereometry; overlaps; profile; multifractal; spectrum width*

1. Introduction

A quantitative characterization of a fracture constitutes an indispensable link in the investigation of the processes of decohesion and crack resistance of a material [1]. A distinguishing feature of the latter is the degree of fracture development, the evaluation of which is conducted on the basis of an analysis of a profile containing possible overlaps and secondary cracks [2]. In order to reduce laborious research procedure of preparing transverse microsections, their image analysis, and to eliminate the minimal representation resulting from examining only one to three profiles, a concept is put forward in the paper to use a profilographometer [3]. The device facilitates obtaining stereometric files of the surface topography very quickly, which permits analysis of an optional number of profiles in selected directions. Since the principle of operation of a profilographometer does not allow disclosure of the existing overlaps and cracks, a transposition by means of a multifractal analysis has been proposed [4–7]. This allowed making the multifractal spectrum spacing dependent on the degree of profile

_____

[*]Corresponding author, e-mail: sstach@us.edu.pl

line development as well as on local changes of the distances between those spectrum points where overlaps and secondary cracks occur [8]. In order to check whether there is a relationship between the multifractal spectrum width and the percentage share of overlaps in real profiles, a regression analysis was made. A high correlation coefficient was obtained ($R = 0.88$) showing that the multifractal analysis of simulated profiles (without overlaps and cracks, i.e. profiles corresponding to the data from the profilographometer [9]) is fully correlated with the degree of the real profile development. Verification of the correlation coefficient allowed significance of $\alpha \leq 0.05$ for the coefficient, which shows potentiality of $\geq 95\%$ trust in relation to the possible estimation error $\delta_{0.05}$ to be assumed.

A consequence of the former stage is the transition to a morphology analysis of a real fracture in 3D [10]. The multifractal analysis methodology presented in papers [3, 8] should constitute a link between both examination methods of a profile and a whole fracture.

The purpose of this study is to show the possibility of describing the fracture development with a high level of accuracy by analyzing all mutually perpendicular profiles (quasi-3D) which form the surface of a fracture examined by stereometric methods using a profilographometer.

2. Tools and materials

The materials studied were seven grades of WC-Co sintered carbides having a two-phase structure: α (WC grains) + β (binding phase – Co). The criterion for the selection of grades for the research was differences of tungsten carbide grain size, from 0.5 to 8.0 μm, and various volume fractions of the cobalt phase, from 6% to 15%, as shown in Table 1.

Table 1. Chemical composition and properties of sintered carbide grades selected for the investigation

Grade	Chemical composition		Average diameter of WC grain, μm	Density, g/cm³	Hardness, HV_{30}
	% WC	% Co			
HF6	94.0	6.0	0.5–0.8	14.9	1800
H10	94.0	6.0	1.0–2.0	14.8	1600
H30	91.0	9.0	1.0–2.0	14.6	1380
G10	94.0	6.0	2.0–3.0	14.9	1430
G30	85.0	15.0	2.0–3.0	14.0	1150
B2	91.0	9.0	2.0–3.0	14.6	1250
B23G	90.5	9.5	6.0–8.0	14.6	1050

The fracture surfaces for the research were the outcome of a three-point static bending test, for which a specially made ZDM-2500 testing machine was used. The

tests were conducted with accurate strain measurement in the force range 0–25 kN. Samples of dimensions: $l = 50$ mm, $b = 6$ mm, $h = 10$ mm were used (Figs. 1, 2).
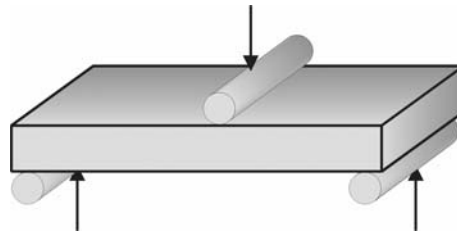
Fig. 1. Diagrammatic drawing of three-point
bending of sintered carbides
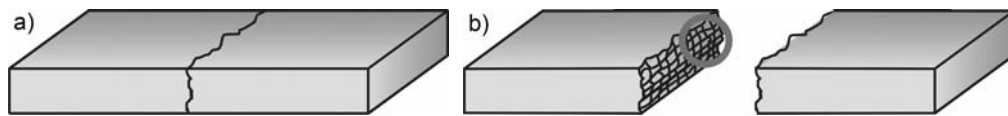
Fig. 2. Sample after three-point bending (a) and fracture surface
with a marked place of stereometric analysis (b)

3. Results and analysis

The fracture surfaces of all sintered carbide grades were subjected to measurement using a Taylor–Hobson's Form TalySurf Series 2 profilographometer. This device (Fig. 3) is fully automated and gives very high accuracy and speed of making measurements.
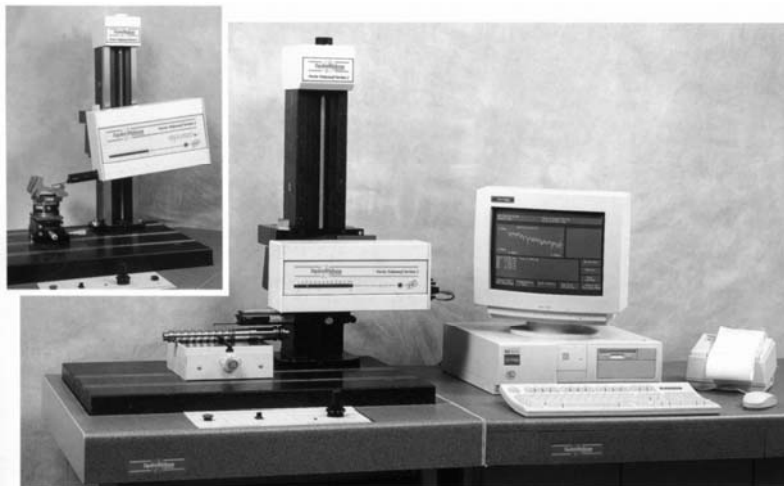
Fig. 3. Stand for stereometric investigations of surface
(Taylor Hobson's profilographometer)

Its software facilitates visualization of the surface microgeometry using topographic maps (Fig. 4) or isometric images (Fig. 5). In the investigation, a sampling step of 1 μm was applied in *X* and *Y* directions with the indication accuracy of 2% or 4 nm. The scope of the measuring head in axis *Z* was 1 mm with 16 nm resolution.
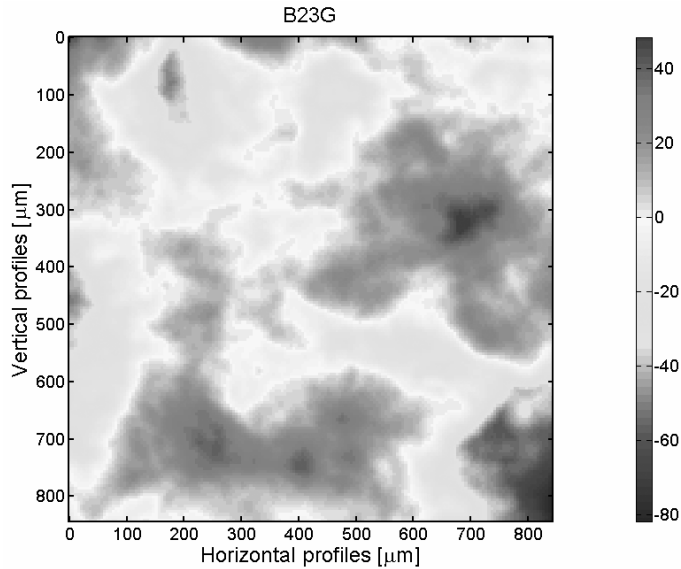
Fig. 4. Example of a topographic map of the investigated surface
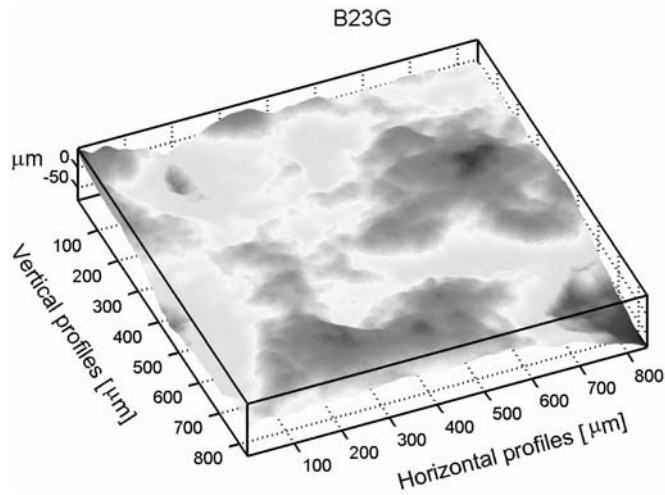
Fig. 5. Isometric view of a surface measured using a profilograph

An area of 841 μm×841 μm was investigated, from which 707 281 measuring points were obtained (Figs. 4, 5). From the whole set, singular, mutually perpendicular profile lines were selected (Fig. 6).
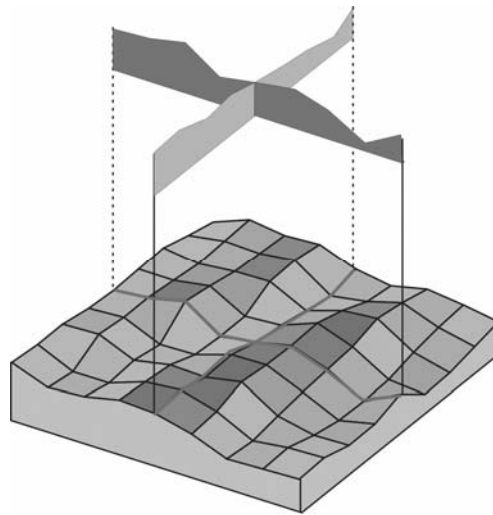
Fig. 6. Examples of mutually perpendicular fracture surface profiles
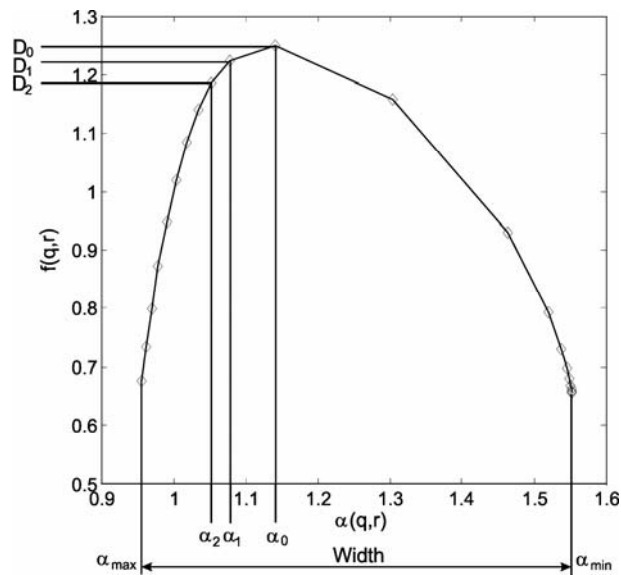
Fig. 7. Characteristic values of a multifractal spectrum. D_0, D_1, D_2
– some fractal dimensions: capacitive, informative and correlative,
respectively; α_0, α_1, α_2 – Hölder's exponents
corresponding to fractal dimensions

These profiles were real equivalents of the simulated profiles obtained as a result of applying a procedure to remove overlaps. Each of the profiles was subjected to a multifractal analysis [3, 6, 8–10]. The complete procedure was applied for the profiles in two mutually perpendicular directions. Altogether, 841 profiles were examined for each direction. Values of the multifractal spectrum (Fig. 7) characteristic of

perpendicular directions were averaged (Table 2). The symbols *V* and *H*, for vertical and horizontal directions respectively, have been used in the table to distinguish between the directions. Table 3 contains averaged values for the entire surface analyzed.

Table 2. Average values of characteristic results
of a multifractal analysis for each of the *V* and *H* directions[1]

Material	D_0	α_0	D_1	α_1	D_2	α_2	α_{min}	α_{max}	Width
B2 *V*	1.0000	1.0004	0.9996	0.9996	0.9981	0.9986	1.0406	0.7944	0.2462
B2 *H*	1.0000	1.0004	0.9996	0.9996	0.9983	0.9988	1.0357	0.8381	0.1976
B23G *V*	1.0000	1.0003	0.9997	0.9997	0.9985	0.9989	1.0478	0.7034	0.3445
B23G *H*	1.0000	1.0002	0.9997	0.9997	0.9989	0.9992	1.0384	0.7902	0.2482
G10 *V*	1.0000	1.0007	0.9992	0.9992	0.9964	0.9974	1.0342	0.8073	0.2269
G10 *H*	1.0000	1.0003	0.9997	0.9997	0.9986	0.9990	1.0292	0.8733	0.1559
G30 *V*	1.0000	1.0003	0.9997	0.9997	0.9987	0.9991	1.0399	0.7848	0.2551
G30 *H*	1.0000	1.0006	0.9994	0.9994	0.9974	0.9981	1.0381	0.7588	0.2793
H10 *V*	1.0000	1.0004	0.9996	0.9996	0.9982	0.9987	1.0373	0.8309	0.2064
H10 *H*	1.0000	1.0001	0.9999	0.9999	0.9996	0.9997	1.0261	0.8703	0.1558
H30 *V*	1.0000	1.0003	0.9997	0.9997	0.9986	0.9989	1.0212	0.8417	0.1795
H30 *H*	1.0000	1.0000	1.0000	1.0000	0.9999	0.9999	1.0217	0.8890	0.1327
HF6 *V*	1.0000	1.0010	0.9989	0.9989	0.9952	0.9964	1.0198	0.8606	0.1592
HF6 *H*	1.0000	1.0002	0.9998	0.9998	0.9990	0.9992	1.0222	0.8570	0.1652

[1]Description of symbols used in the table see Fig. 7.

Table 3. Average values from mutually perpendicular analysis directions containing
a total of 1682 profiles of the entire surface of each material grade[1]

Material	D_0	α_0	D_1	α_1	D_2	α_2	α_{min}	α_{max}	Width
B2	1.0000	1.0004	0.9996	0.9996	0.9982	0.9987	1.0382	0.8163	0.2219
B23G	1.0000	1.0003	0.9997	0.9997	0.9987	0.9990	1.0431	0.7468	0.2963
G10	1.0000	1.0005	0.9995	0.9995	0.9975	0.9982	1.0317	0.8403	0.1914
G30	1.0000	1.0004	0.9996	0.9996	0.9981	0.9986	1.0390	0.7718	0.2672
H10	1.0000	1.0002	0.9998	0.9998	0.9989	0.9992	1.0317	0.8506	0.1811
H30	1.0000	1.0002	0.9998	0.9998	0.9992	0.9994	1.0215	0.8654	0.1561
HF6	1.0000	1.0006	0.9994	0.9994	0.9971	0.9978	1.0210	0.8588	0.1622

[1]Description of symbols used in the table see Fig. 7.

Changes of the multifractal spectrum arms' spacing as a function of distance of the analyzed profile from the beginning of thea sample are shown in Figs. 8 and 9. Significant changes in the spectrum width in perpendicular directions are visible both for the material with the highest (Fig. 8) and the lowest percentage share of overlaps (Fig. 9). The differences may result from the fact that one of the examined directions (vertical) and the crack direction converged, whereas the other (horizontal) was perpendicular to the crack direction.
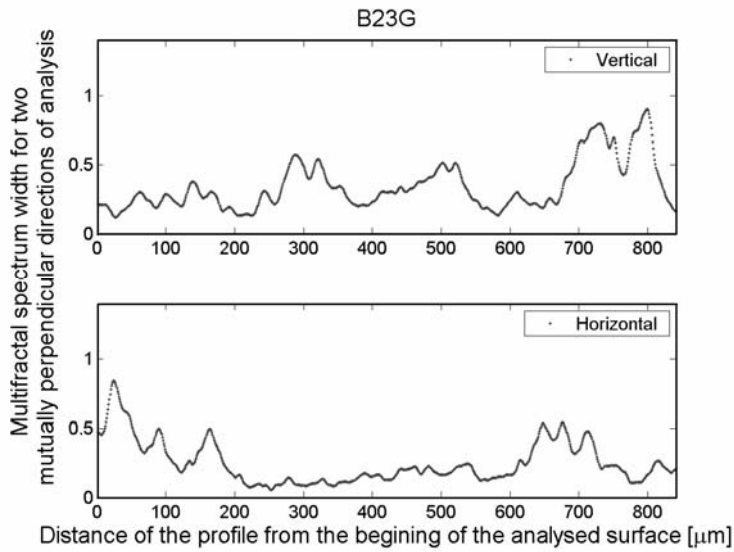
Fig. 8. Change of the multifractal spectrum width for a sample
of the highest percentage share of overlaps (B23G)
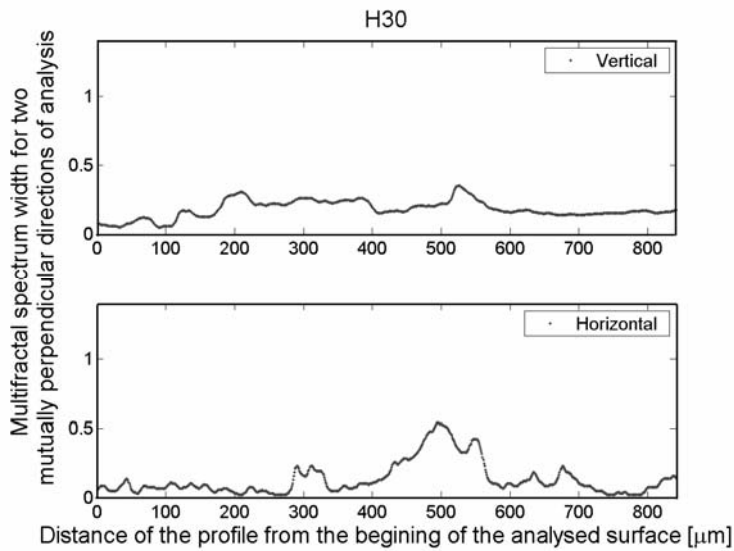

Fig. 9. Change of the multifractal spectrum width for a sample
of the lowest percentage share of overlaps (H30)

The average spectrum widths obtained from the mutually perpendicular directions on the surface (the last column in Table 3) were converted (hence the name – quasi -3D) on the basis of the dependence given in [2] into adequate percentage share of overlaps (Table 4).

Table 4. Comparison of the overlap percentage share values obtained by conventional
method and by applying the quasi-3D profilographometric methodology

Material	Multifractal spectrum width (quasi-3D analysis)	Percentage share of overlaps quasi-3D (read from the correlation plot from 2D analysis)	Percentage share of overlaps (mean from four specimens, microscope)
B2	0.2219	5.60	7.12
B23G	0.2963	9.90	11.40
G10	0.1914	3.84	3.31
G30	0.2672	8.22	7.64
H10	0.1811	3.24	4.70
H30	0.1561	1.80	2.53
HF6	0.1622	2.15	2.79

The results of the calculated percentage share of overlaps obtained by two methods are comparable, however, the quasi-3D method often shows lower values. This may result from the fact that the profilometric analysis for one profile is conducted in one direction only, whereas in the case of the quasi-3D method, the results are obtained for 841 mutually perpendicular profiles.

4. Conclusions

In the study, the stereometric methodology of fracture surface research was applied, supported by a multifractal analysis of mutually perpendicular profiles (quasi-3D). It has been shown that for these profiles, from material of the same grade, the width of the multifractal spectrum is different. This requires the values to be averaged in order to maintain aresults representative of the entire fracture. Measurement of such profiles by profilometry methods, using quantitative fractography to this end, enables data about the secondary cracks and overlaps to be obtained, as well as the share of individual phases in the fracture, simultaneously eliminating randomness of selection of only one, terminal profile for an analysis.

The spectrum widths averaged for both directions and converted, based on the dependence presented in [8], allow approximation, with good consistency, of the percentage share of overlaps determined by a profile analysis method. This means that the application of an algorithm to directly convert a stereometric file of a fracture surface into a multifractal one (full 3D analysis) [11] as well as verification of the solution for other material grades are purposeful. At the same time, this would allow checking the correctness of the dependence given in [8] between the spectrum width and overlaps share. It would then be possible to apply the formula so developed in further studies or directly link the crack mechanics parameters with the multifractal spectrum width as a measure of the material's fracture development.

References

[1] ROSKOSZ S., *Zastosowanie metod stereologicznych w ocenie dekohezji węglików spiekanych*, PhD Thesis, Silesian University of Technology, Katowice, 2000.

[2] WOJNAR L., *Fraktografia ilościowa. Podstawy i komputerowe wspomaganie badań*, Politechnika Krakowska, Kraków, 1990.

[3] STACH S., CYBO J., Materials Characterization, 51 (2003), 79.

[4] MANDELBROT B.B., T*he fractal geometry of nature*, W. H. Freeman and Comp., New York, 2000.

[5] FEDER J., *Fractals*, Plenum Press, New York, 1989.

[6] CHHABRA A., JENSEN R.V., Phys. Rev. Letters, 62 (1989), 1327.

[7] HASTINGS H.M., SUGIHARA G., Fractals, *A User's guide for the natural science*s. Oxford University Press, Oxford, 1993.

[8] STACH S., ROSKOSZ S., CYBO J., CWAJNA J., Materials Characterization, 51 (2003), 87.

[9] STACH S., ROSKOSZ S., CYBO J., *Multifractal description of fracture morphology. Methodology*, unpublished.

[10] XIE H.WANG J.-A.STEIN E., Phys. Letters A, Vol. 242 (1998), 41.

[11] STACH S., CYBO J., CWAJNA J., ROSKOSZ S., Mater. Sci.-Poland, 23 (2004), 583.

Multifractal description of fracture morphology. Full 3D analysis of a fracture surface

SEBASTIAN STACH[1*], JERZY CYBO[1], JAN CWAJNA[2], STANISŁAW ROSKOSZ[2]

[1]Department of Materials Science, Silesian University, ul. Snieżna 2, 41-200 Sosnowiec, Poland

[2]Department of Materials Science, Silesian University of Technology,
ul. Krasińskiego 8, 40-019 Katowice, Poland

Experimental verification of the theoretical methodology for describing a material's fracture morphology using multifractal analyis of a stereometrically examined surface (full 3D analysis) is presented. A high effectiveness of a multifractal analysis has been shown for a diversified multifractal spectrum width and for a quantitative description of overlaps. The values obtained are very similar to those obtained by the quasi 3D method [6] as well as by conventional analysis, that is analysis of the profile images obtained from transverse microsections. The method presented, however, is the least time-consuming, the cheapest and seems to be the most objective for fracture morphology analyses.

Key words: *fracture; surface; stereometry; overlaps; profile; multifractal; spectrum width*

1. Introduction

One of important tasks in material engineering is optimization of the material's properties, inter alia crack resistance [1]. Assuming that a fractal characterization of a profile line reveals more about the crack surface microgeometry and complexity of the crack path, a concept has been proposed for considering the problem of profile development in terms of a multifractal analysis [2–5]. The multifractal spectrum parameters should be closely related to the degree of profile development.

A completely new methodology of stereometric research of a very large number of mutually perpendicular profiles (quasi-3D method) which form a spatial image of the micro-geometry of a fracture surface has been applied [6]. The measurements were made using a Taylor-Hobson's TalySurf Series 2 profilographometer. For each perpendicular direction of a profile's position, a multifractal analysis was performed. The

---

[*]Corresponding author, e-mail: sstach@us.edu.pl

obtained spectrum widths were averaged and the percentage share of overlaps was calculated in accordance with the principles provided in [6–8]. The analyzed materials were seven grades of sintered carbide, WC-Co, of a two-phase structure having different tungsten carbide grain size and volume fractions of the cobalt phase.

The present paper aims at providing an unquestionably simplified research methodology. The idea of the full 3D method is to consider globally a surface measured with a profilographometer, without the need to analyse individual profiles [6]. It is expected that after applying relevant multifractal procedures and determining the width of a spectrum, the percentage share of overlaps should be determined more precisely and at much lower cost and labour usage than in the case with earlier presented methods.

2. Research tools

The research was undertaken with the tools and material described in [6]. The analysis of the fracture's stereometric files was based on an original algorithm consisting of fractal scaling (in many approximation steps) of the surface measured with a profilographometer followed by the calculation of Euclidean distances between the measuring points (for a given scale and box). The measurements of the surface were made with the greatest possible accuracy in order to meet the criterion in which the "box" size in the box-counting method is approaching zero (Fig. 1).
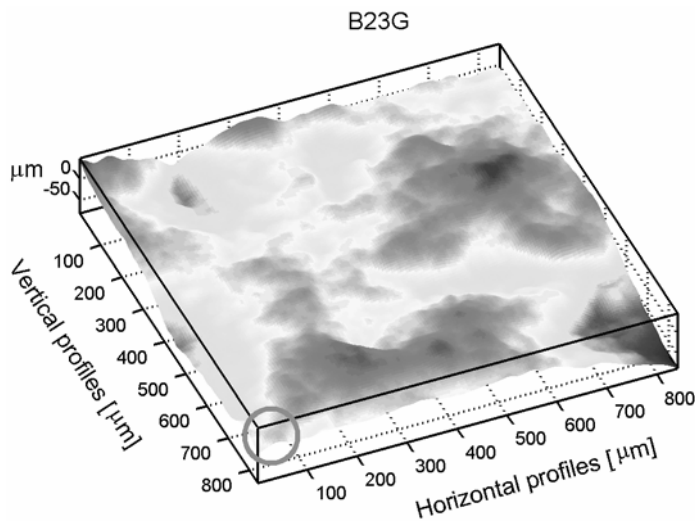

Fig. 1. Isometric view of a surface with a marked small area
whose enlarged image is shown in Fig. 2

Next, changing the size of boxes was simulated by changing the measuring density. By selecting every 1st, 2nd, 3rd, 4th, 5th, 6th, 7th, 8th, 10th, 12th, 14th, 15th,

20th, 21st, 24th, 28th, 30th, 35th, 40th, 42nd, 56th, 60th, 70th, 84th, 105th, 120th, 140th, 168th, 210th, 280th and 420th measuring point from the entire surface measured (Fig. 1) for the analysis, 31 scalings of the surface were obtained (Fig. 2) which approximate to the real appearance of the surface when the distance between the measuring points decreases.
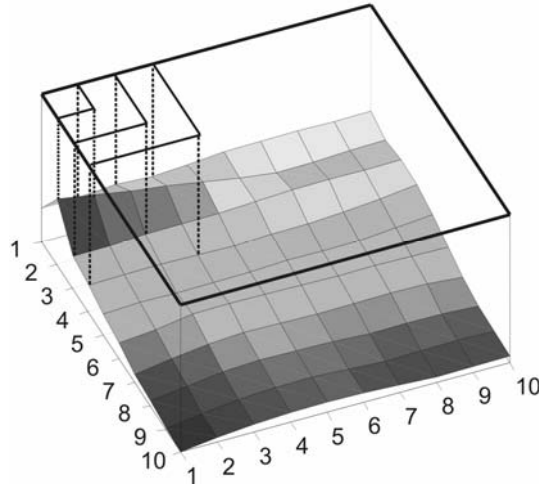

Fig. 2. Three exemplary (every 1, 2, 3 measuring points)
scalings of the surface measured

For the scaling matrices obtained (Fig. 3), an algorithm was applied consisting of calculating Euclidean distances (Fig. 4) between the closest neighbouring measuring points in each scaling step (1):

$$
\begin{bmatrix}
\text{Euc\_dist}_{a-b} = [\,\delta^2 + (h_{ai} - h_{bi})^2\,]^{1/2} \\
\text{Euc\_dist}_{b-c} = [\,\delta^2 + (h_{bi} - h_{ci})^2\,]^{1/2} \\
\text{Euc\_dist}_{c-d} = [\,\delta^2 + (h_{ci} - h_{di})^2\,]^{1/2} \\
\text{Euc\_dist}_{d-a} = [\,\delta^2 + (h_{di} - h_{ai})^2\,]^{1/2}
\end{bmatrix}
\tag{1}
$$

Next, for each of the measuring fields the maximum value was selected from 4 Euclidean distances for a given measuring field (2):

$$
A_i(\delta) = \max
\begin{bmatrix}
\text{Euc\_dist}_{a-b} & \text{Euc\_dist}_{b-c} \\
\text{Euc\_dist}_{c-d} & \text{Euc\_dist}_{d-a}
\end{bmatrix}
\tag{2}
$$

The values of maximum Euclidean distances were recorded in separate matrices (3) for each scale:

$$
\begin{bmatrix}
A_{w,k\ w,k}(\delta) & \cdots & \cdots & A_{1,840\ 1,841}(\delta) \\
\quad {}_{w,k\ w,k} & & & \quad {}_{2,840\ 2,841} \\
\cdots & & & \cdots \\
\cdots & & & \cdots \\
\cdots & & & \cdots \\
A_{5,1\ 5,2}(\delta) & & & \cdots \\
\quad {}_{6,1\ 6,2} & & & \\
\cdots & & & \cdots \\
A_{840,1\ 840,2}(\delta) & \cdots & \cdots & A_i(\delta) \\
\quad {}_{841,1\ 841,2} & & &
\end{bmatrix}
\tag{3}
$$
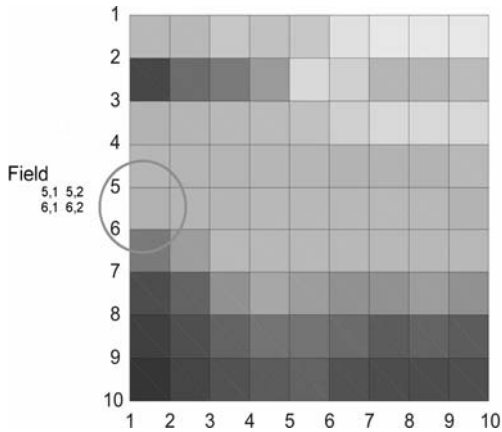
Fig. 3. Exemplary matrix of 9 per 9 measuring fields with a marked single field and its coordinates
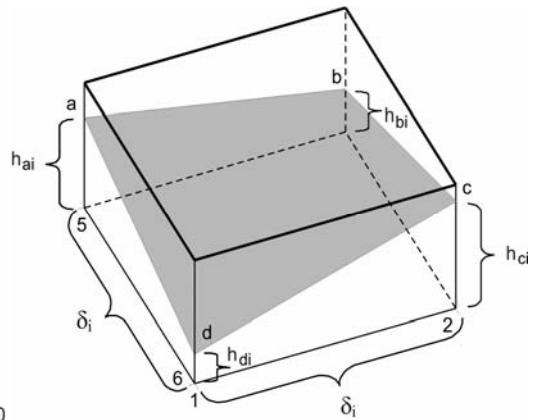
Fig. 4. Enlarged, isometric view of an exemplary measuring field with marked characteristic points

The probability was estimated (4) of the occurrence of each of the maximum Euclidean distance values:

$$
P_i(\delta) = \frac{A_i(\delta)}{A_Y(\delta)}
\tag{4}
$$

As a result, 31 matrices of multifractal measurements were obtained for each specimen (5), which were then subjected to analysis in accordance with the principles provided in [4–9]:

$$\begin{bmatrix} P_{w,k \; w,k}(\delta) & \cdots & \cdots & P_{1,840 \; 1,841}(\delta) \\ _{w,k \; w,k} & & & _{2,840 \; 2,841} \\ \cdots & & & \cdots \\ \cdots & & & \cdots \\ \cdots & & & \cdots \\ P_{5,1 \; 5,2}(\delta) & & & \cdots \\ _{6,1 \; 6,2} & & & \\ \cdots & & & \cdots \\ P_{840,1 \; 840,2}(\delta) & \cdots & \cdots & P_i(\delta) \\ _{841,1 \; 841,2} & & & \end{bmatrix} \tag{5}$$

3. Results and discussion of the multifractal analysis

The outcomes of these procedures were seven multifractal spectra (Fig. 5), the characteristic values of which are shown in Table 1.

The most important parameter from the point of view of the method described, is the width of arm's spacing of the multifractal spectrum whose interpretation has been provided in papers [6–9].

A transition from the quasi-3D analysis [6] to this full 3D analysis implies changes of the capacitive dimension D_0 from the value of 1 to 2. This is caused by the analysis of the two-dimensional matrix of Euclidean distances as opposed to the quasi-3D analysis where a one-dimensional list is subjected to an analysis. The multifractal spectrum widths are, in both cases, in full correlation, which enables a suitable conversion of the spectrum values based on a regression equation (the correlation diagram of both methods). The results are presented in Table 2.

On the basis of the converted widths of spectra, following the idea presented in [8], the percentage share of overlaps was estimated. The results are provided in Table 3.

The calculated percentage share of overlaps shows very high convergence with the values obtained both using the quasi 3D analysis and the conventional analysis based on quantitative fractography.

Although both methods (3D and quasi-3D) are similar, in the case of the former, slight differences in the estimation of the overlap's percentage share can be observed. This is caused by the selection of the maximum value from the four values calculated for each of the measuring fields.
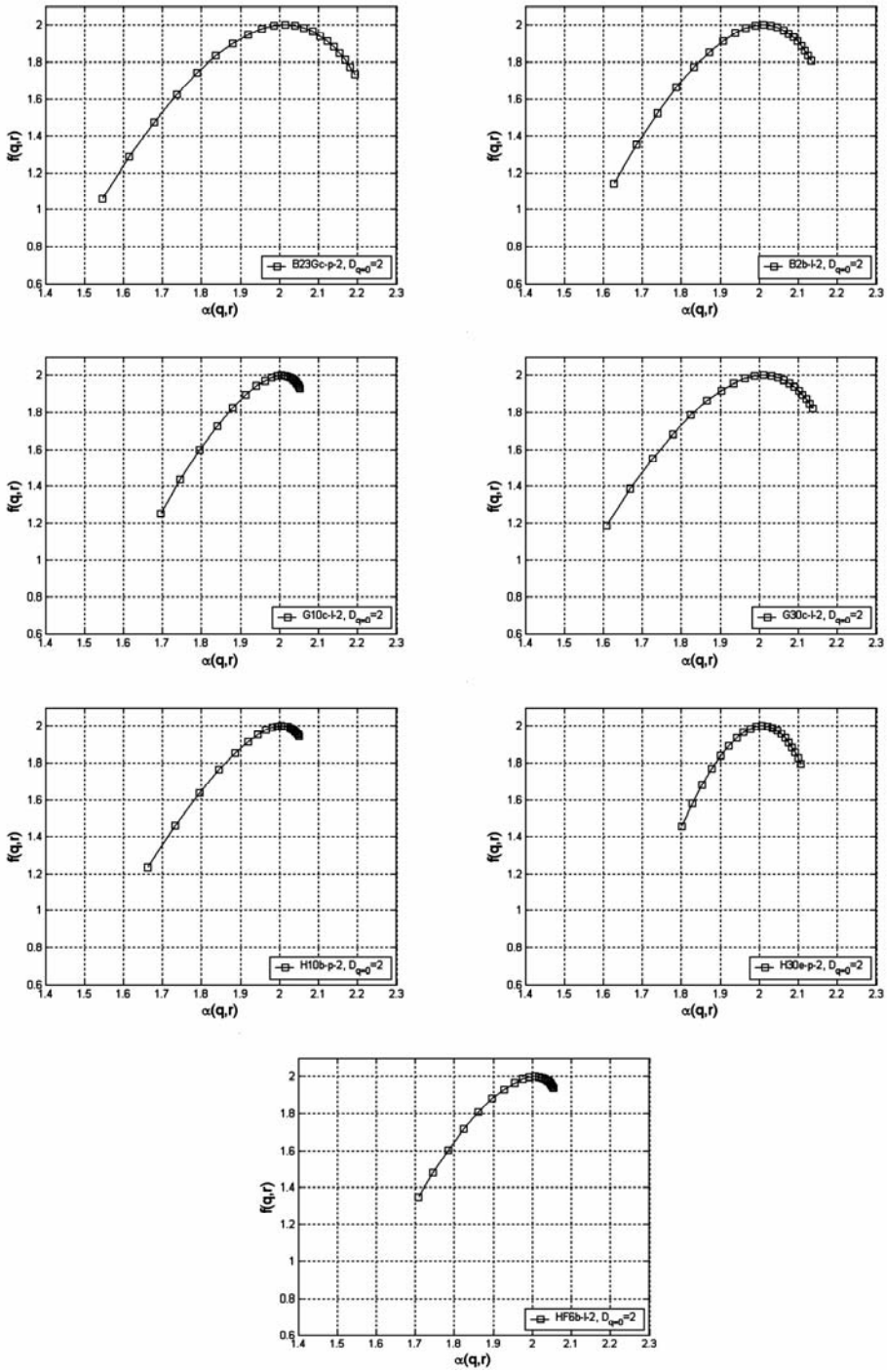
Fig. 5. Results of multifractal analysis for seven sintered carbide grades

Table 1. Characteristic values of multifractal spectra

Material	D_0	α_0	D_1	α_1	D_2	α_2	α_{min}	α_{max}	Width
B23G	2.0000	2.0140	1.9855	1.9855	1.9786	1.9539	2.1938	1.5454	0.6483
B2b	2.0000	2.0105	1.9890	1.9890	1.9819	1.9647	2.1321	1.6275	0.5046
G10	2.0000	2.0054	1.9941	1.9941	1.9895	1.9801	2.0525	1.6955	0.3571
G30	2.0000	2.0109	1.9886	1.9886	1.9832	1.9634	2.1364	1.6075	0.5289
H10	2.0000	2.0051	1.9946	1.9946	1.9916	1.9816	2.0496	1.6614	0.3882
H30	2.0000	2.0073	1.9926	1.9926	1.9852	1.9767	2.1058	1.8013	0.3045
HF6	2.0000	2.0065	1.9929	1.9929	1.9876	1.9757	2.0545	1.7074	0.3471

Table 2. Comparison of the values of multifractal spectrum widths obtained by two methods

Material	Multifractal spectrum width (quasi 3D analysis)	Multifractal spectrum width (3D analysis)	Multifractal spectrum width (3D analysis) (calculated)
B23G	0.2963	0.6483	0.3039
B2	0.2219	0.5046	0.2398
G10	0.1914	0.3571	0.1740
G30	0.2672	0.5289	0.2506
H10	0.1811	0.3882	0.1879
H30	0.1561	0.3045	0.1505
HF6	0.1622	0.3471	0.1695

Table 3. Comparison of the overlaps' percentage share values
obtained by conventional method and by applying multifractal techniques

Material	Percentage share of overlaps (full 3D analysis)	Percentage share of overlaps (quasi 3D analysis)	Percentage share of overlaps (microscope)
B23G	10.35	9.90	11.40
B2	6.73	5.60	7.12
G10	3.01	3.84	3.31
G30	7.34	8.22	7.64
H10	3.79	3.24	4.70
H30	1.68	1.80	2.53
HF6	2.76	2.15	2.79

4. Conclusions

The study aimed at maximum simplification of the research methodology by reducing it to a stereometric measurement of the fracture surface and next, to a multifractal analysis of the file obtained. Eventually, spectrum widths were obtained which in an indirect way enable the estimation of the overlap's percentage share for the en-

tire surface (full 3D analysis). High conformity of this methodology with the quasi 3D method presented in [6] has been shown.

The new method is simple and is characterized by low costs and labour consumption, which together ensure high effectiveness. It allows the right diversity in the fractal characteristics of fracture surface measured with a profilographometer. The multifractal spectrum width changes proportionally to the surface development degree, thus constituting a quantitative characterization of the entire surface analyzed, not only of a single profile.

It should be noted that the presented solution has been verified for one material characterized by a specific type of cracking, i.e. WC-Co carbides. As far as other materials are concerned, similar investigations should be conducted. The conclusions presented corroborate the results obtained for the 34CrMo4 steel [9]. In the same paper, the possibility of using the same formula which allows conversion of the spectrum width into the percentage share of overlaps was identified. This, however, requires confirmation, based on other cases, to be obtained.

References

[1] ROSKOSZ S., *Zastosowanie metod stereologicznych w ocenie dekohezji węglików spiekanych*, PhD Thesis, Silesian University of Technology, Katowice, 2000.
[2] MANDELBROT B. B., *The fractal geometry of nature*, W. H. Freeman and Comp., New York, 2000.
[3] FEDER J., *Fractals*, Plenum Press, New York, 1989.
[4] XIE H. WANG J.-A. STEIN E., Phys. Letters A, 242 (1998), 41.
[5] CHHABRA A., JENSEN R. V., Phys. Rev. Lett., 62 (1989), 1327.
[6] STACH S., CWAJNA J., ROSKOSZ S., CYBO J., Mater. Sci.-Poland, 23 (2005) 573.
[7] STACH S., CYBO J., Materials Characterization, 51 (2003), 79.
[8] STACH S., ROSKOSZ S., CYBO J., CWAJNA J., Materials Characterization, 51 (2003), 87.
[9] STACH S., SOZAŃSKA M., CYBO J., CWAJNA J., Acta Metallurgica Slovaca, 10 (2004), 768.

Methods for estimating the Hurst exponent.
The analysis of its value for fracture surface research

JERZY WAWSZCZAK[*]

School of Technical and Social Sciences, Warsaw University of Technology, Płock

The aim of the work was the selection of the most suitable method for fracture surface analysis using modern tools for mathematical verification of a dataset containing irregular data values and considerable variability of amplitude. The Hurst exponent was used for the verification of the analyzed dataset. The proposed procedure for the Hurst exponent calculations was verified for the profiles obtained from the fracture surface of 18G2A steel and pure iron in the rough state and after wavelet approximations.

Key words: *Hurst exponent; profile; wavelet decomposition*

1. Introduction

The surface obtained during the fracture test is not easy to describe and interpret due to its great level of complexity. Investigation processes usually give a collections of profiles [1]. The Fractal theory application for a description of the nature of the fracture surface has already led to significant developments of the physical interpretation. Application of the wavelet methods could simplify the profile analysis even further [2]. In this work, it has been assumed that the shape of a fracture surface is a natural consequence of the metallic materials crystalline structure, especially for brittle fractures arising from extreme conditions (fast strain rate, low temperature, etc.). The method of light section was used to obtain the shape of profiles from the fracture surface.

When using this method a real shape of the profile is distorted by secondary light beam reflections. In order to remove such reflections, a choice of a suitable filter is necessary. Every profile has to undergo the same procedure of image processing using the same parameters. In the present work, the wavelet decomposition method was applied as the filtration method of the profile.

_____

[*]Corresponding author, e-mail: jerzywa@plocman.pl

Differentiation between chaotic and determined components of the investigated images is another problem in the work presented. Fractals- and multifractals-based theory [3, 4], wavelet decomposition of the profile and estimating of the Hurst exponent have been used for this differentiation [5]. The aim of the study was the selection of the most suitable method for fracture surface analysis using modern tools for the mathematical verification of a dataset containing irregular data values and considerable variability in amplitude. The Hurst exponent analysis is a very popular procedure in many fields of scientific research. In this paper, the efficiency of several of the most popular methods using this exponent have been checked on several selected examples. Three methods were selected for the estimation of the Hurst exponent: the R/S method, the roughness–length (R–L) method and a variogram. The basic dependences have the following forms:

$$\frac{R^*_{(w)}}{S_{(w)}} = \frac{R}{S} = cw^H,$$ (1)

$$\overline{S}_{w(i)} = c\left(w_i\right)^{H^*}$$ (2)

$$V_{(w)i} = \left\{\left[y(x) - y(x + w_i)\right]^2\right\}^*$$ (3)

$$V_{(w)i} = cw_i^{2H}$$ (4)

where: $R_{(w)}$ is the difference of the height of the profile in the window, c – the constant, $S_{(w)}$ – the standard deviation, H – the Hurst exponent, w_i – the width of the window (section, lag), x and y are the data coordinates. The exponent H is the slope of an interpolated straight line in the log–log system. (The mark * denotes the mean value for the data on each of the windows).

The R/S method [6, 7] is commonly perceived as the most suitable for the time series analysis on the stock market or an optimal volume of water reservoirs, because it presents the relationship between irregular (singular) rescaled ranges, signal value and their local statistical properties relative to the scale factor. There is ample evidence of the popularity of this method.

The roughness–length method [8, 9] is the most popular for describing the roughness of surfaces and is descended from RMS profile analysis or calculations of the R_q – surface roughness parameter. The R–L method permits the description of profiles as the relationships between local statistical properties (standard deviation) versus the scale factor (length of part of the profile).

Variogram is similar to the roughness–length method because it uses Variance for the description of the average trend versus the length of windows (lags). The variogram method is the most popular in earth sciences or geomorphology and is very useful for surface approximations for sparse datasets [10].

2. Results

Available libraries of signal processing algorithms make it possible to choose a signal (profile) trace with established the Hurst exponent values. Testing procedures typically use values of $H = 0.3$, $H = 0.5$ and $H = 0.7$. The tested signal (profile) samples were derived from Benoit 1.3 [11] and the tested profiles from fracture surfaces were obtained from a 18G2A steel sample (impact test, -70 °C) and pure Iron 99.65 Fe (impact test, -191 °C). Figure 1 presents the results of the Hurst exponent calculations for the tested signals and the profile from the pure iron sample.
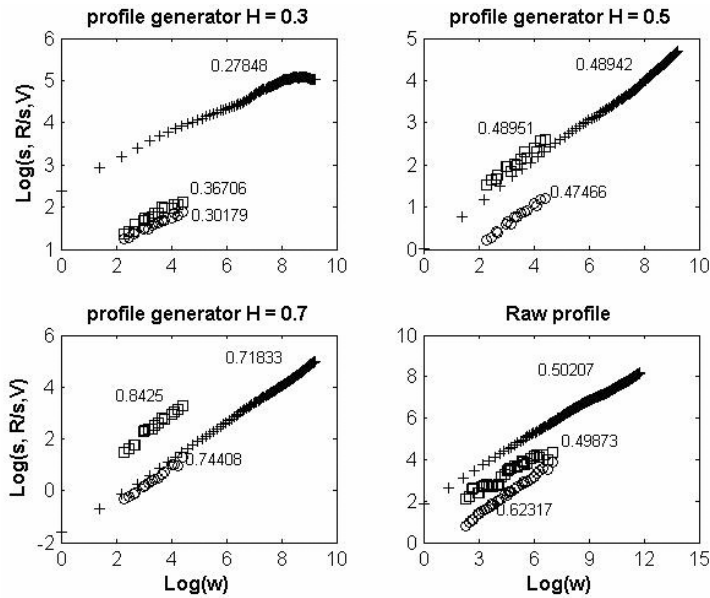

Fig. 1. Results of Hurst exponent calculation for investigated traces. Numbers beside the curve are linear estimation of slope. Marks denote: ○ – RL method, □ – R/S method, + variogram

It can be seen that the same tested trace (profile) gives different results of the Hurst exponent. The average errors of the calculations – the difference between the generated and the computed value of the Hurst exponent were analyzed. The error reached a maximum for the R/S method, the roughness–length and variogram gave very similar and low error values. For several of the calculated raw profiles from both the iron and steel surfaces the results vary. Exponents that are similar can be detected with the R/S method and variogram rather than the roughness–length method. Firstly, the number of points for testing traces ($H = 0.3$, $H = 0.5$ and $H = 0.7$) were 1000, for raw profiles ordinarily more than 3650 points.

Secondly, for the variogram usually the calculated maximum lag values are about 10% of the number of profile points, and for computer generated profiles the maximum lag = 100, and for raw profiles the maximum lag = 366. The other problem was

extraction of optical profiles from the fracture surfaces of the iron and steel samples. Preparation procedure between the raw profile and their graphical representation is shown in Fig. 2 [12].
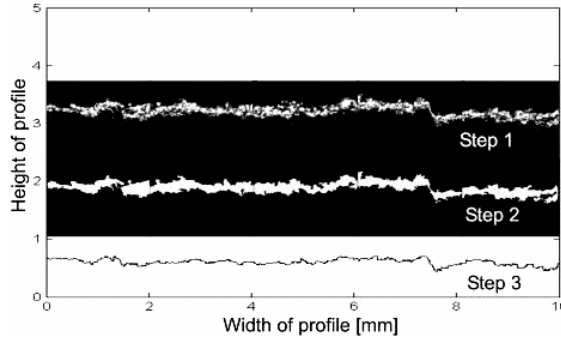

Fig. 2. Three steps profile preparations. Step 1 – acquisition of profile from dual lenses microscopy (originally for one profile we need 5 separated pictures). Step 2 – picture preparation on PhotoShop and Fovea Pro 3.0 (threshold and fill holes procedure). Step 3 – Profile computation and mathematical stitching on Matlab 7

The aim of the research was to find the maximum level of decomposition (with minimum changes of the Hurst exponent values. In this work Symlets3 (Sym3) and Debouchies4 (db4) wavelets were checked. Results of the investigation for R–L method are presented in Fig. 3. All the calculations were made using Matlab 7, where the algorithms were implemented [1–4].
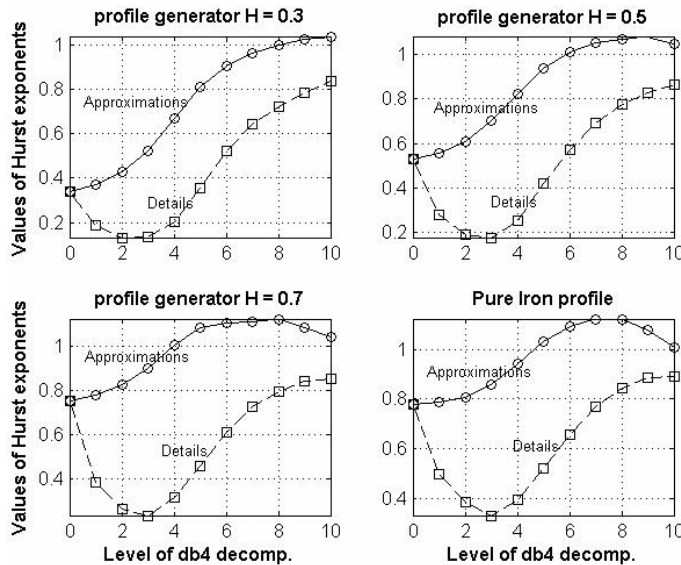

Fig. 3. Values of the Hurst exponent for R–L method, calculated with approximations and details after wavelets decomposition traces and profiles in Fig. 1

In Figure 3, each variant of the investigated profiles is presented. Of course, the results of the wavelet decomposition with levels higher than five or six do not make physical sense.
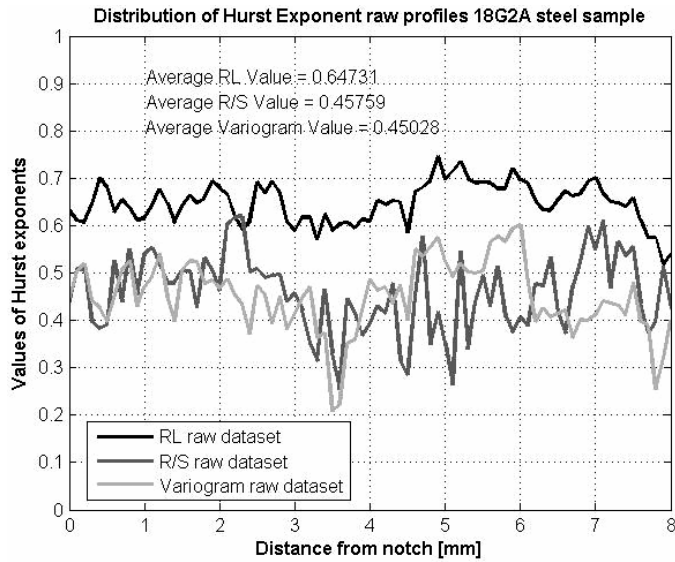

Fig. 4. Distribution of the Hurst exponent calculated on RL, R/S and Variogram algorithms
for fracture surface of 18G2A steel sample, broken (17 J energy, – 70 °C). Raw profiles were calculated
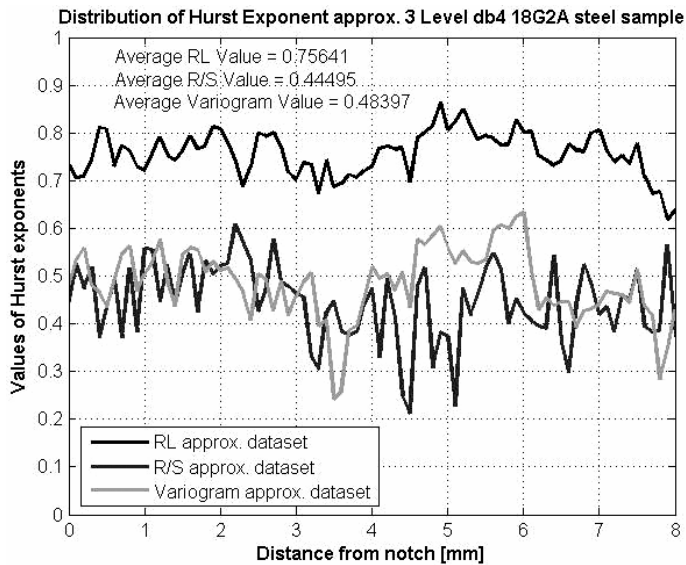

Fig. 5. Distribution of the Hurst exponent calculated on RL, R/S and Variogram
algorithms for fracture surface of 18G2A steel sample, broken (17 J energy, 70 °C).
Approximations of third level db4 profiles were calculated

Figures 4 and 5 present the distribution of the Hurst exponent calculated for the brittle fracture surface of 18G2A steel sample with a notch at the end of the sample. The distance between profiles was 0.1 mm and one pixel resolution was equal to 0.00268 mm. Figure 4 indicates the raw profile, Figure 5 concerns approximation of the same profile after a third level decomposition by db4 wavelets.

The presented results are controversial. Because the methods of calculation used interpret different physical properties, more sophisticated tools are needed, or stronger theoretical assumptions are required, for correct and precise interpretation. The procedure of scale range adjusting in the R/S method can affect the obtained results. The relationships between decomposition level and the R/S Hurst exponent's for approximations and details are under investigation and will probably explain the shapes of the distribution and dispersion as shown in Fig. 5.

3. Conclusions

The methods give described considerably different results. For two methods (R/S and variogram), the average Hurst exponent oscillate around the value of 0.5. The very convenient and popular roughness–length method gives a slightly higher value. Additionally, it is sensitive to high frequency signal removing processes. Nevertheless, locally, a part of the surface profile reveals significant dispersion of the Hurst exponent (especially the R/S method). In spite of similar theoretical foundations, the practical implementation of these methods is dependent on the physical nature of the investigated occurrence. Probably the R–L method offering the best approximation for the investigated case. The calculation is expensive in terms of time and computational power, but gives a very attractive possibility for analysis of profiles and images. The knowledge base in this scientific discipline is growing fast, especially in the areas of interpretation and algorithms of calculation. These facts create a new field and the possibility for materials science investigations.

References

[1] UNDERWOOD E.E., BANERJI K., Q*uantitative Fractography*, ASM Handbook, Vol. 12, Electronic Edition by ASM International, Metal Park Ohio, 1999.

[2] BIAŁASIEWICZ J., *Falki i aproksymacje*, WNT, Warszawa, 2000.

[3] SIMONSEN I., HANSEN A., NES O.M., Phys. Rev. E, 58 (1998), 2779.

[4] RELJIN S., RELJIN B.D., Arch. of Oncology 10 (2002), 283.

[5] MISTI M., MISTI Y., OPPENHEIM G., POGGI J.M., *Wavelet Toolbox Users Guide*, Version 2, The MathWorks Inc., 2002.

[6] *Estimating the Hurst Exponent*, http://www.bearcave.com/misl/misl_tech/wavelets/hurst/.

[7] HURST H.E., BLACK R., SINAIKA Y.M., *Long-Term Storage in Reservoirs: An experimental Study*, Constable, London, 1965.

[8] *Roughness-Length Method for Estimation Hurst Exponent and Fractal Dimension of Trace*s, Help Benoit 1.3 version Software, TruSoft International Inc., 2003.

[9] GÓRECKA R., POLAŃSKI Z., *Metrologia warstwy wierzchniej*, WNT, Warszawa, 1983.
[10] *Surfer 8 User Guide*, Chapter 5. *Variograms*, Golden Software Inc., 2004.
[11] *Self -Affine Trace Generator*, Help Benoit 1.3 version Software, TruSoft International Inc., 2003.
[12] WAWSZCZAK J., Problemy Eksploatacji, 51 (2003), 153.